ADVANCES IN THE IMAGING TECHNIQUES OF RADIOLOGICALLY SUBTLE CNS DISORDERS

EDITED BY: Ahmad Raza Khan, Maryam Ardalan, Brian Hansen and Syed Shadab Raza

PUBLISHED IN: Frontiers in Neuroscience and Frontiers in Human Neuroscience

frontiers Research Topics

ISSN 1664-8714
ISBN 978-2-83250-812-1
DOI 10.3389/978-2-83250-812-1

About Frontiers

Frontiers is more than just an open-access publisher of scholarly articles: it is a pioneering approach to the world of academia, radically improving the way scholarly research is managed. The grand vision of Frontiers is a world where all people have an equal opportunity to seek, share and generate knowledge. Frontiers provides immediate and permanent online open access to all its publications, but this alone is not enough to realize our grand goals.

Frontiers Journal Series

The Frontiers Journal Series is a multi-tier and interdisciplinary set of open-access, online journals, promising a paradigm shift from the current review, selection and dissemination processes in academic publishing. All Frontiers journals are driven by researchers for researchers; therefore, they constitute a service to the scholarly community. At the same time, the Frontiers Journal Series operates on a revolutionary invention, the tiered publishing system, initially addressing specific communities of scholars, and gradually climbing up to broader public understanding, thus serving the interests of the lay society, too.

Dedication to Quality

Each Frontiers article is a landmark of the highest quality, thanks to genuinely collaborative interactions between authors and review editors, who include some of the world's best academicians. Research must be certified by peers before entering a stream of knowledge that may eventually reach the public - and shape society; therefore, Frontiers only applies the most rigorous and unbiased reviews.
Frontiers revolutionizes research publishing by freely delivering the most outstanding research, evaluated with no bias from both the academic and social point of view. By applying the most advanced information technologies, Frontiers is catapulting scholarly publishing into a new generation.

What are Frontiers Research Topics?

Frontiers Research Topics are very popular trademarks of the Frontiers Journals Series: they are collections of at least ten articles, all centered on a particular subject. With their unique mix of varied contributions from Original Research to Review Articles, Frontiers Research Topics unify the most influential researchers, the latest key findings and historical advances in a hot research area! Find out more on how to host your own Frontiers Research Topic or contribute to one as an author by contacting the Frontiers Editorial Office: frontiersin.org/about/contact

ADVANCES IN THE IMAGING TECHNIQUES OF RADIOLOGICALLY SUBTLE CNS DISORDERS

Topic Editors:
Ahmad Raza Khan, Centre of Bio-Medical Research (CBMR), India
Maryam Ardalan, University of Gothenburg, Sweden
Brian Hansen, Aarhus University, Denmark
Syed Shadab Raza, ERA's Lucknow Medical College, India

Citation: Khan, A. R., Ardalan, M., Hansen, B., Raza, S. S., eds. (2022). Advances in the Imaging Techniques of Radiologically subtle CNS Disorders. Lausanne: Frontiers Media SA. doi: 10.3389/978-2-83250-812-1

Table of Contents

frontiers | Frontiers in Neuroscience

TYPE Editorial
PUBLISHED 03 November 2022
DOI 10.3389/fnins.2022.1059705

OPEN ACCESS

EDITED AND REVIEWED BY
Mario Sansone,
University of Naples Federico II, Italy

*CORRESPONDENCE
Ahmad Raza Khan
110ahmadkhan@gmail.com

SPECIALTY SECTION
This article was submitted to Brain Imaging Methods, a section of the journal Frontiers in Neuroscience

RECEIVED 01 October 2022
ACCEPTED 19 October 2022
PUBLISHED 03 November 2022

CITATION
Khan AR, Hansen B, Ardalan M and Raza SS (2022) Editorial: Advances in the imaging techniques of radiologically subtle CNS disorders. *Front. Neurosci.* 16:1059705. doi: 10.3389/fnins.2022.1059705

Editorial: Advances in the imaging techniques of radiologically subtle CNS disorders

Ahmad Raza Khan[1]*, Brian Hansen[2], Maryam Ardalan[3] and Syed Shadab Raza[4]

[1]Centre of Bio-Medical Research (CBMR), Lucknow, India, [2]Centre of Functionally Integrative Neuroscience, Aarhus University, Aarhus, Denmark, [3]Department of Physiology, Institute of Neuroscience and Physiology, Sahlgrenska Academy, University of Gothenburg, Gothenburg, Sweden, [4]Department of Stem Cell Biology and Regenerative Medicine, Era University, Lucknow, India

KEYWORDS

neuroimaging, MRI, radiologically subtle, CNS, MRS, PET, CT

Editorial on the Research Topic
Advances in the imaging techniques of radiologically subtle CNS disorders

Most CNS disorders manifest with subtle structural, biochemical, or physiological alterations at an early stage of the disease. However, most early changes are not detectable with conventional neuroimaging modalities, rendering early diagnosis difficult. While this is valuable for understanding disease origin and development, for this reason, there is a strong need for the development of tools that are sensitive to radiologically subtle CNS alterations. Such tools would be invaluable for accurate, early diagnosis and for objective evaluation of treatment interventions. Therefore, this Research Topic focused on progress in the detection of radiologically subtle CNS disorders.

The title attracted 21 submissions from different parts of the world, such as China, Egypt, Finland, India, Japan, Saudi Arabia, Sweden, and the UK. A total of 12 articles were accepted of which 8 are research articles and 4 review articles. In total, the studies list contributions from 100 authors.

Here, we briefly summarize the articles published in this Research Topic. Algahtany et al. suggested that multimodal techniques, such as positron emission tomography (PET), PET-MRI, single-photon emission computed tomography, functional MRI (f-MRI), magnetic resonance spectroscopy (MRS), and diffusion tensor imaging (DTI), that can be employed in combination to detect a lesion, its connection, and its intimacy with eloquent areas to limit surgery and avoid post-surgical complications, particularly in epileptic patients. Likewise, Sone also suggested employing non-Gaussian diffusion MRI parameters and Arterial Spin Labeling (ASL) techniques can non-invasively detect microstructural parameters and hypo-perfusion, respectively, within the focused lesions. These advancements in technology may also provide usefulness for both focused detection and a better understanding of epilepsy. Quan et al. hypothesized

that the radiomics features extracted from FLAIR and ADC images could be prognostic biomarkers for predicting clinical outcomes in acute ischemic stroke (AIS) patients. They developed a combined prediction model based on radiomics and DWI-ASPECTS and showed the superiority of the combined model. On retrospective data, the combined model showed unfavorable functional outcomes in patients with AIS. Zhu Q. et al. have shown that DKI parameters can significantly differentiate T1-hypointense lesions, T2-hyperintense lesions, normal-appearing white matter (WM), and WM microstructure in healthy controls. The damage in normal-appearing WM reflected by the DKI parameter, mean kurtosis could be a potential biomarker to evaluate the WM damage. This imaging-based classification in WM may help to evaluate the disease severity and progression. Jiang et al. performed a Tract-based Spatial Statistics (TBSS) study to explore WM integrity in the brain of End-Stage and Non-End-Stage Chronic Kidney Disease (ES-CKD and NES-CKD). The study showed that ES-CKD patients have more serious WM microstructure abnormalities than NES-CKD patients. The study also revealed that progressive WM abnormalities are associated with uric acid and phosphate levels in the blood. These findings also suggested that a multiparametric approach can provide a better understanding at a systemic level. Another study by Rawat et al. employed a multiparametric MRI approach that has revealed significant metabolic and volumetric alterations in the brain of patients with gluten ataxia (GA). *In-vivo* MRS revealed significant differences in NAA and NAA/choline ratios in the cerebellum. GA patients also had a significant reduction in total brain WM, cerebrum WM, and lateral ventricle and thalamic volume. Another study by Kumar et al. employed 1H MRS in two different brain regions viz., posterior parietal cortex and dorsolateral prefrontal cortex (DLPFC), to study neurochemical alterations in hyperthyroid patients, before and after antithyroid treatment. The 1H MRS has shown that hyperthyroidism causes changes in key metabolites in both regions, possibly indicating alterations in astrocyte physiology, glutamate/glutamine cycle, and/or oxidative stress. The altered neurometabolic ratios in the brain regions showed reversible changes after anti-thyroid treatment. The study strengthens the use of MRI in radiologically subtle CNS disorders and the outcome of efficient treatment intervention. Zhu L. et al. have used seed-based d mapping (SDM) a statistical technique for meta-analysis of neuroimaging studies. They studied hepatic encephalopathy (HE) patients for regional gray matter abnormalities using voxel-based morphometry. The study found gray matter volume reduction, especially in frontal regions, temporal insular cortex, and the caudate nucleus. The study also found an increase in plasma ammonia, which could be caused by increased blood flow to related brain regions in patients with cirrhosis. The study concludes that in patients with different degrees of HE, the changing area of gray matter volume was similar and the range of symptoms increased with aggravation. Zhu X. et al. explored whether the presence of impulse control disorder (ICD) in Parkinson's disease (PD) patients may determine abnormalities in the topological network by using rs-fMRI and graph theory methods. They divided PD patients into two groups, viz., PD-ICD and PD not ICD (PD-nICD) patients. The study showed that the clustering coefficient and characteristic path length of the brain functional network of PD-ICD patients increased, accompanied by damage to the Default Mode Network (DMN), Control Network (CN), and Dorsal Attention Network (DAN) nodes. The study also provides evidence for PD-ICD patients' brain network abnormalities from the perspective of information exchange. In another rs-MRI study, alterations in brain activity during microlesions in PD patients were investigated by Luo et al. They utilized the amplitude of low-frequency fluctuation (ALFF) and functional connectivity (FC) methods to explore changes associated with spontaneous brain activity and brain networks in PD patients before and after DBS surgery. The results demonstrated that implantation of DBS electrodes not only improves the activity of the basal ganglia-thalamocortical circuit but also reduces the activity of the DMN and ECN-related brain regions. These findings can be helpful for further understanding potential mechanisms that underlie microlesion in PD. Ai et al. have studied Rasmussen's Encephalitis (RE), a rare chronic neurological disorder characterized by unihemispheric brain atrophy and epileptic seizures. To reveal the involvement of genetic factors in the mechanisms of RE, whole-exome sequencing in 15 RE patients was performed in this study. They found single nucleotide variants (SNVs) in genes with the functions of antigen presentation, antiviral infection, epilepsy, schizophrenia, and nerve cell regeneration. The results suggest that RE is a polygenic disease and the triggering factors of the adaptive immune response may be SNVs related to antigen presentation and antiviral infection. Sasaguri et al. have reviewed the animal models of AD. The first-generation animal model expressed amyloid-beta (Aβ) peptide deposition and neuroinflammation. However, they have suffered from some artificial phenotypes, which could lead to erroneous interpretations of the outcome. The second-generation animal models of AD expressed Aβ pathology, neuroinflammation, vascular dysfunction as well as cognitive impairment in an age-dependent manner. However, these animal models also have some limitations. For instance, Aβ is resistant to proteolytic degradation and is therefore prone to aggregation in this model. The third-generation animal model exhibits more specific plaque pathology and neuroinflammation than the second-generation models and thus is more suitable for preclinical studies.

We strongly hope that this Research Topic will attract the attention of clinicians and researchers who are interested in developments toward a better understanding of CNS disorders where disease-related tissue alterations are too subtle to be radiologically visible at present. We thank not only all the

authors for their precious contributions but also the reviewers for sharing their expertise. Their efforts have secured this Research Topic as a collection of high-quality articles, which can be useful to the clinical and research communities.

Author contributions

AK wrote the editorial. BH, MA, and SR edited the editorial. All authors contributed to the article and approved the submitted version.

Funding

AK got support from the Centre of Biomedical Research (CBMR), Government of Uttar Pradesh, and funded by Ramalingaswami Re-entry Fellowship-2019 of the Department of Biotechnology (DBT), Ministry of Science and Technology, Government of India. MA was supported by Lundbeck- an international postdoc fellowship. SR's lab is supported by a generous grant from the International Brain Research Organization.

Conflict of interest

The authors declare that the research was conducted in the absence of any commercial or financial relationships that could be construed as a potential conflict of interest.

Publisher's note

frontiers in Neuroscience

ORIGINAL RESEARCH
published: 20 July 2021
doi: 10.3389/fnins.2021.699010

Altered Spontaneous Neural Activity and Functional Connectivity in Parkinson's Disease With Subthalamic Microlesion

Bei Luo[1†], Yue Lu[1†], Chang Qiu[1], Wenwen Dong[1], Chen Xue[2], Li Zhang[3], Weiguo Liu[4] and Wenbin Zhang[1]*

[1] Department of Functional Neurosurgery, The Affiliated Brain Hospital of Nanjing Medical University, Nanjing, China, [2] Department of Radiology, The Affiliated Brain Hospital of Nanjing Medical University, Nanjing, China, [3] Department of Geriatrics, The Affiliated Brain Hospital of Nanjing Medical University, Nanjing, China, [4] Department of Neurology, The Affiliated Brain Hospital of Nanjing Medical University, Nanjing, China

OPEN ACCESS

Edited by:
Brian Hansen, Aarhus University, Denmark

Reviewed by:
Andreas Wree, University of Rostock, Germany
Drozdstoy Stoyanov Stoyanov, Plovdiv Medical University, Bulgaria

***Correspondence:**
Wenbin Zhang
wenbinzhang@njmu.edu.cn

[†] These authors have contributed equally to this work and share first authorship

Specialty section:
This article was submitted to Neurodegeneration, a section of the journal Frontiers in Neuroscience

Received: *22 April 2021*
Accepted: *28 June 2021*
Published: *20 July 2021*

Citation:
Luo B, Lu Y, Qiu C, Dong W, Xue C, Zhang L, Liu W and Zhang W (2021) Altered Spontaneous Neural Activity and Functional Connectivity in Parkinson's Disease With Subthalamic Microlesion. Front. Neurosci. 15:699010. doi: 10.3389/fnins.2021.699010

Background: Transient improvement in motor symptoms are immediately observed in patients with Parkinson's disease (PD) after an electrode has been implanted into the subthalamic nucleus (STN) for deep brain stimulation (DBS). This phenomenon is known as the microlesion effect (MLE). However, the underlying mechanisms of MLE is poorly understood.

Purpose: We utilized resting state functional MRI (rs-fMRI) to evaluate changes in spontaneous brain activity and networks in PD patients during the microlesion period after DBS.

Method: Overall, 37 PD patients and 13 gender- and age-matched healthy controls (HCs) were recruited for this study. Rs-MRI information was collected from PD patients three days before DBS and one day after DBS, whereas the HCs group was scanned once. We utilized the amplitude of low-frequency fluctuation (ALFF) method in order to analyze differences in spontaneous whole-brain activity among all subjects. Furthermore, functional connectivity (FC) was applied to investigate connections between other brain regions and brain areas with significantly different ALFF before and after surgery in PD patients.

Result: Relative to the PD-Pre-DBS group, the PD-Post-DBS group had higher ALFF in the right putamen, right inferior frontal gyrus, right precentral gyrus and lower ALFF in right angular gyrus, right precuneus, right posterior cingulate gyrus (PCC), left insula, left middle temporal gyrus (MTG), bilateral middle frontal gyrus and bilateral superior frontal gyrus (dorsolateral). Functional connectivity analysis revealed that these brain regions with significantly different ALFF scores demonstrated abnormal FC, largely in the temporal, prefrontal cortices and default mode network (DMN).

Conclusion: The subthalamic microlesion caused by DBS in PD was found to not only improve the activity of the basal ganglia-thalamocortical circuit, but also reduce the activity of the DMN and executive control network (ECN) related brain regions. Results from this study provide new insights into the mechanism of MLE.

Keywords: amplitude of low-frequency fluctuation, deep brain stimulation, functional connectivity, microlesion effect, Parkinson's disease, resting state functional MRI, subthalamic nucleus, Parkinson's patients

INTRODUCTION

Deep Brain Stimulation (DBS) is an operation that is based on stereotactic technology that implants electrodes into specific nerve clusters or tissue structures within the brain, and regulates neuronal activity of the target nucleus by releasing pulsed electrical signals, which can alleviate symptoms of the disease (Miocinovic et al., 2013; Holiga et al., 2015; Lozano et al., 2019; Jakobs et al., 2020). DBS has emerged as an effective surgical treatment for Parkinson's disease (PD) (Miocinovic et al., 2013; Dayal et al., 2017; Habets et al., 2018). To date, common targets of DBS treatment of PD include the subthalamic nucleus (STN) and globus pallidus internus (GPI) (Zavala et al., 2015; Edwards et al., 2017; Thevathasan et al., 2018). Neurosurgeons often observe an interesting phenomenon associated with DBS. After electrodes have been implanted into the brain, patients that suffer from PD experience a transitory improvement in motor symptoms of several days-to-weeks before the pulse generator has been turned on. This phenomenon, known as microlesion effect (MLE), can even be observed in the operating room (Jech et al., 2012; Holiga et al., 2015). However, the exact mechanism behind MLE remains unclear (Jech et al., 2012; Singh et al., 2012; Holiga et al., 2015). Some studies have suggested that MLE is related to the output of abnormal basal ganglia caused by the destruction of cells and their fibers within the target nuclei caused by electrode implantation (DeLong, 1990; Holiga et al., 2015). Additionally, MLE has been associated with rapid leakage of neurotransmitters due to synaptic destruction, as well as postoperative edema in brain tissue around the electrodes (Jech et al., 2012; Holiga et al., 2015). The damage caused by DBS is similar to the damage induced by traditional thalamotomy (Alvarez et al., 2005), except that the damage is less (Alvarez et al., 2005). Some studies have also demonstrated that MLE is likely associated with postoperative deterioration of language fluency, as well as cognitive decline (Mikos et al., 2011; Lefaucheur et al., 2012; Costentin et al., 2019).

Currently, resting state functional MRI (rs-fMRI) has been widely utilized to study brain activity and network changes among patients with neurological and mental illness (Nathan et al., 2014; Poldrack and Farah, 2015; Tessitore et al., 2019; Ge et al., 2020). Compared to fMRI in the task state, rs-fMRI is simple (Park et al., 2020), easy to perform and highly repeatable (Smitha et al., 2019). In fact, there have been a few studies that have used rs-MRI in order to study alterations in the brain activity during microlesions (Jech et al., 2012; Holiga et al., 2015). Holiga et al. (2015) suggested that MLE associated-brainstem and cerebellar activation can compensate for damaged neurons in order to maintain relatively normal motor function during the acute phase of MLE. However, a lack of control groups undermines credibility of these results. Jech et al. (2012) believe that microlesions have a significant effect on fMRI patterns caused by simple finger movement, and that the expected activation of the mesial premotor region, the primary motor cortex and basal ganglia were observed during the tapping test. However, the effect of exercise itself on brain function was ignored.

Amplitude of low-frequency fluctuation (ALFF) and functional connectivity (FC) are frequently-used resting data processing methods that can help study brain activity and networks (İçer et al., 2020). ALFF is able to reflect the magnitude of spontaneous neural activity in the brain at rest (Harrington et al., 2017; Xia et al., 2019). FC detects the correlation between instantaneous nerve activity among different spatially independent brain regions (Aertsen et al., 1989; Pando-Naude et al., 2019).

Herein, ALFF and FC methods were utilized to analyze rs-fMRI whole brain data of the DBS microlesion period in order to study functional changes within the brain region, as well as to further understand the physiological and pathological mechanisms of MLE.

Abbreviations: DBS, deep brain stimulation; PD, Parkinson's disease; STN, subthalamic nucleus; GPI, globus pallidus internus; MLE, microlesion effect; AC, anterior commissure; PC, posterior commissure; TR, repetition time; TE, echo time; FA, flip angle; IFG, inferior frontal gyrus; MFG, middle frontal gyrus; PCC, posterior cingulate gyrus; DMN, default mode network; ECN, executive control network; rs-fMRI, resting state functional MRI; ALFF, Amplitude of low-frequency fluctuation; UPDRS-III, the Unified Parkinson's Disease Rating Scale part-III; PD-Post-DBS, one day after DBS; FC, functional connectivity; HCs, healthy controls; HAMA, Hamilton Anxiety scale; HAMD, Hamilton Depression scale; MMSE, Mini-Mental State Exam; FOV, field of view; DLPFC, dorsolateral prefrontal cortex; FWHM, full width at half maximum; ROIs, regions of interest; ANCOVA, analysis of covariance; FD, Mean frame-wise displacement; FWE, family-wise error; AAL, anatomical automatic labeling; MTG, middle temporal gyrus; MNI, Montreal Neurological Institute; MoCA, Montreal Cognitive Assessment; PDQ-39, the 39-item Parkinson's Disease Questionnaire (PDQ-39); PD-Pre-DBS, three days before DBS.

MATERIALS AND METHODS

Participants and Clinical Assessments

Overall, 43 patients with PD and 13 gender- and age-matched healthy controls (HCs) were recruited for this study. All participants were right-handed. PD patients were diagnosed according to the criteria of the UK Parkinson's Disease Society Brain Bank and underwent surgery after neurosurgeons rigorously assessed DBS surgical adaptation. The exclusion criteria of PD included diagnosis other neurological disorders,

mental illnesses or diseases that can have an effect on the central nervous system (i.e., cerebrovascular disease, brain trauma), presence of a metal foreign body in the head that can affect image quality and contraindication of MRI examination (i.e., cardiac pacemaker implantation). The HCs did not have a history of neurological and psychiatric diseases, as well as contraindications to MRI. The Hamilton Anxiety (HAMA) (Gjerris et al., 1983) and Hamilton Depression (HAMD) (Fava et al., 1982) scales were utilized for the assessment of mental and psychological states of all subjects. The Mini-Mental State Exam (MMSE) (Folstein et al., 1975) and Montreal Cognitive Assessment (MoCA) (Nie et al., 2012) helped assess cognitive and executive function. The quality of life of PD was evaluated by the 39-item Parkinson's Disease Questionnaire (PDQ-39) (Peto et al., 1998). Furthermore, PD patients were assess across three sessions with the Unified Parkinson's Disease Rating Scale part-III (UPDRS-III) (Goetz et al., 2008) and MMSE: three days before DBS (24 to 72 h before DBS), one day after DBS (24 to 48 h after DBS surgery), one month after DBS, and each time during off medication and absence of neurostimulation. The data for each patient three days before DBS and one day after DBS was divided into two groups of PD-Pre-DBS group and PD-Post-DBS group, respectively. The scales and MRI data of PD patients need to be collected at least 12 h after withdrawal of anti-Parkinson drugs (off-medication), in order to reduce the influence of drugs on data collection (Elfmarková et al., 2016; Manza et al., 2018). The study was granted approval by the Ethics Committee of The Brain Hospital affiliated with Nanjing Medical University on March 1, 2016, and written informed consent was obtained from all participants (Protocol Number, 2016-KY009).

Surgery

Herein, all PD patients underwent implantation of bilateral STN deep brain electrodes and all positions of the electrode were not adjusted during the implantation process. We utilized the cartesian stereo coordinate system in order to locate the target, which takes midpoint of the line between the anterior commissure (AC) and posterior commissure (PC) as the stereotactic origin. The STN target was located at 11∼12 mm, beside the midpoint of AC and PC, 3 mm backward, and 4 mm downward. Furthermore, we fine-tuned target coordinates based on the specific location of the nuclear cluster within the MRI image (see **Supplementary Table 1**). Avoiding the brain sulci and deep brain blood vessels, the implanted path arc and ring angles were determined (see **Supplementary Table 1**). A combination of local anesthesia and general anesthesia were utilized during this procedure. The DBS electrode (model E202, PINS) implantation was performed using local anesthesia while the pulse generator (model G102R, PINS) implantation was conducted under general anesthesia. The unified standardized DBS surgery and same target location method were adopted among all PD patients via a neurosurgeon.

Image Acquisition

The MRI data were gathered using a 1.5 Tesla GE Medical Systems scanner (produced by GE Medical System, Milwaukee, WI) using an 8-channel head coil. All subjects were then instructed to remain still, awake and think of nothing during the scan. In order to prevent and reduce the subjects' head movement, the supporting foam pad was utilized to fix the head, and elastic earplugs were provided to reduce interference of the machine noise. The patients were scanned on both three days before DBS and one day after DBS, while the HCs group was scanned only once. The rs-fMRI data was acquired using a gradient-recalled echo-planar imaging (GRE-EPI) sequence with repetition time (TR) of 2,000 ms, echo time (TE) of 40 ms, 28 slices, thickness of 3.0 mm with no gap, flip angle (FA) of 90°, field of view (FOV) of 240 mm × 240 mm, matrix size of 64 × 64, voxel size of 3.75 mm^3 × 3.75 mm^3 × 3 mm^3, and number of total volumes = 128. The T1-weighted anatomical images were acquired using 3D magnetization-prepared rapid gradient-echo (MPRAGE) sequence with TR of 11.864 ms, TE of 4.932 ms, FA of 20°, matrix size of 256 × 256, FOV of 152 mm × 152 mm, thickness of 1.4 mm, 112 slices, and voxel size of 0.59 mm^3 × 0.59 mm^3 × 1.4 mm^3.

Data Preprocessing

Functional data was preprocessed using the rs-fMRI data processing assistant (DPABI_V4.3, Beijing, China)[1] base on the MATLAB 2013b[2] platform. The preprocessing steps are consistent with previous literature (Xue et al., 2019; Li K. et al., 2020; Sun et al., 2020; Wang et al., 2020). The specific steps are described below. After converting the DICOM format of resting data into the NIFTI format, the first five volumes were discarded due to scanner instability. The remaining 123 phases of rs-fMRI data were corrected for differences in acquisition time between all slices of the whole brain, as well as for head movement. Subjects were excluded if they exhibited head translation exceeding 3.0 mm or rotation exceeding 3.0 degrees in any direction. Therefore, six PD patients were excluded due to excessive head movement. Next, the obtained images were normalized to the Montreal Neurological Institute (MNI) space, resampled to a voxel size of 3 mm^3 × 3 mm^3 × 3 mm^3 and then spatially smoothed with a gaussian kernel with full width at half maximum (FWHM) of 4 mm × 4 mm × 4 mm. The nuisance variables included 24 motion parameters, global signals, white matter signals, cerebrospinal fluid signals, as well as linear trends were regressed out using a general linear mode. Finally, a time-bandpass filter was carried out ($0.01\ Hz < f < 0.10\ Hz$) to eliminate the influence of high frequency physiological noise, as well as low frequency drift noise.

ALFF and FC Analysis

ALFF calculation was carried out using the DPABI_V4.3 software. All voxels were converted from the time domain to frequency domain through the use of the Fast Fourier Transform (Luo et al., 2020). The ALFF value of each voxel was obtained by averaging the square root of the power spectrum in the range of 0.01–0.10 Hz. Finally, the ALFF value of whole brain voxels was divided by mean ALFF value of all voxels in order to obtain a standardized ALFF map.

[1] http://rfmri.org/dpabi

[2] https://www.mathworks.com/products/matlab

Regions that had significant ALFF differences between before and after surgery in PD patients were identified as regions of interest (ROIs). A seed-based FC analysis was carried out through the use of Resting-State f-MRI Data Analysis Toolkit (REST_V1.8, Beijing, China)[3] (Song et al., 2011). The average time series of each ROIs was extracted, and correlation between the ROIs and the time series of each voxel in the whole brain was calculated in order to obtain FC maps. Finally, Fisher's z transformation (Long et al., 2016) helped normalize all FC maps in order to improve the normality of the data distribution.

Statistical Analysis

The SPSS22 software (Chicago, IL, United States) was utilized to statistically analyze the general clinical data of PD patients and HCs using Chi-square test and two-sample *t*-test, as appropriate. $P < 0.05$ is considered a statistically significant difference. Repeated measures ANOVA test was applied in order to compare the UPDRS-III scores of PD patients across different sessions.

An analysis of covariance (ANCOVA) was carried out to assess brain areas with significant ALFF/FC differences among the three cohorts (the PD-Pre-DBS group, the PD-Post-DBS group and HCs), with age and gender as covariates using SPM12.[4] Then, significantly different ALFF/FC brain regions among the three groups were extracted as a mask for *post hoc t*-tests. Two-sample *t* test was utilized to assess ALFF differences with age and gender as covariates between HC and PD-Pre-DBS group within this extracted ALFF mask. The differences of ALFF/FC between the PD-Pre-DBS group and the PD-Post-DBS group were analyzed through the use of paired *t*-tests with mean frame-wise displacement (FD) as covariates within the above extracted ALFF/FC mask. We applied an uncorrected voxel-level threshold $p < 0.001$ to display all results. Multiple comparisons of the family-wise error (FWE) rate with cluster $p < 0.05$ was also carried out for all results. The names of the brain regions with statistically significant differences were recorded according to anatomical automatic labeling (AAL) partitioning template (Rolls et al., 2015).

RESULTS

Demographic and Clinical Features

Overall, 37 PD patients and 13 HCs were included in the study (see **Table 1**), after excluding six patients. There were no significant differences with regards to gender ($p = 0.99$), age ($p = 0.76$) and MMSE scores ($p = 0.14$) between PD patients and HCs. However, there were significant differences in HAMA ($P < 0.001$), HAMD ($P < 0.001$) and MoCA scores ($P < 0.001$) between PD patients and HCs. The UPDRS-III ($p < 0.001$) and MMSE ($P = 0.004$) for PD patients varied significantly over three sessions.

[3]http://restfmri.net/forum/REST_V1.8

[4]https://www.fil.ion.ucl.ac.uk/spm/software/spm12/

ALFF Alterations

Compared to HCs, the PD-Pre-DBS group demonstrated increased ALFF in the right middle temporal gyrus (MTG), but decreased ALFF in the left MTG, left angular gyrus and bilateral precuneus (see **Table 2** and **Figure 1A**).

Relative to the PD-Pre-DBS group, the PD-Post-DBS group had higher ALFF in the right putamen, right inferior frontal gyrus (IFG) (triangular and opercular part), left middle frontal gyrus (MFG) and right precentral gyrus. However, the PD-Post-DBS group had lower ALFF in the right angular gyrus, right precuneus, right posterior cingulate gyrus (PCC), left insula, left MTG, bilateral MFG and bilateral superior frontal gyrus (dorsolateral prefrontal cortex; DLPFC) (see **Table 2** and **Figure 1B**).

FC Alterations

Based on differences between the PD-Pre-DBS and PD-Post-DBS groups, we chose left MTG, left insula, left MFG, right precuneus, right angular gyrus, right DLPFC, right putamen, right IFG and right precentral as ROIs and performed a voxel-wise analysis of the whole brain FC. There were no significant intergroup differences found in FC for three ROIs (left insula, right putamen and right precentral gyrus). Compared to the PD-Pre-DBS group, the PD-Post-DBS group demonstrated significantly decreased left MTG FC with left MTG and right superior temporal gyrus. Relative to the PD-Pre-DBS group, in right precuneus/PCC and right angular gyrus, the PD-Post-DBS group exhibited

TABLE 1 | Demographic and clinical data of all subjects.

	HCs (*n* = 13) Mean ± SD	PD (*n* = 37) Mean ± SD	*P*-value
Age (years)	62.46 ± 9.59	61.46 ± 9.47	0.76[a]
Sex (male/female)	6/7	17/20	0.99[b]
MoCA score	28.77 ± 1.09	24.14 ± 4.58	<0.001[a]*
HAMA score	0.39 ± 0.51	6.43 ± 3.93	<0.001[a]*
HAMD score	0.69 ± 0.85	6.49 ± 4.13	<0.001[a]*
PDQ-39 score	NA	45.32 ± 13.44	–
MMSE score			
Three days before DBS	28.08 ± 1.75	26.78 ± 2.88	0.14[a]
One day after DBS	–	25.51 ± 3.97	
One month after DBS	–	26.62 ± 2.98	0.004[c]*
UPDRS-III score			
Three days before DBS	NA	38.19 ± 14.85	–
One day after DBS	NA	27.78 ± 11.31	–
One month after DBS	NA	38.89 ± 12.73	<0.001[c]*

HCs, healthy controls; PD, Parkinson's disease; MMSE, Mini-Mental State Examination; MoCA, Montreal Cognitive Assessment; HAMA, Hamilton Anxiety Scale; HAMD, Hamilton Depression Scale; UPDRS-III, the Unified Parkinson's Disease Rating Scale part-III; PDQ-39, the 39-item Parkinson's Disease Questionnaire; NA, not applicable; PD-Pre-DBS, three days before DBS, PD-Post-DBS, one day after DBS, each time in the off medication and absence of neurostimulation; DBS, deep brain stimulation.

[a]P-value was obtained by a two-sample t-test between PD and HCs groups.

[b]P-value was obtained by a chi-square test between PD and HCs groups.

[c]P-value was obtained by a repeated measures ANOVA test in three sessions.

**P < 0.05.*

TABLE 2 | Alterations of ALFF between the PD-Pre-DBS group and HCs, as well as between the PD-Pre-DBS group and the PD-Post-DBS group (voxel $p < 0.001$, FWE correction with cluster $p < 0.05$).

	Brain region (AAL)	Cluster size	Peak MNI coordinate (X, Y, Z)			Peak intensity
PD-Pre-DBS > HCs						
Cluster1	Temporal_Mid_R	32	57	3	−21	5.4002
HCs > PD-Pre-DBS						
Cluster1	Temporal_Mid_L Angular_L	63	−45	−60	24	−4.8854
Cluster2	Precuneus_R Precuneus_L	122	3	−66	30	−5.0823
PD-Pre-DBS > PD-Post-DBS						
Cluster1	Temporal_Mid_L SupraMarginal_L	1863	−63	−57	6	14.9574
Cluster2	Insula_L	37	−39	−15	6	6.6421
Cluster3	Precuneus_R Cingulum_Post_R	200	3	−42	24	7.1653
Cluster4	Angular_R	77	36	−78	48	5.6689
Cluster5	Frontal_Mid_L Frontal_Sup_L	382	−39	15	57	10.5341
Cluster6	Frontal_Sup_R Frontal_Mid_R	157	27	36	48	6.5654
PD-Post-DBS > PD-Pre-DBS						
Cluster1	Putamen_R	223	27	0	9	−6.1208
Cluster2	Frontal_Inf_Tri_R Frontal_Inf_OperR	46	60	27	12	−4.9739
Cluster3	Precentral_R	72	42	−3	48	−6.768
Cluster4	Frontal_Mid_L	48	−24	24	33	−5.4787
Cluster5	Precentral_R Postcentral_R	191	36	−27	66	−5.7233

HCs, healthy controls; PD, Parkinson's disease; ALFF, amplitude of low-frequency fluctuation; FWE, the family-wise error; PD-Pre-DBS, three days before DBS, PD-Post-DBS, one day after DBS, one month after DBS, each time in the off medication and absence of neurostimulation; AAL, anatomical automatic labeling; MNI, Montreal Neurological Institute; DBS, deep brain stimulation.

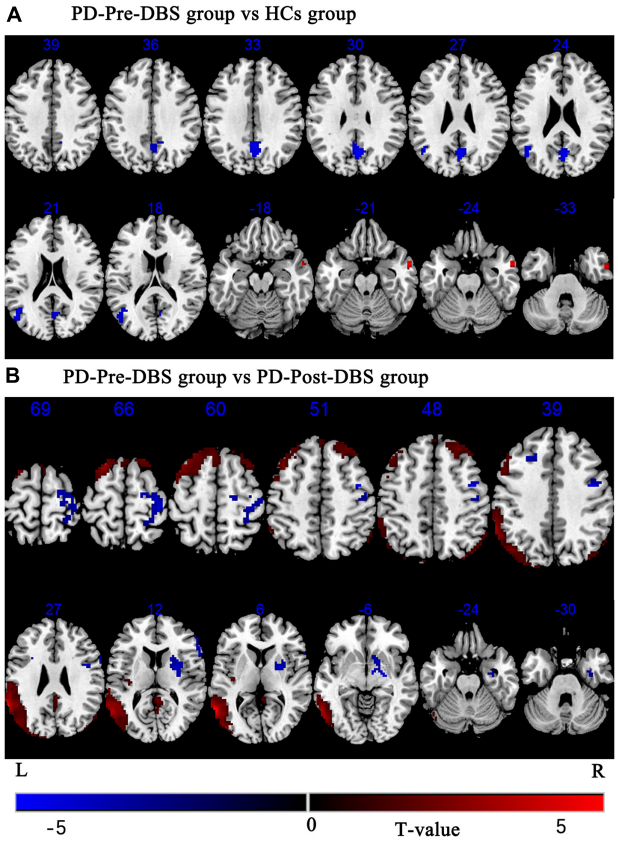

FIGURE 1 | Brain regions with altered ALFF between the PD-Pre-DBS group and HCs, the PD-Pre-DBS group and the PD-Post-DBS group were shown in **(A)** (PD-Pre-DBS group vs HCs group) and **(B)** (PD-Pre-DBS group vs PD-Post-DBS group), respectively. Regions showing increased ALFF in red and decreased ALFF in blue; L and R represent left and right hemispheres, respectively; The results were corrected by multiple comparisons of the family-wise error (FWE) (voxel $p < 0.001$, cluster $p < 0.05$); ALFF, amplitude of low-frequency fluctuation; PD-Pre-DBS, three days before DBS, PD-Post-DBS, one day after DBS, each time in the off medication and absence of neurostimulation; PD, Parkinson's disease; DBS, deep brain stimulation; vs, versus.

similar reduced FC in the right precuneus and bilateral MFG. Interestingly, we did not find increased FC. However, the PD-Post-DBS group had increased right IFG FC with right DLPFC. In addition, the PD-Post-DBS group had decreased left MFG FC with left precuneus and bilateral angular gyrus, but increased FC in the right temporal pole and bilateral supramarginal gyrus compared to the PD-Pre-DBS group. Furthermore, there were lower right DLPFC FC with left MTG, left cerebellum, right angular gyrus and bilateral precuneus, but higher FC with the right MTG, left superior temporal gyrus, left inferior parietal gyrus and left supramarginal gyrus in the PD-Post-DBS group than PD-Pre-DBS group. All of the above results were shown in **Table 3** and **Figure 2**.

DISCUSSION

Herein, we utilized ALFF combined with FC methods in order to explore changes associated with spontaneous brain activity and brain networks between HCs and PD patients before and after undergoing DBS surgery for the first time. The main focus of this study was to examine alterations of neural activity and functional networks in PD with subthalamic microlesions. After deep brain electrodes were implanted, compared to the PD-Pre-DBS group, the PD-Post-DBS group exhibited significantly increased ALFF in the basal ganglia-thalamocortical circuit (putamen, precentral gyrus), as well as decreased ALFF in the right precuneus/PCC and right angular gyrus within the default mode network (DMN) and DLPFC and MFG that belong to the executive control network (ECN). Furthermore, we observed aberrant FC in these regions with prefrontal and temporal lobes. Herein, we concluded that the brain activity and networks of PD patients were altered during the microlesion period. The results of this study complemented findings from previous studies (Jech et al., 2012; Holiga et al., 2015). On one day after surgery, the

TABLE 3 | Difference in functional connectivity between the PD-Pre-DBS group and the PD-Post-DBS group (voxel $p < 0.001$, FWE correction with cluster $p < 0.05$).

Seed area	Brain region (AAL)	Cluster size	Peak MNI coordinate (X, Y, Z)			Peak intensity
PD-Pre-DBS > PD-Post-DBS						
Left MTG						
Cluster 1	Temporal_Mid_L	82	−51	−42	−6	5.8543
Cluster 2	Temporal_Mid_L	268	−60	−57	21	8.7876
Cluster 3	Temporal_Sup_R	10	63	−45	21	3.9255
Right precuneus						
Cluster 1	Precuneus_R	51	6	−45	12	5.0775
Cluster 2	Angular_L	153	−48	−63	36	5.5852
Cluster 3	Frontal_Mid_R	25	33	21	42	4.6804
Cluster 4	Frontal_Mid_L	46	−30	24	48	4.4671
Right angular gyrus						
Cluster 1	Occipital_Mid_L	161	−33	−75	39	6.703
Cluster 2	Frontal_Mid_R	165	36	24	48	7.1617
Cluster 3	Frontal_Mid_L	51	−27	30	51	7.2077
Cluster 4	Precuneus_R	37	12	−60	48	5.0676
Left MFG						
Cluster 1	Precuneus_L	282	0	−54	24	5.2609
Cluster 2	Angular_L	217	−48	−66	36	5.8502
Cluster 3	Angular_R	130	42	−69	42	6.4341
Right DLPFC						
Cluster 1	Cerebelum_Crus1/2_L	57	−39	−72	−36	5.3958
Cluster 2	Temporal_Mid_L	45	−63	−54	−9	4.4681
Cluster 3	Angular_R	118	45	−69	39	5.0381
Cluster 4	Precuneus_L/R	22	3	−69	45	3.9463
PD-Post-DBS > PD-Pre-DBS						
Left MFG						
Cluster 1	Temporal_Pole_Sup_R	41	33	9	−33	−4.7855
Cluster 2	SupraMarginal_L	222	−60	−39	24	−6.9765
Cluster 3	SupraMarginal_R	36	54	−24	36	−4.2578
Right DLPFC						
Cluster 1	Frontal_Mid_R	49	42	48	15	−6.2616
Cluster 2	Temporal_Sup_L	20	−57	−27	18	−4.995
Cluster 3	Parietal_Inf_L	17	−60	−39	39	−4.2406
Right IFG						
Cluster 1	Frontal_Sup_R	23	21	48	36	−4.362

PD-Pre-DBS, three days before DBS, PD-Post-DBS, one day after DBS, each time in the off medication and absence of neurostimulation; MTG, middle temporal gyrus; MFG, middle frontal gyrus; DLPFC, dorsolateral prefrontal cortex; IFG, inferior frontal gyrus; AAL, anatomical automatic labeling; MNI, Montreal Neurological Institute; PD, Parkinson's disease; DBS, deep brain stimulation.

UPDRS-III scores for PD patients decreased significantly from 38.19 ± 14.85 to 27.78 ± 11.31, which is consistent with the patient's improved postoperative symptoms. However, after one month, the scores were found to be deteriorated by 38.89 ± 12.73, which reflects a transitory characteristic of MLE (Sitburana et al., 2010; Tykocki et al., 2013). Some patients had persisted for even longer (Kondziolka and Lee, 2004). This is in line with a study that suggests that the long-term clinical effects of MLE are small (Sitburana et al., 2010). In addition, one study observed a positive correlation between MLE and the degree of motor improvement that was induced by active stimulation after surgery (Tykocki et al., 2013).

Compared to the PD-Pre-DBS group, there was significantly increased ALFF value in the right putamen of the PD-Post-DBS group. The pathophysiology of PD is characterized by a striatal dopamine deficiency due to degeneration of dopaminergic nigrostriatal neurons (Hacker et al., 2012; Huot et al., 2016; Poewe et al., 2017; Shen et al., 2020). In particular, dopamine depletion is most pronounced within the putamen (Kish et al., 1988; Goldstein et al., 2017). Additionally, the putamen is a crucial component of basal ganglia-thalamocortical circuit (Amemori et al., 2011; Morigaki and Goto, 2016), which plays a key function in the development of movement disorders in PD (DeLong and Wichmann, 2015; Morigaki and Goto, 2016; McGregor and Nelson, 2019). Many previous studies have found consistent results of reduced putamen activity in PD (Zhang et al., 2015; Wang J. et al., 2018; Hu et al., 2020). Wang J. et al. (2018) have identified a consistent decrease in putamen activity in PD using a meta-analysis and an independent validation. Zhang et al. (2015) found that tremor-dominant PD patients showed decreased regional homogeneity in right putamen compared with HCs. There are lower ALFF in the bilateral putamen compared to HCs (Hu et al., 2020). Furthermore, there was also a significantly elevated ALFF in the right precentral gyrus in PD-Post-DBS, compared to the PD-Pre-DBS group. Previous imaging studies of PD have also observed abnormalities in the precentral gyrus (Uribe et al., 2016; Li J. Y. et al., 2020). The precentral gyrus is an area that is responsible for the output of movement and a key node of the basal ganglia-thalamocortical circuit (Bradberry et al., 2012; Burciu and Vaillancourt, 2018). Some studies have discovered a decrease of regional homogeneity (Li J. Y. et al., 2020) and cortical atrophy (Huang et al., 2016; Uribe et al., 2016) within the precentral gyrus of PD. These studies even suggested that they can be used as biomarkers for PD diagnosis or prognosis (Uribe et al., 2016; Li J. Y. et al., 2020). In addition, a study of the akinetic motor subtype of PD demonstrated a decrease in gray matter volume within the motor cortex, as well as abnormal FC between these areas and the cortex involved in motor planning and execution (Kann et al., 2020). These regions may play a key role in the unique longitudinal trajectory the akinetic motor subtype of PD (Kann et al., 2020). Therefore, we thought that development of PD was related to aberrant structure and function of the motor cortex, including its neural activity (Li J. Y. et al., 2020), gray matter volume (Kann et al., 2020), cortical thickness (Huang et al., 2016) and FC (Kann et al., 2020). Herein, we hypothesized that the increased activity of PD with the subthalamic microlesion in the putamen and precentral gyrus may relatively normalize neural activity of the PD-related motor cortex and enhance functioning of the basal ganglia-thalamocortical circuit, which causes transitory improvement of patients' symptoms after DBS. It was also helpful to understand the mechanisms of traditional thalamotomy (Alvarez et al., 2005) by studying the different causes of MLE.

Relative to the PD-Pre-DBS group, the PD-Post-DBS group had lower ALFF in the right precuneus/PCC and the right angular gyrus. These brain regions are all key components of the DMN (Seghier, 2013; Cunningham et al., 2017).

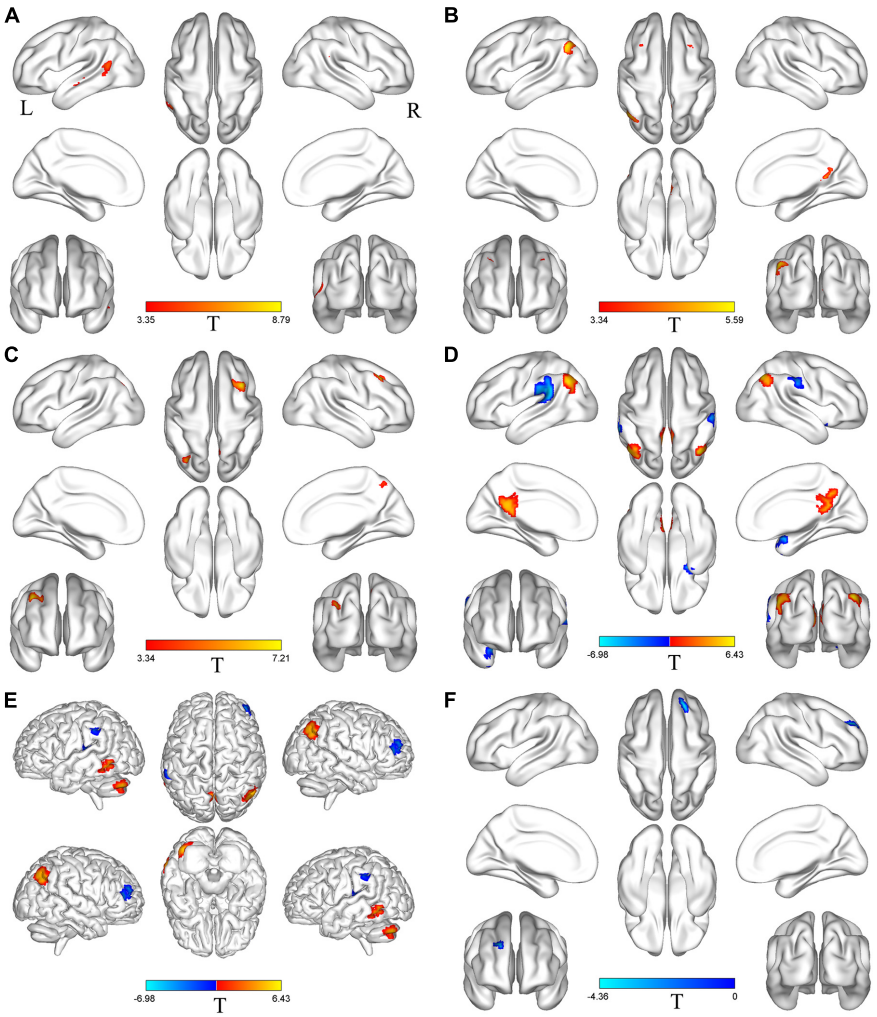

FIGURE 2 | Brain regions with altered FC between the PD-Pre-DBS group and the PD-Post-DBS group. Left middle temporal gyrus **(A)**, Right precuneus **(B)**, Right angular gyrus **(C)**, Left middle frontal gyrus **(D)**, Right dorsolateral prefrontal cortex **(E)**, Right inferior frontal gyrus **(F)** as ROIs and performed a voxel-wise analysis of the whole brain FC; Regions showing increased FC in red and decreased FC in blue; L and R represent left and right hemispheres, respectively; The results were corrected by multiple comparisons of the family-wise error (FWE) (voxel $p < 0.001$, cluster $p < 0.05$); FC, functional connectivity; PD-Pre-DBS, three days before DBS, PD-Post-DBS, one day after DBS, each time in the off medication and absence of neurostimulation; PD, Parkinson's disease; DBS, deep brain stimulation.

Numerous studies had demonstrated that DMN has a vital function in cognitive processing of neurodegenerative diseases (Lucas-Jiménez et al., 2016; Mohan et al., 2016; Kvavilashvili et al., 2020). In addition, DMN is related to the processing of emotionally-salient stimuli, working memory and consolidation of memory (Mohan et al., 2016). Some previous studies of PD patients with mild cognitive impairments have found similar results and that the dysfunction of DMN is associated with cognitive decline in PD (Hou et al., 2016; Lucas-Jiménez et al., 2016). These findings are consistent with our research results. Our observations regarding the alterations of ALFF between the PD-Pre-DBS group and HC are in line with these studies. Our results indicated reduced ALFF in the precuneus and angular gyrus in the PD-Pre-DBS group, compared to the HCs cohort. In addition, a study discovered that the function of DMN had been compromised in cognitively unimpaired patients with PD (Tessitore et al., 2012), which suggests that PD patients had an early functional disruption of the DMN in advance of any clinical evidence of cognitive impairment. Furthermore, the right precuneus/PCC and the right angular gyrus exhibited significantly reduced FC with right precuneus, left angular gyrus and bilateral MFG in the PD-Post-DBS group compared with PD-Pre-DBS group through further FC analysis. Therefore, these results indicate that reduction of neural activity of the precuneus/PCC may cause FC impairments of the DMN (Sandrone and Catani, 2013). We also observed lower ALFF values in the left insula in the PD-Post-DBS group. The insular lobe was thought to regulate DMN, as well as the fronto-parietal network (Fathy et al., 2020), and is associated with cognitive impairment in PD (Deen et al., 2011; Fathy et al., 2020). After STN-DBS, the cognitive decline on frontal executive function (Mikos et al., 2011; Lefaucheur et al., 2012), particularly verbal

fluency (Okun et al., 2009; Mikos et al., 2011; Lefaucheur et al., 2012), found in many studies is considered to be due to the surgical microlesion (Mikos et al., 2011; Lefaucheur et al., 2012). Verbal fluency still declines in the off STN-DBS states, which indicates that it is caused by surgery, rather than a stimulation-induced effect (Morrison et al., 2004; Mikos et al., 2011). The abnormality of the DMN function, caused by subthalamic microlesion, may be partly responsible for a decline in cognition, especially verbal fluency (Okun et al., 2009). Nevertheless, the absence of the assessment of postoperative language function in our study has prevented us from validating our considerations.

Compared to the PD-Pre-DBS group, the PD-Post-DBS group exhibited lower activities in the bilateral MFG and DLPFC. A PD study discovered significantly decreased gray matter volume in the superior frontal gyrus and MFG, compared to HCs (Li Y. et al., 2016). DLPFC and MFG are core and key regions of the ECN (Ham et al., 2015; Taren et al., 2017), and play an important role in maintenance and regulation of top-down modulation (Seminowicz and Moayedi, 2017), as well as driving appropriate behavioral responses (O'Reilly, 2010; Sallet et al., 2013). Furthermore, DLPFC was thought to be involved in cognitive processes (Cieslik et al., 2013; Seminowicz and Moayedi, 2017), such as attention and emotional regulation (Buhle et al., 2014; Bidet-Caulet et al., 2015). Hence, we suspected that DLPFC and MFG are involved in post-surgical cognitive decline. Further FC analysis, DLPFC and MFG exhibited decreased FC with DMN-related regions, such as the angular gyrus and precuneus, which further validated our theory. Additionally, we found a significantly elevated ALFF in the right IFG in the PD-Post-DBS group, when compared to the PD-Pre-DBS group. In some studies, this area was widely considered to have an important role in executive control function (Hampshire et al., 2010; Wang Z. et al., 2018). This finding is consistent with that of one previous study on PD patients with mild cognitive impairment that demonstrated higher ALFF in the right IFG (opercular part), which was also negatively correlated to the MoCA score (Wang Z. et al., 2018). At the same time, the PD-Post-DBS group had a significantly higher right IFG FC with right DLPFC, compared to the PD-Pre-DBS group. Therefore, we thought that hyperactivity of IFG likely indicates a compensatory effect of cognitive decline, caused by electrode implantation in PD.

FMRI has been widely utilized to study abnormal patterns of brain activity and connectivity in PD during rest and task (Wu et al., 2011; Mohl et al., 2017). In contrast to rs-fMRI, task-based fMRI requires subjects to carry out a series of specific experimental actions. Many previous studies have investigated altered brain function of the cortical and subcortical regions of the motor network in PD based on task-based MRI (Herz et al., 2014; Filippi et al., 2018). A study of Mohl et al. found that the effective connectivity of different motor networks responses to levodopa during a tapping task can distinguish the subtypes of PD (Mohl et al., 2017). In addition, PD patients exhibited decreased connectivity between the striato-cortical and striato-cerebellar pathways, while there is an elevated connectivity in the cortico-cerebellar motor areas that can possibly compensate for basal ganglia dysfunction during self-initiated movements (Wu et al., 2011). Tessa et al. discovered that PD patients have higher activity in the left primary sensorimotor cortex whose hypoactivation is associated with severity of the disease during hand motor tasks (Tessa et al., 2012). The purpose of our study is to examine changes in brain activity patterns of PD patients during microlesion stage in the resting state. Therefore, we used rs-fMRI as the imaging method in this experiment. This can help avoid a decrease in comparability of experimental results in task-based research due to different task designs and different performance of subjects. In the following study, we will use task-based fMRI in order to further explore the abnormalities of the motor network cortex in PD with subthalamic microlesions.

LIMITATIONS

There were several limitations to our study. First, the language function were not evaluated after surgery. The main purpose of our study was to investigate the changes of motor symptoms and explore alterations of spontaneous brain activity and brain networks during the microlesion period. Therefore, we only used the UPDRS scale to evaluate the fluctuation of motor symptoms after DBS and did not evaluate the changes in speech function after DBS operation. The assessment of lack of language function did not affect the results of this study. In the following studies, we will further evaluate the cognitive and language function of patients after DBS. Secondly, although the unified standardized DBS surgery was adopted among PD patients via a neurosurgeon, we were still not able to control the absolute consistency of the position of electrodes implanted in all patients. In addition, the target implanted in this study was STN, which is divided into different sub-regions (van Wijk et al., 2020; van Wouwe et al., 2020). The damage caused by implantation in different sub-regions can induce different alterations in brain function. However, due to the small size of STN and the overlapping between functional subregions (Karachi et al., 2005), we thought that all subregions of STN were passed through by the implanted stimulation electrode (Yelnik et al., 2003), which caused minor damage to all subregions. Finally, there were much fewer HCs in our study compared to the PD group. Although the difference in sample size was a limitation of this study, there was no significant difference between demographic variables in two groups. In the future, the sample size will be expanded in order to validate results of this study.

CONCLUSION

Our results demonstrate that implantation of DBS electrodes not only improves the activity of the basal ganglia-thalamocortical circuit, but also reduces activity of the DMN and ECN-related brain regions. These findings can be helpful for further understanding of potential mechanisms that underlie MLE in PD.

DATA AVAILABILITY STATEMENT

The datasets presented in this article are not readily available because the datasets analyzed in this manuscript are not publicly

available. Requests to access the datasets should be directed to 18895319801@163.com.

ETHICS STATEMENT

The studies involving human participants were reviewed and approved by the Ethics Committee of The Brain Hospital affiliated with Nanjing Medical University. The patients/participants provided their written informed consent to participate in this study.

AUTHOR CONTRIBUTIONS

BL and YL designed and wrote this manuscript. CQ and WD were responsible for data collection. CX and BL were responsible for data processing and analysis. LZ and WL contributed to the design of the study. WZ edited and revised the manuscript. All authors contributed to and approved the final manuscript.

FUNDING

This study was supported by the grant from subtopic of the 13th Five-Year National Key Research and Development Plan (No. 2016YFC0105901NNZ).

SUPPLEMENTARY MATERIAL

The Supplementary Material for this article can be found online at: https://www.frontiersin.org/articles/10.3389/fnins.2021.699010/full#supplementary-material

REFERENCES

Aertsen, A. M., Gerstein, G. L., Habib, M. K., and Palm, G. (1989). Dynamics of neuronal firing correlation: modulation of "effective connectivity". *J. Neurophysiol.* 61, 900–917. doi: 10.1152/jn.1989.61.5.900

Alvarez, L., Macias, R., Lopez, G., Alvarez, E., Pavon, N., Rodriguez-Oroz, M. C., et al. (2005). Bilateral subthalamotomy in Parkinson's disease: initial and long-term response. *Brain* 128(Pt 3), 570–583. doi: 10.1093/brain/awh397

Amemori, K., Gibb, L. G., and Graybiel, A. M. (2011). Shifting responsibly: the importance of striatal modularity to reinforcement learning in uncertain environments. *Front. Hum. Neurosci.* 5:47. doi: 10.3389/fnhum.2011.00047

Bidet-Caulet, A., Buchanan, K. G., Viswanath, H., Black, J., Scabini, D., Bonnet-Brilhault, F., et al. (2015). Impaired facilitatory mechanisms of auditory attention after damage of the lateral prefrontal cortex. *Cereb. Cortex* 25, 4126–4134. doi: 10.1093/cercor/bhu131

Bradberry, T. J., Metman, L. V., Contreras-Vidal, J. L., van den Munckhof, P., Hosey, L. A., Thompson, J. L., et al. (2012). Common and unique responses to dopamine agonist therapy and deep brain stimulation in Parkinson's disease: an H(2)(15)O PET study. *Brain Stimul.* 5, 605–615. doi: 10.1016/j.brs.2011.09.002

Buhle, J. T., Silvers, J. A., Wager, T. D., Lopez, R., Onyemekwu, C., Kober, H., et al. (2014). Cognitive reappraisal of emotion: a meta-analysis of human neuroimaging studies. *Cereb. Cortex* 24, 2981–2990. doi: 10.1093/cercor/bht154

Burciu, R. G., and Vaillancourt, D. E. (2018). Imaging of motor cortex physiology in Parkinson's disease. *Mov. Disord.* 33, 1688–1699. doi: 10.1002/mds.102

Cieslik, E. C., Zilles, K., Caspers, S., Roski, C., Kellermann, T. S., Jakobs, O., et al. (2013). Is there "one" DLPFC in cognitive action control? Evidence for heterogeneity from co-activation-based parcellation. *Cereb. Cortex* 23, 2677–2689. doi: 10.1093/cercor/bhs256

Costentin, G., Derrey, S., Gérardin, E., Cruypeninck, Y., Pressat-Laffouilhere, T., Anouar, Y., et al. (2019). White matter tracts lesions and decline of verbal fluency after deep brain stimulation in Parkinson's disease. *Hum. Brain Mapp.* 40, 2561–2570. doi: 10.1002/hbm.24544

Cunningham, S. I., Tomasi, D., and Volkow, N. D. (2017). Structural and functional connectivity of the precuneus and thalamus to the default mode network. *Hum. Brain Mapp.* 38, 938–956. doi: 10.1002/hbm.23429

Dayal, V., Limousin, P., and Foltynie, T. (2017). Subthalamic nucleus deep brain stimulation in Parkinson's disease: the effect of varying stimulation parameters. *J. Parkinsons Dis.* 7, 235–245. doi: 10.3233/jpd-171077

Deen, B., Pitskel, N. B., and Pelphrey, K. A. (2011). Three systems of insular functional connectivity identified with cluster analysis. *Cereb. Cortex* 21, 1498–1506. doi: 10.1093/cercor/bhq186

DeLong, M. R. (1990). Primate models of movement disorders of basal ganglia origin. *Trends Neurosci.* 13, 281–285. doi: 10.1016/0166-2236(90)90110-v

DeLong, M. R., and Wichmann, T. (2015). Basal ganglia circuits as targets for neuromodulation in Parkinson disease. *JAMA Neurol.* 72, 1354–1360. doi: 10.1001/jamaneurol.2015.2397

Edwards, C. A., Kouzani, A., Lee, K. H., and Ross, E. K. (2017). Neurostimulation devices for the treatment of neurologic disorders. *Mayo Clin. Proc.* 92, 1427–1444. doi: 10.1016/j.mayocp.2017.05.005

Elfmarková, N., Gajdoš, M., Mračková, M., Mekyska, J., Mikl, M., and Rektorová, I. (2016). Impact of Parkinson's disease and levodopa on resting state functional connectivity related to speech prosody control. *Parkinsonism Relat. Disord.* 22(Suppl. 1), S52–S55. doi: 10.1016/j.parkreldis.2015.09.006

Fathy, Y. Y., Hepp, D. H., de Jong, F. J., Geurts, J. J. G., Foncke, E. M. J., Berendse, H. W., et al. (2020). Anterior insular network disconnection and cognitive impairment in Parkinson's disease. *Neuroimage Clin.* 28:102364. doi: 10.1016/j.nicl.2020.102364

Fava, G. A., Kellner, R., Munari, F., and Pavan, L. (1982). The Hamilton Depression Rating Scale in normals and depressives. *Acta Psychiatr. Scand.* 66, 26–32. doi: 10.1111/j.1600-0447.1982.tb00911.x

Filippi, M., Elisabetta, S., Piramide, N., and Agosta, F. (2018). Functional MRI in idiopathic Parkinson's disease. *Int. Rev. Neurobiol.* 141, 439–467. doi: 10.1016/bs.irn.2018.08.005

Folstein, M. F., Folstein, S. E., and McHugh, P. R. (1975). "Mini-mental state". A practical method for grading the cognitive state of patients for the clinician. *J. Psychiatr. Res.* 12, 189–198. doi: 10.1016/0022-3956(75)90026-6

Ge, R., Downar, J., Blumberger, D. M., Daskalakis, Z. J., and Vila-Rodriguez, F. (2020). Functional connectivity of the anterior cingulate cortex predicts treatment outcome for rTMS in treatment-resistant depression at 3-month follow-up. *Brain Stimul.* 13, 206–214. doi: 10.1016/j.brs.2019.10.012

Gjerris, A., Bech, P., Bøjholm, S., Bolwig, T. G., Kramp, P., Clemmesen, L., et al. (1983). The Hamilton anxiety scale. Evaluation of homogeneity and inter-observer reliability in patients with depressive disorders. *J. Affect. Disord.* 5, 163–170. doi: 10.1016/0165-0327(83)90009-5

Goetz, C. G., Tilley, B. C., Shaftman, S. R., Stebbins, G. T., Fahn, S., Martinez-Martin, P., et al. (2008). Movement disorder society-sponsored revision of the Unified Parkinson's disease rating scale (MDS-UPDRS): scale presentation and clinimetric testing results. *Mov. Disord.* 23, 2129–2170. doi: 10.1002/mds.22340

Goldstein, D. S., Sullivan, P., Holmes, C., Mash, D. C., Kopin, I. J., and Sharabi, Y. (2017). Determinants of denervation-independent depletion of putamen dopamine in Parkinson's disease and multiple system atrophy. *Parkinsonism Relat. Disord.* 35, 88–91. doi: 10.1016/j.parkreldis.2016.12.011

Habets, J. G. V., Heijmans, M., Kuijf, M. L., Janssen, M. L. F., Temel, Y., and Kubben, P. L. (2018). An update on adaptive deep brain stimulation in Parkinson's disease. *Mov. Disord.* 33, 1834–1843. doi: 10.1002/mds.115

Hacker, C. D., Perlmutter, J. S., Criswell, S. R., Ances, B. M., and Snyder, A. Z. (2012). Resting state functional connectivity of the striatum in Parkinson's disease. *Brain* 135(Pt 12), 3699–3711. doi: 10.1093/brain/aws281

Ham, J. H., Cha, J., Lee, J. J., Baek, G. M., Sunwoo, M. K., Hong, J. Y., et al. (2015). Nigrostriatal dopamine-independent resting-state functional networks in Parkinson's disease. *Neuroimage* 119, 296–304. doi: 10.1016/j.neuroimage.2015.06.077

Hampshire, A., Chamberlain, S. R., Monti, M. M., Duncan, J., and Owen, A. M. (2010). The role of the right inferior frontal gyrus: inhibition and attentional control. *Neuroimage* 50, 1313–1319. doi: 10.1016/j.neuroimage.2009.12.109

Harrington, D. L., Shen, Q., Castillo, G. N., Filoteo, J. V., Litvan, I., Takahashi, C., et al. (2017). Aberrant intrinsic activity and connectivity in cognitively normal Parkinson's disease. *Front. Aging Neurosci.* 9:197. doi: 10.3389/fnagi.2017.00197

Herz, D. M., Eickhoff, S. B., Løkkegaard, A., and Siebner, H. R. (2014). Functional neuroimaging of motor control in Parkinson's disease: a meta-analysis. *Hum. Brain Mapp.* 35, 3227–3237. doi: 10.1002/hbm.22397

Holiga, Š, Mueller, K., Möller, H. E., Urgošík, D., Růžička, E., Schroeter, M. L., et al. (2015). Resting-state functional magnetic resonance imaging of the subthalamic microlesion and stimulation effects in Parkinson's disease: indications of a principal role of the brainstem. *Neuroimage Clin.* 9, 264–274. doi: 10.1016/j.nicl.2015.08.008

Hou, Y., Yang, J., Luo, C., Song, W., Ou, R., Liu, W., et al. (2016). Dysfunction of the default mode network in drug-naïve Parkinson's disease with mild cognitive impairments: a resting-state fMRI study. *Front. Aging Neurosci.* 8:247. doi: 10.3389/fnagi.2016.00247

Hu, H., Chen, J., Huang, H., Zhou, C., Zhang, S., Liu, X., et al. (2020). Common and specific altered amplitude of low-frequency fluctuations in Parkinson's disease patients with and without freezing of gait in different frequency bands. *Brain Imaging Behav.* 14, 857–868. doi: 10.1007/s11682-018-0031-x

Huang, P., Lou, Y., Xuan, M., Gu, Q., Guan, X., Xu, X., et al. (2016). Cortical abnormalities in Parkinson's disease patients and relationship to depression: a surface-based morphometry study. *Psychiatry Res. Neuroimaging* 250, 24–28. doi: 10.1016/j.pscychresns.2016.03.002

Huot, P., Fox, S. H., and Brotchie, J. M. (2016). Dopamine reuptake inhibitors in Parkinson's disease: a review of nonhuman primate studies and clinical trials. *J. Pharmacol. Exp. Ther.* 357, 562–569. doi: 10.1124/jpet.116.232371

İçer, S., Acer, İ, and Bas, A. (2020). Gender-based functional connectivity differences in brain networks in childhood. *Comput. Methods Programs Biomed.* 192:105444. doi: 10.1016/j.cmpb.2020.105444

Jakobs, M., Lee, D. J., and Lozano, A. M. (2020). Modifying the progression of Alzheimer's and Parkinson's disease with deep brain stimulation. *Neuropharmacology* 171:107860. doi: 10.1016/j.neuropharm.2019.107860

Jech, R., Mueller, K., Urgošík, D., Sieger, T., Holiga, Š, Růžička, F., et al. (2012). The subthalamic microlesion story in Parkinson's disease: electrode insertion-related motor improvement with relative cortico-subcortical hypoactivation in fMRI. *PLoS One* 7:e49056. doi: 10.1371/journal.pone.0049056

Kann, S. J., Chang, C., Manza, P., and Leung, H. C. (2020). Akinetic rigid symptoms are associated with decline in a cortical motor network in Parkinson's disease. *NPJ Parkinsons Dis.* 6:19. doi: 10.1038/s41531-020-00120-3

Karachi, C., Yelnik, J., Tandé, D., Tremblay, L., Hirsch, E. C., and François, C. (2005). The pallidosubthalamic projection: an anatomical substrate for nonmotor functions of the subthalamic nucleus in primates. *Mov. Disord.* 20, 172–180. doi: 10.1002/mds.20302

Kish, S. J., Shannak, K., and Hornykiewicz, O. (1988). Uneven pattern of dopamine loss in the striatum of patients with idiopathic Parkinson's disease. Pathophysiologic and clinical implications. *N. Engl. J. Med.* 318, 876–880. doi: 10.1056/nejm198804073181402

Kondziolka, D., and Lee, J. Y. (2004). Long-lasting microthalamotomy effect after temporary placement of a thalamic stimulating electrode. *Stereotact. Funct. Neurosurg.* 82, 127–130. doi: 10.1159/000079844

Kvavilashvili, L., Niedźwieńska, A., Gilbert, S. J., and Markostamou, I. (2020). Deficits in spontaneous cognition as an early marker of Alzheimer's disease. *Trends Cogn. Sci.* 24, 285–301. doi: 10.1016/j.tics.2020.01.005

Lefaucheur, R., Derrey, S., Martinaud, O., Wallon, D., Chastan, N., Gérardin, E., et al. (2012). Early verbal fluency decline after STN implantation: is it a cognitive microlesion effect? *J. Neurol. Sci.* 321, 96–99. doi: 10.1016/j.jns.2012.07.033

Li, J. Y., Lu, Z. J., Suo, X. L., Li, N. N., Lei, D., Wang, L., et al. (2020). Patterns of intrinsic brain activity in essential tremor with resting tremor and tremor-dominant Parkinson's disease. *Brain Imaging Behav.* 14, 2606–2617. doi: 10.1007/s11682-019-00214-4

Li, K., Su, W., Chen, M., Li, C. M., Ma, X. X., Wang, R., et al. (2020). Abnormal spontaneous brain activity in left-onset Parkinson disease: a resting-state functional MRI study. *Front. Neurol.* 11:727. doi: 10.3389/fneur.2020.00727

Li, Y., Liang, P., Jia, X., and Li, K. (2016). Abnormal regional homogeneity in Parkinson's disease: a resting state fMRI study. *Clin. Radiol.* 71, e28–e34. doi: 10.1016/j.crad.2015.10.006

Long, L., Zeng, L. L., Song, Y., Shen, H., Fang, P., Zhang, L., et al. (2016). Altered cerebellar-cerebral functional connectivity in benign adult familial myoclonic epilepsy. *Epilepsia* 57, 941–948. doi: 10.1111/epi.13372

Lozano, A. M., Lipsman, N., Bergman, H., Brown, P., Chabardes, S., Chang, J. W., et al. (2019). Deep brain stimulation: current challenges and future directions. *Nat. Rev. Neurol.* 15, 148–160. doi: 10.1038/s41582-018-0128-2

Lucas-Jiménez, O., Ojeda, N., Peña, J., Díez-Cirarda, M., Cabrera-Zubizarreta, A., Gómez-Esteban, J. C., et al. (2016). Altered functional connectivity in the default mode network is associated with cognitive impairment and brain anatomical changes in Parkinson's disease. *Parkinsonism Relat. Disord.* 33, 58–64. doi: 10.1016/j.parkreldis.2016.09.012

Luo, F. F., Wang, J. B., Yuan, L. X., Zhou, Z. W., Xu, H., Ma, S. H., et al. (2020). Higher sensitivity and reproducibility of wavelet-based amplitude of resting-state fMRI. *Front. Neurosci.* 14:224. doi: 10.3389/fnins.2020.00224

Manza, P., Schwartz, G., Masson, M., Kann, S., Volkow, N. D., Li, C. R., et al. (2018). Levodopa improves response inhibition and enhances striatal activation in early-stage Parkinson's disease. *Neurobiol. Aging* 66, 12–22. doi: 10.1016/j.neurobiolaging.2018.02.003

McGregor, M. M., and Nelson, A. B. (2019). Circuit mechanisms of Parkinson's disease. *Neuron* 101, 1042–1056. doi: 10.1016/j.neuron.2019.03.004

Mikos, A., Bowers, D., Noecker, A. M., McIntyre, C. C., Won, M., Chaturvedi, A., et al. (2011). Patient-specific analysis of the relationship between the volume of tissue activated during DBS and verbal fluency. *Neuroimage* 54(Suppl. 1), S238–S246. doi: 10.1016/j.neuroimage.2010.03.068

Miocinovic, S., Somayajula, S., Chitnis, S., and Vitek, J. L. (2013). History, applications, and mechanisms of deep brain stimulation. *JAMA Neurol.* 70, 163–171. doi: 10.1001/2013.jamaneurol.45

Mohan, A., Roberto, A. J., Mohan, A., Lorenzo, A., Jones, K., Carney, M. J., et al. (2016). The significance of the default mode network (DMN) in neurological and neuropsychiatric disorders: a review. *Yale J. Biol. Med.* 89, 49–57.

Mohl, B., Berman, B. D., Shelton, E., and Tanabe, J. (2017). Levodopa response differs in Parkinson's motor subtypes: a task-based effective connectivity study. *J. Comp. Neurol.* 525, 2192–2201. doi: 10.1002/cne.24197

Morigaki, R., and Goto, S. (2016). Putaminal mosaic visualized by tyrosine hydroxylase immunohistochemistry in the human Neostriatum. *Front. Neuroanat.* 10:34. doi: 10.3389/fnana.2016.00034

Morrison, C. E., Borod, J. C., Perrine, K., Beric, A., Brin, M. F., Rezai, A., et al. (2004). Neuropsychological functioning following bilateral subthalamic nucleus stimulation in Parkinson's disease. *Arch. Clin. Neuropsychol.* 19, 165–181. doi: 10.1016/s0887-6177(03)00004-0

Nathan, P. J., Phan, K. L., Harmer, C. J., Mehta, M. A., and Bullmore, E. T. (2014). Increasing pharmacological knowledge about human neurological and psychiatric disorders through functional neuroimaging and its application in drug discovery. *Curr. Opin. Pharmacol.* 14, 54–61. doi: 10.1016/j.coph.2013.11.009

Nie, K., Zhang, Y., Wang, L., Zhao, J., Huang, Z., Gan, R., et al. (2012). A pilot study of psychometric properties of the Beijing version of Montreal Cognitive Assessment in patients with idiopathic Parkinson's disease in China. *J. Clin. Neurosci.* 19, 1497–1500. doi: 10.1016/j.jocn.2011.11.039

O'Reilly, R. C. (2010). The what and how of prefrontal cortical organization. *Trends Neurosci.* 33, 355–361. doi: 10.1016/j.tins.2010.05.002

Okun, M. S., Fernandez, H. H., Wu, S. S., Kirsch-Darrow, L., Bowers, D., Bova, F., et al. (2009). Cognition and mood in Parkinson's disease in subthalamic nucleus versus globus pallidus interna deep brain stimulation: the COMPARE trial. *Ann. Neurol.* 65, 586–595. doi: 10.1002/ana.21596

Pando-Naude, V., Barrios, F. A., Alcauter, S., Pasaye, E. H., Vase, L., Brattico, E., et al. (2019). Functional connectivity of music-induced analgesia in fibromyalgia. *Sci. Rep.* 9:15486. doi: 10.1038/s41598-019-51990-4

Park, K. Y., Lee, J. J., Dierker, D., Marple, L. M., Hacker, C. D., Roland, J. L., et al. (2020). Mapping language function with task-based vs. resting-state functional MRI. *PLoS One* 15:e0236423. doi: 10.1371/journal.pone.0236423

Peto, V., Jenkinson, C., and Fitzpatrick, R. (1998). PDQ-39: a review of the development, validation and application of a Parkinson's disease quality of life questionnaire and its associated measures. *J. Neurol.* 245 Suppl. 1), S10–S14. doi: 10.1007/pl00007730

Poewe, W., Seppi, K., Tanner, C. M., Halliday, G. M., Brundin, P., Volkmann, J., et al. (2017). Parkinson disease. *Nat. Rev. Dis. Primers* 3:17013. doi: 10.1038/nrdp.2017.13

Poldrack, R. A., and Farah, M. J. (2015). Progress and challenges in probing the human brain. *Nature* 526, 371–379. doi: 10.1038/nature15692

Rolls, E. T., Joliot, M., and Tzourio-Mazoyer, N. (2015). Implementation of a new parcellation of the orbitofrontal cortex in the automated anatomical labeling atlas. *Neuroimage* 122, 1–5. doi: 10.1016/j.neuroimage.2015.07.075

Sallet, J., Mars, R. B., Noonan, M. P., Neubert, F. X., Jbabdi, S., O'Reilly, J. X., et al. (2013). The organization of dorsal frontal cortex in humans and macaques. *J. Neurosci.* 33, 12255–12274. doi: 10.1523/jneurosci.5108-12.2013

Sandrone, S., and Catani, M. (2013). Journal club. Default-mode network connectivity in cognitively unimpaired patients with Parkinson disease. *Neurology* 81, e172–e175. doi: 10.1212/01.wnl.0000436943.62904.09

Seghier, M. L. (2013). The angular gyrus: multiple functions and multiple subdivisions. *Neuroscientist* 19, 43–61. doi: 10.1177/1073858412440596

Seminowicz, D. A., and Moayedi, M. (2017). The dorsolateral prefrontal cortex in acute and chronic pain. *J. Pain* 18, 1027–1035. doi: 10.1016/j.jpain.2017.03.008

Shen, B., Pan, Y., Jiang, X., Wu, Z., Zhu, J., Dong, J., et al. (2020). Altered putamen and cerebellum connectivity among different subtypes of Parkinson's disease. *CNS Neurosci. Ther.* 26, 207–214. doi: 10.1111/cns.13259

Singh, A., Kammermeier, S., Mehrkens, J. H., and Bötzel, K. (2012). Movement kinematic after deep brain stimulation associated microlesions. *J. Neurol. Neurosurg. Psychiatry* 83, 1022–1026. doi: 10.1136/jnnp-2012-302309

Sitburana, O., Almaguer, M., and Ondo, W. G. (2010). A pilot study: microlesion effects and tremor outcome in the ventrointermediate deep brain stimulation (VIM-DBS). *Clin. Neurol. Neurosurg.* 112, 106–109. doi: 10.1016/j.clineuro.2009.10.004

Smitha, K. A., Arun, K. M., Rajesh, P. G., Thomas, B., Radhakrishnan, A., Sarma, P. S., et al. (2019). Resting fMRI as an alternative for task-based fMRI for language lateralization in temporal lobe epilepsy patients: a study using independent component analysis. *Neuroradiology* 61, 803–810. doi: 10.1007/s00234-019-02209-w

Song, X. W., Dong, Z. Y., Long, X. Y., Li, S. F., Zuo, X. N., Zhu, C. Z., et al. (2011). REST: a toolkit for resting-state functional magnetic resonance imaging data processing. *PLoS One* 6:e25031. doi: 10.1371/journal.pone.0025031

Sun, H. H., Hu, J. B., Chen, J., Wang, X. Y., Wang, X. L., Pan, P. L., et al. (2020). Abnormal spontaneous neural activity in Parkinson's disease with "pure" apathy. *Front. Neurosci.* 14:830. doi: 10.3389/fnins.2020.00830

Taren, A. A., Gianaros, P. J., Greco, C. M., Lindsay, E. K., Fairgrieve, A., Brown, K. W., et al. (2017). Mindfulness meditation training and executive control network resting state functional connectivity: a randomized controlled trial. *Psychosom. Med.* 79, 674–683. doi: 10.1097/psy.0000000000000466

Tessa, C., Lucetti, C., Diciotti, S., Paoli, L., Cecchi, P., Giannelli, M., et al. (2012). Hypoactivation of the primary sensorimotor cortex in de novo Parkinson's disease : a motor fMRI study under controlled conditions. *Neuroradiology* 54, 261–268. doi: 10.1007/s00234-011-0955-y

Tessitore, A., Cirillo, M., and De Micco, R. (2019). Functional connectivity signatures of Parkinson's disease. *J. Parkinsons Dis.* 9, 637–652. doi: 10.3233/jpd-191592

Tessitore, A., Esposito, F., Vitale, C., Santangelo, G., Amboni, M., Russo, A., et al. (2012). Default-mode network connectivity in cognitively unimpaired patients with Parkinson disease. *Neurology* 79, 2226–2232. doi: 10.1212/WNL.0b013e31827689d6

Thevathasan, W., Debu, B., Aziz, T., Bloem, B. R., Blahak, C., Butson, C., et al. (2018). Pedunculopontine nucleus deep brain stimulation in Parkinson's disease: a clinical review. *Mov. Disord.* 33, 10–20. doi: 10.1002/mds.27098

Tykocki, T., Nauman, P., Koziara, H., and Mandat, T. (2013). Microlesion effect as a predictor of the effectiveness of subthalamic deep brain stimulation for Parkinson's disease. *Stereotact. Funct. Neurosurg.* 91, 12–17. doi: 10.1159/000342161

Uribe, C., Segura, B., Baggio, H. C., Abos, A., Marti, M. J., Valldeoriola, F., et al. (2016). Patterns of cortical thinning in nondemented Parkinson's disease patients. *Mov. Disord.* 31, 699–708. doi: 10.1002/mds.26590

van Wijk, B. C. M., Alkemade, A., and Forstmann, B. U. (2020). Functional segregation and integration within the human subthalamic nucleus from a micro- and meso-level perspective. *Cortex* 131, 103–113. doi: 10.1016/j.cortex.2020.07.004

van Wouwe, N. C., Neimat, J. S., van den Wildenberg, W. P. M., Hughes, S. B., Lopez, A. M., Phibbs, F. T., et al. (2020). Subthalamic nucleus subregion stimulation modulates inhibitory control. *Cereb. Cortex Commun.* 1:tgaa083. doi: 10.1093/texcom/tgaa083

Wang, J., Zhang, J. R., Zang, Y. F., and Wu, T. (2018). Consistent decreased activity in the putamen in Parkinson's disease: a meta-analysis and an independent validation of resting-state fMRI. *Gigascience* 7:giy071. doi: 10.1093/gigascience/giy071

Wang, X., Wang, M., Yuan, Y., Li, J., Shen, Y., and Zhang, K. (2020). Altered amplitude of low-frequency fluctuations and functional connectivity in excessive daytime sleepiness in Parkinson disease. *Front. Neurosci.* 14:29. doi: 10.3389/fnins.2020.00029

Wang, Z., Jia, X., Chen, H., Feng, T., and Wang, H. (2018). Abnormal spontaneous brain activity in early Parkinson's disease with mild cognitive impairment: a resting-state fMRI study. *Front. Physiol.* 9:1093. doi: 10.3389/fphys.2018.01093

Wu, T., Wang, L., Hallett, M., Chen, Y., Li, K., and Chan, P. (2011). Effective connectivity of brain networks during self-initiated movement in Parkinson's disease. *Neuroimage* 55, 204–215. doi: 10.1016/j.neuroimage.2010.11.074

Xia, J., Fan, J., Du, H., Liu, W., Li, S., Zhu, J., et al. (2019). Abnormal spontaneous neural activity in the medial prefrontal cortex and right superior temporal gyrus correlates with anhedonia severity in obsessive-compulsive disorder. *J. Affect. Disord.* 259, 47–55. doi: 10.1016/j.jad.2019.08.019

Xue, C., Yuan, B., Yue, Y., Xu, J., Wang, S., Wu, M., et al. (2019). Distinct disruptive patterns of default mode subnetwork connectivity across the spectrum of preclinical Alzheimer's disease. *Front. Aging Neurosci.* 11:307. doi: 10.3389/fnagi.2019.00307

Yelnik, J., Damier, P., Demeret, S., Gervais, D., Bardinet, E., Bejjani, B. P., et al. (2003). Localization of stimulating electrodes in patients with Parkinson disease by using a three-dimensional atlas-magnetic resonance imaging coregistration method. *J. Neurosurg.* 99, 89–99. doi: 10.3171/jns.2003.99.1.0089

Zavala, B., Zaghloul, K., and Brown, P. (2015). The subthalamic nucleus, oscillations, and conflict. *Mov. Disord.* 30, 328–338. doi: 10.1002/mds.26072

Zhang, J., Wei, L., Hu, X., Xie, B., Zhang, Y., Wu, G. R., et al. (2015). Akinetic-rigid and tremor-dominant Parkinson's disease patients show different patterns of intrinsic brain activity. *Parkinsonism Relat. Disord.* 21, 23–30. doi: 10.1016/j.parkreldis.2014.10.017

Conflict of Interest: The authors declare that the research was conducted in the absence of any commercial or financial relationships that could be construed as a potential conflict of interest.

frontiers in Neuroscience

REVIEW
published: 27 July 2021
doi: 10.3389/fnins.2021.699176

Making the Invisible Visible: Advanced Neuroimaging Techniques in Focal Epilepsy

Daichi Sone[1,2]*

[1] Department of Psychiatry, The Jikei University School of Medicine, Tokyo, Japan, [2] Department of Clinical and Experimental Epilepsy, UCL Institute of Neurology, London, United Kingdom

It has been a clinically important, long-standing challenge to accurately localize epileptogenic focus in drug-resistant focal epilepsy because more intensive intervention to the detected focus, including resection neurosurgery, can provide significant seizure reduction. In addition to neurophysiological examinations, neuroimaging plays a crucial role in the detection of focus by providing morphological and neuroanatomical information. On the other hand, epileptogenic lesions in the brain may sometimes show only subtle or even invisible abnormalities on conventional MRI sequences, and thus, efforts have been made for better visualization and improved detection of the focus lesions. Recent advance in neuroimaging has been attracting attention because of the potentials to better visualize the epileptogenic lesions as well as provide novel information about the pathophysiology of epilepsy. While the progress of newer neuroimaging techniques, including the non-Gaussian diffusion model and arterial spin labeling, could non-invasively detect decreased neurite parameters or hypoperfusion within the focus lesions, advances in analytic technology may also provide usefulness for both focus detection and understanding of epilepsy. There has been an increasing number of clinical and experimental applications of machine learning and network analysis in the field of epilepsy. This review article will shed light on recent advances in neuroimaging for focal epilepsy, including both technical progress of images and newer analytical methodologies and discuss about the potential usefulness in clinical practice.

Keywords: focal epilepsy, magnetic resonance imaging, advanced neuroimaging, structural neuroimaging, diffusion neuroimaging, functional neuroimaging

OPEN ACCESS

Edited by:
Ahmad Raza Khan,
Centre of Bio-Medical Research (CBMR), India

Reviewed by:
Vivek Tiwari,
Indian Institute of Science, India
Shilpi Modi,
Institute of Nuclear Medicine & Allied Sciences (DRDO), India

***Correspondence:**
Daichi Sone
d.sone@ucl.ac.uk

Specialty section:
This article was submitted to Brain Imaging Methods, a section of the journal Frontiers in Neuroscience

Received: *23 April 2021*
Accepted: *28 June 2021*
Published: *27 July 2021*

Citation:
Sone D (2021) Making the Invisible Visible: Advanced Neuroimaging Techniques in Focal Epilepsy. Front. Neurosci. 15:699176. doi: 10.3389/fnins.2021.699176

INTRODUCTION

Epilepsy is a common chronic brain disease, which affects around 50 million people all over the world (Leonardi and Ustun, 2002; GBD 2016 Epilepsy Collaborators, 2019). The burden of epilepsy includes recurrent seizures, their physical and psychosocial problems, and various comorbidities (GBD 2016 Epilepsy Collaborators, 2019). While seizures can be controlled by anti-seizure medicine in over 60% of patients with epilepsy (Kwan and Brodie, 2000; Chen et al., 2018b), the rest of them experience drug-resistant seizures, which may result in poorer quality of life (Kubota and Awaya, 2010). Epilepsy surgery is a well-established option to remediate patients with

drug-resistant epilepsy, and particularly accurate localization of epileptogenic focus has a key role for the successful surgical resection in focal epilepsy (Rathore and Radhakrishnan, 2015).

Neuroimaging is an essential examination for epilepsy, and one of its major roles is to visualize epileptogenic lesions, particularly in patients with drug-resistant focal seizures (Bernasconi et al., 2019). However, a part of cases with focal epilepsy show visually normal MRI, which is called "MRI-negative" epilepsy (So and Lee, 2014), and the proportion of MRI-negative cases was supposed to be up to 30% in temporal lobe epilepsy (Muhlhofer et al., 2017). Since unsuccessful localization of focus by MRI may lead to poorer surgical seizure outcome (So and Lee, 2014), accurate visualization of epileptogenic lesions by neuroimaging techniques has been a long-standing challenge in epilepsy.

Thus, the current review will shed light on recent advanced neuroimaging techniques for focus detection as well as conventional standard and quantitative analysis.

CONVENTIONALLY "VISIBLE" STRUCTURAL LESIONS

Even though a lot of quantitative methodologies have been developed, visual inspection is still an important and standard approach for focus detection. **Figure 1** presents an overview of conventionally visible epileptogenic lesions, including hippocampal sclerosis, focal cortical dysplasia and other malformation of cortical development, neoplasms, vascular malformations, and cerebrovascular diseases. Before discussing about MRI-negative epilepsy, epileptologists should be aware of these common epileptogenic lesions. Particularly, the two common etiologies, i.e., hippocampal sclerosis and focal cortical dysplasia, may need careful and specific attention for detection, as only subtle abnormalities may sometimes be found (Bernasconi et al., 2019). Additionally, meningoencephalocele has been recently recognized as another etiology in drug-resistant focal epilepsy, which may sometimes show only subtle abnormalities (Saavalainen et al., 2015; Tse et al., 2020). In cases with encephalocele, constructive interference in steady-state (CISS) imaging may be helpful for detection by enhancing the contrast between brain parenchyma and cerebrospinal fluid (Wang et al., 2017) (**Figure 2**). On the other hand, we need to keep in mind that the detected abnormalities may not always cause the seizures, in cases with incidental lesions.

It is also important to differentiate epileptogenic lesions, particularly focal cortical dysplasia, from other findings, such as unspecific aging-related changes showing T2 hyperintensity. For that, we need to consider the main features of focal cortical dysplasia, including cortical thickening, blurring of gray–white matter junction, cortical or white matter T2 hyperintensity, and transmantle sign (De Vito et al., 2021) (**Figures 1B**, **3**). To detect hippocampal sclerosis, which is the most common etiology of temporal lobe epilepsy (Thom, 2014), attention should be paid to hippocampal atrophy and T2 hyperintensity, and thinning and blurring of the molecular layer (Bernasconi et al., 2019; De Vito et al., 2021) (**Figure 4**). As described, epileptogenic lesions are sometimes subtle, and 3D acquisition with reformats is important (De Vito et al., 2021). Therefore, we should be careful about motion artifact and quality control.

RECOMMENDATION OF THE OFFICIAL STANDARD PROTOCOL FOR EPILEPSY

In 2019, the International League Against Epilepsy (ILAE) published the official recommendation of structural MRI for epilepsy (Bernasconi et al., 2019). In that, the following protocols were recommended as a standard: 3D millimetric T1-weighted images (T1WI) and fluid-attenuated inversion recovery (FLAIR) images, and 2D submillimetric coronal T2-weighted images (T2WI). **Figure 3** shows a representative case with drug-resistant focal epilepsy, who benefited from 3D millimetric FLAIR images. It was impossible to detect any abnormalities in both coronal and axial 2D FLAIR images with 3-mm slice thickness (**Figure 3A**), but the 3D FLAIR images revealed findings of a bottom-of-sulcus-type focal cortical dysplasia with transmantle sign (**Figure 3B**), and changing the signal range may sometimes be helpful to clearly visualize the lesion (**Figure 3C**). The patient underwent surgical resection, and the pathological result was focal cortical dysplasia type IIb. Thus, the optimal MRI protocol for epilepsy may be able to make the previously invisible lesions visible.

However, even with such optimized protocols, we sometimes encounter patients with visually normal MRI. To detect the conventionally invisible epileptogenic lesions, efforts have been made to seek for useful advanced neuroimaging techniques in drug-resistant focal epilepsy (Bernasconi and Wang, 2021).

ADVANCED STRUCTURAL IMAGING

Beyond the recommended MRI protocol, newer structural MRI sequences have been suggested to provide additional usefulness. Double inversion recovery (DIR), which shows a high contrast between gray and white matters (Ryan, 2016), has been increasingly reported as a useful sequence to detect epileptogenic lesions in temporal lobe epilepsy (TLE) and extratemporal focal epilepsy (Li et al., 2011; Morimoto et al., 2013a,b; Granata et al., 2016; Wong-Kisiel et al., 2016; Wychowski et al., 2016; Sone et al., 2021). In TLE, the superiority of DIR to FLAIR for the detection of anterior temporal white matter abnormalities in the focus side in TLE was reported by both qualitative and quantitative evaluations (Morimoto et al., 2013a; Sone et al., 2021). **Figure 5** describes a case of conventionally MRI-negative PET-positive unilateral TLE, in which increased DIR signals can be found in the focus side, while it was difficult to detect on FLAIR, T1WI, and T2WI. More recently, fluid and white matter suppression (FLAWS) has been reported for better visualization of focal cortical dysplasia even in conventionally MRI-negative cases (Chen et al., 2018a; Sun et al., 2021). FLAWS suppresses the white matter and cerebrospinal fluid signals and then generate gray matter-specific images (Tanner et al., 2012; Chen et al., 2018a).

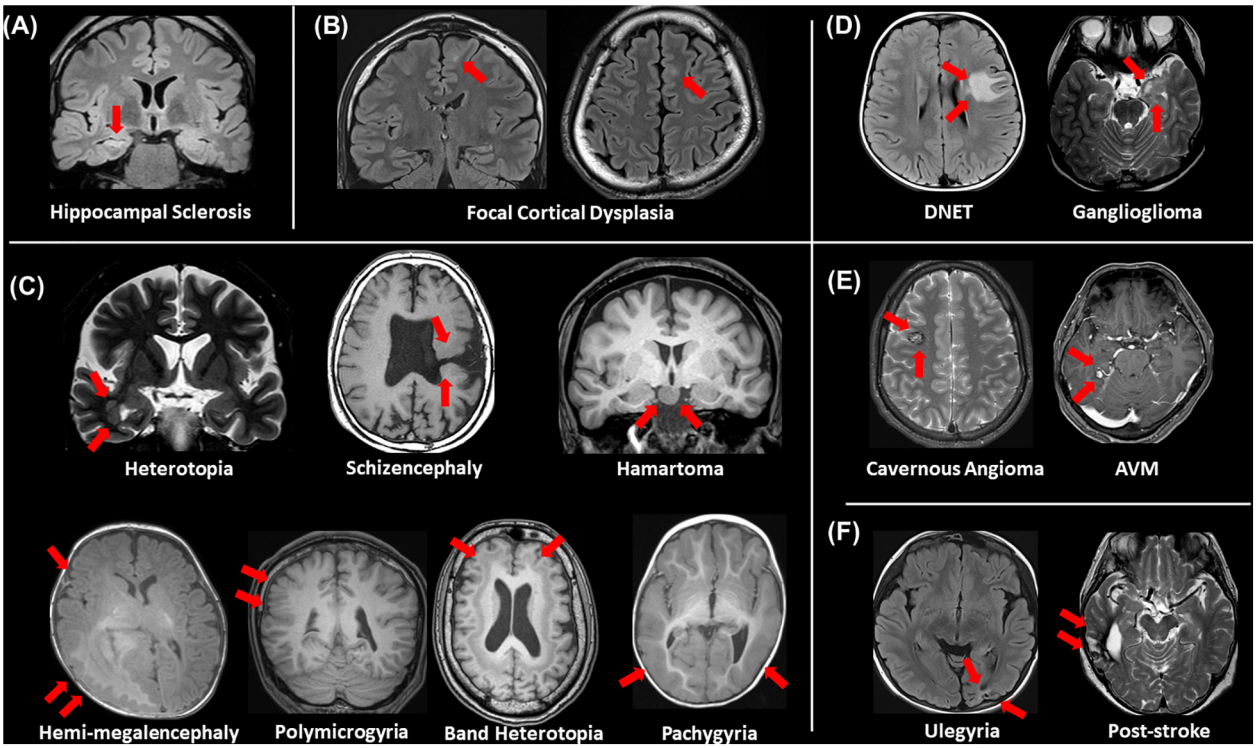

FIGURE 1 | An overview of visible epileptogenic lesions (red arrows). **(A)** Hippocampal sclerosis, **(B)** focal cortical dysplasia, **(C)** other malformations of cortical development, **(D)** neoplasms, **(E)** vascular malformations, and **(F)** cerebrovascular lesions.

Thus, the enhanced contrast between gray and white matters by these newer sequences may improve the visualization of epileptic foci. In addition, edge-enhancing gradient echo (EDGE) imaging was reported to allow us to detect focal cortical dysplasia by directly visualizing the boundary between gray and white matters (Middlebrooks et al., 2020).

ADVANCED DIFFUSION IMAGING

The progress in diffusion MRI has been an emerging topic in the field of neurology and psychiatry. Particularly, multi-shell protocols of diffusion MRI, including diffusion kurtosis imaging (DKI), q-space imaging (QSI), restriction spectrum imaging (RSI), and neurite orientation dispersion and density imaging (NODDI), have provided further information on brain microstructures (Cohen and Assaf, 2002; Jensen et al., 2005; White et al., 2013; Sone, 2019). In the field of epilepsy, NODDI and RSI have been repeatedly reported for their usefulness (Winston et al., 2014; Loi et al., 2016; Reyes et al., 2018; Rostampour et al., 2018; Sone et al., 2018; Lorio et al., 2020; Winston et al., 2020; Shao et al., 2021). Neurite orientation dispersion and density imaging allows us to investigate neurite density and orientation dispersion of the brain microstructures, and reduced neurite density has been consistently found in visible focal cortical dysplasia (Winston et al., 2014; Lorio et al., 2020). Neurite orientation dispersion and density imaging may also visualize neurite abnormalities within the focus even in MRI-negative cases (Sone et al., 2018). **Figure 6** represents two cases with conventionally MRI-negative PET-positive unilateral TLE, which showed reduced neurite density within the anterior temporal lobe of the focus side. In TLE with hippocampal

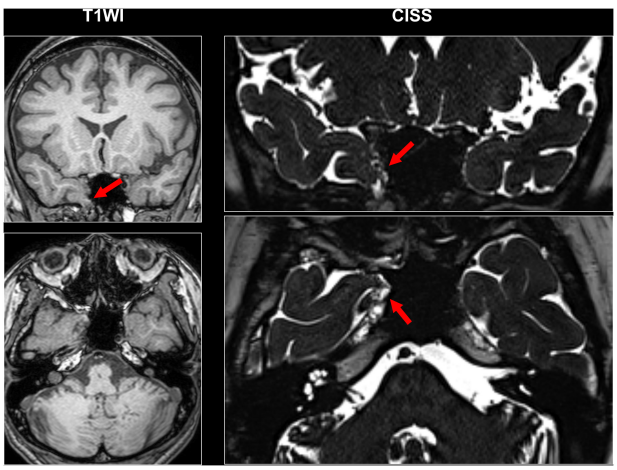

FIGURE 2 | A case with drug-resistant temporal lobe epilepsy and encephalocele. Constructive interference in steady-state (CISS) imaging was helpful for detection by enhancing the contrast between brain parenchyma and cerebrospinal fluid.

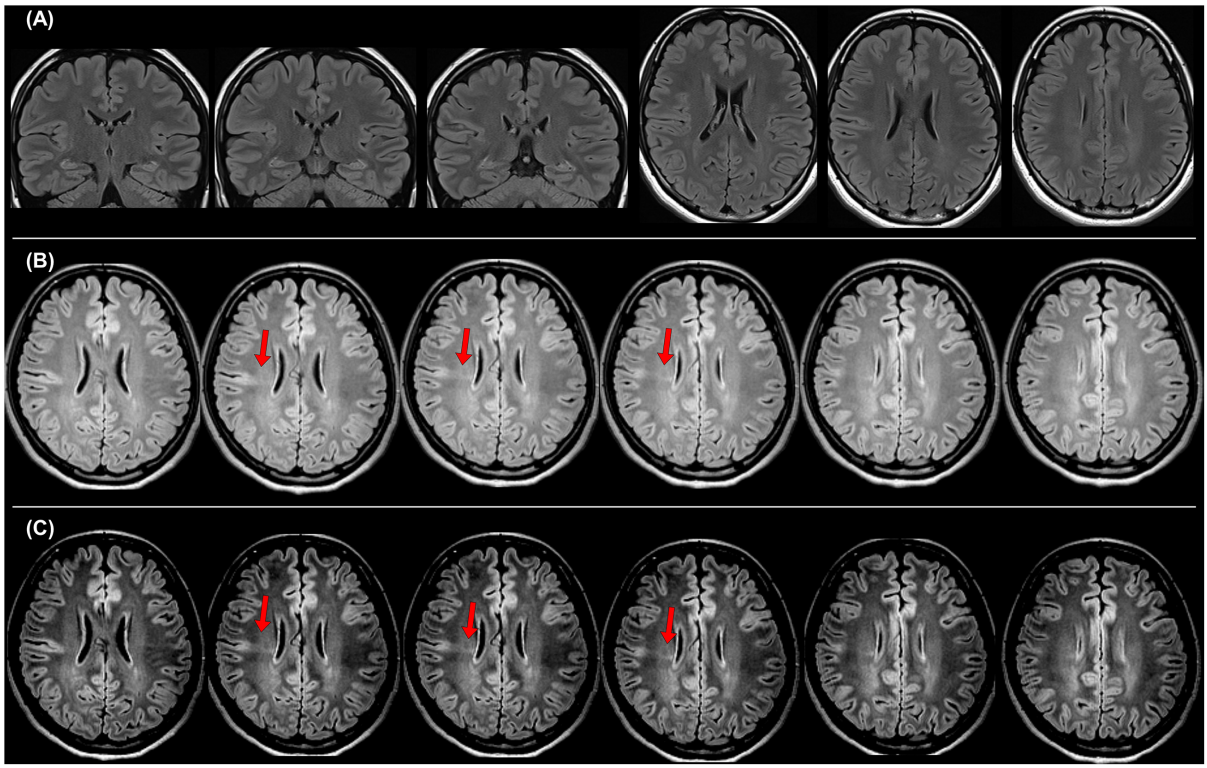

FIGURE 3 | A case with drug-resistant focal epilepsy, who benefited from the official standard protocol for epilepsy. It was impossible to detect any abnormalities in both coronal and axial 2D fluid-attenuated inversion recovery (FLAIR) images with 3-mm slice thickness **(A)**, but the 3D FLAIR images revealed findings of a bottom-of-sulcus-type focal cortical dysplasia with transmantle sign **(B)**, and changing the signal range is sometimes helpful to clearly visualize the lesion **(C)**. The pathological finding was focal cortical dysplasia type IIb.

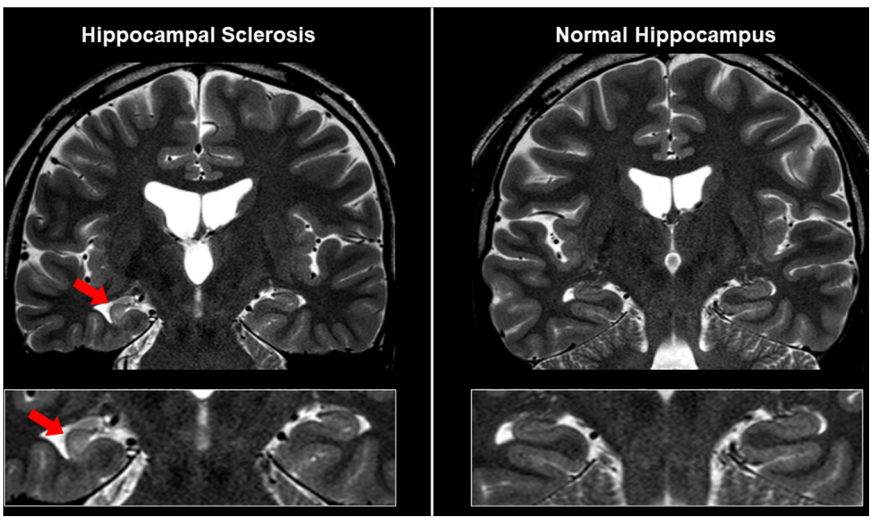

FIGURE 4 | MRI findings in a case with unilateral hippocampal sclerosis (left). The affected hippocampus showed hippocampal atrophy and T2 hyperintensity, and thinning and blurring of the molecular layer, compared with the contralateral side or normal case (right).

sclerosis, reductions of neurite orientation dispersion as well as neurite density were reported (Sone et al., 2018). Additionally, NODDI could help in better visualization of cortical tubers in tuberous sclerosis (Shao et al., 2021). RSI is another advanced diffusion MRI using multi-shell, reduced neurite density, and its correlation with clinical symptoms in epilepsy was also confirmed

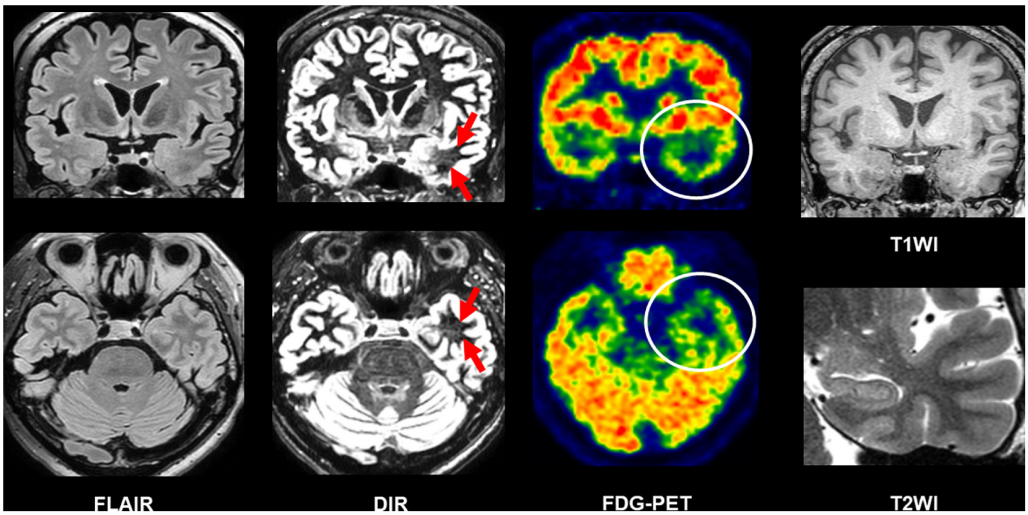

FIGURE 5 | A case of conventionally MRI-negative PET-positive temporal lobe epilepsy (TLE). While it was difficult to detect abnormalities on FLAIR, double inversion recovery (DIR) visualized hyperintensity within the anterior temporal white matter of the focus side. T1-weighted images (T1WI) and T2WI were also intact including the hippocampus.

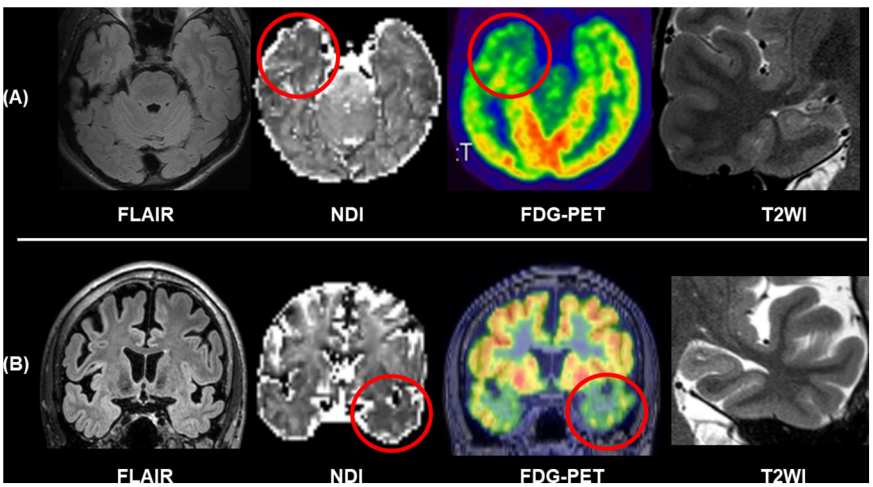

FIGURE 6 | Two cases of conventionally MRI-negative PET-positive TLE. While no abnormalities were found in FLAIR and T2WI including the hippocampus, neurite orientation dispersion and density imaging (NODDI) revealed reduced neurite density of the focus side. **(A)** Modified from Sone et al. (2018). **(B)** Modified from Sone (2019).

by RSI (Loi et al., 2016; Reyes et al., 2018). Thus, advances in diffusion MRI may be a promising tool for patients with drug-resistant focal epilepsy and invisible lesions on conventional MRI.

ADVANCED FUNCTIONAL NEUROIMAGING

Interictal reduction of glucose metabolisms in ^{18}F-FDG PET and ictal hyperperfusion detected by SPECT are traditional and established biomarkers for the detection of focus in drug-resistant epilepsy and often effective for MRI-negative cases (Kumar and Chugani, 2013; Shigemoto et al., 2020). In addition to nuclear imaging, recent advances in functional neuroimaging may further improve the detection of focus. Arterial spin labeling (ASL) is a non-invasive method to visualize brain perfusion by MRI (Haller et al., 2016) and, thus, expected to detect abnormal cerebral blood flow, particularly interictal reduction, around the epileptogenic foci in epilepsy (**Figure 7**) (Boscolo Galazzo et al., 2016; Shang et al., 2018; Wang et al., 2018; Sone et al., 2019; Lam et al., 2020). Although ASL might not surpass ^{18}F-FDG PET in terms of detectability of focus (Sone et al., 2019), its non-invasive nature and wide availability will guarantee a supplemental role in clinical practice. Functional MRI triggered by electroencephalogram (EEG-fMRI) is another newer tool of functional imaging for focus detection. EEG-fMRI

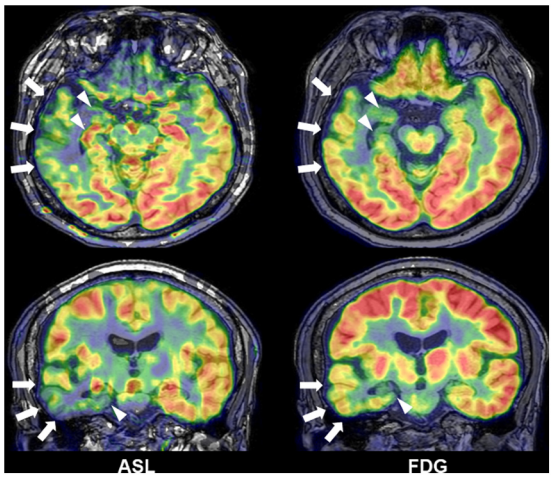

FIGURE 7 | A case of temporal lobe epilepsy with hippocampal sclerosis. Both Arterial spin labeling (ASL) and 18F-FDG PET showed reduced signals around the temporal lobe of focus side (modified from Sone et al., 2019).

can non-invasively detect the hemodynamic signals related with interictal epileptic discharges on EEG (van Graan et al., 2015), and then it can be utilized to visualize the epileptogenic zone and its propagations (Khoo et al., 2017, 2018).

QUANTITATIVE ANALYSIS AND POST-PROCESSING

Another solution for MRI-negative drug-resistant epilepsy is quantitative analysis and post-processing of images. It is known that quantitative hippocampal volumetry and signal analysis improve the visual detectability of hippocampal sclerosis (Coan et al., 2014), and better segmentation and detailed hippocampal profiling methods have also been developed (Winston et al., 2013; Vos et al., 2020). The Morphometric Analysis Program (MAP) is a well-investigated software to generate voxel-based morphometric maps, which can visualize subtle blurring of the gray–white boundary or abnormal cortical surface, using 3D T1WI. In fact, many studies confirmed the usefulness of MAP for the detection of focal cortical dysplasia (Kassubek et al., 2002; Huppertz et al., 2005; Wagner et al., 2011; Wang et al., 2015; Lin et al., 2018; Demerath et al., 2020) or band heterotopia (Huppertz et al., 2008). In addition to T1WI, usefulness of quantitative FLAIR or DIR analysis was also reported (Rugg-Gunn et al., 2006; Focke et al., 2009).

Machine learning is an emerging topic in this field; the advantage of machine-learning may include the accurate, automated, and fast pattern learning, which could be utilized to develop and/optimize clinical algorithms. Currently, studies on machine learning and epilepsy imaging reported its usefulness in the lateralization of TLE (Pustina et al., 2015; Bennett et al., 2019; Beheshti et al., 2020a,b) or automated detection of focal cortical dysplasia (Hong et al., 2014; Hong et al., 2016; Adler et al., 2017; Tan et al., 2018). While machine leaning has provided promising results for the detection of focus in epilepsy, we may need to develop and validate consistent methodology given the diversity of methods (Sone and Beheshti, 2021). Furthermore, network analysis is another trend in epilepsy (Bernhardt et al., 2015), and literature suggested that network metrics derived from neuroimaging could also be used for focus detection when combined with machine learning (Chiang et al., 2015; Yang et al., 2015; Kamiya et al., 2016; Fallahi et al., 2020).

MULTIMODAL IMAGING

Combination of multimodal imaging is also important for precise localization of focus (Kurian et al., 2007). Concordance across different modalities supports successful epilepsy surgery (Rathore and Radhakrishnan, 2015), and in addition, coregistered images would improve visual detectability of epileptogenic foci, which was demonstrated by a study using MRI and ^{18}F-FDG PET (Salamon et al., 2008). Multimodal imaging is also a topic in machine learning studies (Pustina et al., 2015; Bennett et al., 2019). Given the importance of multiple modalities in epilepsy, developing a platform for fusion of data (Marecek et al., 2021) would become a significant work for the future.

SEVEN-TESLA MRI

Seven-tesla (7T) MRI is expected to yield improved detectability over 3T MRI, by the ultra-high-field magnetic strength (van Lanen et al., 2021). Despite the still limited access to 7T MRI, there have been several studies reporting its usefulness in epilepsy (De Ciantis et al., 2016; Veersema et al., 2017; Bartolini et al., 2019; Feldman et al., 2019). On the other hand, diagnostic gain of 7T over conventional MRI has been variable, ranging from 8 to 67% (van Lanen et al., 2021), and thus, further studies would be needed to establish the utility of 7T MRI for clinical use in patients with epilepsy.

ESTABLISHMENT OF CLINICAL MRI STANDARDS FOR EPILEPSY

While this review focused on the recent progress in newer imaging techniques, uniformity of the MRI protocols is of great relevance in clinical epileptology. To establish a practical standard, various aspects need to be considered, including magnetic field strength, imaging resolution, and acquisition time.

Regarding the magnetic field strength, 1.5- or 3-T MRI scanners are currently utilized in clinical practice. In principle, 3-T MRI provides a better signal-to-noise ratio and higher resolution of images, although we need to pay more careful attention to flow and motion artifact in 3-T scanners (Martinez-Rios et al., 2016; De Vito et al., 2021). Indeed, some previous studies reported better identification of epileptogenic lesions by 3- than by 1.5-T MRI, and the use of 3-T MRI may improve the clinical decision making (Knake et al., 2005; Zijlmans et al., 2009; Mellerio et al., 2014; Rubinger et al., 2016). The imaging

resolution should be along with the official recommendation of ILAE (Bernasconi et al., 2019), i.e., 3D isotropic T1WI and FLAIR images with millimetric voxels ($1 \times 1 \times 1$ mm^3), and 2D submillimetric T2WI designed for hippocampal evaluation. More advanced techniques, which were reviewed in this article, may be considered as additional imaging. On the other hand, however, such additions usually require longer acquisition time, which may become a trade-off dilemma for clinically acceptable epilepsy imaging. Thus, those advanced imaging methods need to become more established, particularly by robustly revealing the clinical usefulness, e.g., long-term prognosis of surgery. The manufacturer of MRI scanners is another important factor for the uniformity of epilepsy protocols, as some newer sequences have been developed by each specific manufacturer.

LIMITATION AND FUTURE CHALLENGE

As noted above, compared with conventionally established sequences, the usefulness of advanced imaging still needs to be more robustly elucidated. Although most studies reported potentials of better focus detection, long-term seizure outcomes after resection of the abnormal areas are rarely investigated, so far. Additionally, the cost effectiveness of acquisition time should be kept in mind. Thus, future studies should include more comprehensive and robust comparisons between imaging modalities and clinical parameters, as well as consideration of time efficiency. Another important topic in epilepsy imaging is the preclinical MRI studies to identify the underlying mechanism and time course of epileptogenesis (Immonen et al., 2019; Reddy et al., 2019). Advanced neuroimaging methods may provide further information for basic research on epilepsy. Eventually, in addition to focus detection, neuroimaging could contribute to elucidation of the neurobiological mechanisms, brain functions, and longitudinal brain changes in epilepsy (Galovic et al., 2019; Bernasconi and Wang, 2021). Thus, clinical and basic applications of advanced neuroimaging would be promising for better understanding and improved clinical practice for epilepsy.

CONCLUSION

There have been various, continuous efforts to better visualize epileptogenic foci in drug-resistant focal epilepsy. The promising advances in structural, diffusion, and functional neuroimaging, as well as quantitative processing and machine learning, may provide critical information for epilepsy surgery and benefit patients with drug-resistant focal epilepsy.

AUTHOR CONTRIBUTIONS

DS was the sole author of this manuscript and contributed to all aspects.

FUNDING

This work was supported by the Japan Society for the Promotion of Science (KAKENHI Grant Number JP21K15720) to DS.

ACKNOWLEDGMENTS

I am grateful to the colleagues in the Department of Radiology, National Center of Neurology and Psychiatry, Tokyo, Japan.

REFERENCES

Adler, S., Wagstyl, K., Gunny, R., Ronan, L., Carmichael, D., Cross, J. H., et al. (2017). Novel surface features for automated detection of focal cortical dysplasias in paediatric epilepsy. *Neuroimage Clin.* 14, 18–27. doi: 10.1016/j.nicl.2016.12.030

Bartolini, E., Cosottini, M., Costagli, M., Barba, C., Tassi, L., Spreafico, R., et al. (2019). Ultra-High-Field targeted imaging of focal cortical dysplasia: the intracortical black line sign in type IIb. *AJNR Am. J. Neuroradiol.* 40, 2137–2142. doi: 10.3174/ajnr.A6298

Beheshti, I., Sone, D., Maikusa, N., Kimura, Y., Shigemoto, Y., Sato, N., et al. (2020a). FLAIR-Wise machine-learning classification and lateralization of MRI-Negative (18)F-FDG PET-Positive temporal lobe epilepsy. *Front. Neurol.* 11:580713. doi: 10.3389/fneur.2020.580713

Beheshti, I., Sone, D., Maikusa, N., Kimura, Y., Shigemoto, Y., Sato, N., et al. (2020b). Pattern analysis of glucose metabolic brain data for lateralization of MRI-negative temporal lobe epilepsy. *Epilepsy Res.* 167:106474. doi: 10.1016/j.eplepsyres.2020.106474

Bennett, O. F., Kanber, B., Hoskote, C., Cardoso, M. J., Ourselin, S., Duncan, J. S., et al. (2019). Learning to see the invisible: a data-driven approach to finding the underlying patterns of abnormality in visually normal brain magnetic resonance images in patients with temporal lobe epilepsy. *Epilepsia* 60, 2499–2507. doi: 10.1111/epi.16380

Bernasconi, A., Cendes, F., Theodore, W. H., Gill, R. S., Koepp, M. J., Hogan, R. E., et al. (2019). Recommendations for the use of structural magnetic resonance imaging in the care of patients with epilepsy: a consensus report from the international league against epilepsy neuroimaging task force. *Epilepsia* 60, 1054–1068. doi: 10.1111/epi.15612

Bernasconi, N., and Wang, I. (2021). Emerging trends in neuroimaging of epilepsy. *Epilepsy Curr.* 21, 79–82. doi: 10.1177/1535759721991161

Bernhardt, B. C., Bonilha, L., and Gross, D. W. (2015). Network analysis for a network disorder: the emerging role of graph theory in the study of epilepsy. *Epilepsy Behav.* 50, 162–170. doi: 10.1016/j.yebeh.2015.06.005

Boscolo Galazzo, I., Mattoli, M. V., Pizzini, F. B., De Vita, E., Barnes, A., Duncan, J. S., et al. (2016). Cerebral metabolism and perfusion in MR-negative individuals with refractory focal epilepsy assessed by simultaneous acquisition of (18)F-FDG PET and arterial spin labeling. *Neuroimage Clin.* 11, 648–657. doi: 10.1016/j.nicl.2016.04.005

Chen, X., Qian, T., Kober, T., Zhang, G., Ren, Z., Yu, T., et al. (2018a). Gray-matter-specific MR imaging improves the detection of epileptogenic zones in focal cortical dysplasia: a new sequence called fluid and white matter suppression (FLAWS). *Neuroimage Clin.* 20, 388–397. doi: 10.1016/j.nicl.2018.08.010

Chen, Z., Brodie, M. J., Liew, D., and Kwan, P. (2018b). Treatment outcomes in patients with newly diagnosed epilepsy treated with established and new antiepileptic drugs: a 30-Year longitudinal cohort study. *JAMA Neurol.* 75, 279–286. doi: 10.1001/jamaneurol.2017.3949

Chiang, S., Levin, H. S., and Haneef, Z. (2015). Computer-automated focus lateralization of temporal lobe epilepsy using fMRI. *J. Magn. Reson. Imaging* 41, 1689–1694. doi: 10.1002/jmri.24696

Coan, A. C., Kubota, B., Bergo, F. P., Campos, B. M., and Cendes, F. (2014). 3T MRI quantification of hippocampal volume and signal in mesial temporal lobe epilepsy improves detection of hippocampal sclerosis. *AJNR Am. J. Neuroradiol.* 35, 77–83. doi: 10.3174/ajnr.A3640

Cohen, Y., and Assaf, Y. (2002). High b-value q-space analyzed diffusion-weighted MRS and MRI in neuronal tissues - a technical review. *NMR Biomed.* 15, 516–542. doi: 10.1002/nbm.778

De Ciantis, A., Barba, C., Tassi, L., Cosottini, M., Tosetti, M., Costagli, M., et al. (2016). 7T MRI in focal epilepsy with unrevealing conventional field strength imaging. *Epilepsia* 57, 445–454. doi: 10.1111/epi.13313

De Vito, A., Mankad, K., Pujar, S., Chari, A., Ippolito, D., and D'Arco, F. (2021). Narrative review of epilepsy: getting the most out of your neuroimaging. *Transl. Pediatr.* 10, 1078–1099. doi: 10.21037/tp-20-261

Demerath, T., Rubensdorfer, L., Schwarzwald, R., Schulze-Bonhage, A., Altenmuller, D. M., Kaller, C., et al. (2020). Morphometric MRI analysis: improved detection of focal cortical dysplasia using the MP2RAGE sequence. *AJNR Am. J. Neuroradiol.* 41, 1009–1014. doi: 10.3174/ajnr.A6579

Fallahi, A., Pooyan, M., Lotfi, N., Baniasad, F., Tapak, L., Mohammadi-Mobarakeh, N., et al. (2020). Dynamic functional connectivity in temporal lobe epilepsy: a graph theoretical and machine learning approach. *Neurol. Sci.* 42, 2379–2390. doi: 10.1007/s10072-020-04759-x

Feldman, R. E., Delman, B. N., Pawha, P. S., Dyvorne, H., Rutland, J. W., Yoo, J., et al. (2019). 7T MRI in epilepsy patients with previously normal clinical MRI exams compared against healthy controls. *PLoS One* 14:e0213642. doi: 10.1371/journal.pone.0213642

Focke, N. K., Bonelli, S. B., Yogarajah, M., Scott, C., Symms, M. R., and Duncan, J. S. (2009). Automated normalized FLAIR imaging in MRI-negative patients with refractory focal epilepsy. *Epilepsia* 50, 1484–1490. doi: 10.1111/j.1528-1167.2009.02022.x

Galovic, M., van Dooren, V. Q. H., Postma, T., Vos, S. B., Caciagli, L., Borzi, G., et al. (2019). Progressive cortical thinning in patients with focal epilepsy. *JAMA Neurol.* 76, 1230–1239. doi: 10.1001/jamaneurol.2019.1708

GBD 2016 Epilepsy Collaborators (2019). Global, regional, and national burden of epilepsy, 1990-2016: a systematic analysis for the global burden of disease study 2016. *Lancet Neurol.* 18, 357–375. doi: 10.1016/S1474-4422(18)30454-X

Granata, F., Morabito, R., Mormina, E., Alafaci, C., Marino, S., Lagana, A., et al. (2016). 3T double inversion recovery magnetic resonance imaging: diagnostic advantages in the evaluation of cortical development anomalies. *Eur. J. Radiol.* 85, 906–914. doi: 10.1016/j.ejrad.2016.02.018

Haller, S., Zaharchuk, G., Thomas, D. L., Lovblad, K. O., Barkhof, F., and Golay, X. (2016). Arterial spin labeling perfusion of the brain: emerging clinical applications. *Radiology* 281, 337–356. doi: 10.1148/radiol.2016150789

Hong, S. J., Bernhardt, B. C., Schrader, D. S., Bernasconi, N., and Bernasconi, A. (2016). Whole-brain MRI phenotyping in dysplasia-related frontal lobe epilepsy. *Neurology* 86, 643–650. doi: 10.1212/wnl.0000000000002374

Hong, S. J., Kim, H., Schrader, D., Bernasconi, N., Bernhardt, B. C., and Bernasconi, A. (2014). Automated detection of cortical dysplasia type II in MRI-negative epilepsy. *Neurology* 83, 48–55. doi: 10.1212/wnl.0000000000000543

Huppertz, H. J., Grimm, C., Fauser, S., Kassubek, J., Mader, I., Hochmuth, A., et al. (2005). Enhanced visualization of blurred gray-white matter junctions in focal cortical dysplasia by voxel-based 3D MRI analysis. *Epilepsy Res.* 67, 35–50. doi: 10.1016/j.eplepsyres.2005.07.009

Huppertz, H. J., Wellmer, J., Staack, A. M., Altenmuller, D. M., Urbach, H., and Kroll, J. (2008). Voxel-based 3D MRI analysis helps to detect subtle forms of subcortical band heterotopia. *Epilepsia* 49, 772–785. doi: 10.1111/j.1528-1167.2007.01436.x

Immonen, R., Harris, N. G., Wright, D., Johnston, L., Manninen, E., Smith, G., et al. (2019). Imaging biomarkers of epileptogenecity after traumatic brain injury - preclinical frontiers. *Neurobiol. Dis.* 123, 75–85. doi: 10.1016/j.nbd.2018.10.008

Jensen, J. H., Helpern, J. A., Ramani, A., Lu, H., and Kaczynski, K. (2005). Diffusional kurtosis imaging: the quantification of non-gaussian water diffusion by means of magnetic resonance imaging. *Magn. Reson. Med.* 53, 1432–1440. doi: 10.1002/mrm.20508

Kamiya, K., Amemiya, S., Suzuki, Y., Kunii, N., Kawai, K., Mori, H., et al. (2016). Machine learning of DTI structural brain connectomes for lateralization of temporal lobe epilepsy. *Magn. Reson. Med. Sci.* 15, 121–129. doi: 10.2463/mrms.2015-2027

Kassubek, J., Huppertz, H. J., Spreer, J., and Schulze-Bonhage, A. (2002). Detection and localization of focal cortical dysplasia by voxel-based 3-D MRI analysis. *Epilepsia* 43, 596–602. doi: 10.1046/j.1528-1157.2002.41401.x

Khoo, H. M., Hao, Y., von Ellenrieder, N., Zazubovits, N., Hall, J., Olivier, A., et al. (2017). The hemodynamic response to interictal epileptic discharges localizes the seizure-onset zone. *Epilepsia* 58, 811–823. doi: 10.1111/epi.13717

Khoo, H. M., von Ellenrieder, N., Zazubovits, N., He, D., Dubeau, F., and Gotman, J. (2018). The spike onset zone: the region where epileptic spikes start and from where they propagate. *Neurology* 91, e666–e674. doi: 10.1212/WNL.0000000000005998

Knake, S., Triantafyllou, C., Wald, L. L., Wiggins, G., Kirk, G. P., Larsson, P. G., et al. (2005). 3T phased array MRI improves the presurgical evaluation in focal epilepsies: a prospective study. *Neurology* 65, 1026–1031.

Kubota, H., and Awaya, Y. (2010). Assessment of health-related quality of life and influencing factors using QOLIE-31 in Japanese patients with epilepsy. *Epilepsy Behav.* 18, 381–387. doi: 10.1016/j.yebeh.2010.04.045

Kumar, A., and Chugani, H. T. (2013). The role of radionuclide imaging in epilepsy, Part 1: sporadic temporal and extratemporal lobe epilepsy. *J. Nucl. Med.* 54, 1775–1781. doi: 10.2967/jnumed.112.114397

Kurian, M., Spinelli, L., Delavelle, J., Willi, J. P., Velazquez, M., Chaves, V., et al. (2007). Multimodality imaging for focus localization in pediatric pharmacoresistant epilepsy. *Epileptic Disord.* 9, 20–31. doi: 10.1684/epd.2007.0070

Kwan, P., and Brodie, M. J. (2000). Early identification of refractory epilepsy. *N. Engl. J. Med.* 342, 314–319. doi: 10.1056/NEJM200002033420503

Lam, J., Tomaszewski, P., Gilbert, G., Moreau, J. T., Guiot, M. C., Albrecht, S., et al. (2020). The utility of arterial spin labeling in the presurgical evaluation of poorly defined focal epilepsy in children. *J. Neurosurg. Pediatr.* 25, 1–10. doi: 10.3171/2020.7.PEDS20397

Leonardi, M., and Ustun, T. B. (2002). The global burden of epilepsy. *Epilepsia* 43(Suppl. 6), 21–25.

Li, Q., Zhang, Q., Sun, H., Zhang, Y., and Bai, R. (2011). Double inversion recovery magnetic resonance imaging at 3 T: diagnostic value in hippocampal sclerosis. *J. Comput. Assist. Tomogr.* 35, 290–293. doi: 10.1097/RCT.0b013e3182073c56

Lin, Y., Fang, Y. D., Wu, G., Jones, S. E., Prayson, R. A., Moosa, A. N. V., et al. (2018). Quantitative positron emission tomography-guided magnetic resonance imaging postprocessing in magnetic resonance imaging-negative epilepsies. *Epilepsia* 59, 1583–1594. doi: 10.1111/epi.14474

Loi, R. Q., Leyden, K. M., Balachandra, A., Uttarwar, V., Hagler, D. J. Jr., et al. (2016). Restriction spectrum imaging reveals decreased neurite density in patients with temporal lobe epilepsy. *Epilepsia* 57, 1897–1906. doi: 10.1111/epi.13570

Lorio, S., Adler, S., Gunny, R., D'Arco, F., Kaden, E., Wagstyl, K., et al. (2020). MRI profiling of focal cortical dysplasia using multi-compartment diffusion models. *Epilepsia* 61, 433–444. doi: 10.1111/epi.16451

Marecek, R., Riha, P., Bartonova, M., Kojan, M., Lamos, M., Gajdos, M., et al. (2021). Automated fusion of multimodal imaging data for identifying epileptogenic lesions in patients with inconclusive magnetic resonance imaging. *Hum. Brain Mapp.* 42, 2921–2930. doi: 10.1002/hbm.25413

Martinez-Rios, C., McAndrews, M. P., Logan, W., Krings, T., Lee, D., and Widjaja, E. (2016). MRI in the evaluation of localization-related epilepsy. *J. Magn. Reson. Imaging* 44, 12–22. doi: 10.1002/jmri.25269

Mellerio, C., Labeyrie, M. A., Chassoux, F., Roca, P., Alami, O., Plat, M., et al. (2014). 3T MRI improves the detection of transmantle sign in type 2 focal cortical dysplasia. *Epilepsia* 55, 117–122. doi: 10.1111/epi.12464

Middlebrooks, E. H., Lin, C., Westerhold, E., Okromelidze, L., Vibhute, P., Grewal, S. S., et al. (2020). Improved detection of focal cortical dysplasia using a novel 3D imaging sequence: edge-Enhancing gradient echo (3D-EDGE) MRI. *Neuroimage Clin.* 28:102449. doi: 10.1016/j.nicl.2020.102449

Morimoto, E., Kanagaki, M., Okada, T., Yamamoto, A., Mori, N., Matsumoto, R., et al. (2013a). Anterior temporal lobe white matter abnormal signal (ATLAS) as an indicator of seizure focus laterality in temporal lobe epilepsy: comparison of double inversion recovery. FLAIR and T2W MR imaging. *Eur. Radiol.* 23, 3–11. doi: 10.1007/s00330-012-2565-2564

Morimoto, E., Okada, T., Kanagaki, M., Yamamoto, A., Fushimi, Y., Matsumoto, R., et al. (2013b). Evaluation of focus laterality in temporal lobe epilepsy: a quantitative study comparing double inversion-recovery MR imaging at 3T with FDG-PET. *Epilepsia* 54, 2174–2183. doi: 10.1111/epi.12396

Muhlhofer, W., Tan, Y. L., Mueller, S. G., and Knowlton, R. (2017). MRI-negative temporal lobe epilepsy-what do we know? *Epilepsia* 58, 727–742. doi: 10.1111/epi.13699

Pustina, D., Avants, B., Sperling, M., Gorniak, R., He, X., Doucet, G., et al. (2015). Predicting the laterality of temporal lobe epilepsy from PET, MRI, and DTI: a multimodal study. *Neuroimage Clin.* 9, 20–31. doi: 10.1016/j.nicl.2015.07.010

Rathore, C., and Radhakrishnan, K. (2015). Concept of epilepsy surgery and presurgical evaluation. *Epileptic Disord.* 17, 19–31; quiz31. doi: 10.1684/epd.2014.0720

Reddy, S. D., Younus, I., Sridhar, V., and Reddy, D. S. (2019). Neuroimaging biomarkers of experimental epileptogenesis and refractory epilepsy. *Int. J. Mol. Sci.* 20:220. doi: 10.3390/ijms20010220

Reyes, A., Uttarwar, V. S., Chang, Y. A., Balachandra, A. R., Pung, C. J., Hagler, D. J., et al. (2018). Decreased neurite density within frontostriatal networks is associated with executive dysfunction in temporal lobe epilepsy. *Epilepsy Behav.* 78, 187–193. doi: 10.1016/j.yebeh.2017.09.012

Rostampour, M., Hashemi, H., Najibi, S. M., and Oghabian, M. A. (2018). Detection of structural abnormalities of cortical and subcortical gray matter in patients with MRI-negative refractory epilepsy using neurite orientation dispersion and density imaging. *Phys. Med.* 48, 47–54. doi: 10.1016/j.ejmp.2018.03.005

Rubinger, L., Chan, C., D'Arco, F., Moineddin, R., Muthaffar, O., Rutka, J. T., et al. (2016). Change in presurgical diagnostic imaging evaluation affects subsequent pediatric epilepsy surgery outcome. *Epilepsia* 57, 32–40. doi: 10.1111/epi.13229

Rugg-Gunn, F. J., Boulby, P. A., Symms, M. R., Barker, G. J., and Duncan, J. S. (2006). Imaging the neocortex in epilepsy with double inversion recovery imaging. *Neuroimage* 31, 39–50. doi: 10.1016/j.neuroimage.2005.11.034

Ryan, M. E. (2016). Utility of double inversion recovery sequences in MRI. *Pediatr. Neurol. Briefs* 30:26. doi: 10.15844/pedneurbriefs-30-4-1

Saavalainen, T., Jutila, L., Mervaala, E., Kalviainen, R., Vanninen, R., and Immonen, A. (2015). Temporal anteroinferior encephalocele: an underrecognized etiology of temporal lobe epilepsy? *Neurology* 85, 1467–1474. doi: 10.1212/WNL.0000000000002062

Salamon, N., Kung, J., Shaw, S. J., Koo, J., Koh, S., Wu, J. Y., et al. (2008). FDG-PET/MRI coregistration improves detection of cortical dysplasia in patients with epilepsy. *Neurology* 71, 1594–1601. doi: 10.1212/01.wnl.0000334752.41807.2f

Shang, K., Wang, J., Fan, X., Cui, B., Ma, J., Yang, H., et al. (2018). Clinical value of hybrid TOF-PET/MR imaging-based multiparametric imaging in localizing seizure focus in patients with MRI-Negative temporal lobe epilepsy. *AJNR Am. J. Neuroradiol.* 39, 1791–1798. doi: 10.3174/ajnr.A5814

Shao, X., Zhang, X., Xu, W., Zhang, Z., Zhang, J., Guo, H., et al. (2021). Neurite orientation dispersion and density imaging parameters may help for the evaluation of epileptogenic tubers in tuberous sclerosis complex patients. *Eur. Radiol.* 31, 5605–5614. doi: 10.1007/s00330-020-07626-7627

Shigemoto, Y., Sone, D., Kimura, Y., Sato, N., and Matsuda, H. (2020). Nuclear imaging in epilepsy: principles and progress. *Epilepsy Seizure* 12, 40–48. doi: 10.3805/eands.12.40

So, E. L., and Lee, R. W. (2014). Epilepsy surgery in MRI-negative epilepsies. *Curr. Opin. Neurol.* 27, 206–212. doi: 10.1097/WCO.0000000000000078

Sone, D. (2019). Neurite orientation and dispersion density imaging: clinical utility, efficacy, and role in therapy. *Rep. Med. Imag.* 12, 17–29. doi: 10.2147/RMI.S194083

Sone, D., and Beheshti, I. (2021). Clinical application of machine learning models for brain imaging in epilepsy: a review. *Front. Neurosci.* 15:684825. doi: 10.3389/fnins.2021.684825

Sone, D., Maikusa, N., Sato, N., Kimura, Y., Ota, M., and Matsuda, H. (2019). Similar and differing distributions between 18F-FDG-PET and arterial spin labeling imaging in temporal lobe epilepsy. *Front. Neurol* 10:318. doi: 10.3389/fneur.2019.00318

Sone, D., Sato, N., Kimura, Y., Maikusa, N., Shigemoto, Y., and Matsuda, H. (2021). Quantitative analysis of double inversion recovery and FLAIR signals in temporal lobe epilepsy. *Epilepsy Res.* 170:106540. doi: 10.1016/j.eplepsyres.2020.106540

Sone, D., Sato, N., Ota, M., Maikusa, N., Kimura, Y., and Matsuda, H. (2018). Abnormal neurite density and orientation dispersion in unilateral temporal lobe epilepsy detected by advanced diffusion imaging. *Neuroimage Clin.* 20, 772–782. doi: 10.1016/j.nicl.2018.09.017

Sun, K., Yu, T., Yang, D., Ren, Z., Qiao, L., Ni, D., et al. (2021). Fluid and white matter suppression imaging and voxel-based morphometric analysis in conventional magnetic resonance imaging-negative epilepsy. *Front. Neurol.* 12:651592. doi: 10.3389/fneur.2021.651592

Tan, Y. L., Kim, H., Lee, S., Tihan, T., Ver Hoef, L., Mueller, S. G., et al. (2018). Quantitative surface analysis of combined MRI and PET enhances detection of focal cortical dysplasias. *Neuroimage* 166, 10–18. doi: 10.1016/j.neuroimage.2017.10.065

Tanner, M., Gambarota, G., Kober, T., Krueger, G., Erritzoe, D., Marques, J. P., et al. (2012). Fluid and white matter suppression with the MP2RAGE sequence. *J. Magn. Reson. Imaging* 35, 1063–1070. doi: 10.1002/jmri.23532

Thom, M. (2014). Review: hippocampal sclerosis in epilepsy: a neuropathology review. *Neuropathol. Appl. Neurobiol.* 40, 520–543. doi: 10.1111/nan.12150

Tse, G. T., Frydman, A. S., O'Shea, M. F., Fitt, G. J., Weintrob, D. L., Murphy, M. A., et al. (2020). Anterior temporal encephaloceles: elusive, important, and rewarding to treat. *Epilepsia.* 61, 2675–2684. doi: 10.1111/epi.16729

van Graan, L. A., Lemieux, L., and Chaudhary, U. J. (2015). Methods and utility of EEG-fMRI in epilepsy. *Quant. Imaging Med. Surg.* 5, 300–312. doi: 10.3978/j.issn.2223-4292.2015.02.04

van Lanen, R., Colon, A. J., Wiggins, C. J., Hoeberigs, M. C., Hoogland, G., Roebroeck, A., et al. (2021). Ultra-high field magnetic resonance imaging in human epilepsy: a systematic review. *Neuroimage Clin.* 30:102602. doi: 10.1016/j.nicl.2021.102602

Veersema, T. J., Ferrier, C. H., van Eijsden, P., Gosselaar, P. H., Aronica, E., Visser, F., et al. (2017). Seven tesla MRI improves detection of focal cortical dysplasia in patients with refractory focal epilepsy. *Epilepsia Open* 2, 162–171. doi: 10.1002/epi4.12041

Vos, S. B., Winston, G. P., Goodkin, O., Pemberton, H. G., Barkhof, F., Prados, F., et al. (2020). Hippocampal profiling: localized magnetic resonance imaging volumetry and T2 relaxometry for hippocampal sclerosis. *Epilepsia* 61, 297–309. doi: 10.1111/epi.16416

Wagner, J., Weber, B., Urbach, H., Elger, C. E., and Huppertz, H. J. (2011). Morphometric MRI analysis improves detection of focal cortical dysplasia type II. *Brain* 134(Pt 10), 2844–2854. doi: 10.1093/brain/awr204

Wang, Y. H., An, Y., Fan, X. T., Lu, J., Ren, L. K., Wei, P. H., et al. (2018). Comparison between simultaneously acquired arterial spin labeling and (18)F-FDG PET in mesial temporal lobe epilepsy assisted by a PET/MR system and SEEG. *Neuroimage Clin.* 19, 824–830. doi: 10.1016/j.nicl.2018.06.008

Wang, Z. I., Jones, S. E., Jaisani, Z., Najm, I. M., Prayson, R. A., Burgess, R. C., et al. (2015). Voxel-based morphometric magnetic resonance imaging (MRI) postprocessing in MRI-negative epilepsies. *Ann. Neurol.* 77, 1060–1075. doi: 10.1002/ana.24407

Wang, Z. I., McBride, A., Grinenko, O., Blumcke, I., Overmyer, M., Bingaman, W., et al. (2017). Utility of CISS sequence in detecting anteroinferior temporal encephalocele. *J. Neurol. Sci.* 381, 59–61. doi: 10.1016/j.jns.2017.08.004

White, N. S., Leergaard, T. B., D'Arceuil, H., Bjaalie, J. G., and Dale, A. M. (2013). Probing tissue microstructure with restriction spectrum imaging: histological and theoretical validation. *Hum. Brain Mapp.* 34, 327–346. doi: 10.1002/hbm.21454

Winston, G. P., Cardoso, M. J., Williams, E. J., Burdett, J. L., Bartlett, P. A., Espak, M., et al. (2013). Automated hippocampal segmentation in patients with epilepsy: available free online. *Epilepsia* 54, 2166–2173. doi: 10.1111/epi.12408

Winston, G. P., Micallef, C., Symms, M. R., Alexander, D. C., Duncan, J. S., and Zhang, H. (2014). Advanced diffusion imaging sequences could aid assessing patients with focal cortical dysplasia and epilepsy. *Epilepsy Res.* 108, 336–339. doi: 10.1016/j.eplepsyres.2013.11.004

Winston, G. P., Vos, S. B., Caldairou, B., Hong, S. J., Czech, M., Wood, T. C., et al. (2020). Microstructural imaging in temporal lobe epilepsy: diffusion imaging changes relate to reduced neurite density. *Neuroimage Clin.* 26:102231. doi: 10.1016/j.nicl.2020.102231

Wong-Kisiel, L. C., Britton, J. W., Witte, R. J., Kelly-Williams, K. M., Kotsenas, A. L., Krecke, K. N., et al. (2016). Double inversion recovery magnetic resonance imaging in identifying focal cortical dysplasia. *Pediatr. Neurol.* 61, 87–93. doi: 10.1016/j.pediatrneurol.2016.04.013

Wychowski, T., Hussain, A., Tivarus, M. E., Birbeck, G. L., Berg, M. J., and Potchen, M. (2016). Qualitative analysis of double inversion recovery MRI in drug-resistant epilepsy. *Epilepsy Res.* 127, 195–199. doi: 10.1016/j.eplepsyres.2016.\break09.001

Yang, Z., Choupan, J., Reutens, D., and Hocking, J. (2015). Lateralization of temporal lobe epilepsy based on resting-state functional magnetic resonance imaging and machine learning. *Front. Neurol.* 6:184. doi: 10.3389/fneur.2015.00184

Zijlmans, M., de Kort, G. A., Witkamp, T. D., Huiskamp, G. M., Seppenwoolde, J. H., van Huffelen, A. C., et al. (2009). 3T versus 1.5T phased-array MRI in the presurgical work-up of patients with partial epilepsy of uncertain focus. *J. Magn. Reson. Imaging.* 30, 256–262. doi: 10.1002/jmri.21811

Conflict of Interest: The author declares that the research was conducted in the absence of any commercial or financial relationships that could be construed as a potential conflict of interest.

frontiers in Neuroscience

REVIEW
published: 06 August 2021
doi: 10.3389/fnins.2021.699123

Advances in Brain Imaging Techniques for Patients With Intractable Epilepsy

Mubarak Algahtany[1], Ahmed Abdrabou[2], Ahmed Elhaddad[3] and Abdulrahman Alghamdi[4]*

[1] Division of Neurosurgery, Department of Surgery, College of Medicine, King Khalid University, Abha, Saudi Arabia, [2] Department of Radiology, Ain Shams University, Cairo, Egypt, [3] Department of Radiology, Mansoura University, Mansoura, Egypt, [4] Department of Radiology, Aseer Central Hospital, Abha, Saudi Arabia

Intractable epilepsy, also known as drug resistance or refractory epilepsy, is a major problem affecting nearly one-third of epilepsy patients. Surgical intervention could be an option to treat these patients. Correct identification and localization of epileptogenic foci is a crucial preoperative step. Some of these patients, however, have no abnormality on routine magnetic resonance imaging (MRI) of the brain. Advanced imaging techniques, therefore, can be helpful to identify the area of concern. Moreover, a clear delineation of certain anatomical brain structures and their relation to the surgical lesion or the surgical approach is essential to avoid postoperative complications, and advanced imaging techniques can be very helpful. In this review, we discuss and highlight the use of advanced imaging techniques, particularly positron emission tomography (PET)–MRI, single-photon emission computed tomography, functional MRI, and diffusion tensor imaging–tractography for the preoperative assessment of epileptic patients.

Keywords: subtle lesion, surgery, brain imaging, epilpesy, advance

OPEN ACCESS

Edited by:
Ahmad Raza Khan, Centre of Bio-Medical Research (CBMR), India

Reviewed by:
Wen Qin, Tianjin Medical University General Hospital, China
Jiajia Zhu, First Affiliated Hospital of Anhui Medical University, China

****Correspondence:***
Mubarak Algahtany
mbalgahtany@kku.edu.sa

Specialty section:
This article was submitted to Brain Imaging Methods, a section of the journal Frontiers in Neuroscience

Received: *22 April 2021*
Accepted: *20 July 2021*
Published: *06 August 2021*

Citation:
Algahtany M, Abdrabou A, Elhaddad A and Alghamdi A (2021) Advances in Brain Imaging Techniques for Patients With Intractable Epilepsy. Front. Neurosci. 15:699123. doi: 10.3389/fnins.2021.699123

INTRODUCTION

Temporary onset of signs and/or symptoms due to irregular excessive or synchronous neuronal activity in the brain is known as an epileptic seizure (Fisher et al., 2005). Epilepsy is defined as drug-resistant, or intractable, when the two main antiepileptic drugs are not capable of eliminating seizure activity, according to the International League Against Epilepsy (ILAE) (Duncan et al., 2016).

The epileptic focus is the site where the seizure starts (Munari and Bancaud, 1985). Epilepsy surgery aims to identify, remove, or disconnect this focus to achieve seizure-free conditions (Bonelli et al., 2012). The radiological identification of this focus and defining its relations to adjacent critical brain structures, however, could be challenging (Duncan et al., 2016).

For example, one of the most common causes of focal seizures in adults and infants is temporal lobe epilepsy (TLE), which accounts for 30% of all epilepsies (Rastogi et al., 2008). Nearly one-third of patients with TLE develop drug resistance, and in one-third of them, routine magnetic resonance imaging (MRI) of the brain will be normal (Bernardino et al., 2005).

Preoperative workup is required for the evaluation of patients with intractable epilepsy. MRI is the investigation of the choice for regular assessment. An epilepsy-tailored MRI technique was established to detect subtle lesions. This includes three-dimensional (3D) T1-weighted image

gradient echo (MPRAGE) and 3D fluid-attenuated inversion recovery (FLAIR) images with isotropic voxels for the detection of focal cortical dysplasia (FCD) and mesial temporal sclerosis (MTS). Coronal and axial high-resolution T2-weighted images with 2–3 mm slice thickness are also used for the same reason. A 3D susceptibility-weighted imaging (SWI) sequence is required for microbleeds and faint calcification. Moreover, coronal T1 inversion recovery is used for better delineation of the gray–white matter interface, 3D T2 if suspected encephalocele, diffusion-weighted imaging (DWI) for detection of ischemic lesion, and post-contrast scan in case of inflammation or tumors. The use of 3T MRI is favored over regular 1.5T MRI machines (Gonçalves Pereira et al., 2006; Coan et al., 2014; Shah and Mittal, 2014).

The most challenging lesions to detect are MTS and FCD. The age of onset of MTS is usually between 4 and 16 years of age, with no gender preference. There may also be a family history of seizures. The diagnosis of MTS requires 3 mm coronal section T2-weighted image or FLAIR, in which gliotic changes appear as hyperintense signals. Atrophy and neuronal loss can also be observed in the T1-weighted image. Surgical intervention in MTS shows a success rate of 90% (Bradley and Shey, 2000; Rastogi et al., 2008; Tsai et al., 2016).

In contrast, FCD is the most common cause of intractable epilepsy in children younger than 3 years of age. It is considered a focal form of malformation of cortical development (MCD) and is thought to be related to an insult during gray matter differentiation. These insults could be ischemic, infectious, toxic, or genetic, and the associated epilepsy is drug-resistant and usually requires surgery (Rastogi et al., 2008).

In many situations, epilepsy-tailored MRI techniques are not sufficient to detect a lesion, and delineate its relations to adjacent eloquent brain structures. Therefore, other advanced techniques, such as positron emission tomography (PET), PET–MRI, functional MRI (fMRI), magnetic resonance spectroscopy (MRS), and diffusion tensor imaging (DTI), can be used. These techniques aim to detect a lesion, its connection, and its intimacy with an eloquent area to limit surgery and avoid post-surgical complications (Knake et al., 2005).

We review different advanced imaging techniques that are useful to detect epilepsy lesions and outline their relations to nearby critical brain structures and highlight the value of these techniques in improving the outcome and safety of epilepsy surgery.

POSITRON EMISSION TOMOGRAPHY

Positron emission tomography is a functional imaging technique that detects glucose uptake and metabolism in various tissues. The most used tracer is 2-deoxy-2[^{18}F] fluoro-D-glucose (FDG), which is manufactured in a cyclotron, produces gamma radiation, and can cross the blood–brain barrier. After intravenous injection of FDG, tissue uptake, accumulation, and processing can be detected using a specific PET scanner (Juhász and John, 2020).

Positron emission tomography scanning requires a long imaging time (approximately 30 min), so it is suitable to detect epileptic focus, or in another term, the functional deficit zone, during the interictal period. Epileptic focus, which could be a small FCD that is often missed on MRI, appears as an area of low metabolism (reduced uptake) due to low neuronal activity as compared to the rest of the brain tissue (**Figure 1**). Even if the lesion is detected by conventional MRI, the extent of this lesion is beyond what is visible, and PET can detect the exact damaged area. Therefore, PET provides lateralization and localization information to guide epilepsy surgeons to remove or disconnect only the area of concern while avoiding major surgical procedures and poor postoperative outcomes (Rosenow and Lüders, 2001; Juhász and John, 2020).

Positron emission tomography is superior to conventional MRI in detecting mild malformations of cortical development, which was missed in up to 66% of patients by MRI, while detected in 77% of patients by PET in some of the studies (Kim et al., 2011).

Co-registration of MRI with PET (**Figure 1**) adds more localizing capability and increases the sensitivity of PET to detect FCD, particularly type I, up to 98% which is commonly missed on routine MRI examination (Salamon et al., 2008). Moreover, surgical resection of the PET–MRI-positive region is associated with better seizure-free outcomes (Lin et al., 2018).

Hybrid PET–MRI has the same sensitivity as PET–CT but has the advantage of less radiation exposure and lower absorbed dose to the brain and eye as the images are acquired in a single session (Oldan et al., 2018). Limitations include high cost, long scan time, and the use of radioactive material which should be prepared in advance (Juhász and John, 2020).

SINGLE-PHOTON EMISSION COMPUTED TOMOGRAPHY

Single-photon emission computed tomography (SPECT) is another nuclear medicine technique that can detect epileptogenic foci during seizure activity. During seizures, blood perfusion to the abnormal area increases up to threefold. SPECT can detect this focal hyperperfusion during ictus; hence, it is called ictal SPECT (Valmier et al., 1989). Technetium-99m hexamethylpropyleneamine oxime (99^{m}Tc HMPAO) is used as an isotope agent, and a gamma camera is used to detect the radiation emission from the isotope. The injected dose is divided into two halves. The first half is injected during the interictal period, while the second half is injected during seizures, which is detected by an electroencephalograph (EEG) connected to the patient's scalp. The uptake of the interictal scan is subtracted from the uptake of the ictal scan and the result refers to the focal area of hyperperfusion, and hence the epileptogenic focus (Duncan et al., 2016).

Furthermore, ictal SPECT can be co-registered with MRI, as with PET, and this again increases its accuracy and ability to show better anatomical localization. The new technique is called subtraction ictal SPECT co-registered with MRI (SISCOM). Identifying the epileptogenic focus by SISCOM is associated with good postoperative outcomes and elimination of seizures (Lerner et al., 2009).

SPECT co-registered with MRI is also useful in determining the exact location during placement of intracranial EEG leads for invasive recording that reduces possible complications.

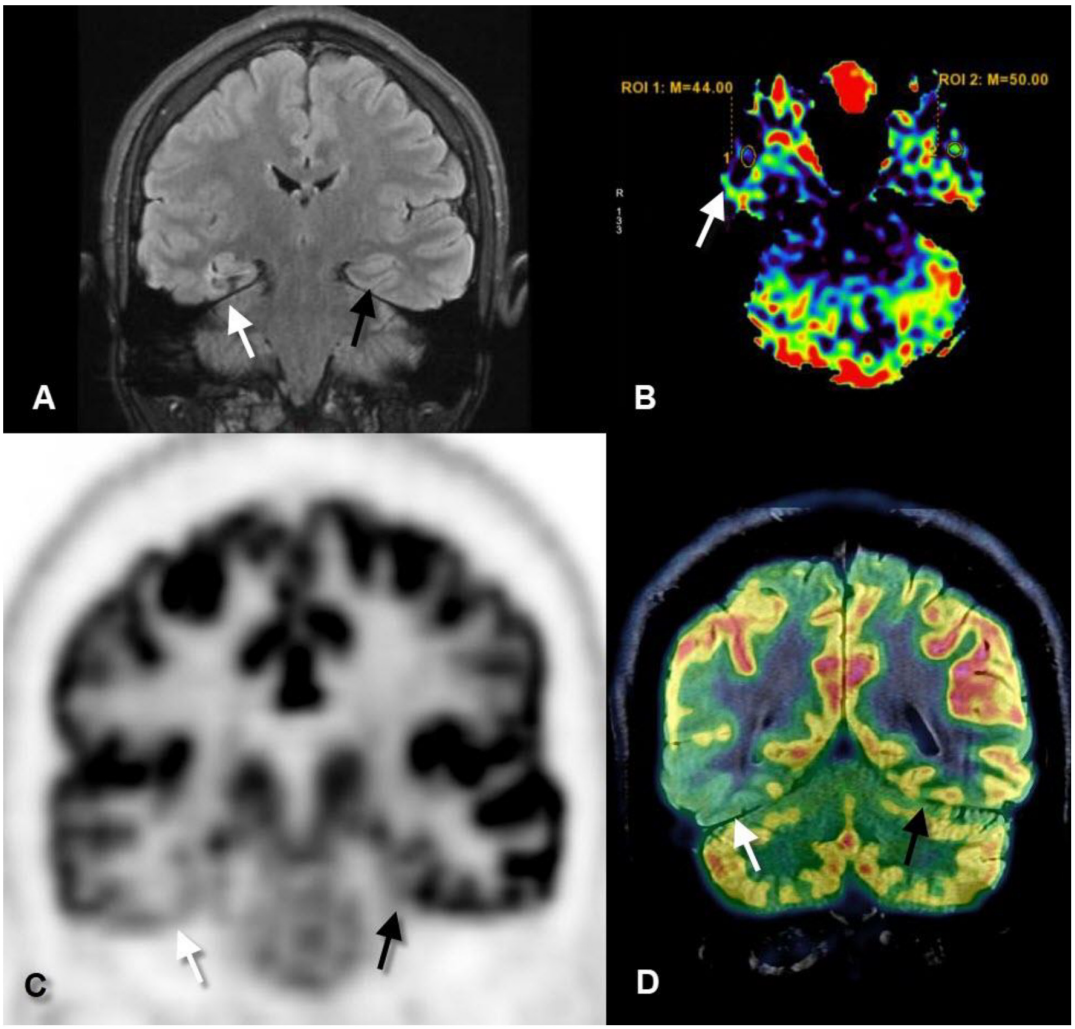

FIGURE 1 | Coronal fluid-attenuated inversion recovery (FLAIR) **(A)**, axial perfusion-weighted imaging-arterial spin-labeled (PWI-ASL) **(B)**, coronal positron emission tomography (PET) **(C)**, and coronal PET–MRI fusion **(D)** images of a 23-year-old male with longstanding epilepsy and underwent the scans in the interictal period. FLAIR image revealed mild increased signal and mild gliotic changes of the right hippocampus (white arrows) as compared to the left one (black arrows). PWI-ASL revealed a decrease in the cerebral blood flow (CBF) in the right hippocampus [region of interest (ROI) 1 = 44] as compared to the left hippocampus (ROI 2 = 50) denoting hypoperfusion. PET and PET–MRI images revealed pronounced hypometabolism of the right temporal lobe particularly the hippocampal formation as compared to the contralateral side. Quantitative data showed standardized uptake value (SUV) of right hippocampus measured 2.56 while on the left hippocampus measured 4.88 (Case courtesy of Prof. Dr. Yasser Abdel Azeem, Ain Shams University).

Nevertheless, it is sensitive to detect ictal focus in cases of extratemporal lobe epilepsy (Kim et al., 2009).

One limitation of ictal SPECT is the timing of radiotracer injection, which should be within 25 s after onset of ictus to achieve good sensitivity and avoid misleading results (Stamoulis et al., 2017).

PERFUSION MRI

Magnetic resonance imaging can detect changes in blood flow and volume using perfusion techniques. This can be done with intravenous contrast administration, for example, dynamic susceptibility contrast (DSC) or without intravenous contrast administration, for example, arterial spin labeling (ASL). The acquisition time is relatively long (3–4 min), which is why MR perfusion detects hyperperfusion in the early post-ictal period. Perfusion may be performed in the interictal period and the results can be subtracted from the early post-ictal perfusion images which confirmed the epileptogenic focus (Shah and Mittal, 2014; Abud et al., 2015).

In ASL (**Figure 1**), protons of the arterial blood are labeled by a radiofrequency pulse generated from the MR machine before they enter the cerebral vasculature and exchange with unlabeled protons. ASL can measure the cerebral blood volume (CBV) and cerebral blood flow (CBF) at the area of interest and hence can measure seizure related changes. It is widely

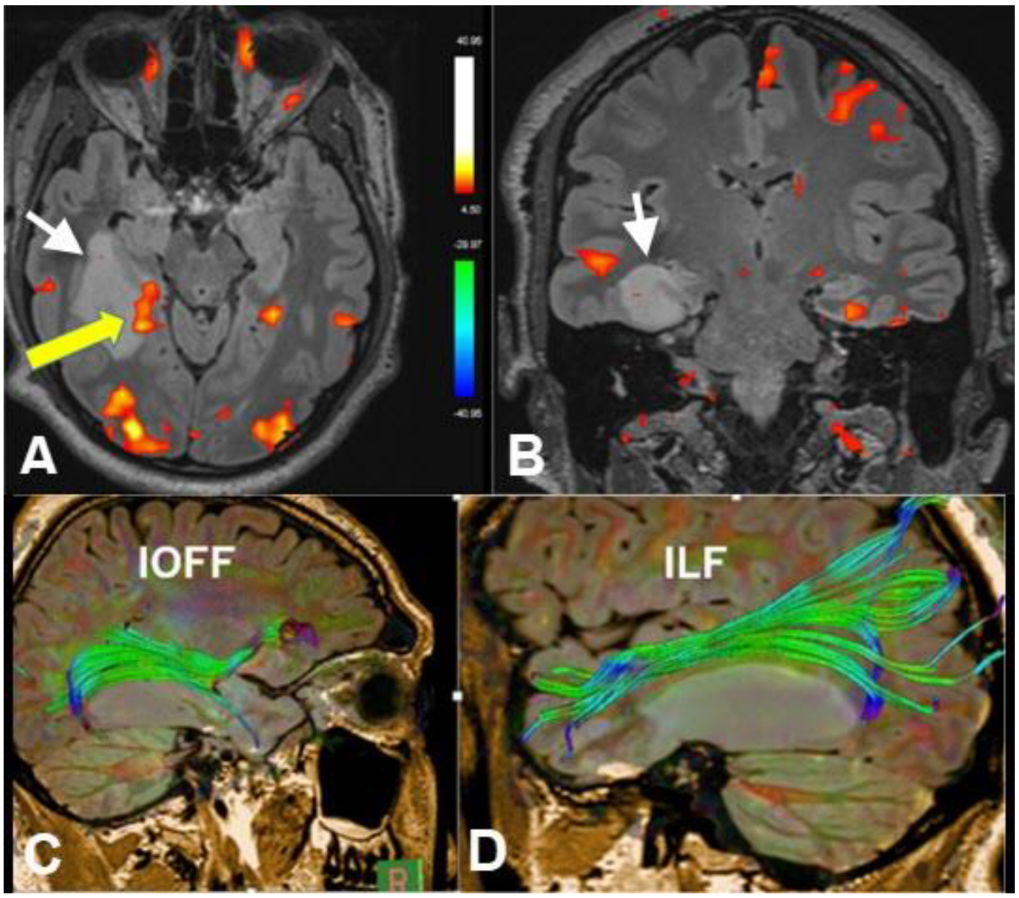

FIGURE 2 | Axial **(A)** and coronal **(B)** functional MRI (fMRI) (memory paradigm), diffusion tensor imaging (DTI)-tractography of the inferior occipitofrontal fasciculus (IOFF) **(C)** and inferior longitudinal fasciculus (ILF) **(D)** of a 30-year-old male with recurrent epilepsy due to right hippocampal low-grade glioma (white arrows). Yellow arrow referred to cortical representation at the posterior aspect of the hippocampus in relation to the lesion after memory activation. Tractography revealed deviation of the IOFF and ILF by the lesion without disruption of the fibers. These data are important in pre-operative planning (Case courtesy of Prof. Dr. Yasser Abdel Azeem, Ain Shams University).

used in accompany with conventional MRI as it doesn't require intravenous contrast injection, it has a low cost, less time, and doesn't subject the patients to radiation or radioactive hazards. On the contrary, the sensitivity of ASL is affected by the time delay between the onset of seizure and beginning of the scan (Kim et al., 2016).

DIFFUSION TENSOR IMAGING AND FIBER TRACTOGRAPHY

Diffusion tensor imaging is an advanced MRI technique that monitors the continuous movement of water molecules (Brownian movement). In an isotropic medium, for example, the gray matter, water molecules tend to be distributed randomly with no preferred direction. In an anisotropic medium, for example, white matter fibers, water molecules prefer to diffuse along the long axis of the nerve fibers rather than perpendicular to this axis (preferred direction) (Fujiyoshi et al., 2016; San Martín Molina et al., 2020).

By dividing the matrix into voxels and determining the water movement direction of each voxel, reconstruction of the white matter tracts can be performed by combining voxel directions, which is called tractography (**Figure 2**). Several tractography algorithms can be used, either deterministic or probabilistic, and the fiber tracts of every white matter bundle can be generated (Rosazza et al., 2018).

An important step in preoperative evaluation in patients with intractable epilepsy is to identify Meyer's loop at the site of surgery. Mayer's loop is the anterior bundle of optic radiation, which projects variably into the temporal lobe (**Figure 3**). Anterior temporal lobe resection can cause injury of Meyer's loop and, consequently, postoperative visual field defects. Identification of Meyer's loop and measuring the distance from the anterior pole of the temporal lobe is crucial to salvage the bundle during surgery and avoid postoperative complications (Yogarajah et al., 2009; James et al., 2015).

Another white matter bundle that should be preserved during surgery is the arcuate fasciculus. The arcuate fasciculus connects the language areas at the temporal (Wernicke's) and frontal lobes

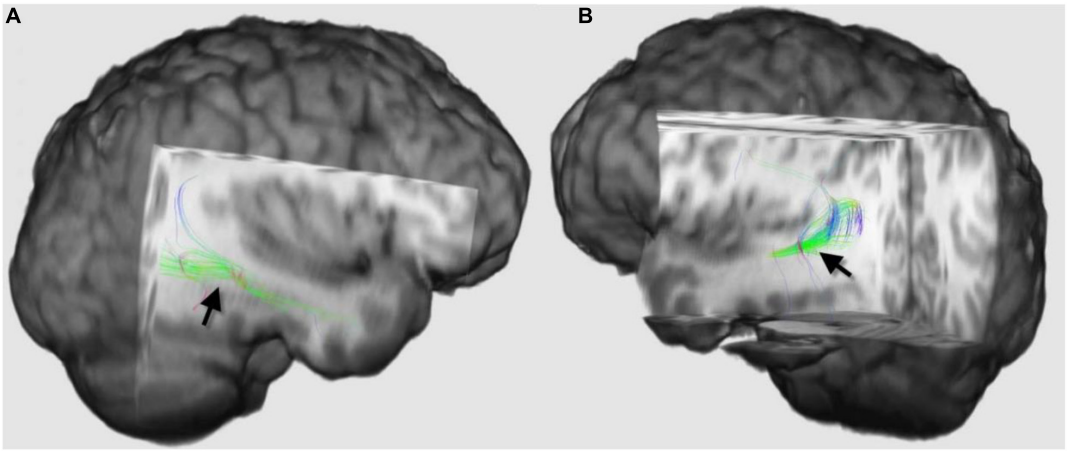

FIGURE 3 | Three-dimensional diffusion tensor imaging (DTI)-tractography images of the Meyer's loops on the right side **(A)** and left side **(B)** of the same patient (black arrows), which demonstrated how asymmetrical Meyer's loop could be in the same individual. The loop on the right side projected more into the temporal lobe than the left side. Tractography of this loop and estimation of the distance between the anterior pole of the temporal lobe and these fibers are recommended before anterior temporal lobe resection to guard against postoperative visual field defect.

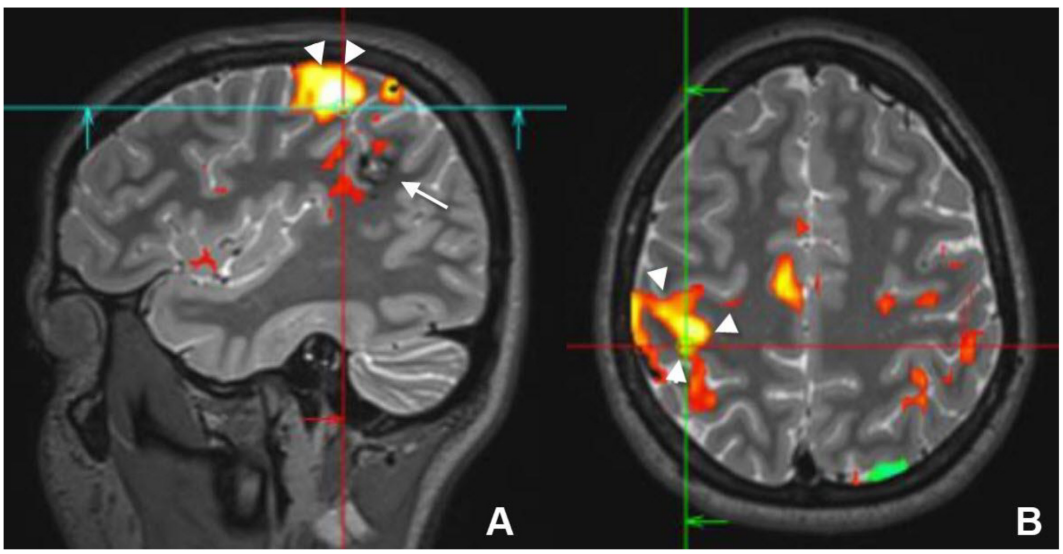

FIGURE 4 | Sagittal **(A)** and axial **(B)** preoperative functional MRI (fMRI) of a young female who had a cavernous hemangioma on the right parietal lobe (white arrow) that caused recurrent seizure. Activation of the motor cortex (white arrowheads) by finger tapping test revealed that the lesion was separable from the motor cortex and it could be resected without postoperative motor deficit.

(Broca's) and is larger in the dominant hemisphere (Ellmore et al., 2010). Injury or disconnection of this tract during surgery results in conduction aphasia; therefore, DTI-tractography is recommended before frontotemporal resection to preserve this bundle (Li et al., 2013).

FUNCTIONAL MRI

In the preoperative setting, DTI should be combined with fMRI to estimate the exact risk of surgical intervention. fMRI is a functional imaging technique that is sensitive to changes in oxygen concentration. Activated cortical areas within the brain extract more oxygen from the blood, and its blood oxygen level-dependent (BOLD) signal will change (**Figure 2**; Gaillard, 2000).

Each cortical area requires a specific task and a tailored paradigm for its activation and assessment. Activation of the cortical area will result in focal hyperemia and a transient increase in oxygenic consumption (**Figures 2**, **4**), which will consequently cause a detectable increase in the T2* signal in this region (Yerys et al., 2009).

Evaluation of language function and its side of dominance is essential for safe epilepsy surgery and requires the assessment of receptive (Wernicke) and expressive (Broca's) language areas.

In most healthy right-handed individuals, the left hemisphere is dominant, while in patients with TLE, this pattern is changed; there is a higher incidence of bilateral and right hemisphere dominance (Rosazza et al., 2013). Lateralization of the dominant hemisphere for language was previously carried out by the intracarotid amytal injection (Wada) test or electrocortical stimulation mapping, which are invasive techniques. Consequently, fMRI has been increasingly used to replace such invasive techniques (de Ribaupierre et al., 2012).

Several tasks are required to assess the comprehensive and productive capability of language areas. These include the verbal generation task, which is an easy task that stimulates both frontal and temporal language areas, semantic comprehension tasks that require naming objects and result in activation of temporal areas as well as verbal fluency tasks that activate the frontal more than the temporal regions (Vitali et al., 2011).

Localizing the motor area before surgery is an important step to avoid post-surgical paralysis. Localization of the dominant hemisphere is important before hemispherectomy, and the assessment of the closeness of the epileptogenic focus to the motor area is crucial. Tasks that involve stimulating the foot, finger, and mouth can be used to assess the motor cortex (**Figure 4**). In children less than 2 years of age and in sedated patients, activation of the motor cortex can be successfully performed using passive movement (Choudhri et al., 2015).

Resting-state fMRI (rs-fMRI) is another emerging technique that does not require a specific task for activation. It detects spontaneous neural activity, which creates fluctuations in the BOLD signal. Some studies have revealed that patients with epilepsy have an abnormal pattern of the resting-state network including decreased connectivity in comparison to the healthy group (Pizoli et al., 2011; Roland et al., 2017).

Although fMRI has a lower risk, lower cost, and more functional localization capability than Wada test, yet it still has some drawbacks. For example, there is no standard threshold to differentiate between activated and non-activated areas, the complexity of some tasks like language and memory requires high level of cooperation between staff and participants and the lack of ideal paradigms for the assessment of some tasks such as memory (Limotai and Mirsattari, 2012; Szaflarski et al., 2017).

CONCLUSION

Surgery can be a good treatment option for medically refractory epilepsy. The surgical success may depend on the use of advanced brain imaging techniques to identify the epileptic focus. We recommend the use of multiparametric imaging like conventional MRI with the use of perfusion, SPECT, PET–MRI to increase the chance of correct identification of the epileptogenic focus and the use of fMRI as well as DTI before surgical intervention to map the eloquent cortical areas, such as the language and motor cortex, as well as the connecting white matter tracts, to avoid accidental damage and faulty disconnection during surgery.

AUTHOR CONTRIBUTIONS

MA: conceptualization, writing review and editing, and supervision. AAb, AE, and AAl: writing review and editing. All authors contributed to the article and approved the submitted version.

REFERENCES

Abud, L. G., Thivard, L., Abud, T. G., Nakiri, G. S., Santos, A. C., and Dormont, D. (2015). Partial epilepsy: a pictorial review of 3 TESLA magnetic resonance imaging features. *Clinics (Sao Paulo)* 70, 654–661. doi: 10.6061/clinics/2015(09)10

Bernardino, L., Ferreira, R., Cristóvao, A. J., Sales, F., and Malva, J. O. (2005). Inflammation and neurogenesis in temporal lobe epilepsy. *Curr. Drug Targets CNS Neurol. Disord.* 4, 349–360. doi: 10.2174/1568007054546171

Bonelli, S. B., Thompson, P. J., Yogarajah, M., Vollmar, C., Powell, R. H. W., Symms, M. R., et al. (2012). Imaging language networks before and after anterior temporal lobe resection: results of a longitudinal fMRI study. *Epilepsia* 53, 639–650. doi: 10.1111/j.1528-1167.2012.03433.x

Bradley, W. G., and Shey, R. B. (2000). MR imaging evaluation of seizures. *Radiology* 214, 651–656. doi: 10.1148/radiology.214.3.r00mr42651

Choudhri, A. F., Patel, R. M., Siddiqui, A., Whitehead, M. T., and Wheless, J. W. (2015). Cortical activation through passive-motion functional MRI. *AJNR Am. J. Neuroradiol.* 36, 1675–1681. doi: 10.3174/ajnr.A4345

Coan, A. C., Kubota, B., Bergo, F. P., Campos, B. M., and Cendes, F. (2014). 3T MRI quantification of hippocampal volume and signal in mesial temporal lobe epilepsy improves detection of hippocampal sclerosis. *AJNR Am. J. Neuroradiol.* 35, 77–83. doi: 10.3174/ajnr.A3640

de Ribaupierre, S., Fohlen, M., Bulteau, C., Dorfmüller, G., Delalande, O., Dulac, O., et al. (2012). Presurgical language mapping in children with epilepsy: clinical usefulness of functional magnetic resonance imaging for the planning of cortical stimulation. *Epilepsia* 53, 67–78. doi: 10.1111/j.1528-1167.2011.03329.x

Duncan, J. S., Winston, G. P., Koepp, M. J., and Ourselin, S. (2016). Brain imaging in the assessment for epilepsy surgery. *Lancet Neurol.* 15, 420–433. doi: 10.1016/S1474-4422(15)00383-X

Ellmore, T. M., Beauchamp, M. S., Breier, J. I., Slater, J. D., Kalamangalam, G. P., O'Neill, T. J., et al. (2010). Temporal lobe white matter asymmetry and language laterality in epilepsy patients. *Neuroimage* 49, 2033–2044. doi: 10.1016/j.neuroimage.2009.10.055

Fisher, R. S., van Emde Boas, W., Blume, W., Elger, C., Genton, P., Lee, P., et al. (2005). Epileptic seizures and epilepsy: definitions proposed by the International League Against Epilepsy (ILAE) and the International Bureau for Epilepsy (IBE). *Epilepsia* 46, 470–472. doi: 10.1111/j.0013-9580.2005.66104.x

Fujiyoshi, K., Hikishima, K., Nakahara, J., Tsuji, O., Hata, J., Konomi, T., et al. (2016). Application of q-Space diffusion MRI for the visualization of white matter. *J. Neurosci.* 36, 2796–2808. doi: 10.1523/JNEUROSCI.1770-15.2016

Gaillard, W. D. (2000). Structural and functional imaging in children with partial epilepsy. *Ment. Retard. Dev. Disabil. Res. Rev.* 6, 220–226.

Gonçalves Pereira, P. M., Oliveira, E., and Rosado, P. (2006). Apparent diffusion coefficient mapping of the hippocampus and the amygdala in pharmaco-resistant temporal lobe epilepsy. *AJNR Am. J. Neuroradiol.* 27, 671–683.

James, J. S., Radhakrishnan, A., Thomas, B., Madhusoodanan, M., Kesavadas, C., Abraham, M., et al. (2015). Diffusion tensor imaging tractography of Meyer's loop in planning resective surgery for drug-resistant temporal lobe epilepsy. *Epilepsy Res.* 110, 95–104. doi: 10.1016/j.eplepsyres.2014.11.020

Juhász, C., and John, F. (2020). Utility of MRI, PET, and ictal SPECT in presurgical evaluation of non-lesional pediatric epilepsy. *Seizure* 77, 15–28. doi: 10.1016/j.seizure.2019.05.008

Kim, B. S., Lee, S. T., Yun, T. J., Lee, S. K., Paeng, J. C., Jun, J., et al. (2016). Capability of arterial spin labeling MR imaging in localizing seizure focus in clinical seizure activity. *Eur. J. Radiol.* 85, 1295–1303. doi: 10.1016/j.ejrad.2016.04.015

Kim, J. T., Bai, S. J., Choi, K. O., Lee, Y. J., Park, H. J., Kim, D. S., et al. (2009). Comparison of various imaging modalities in localization of epileptogenic lesion using epilepsy surgery outcome in pediatric patients. *Seizure* 18, 504–510. doi: 10.1016/j.seizure.2009.04.012

Kim, Y. H., Kang, H. C., al Kim, D. S., Kim, S. H., Shim, K. W., Kim, H. D., et al. (2011). Neuroimaging in identifying focal cortical dysplasia and prognostic factors in pediatric and adolescent epilepsy surgery. *Epilepsia* 52, 722–727. doi: 10.1111/j.1528-1167.2010.02950.x

Knake, S., Triantafyllou, C., Wald, L. L., Wiggins, G., Kirk, G. P., Larsson, P. G., et al. (2005). 3T phased array MRI improves the presurgical evaluation in focal epilepsies: a prospective study. *Neurology* 65, 1026–1031. doi: 10.1212/01.wnl.0000179355.04481.3c

Lerner, J. T., Salamon, N., Hauptman, J. S., Velasco, T. R., Hemb, M., Wu, J. Y., et al. (2009). Assessment and surgical outcomes for mild type I and severe type II cortical dysplasia: a critical review and the UCLA experience. *Epilepsia* 50, 1310–1335. doi: 10.1111/j.1528-1167.2008.01998.x

Li, Z., Peck, K. K., Brennan, N. P., Jenabi, M., Hsu, M., Zhang, Z., et al. (2013). Diffusion tensor tractography of the arcuate fasciculus in patients with brain tumors: comparison between deterministic and probabilistic models. *J. Biomed. Sci. Eng.* 6, 192–200. doi: 10.4236/jbise.2013.62023

Limotai, C., and Mirsattari, S. M. (2012). Role of functional MRI in presurgical evaluation of memory function in temporal lobe epilepsy. *Epilepsy Res. Treat.* 2012:687219. doi: 10.1155/2012/687219

Lin, Y., Fang, Y. D., Wu, G., Jones, S. E., Prayson, R. A., Moosa, A. N. V., et al. (2018). Quantitative positron emission tomography-guided magnetic resonance imaging postprocessing in magnetic resonance imaging-negative epilepsies. *Epilepsia* 59, 1583–1594. doi: 10.1111/epi.14474

Munari, C., and Bancaud, J. (1985). *The Role of Stereoelectroencephalography (SEEG) in the Evaluation of Partial Epileptic Seizures in the Epilepsies*, eds R. Porter and P. Morselli London: Butterworth & Co, 267–306.

Oldan, J. D., Shin, H. W., Khandani, A. H., Zamora, C., Benefield, T., and Jewells, V. (2018). Subsequent experience in hybrid PET-MRI for evaluation of refractory focal onset epilepsy. *Seizure* 61, 128–134. doi: 10.1016/j.seizure.2018.07.022

Pizoli, C. E., Shah, M. N., Snyder, A. Z., Shimony, J. S., Limbrick, D. D., Raichle, M. E., et al. (2011). Resting-state activity in development and maintenance of normal brain function. *Proc. Natl. Acad. Sci. U.S.A.* 108, 11638–11643. doi: 10.1073/pnas.1109144108

Rastogi, S., Lee, C., and Salamon, N. (2008). Neuroimaging in pediatric epilepsy: a multimodality approach. *RadioGraphics* 28, 1079–1095. doi: 10.1148/rg.284075114

Roland, J. L., Griffin, N., Hacker, C. D., Vellimana, A. K., Akbari, S. H., Shimony, J. S., et al. (2017). Resting-state functional magnetic resonance imaging for surgical planning in pediatric patients: a preliminary experience. *J. Neurosurg. Pediatr.* 20, 583–590. doi: 10.3171/2017.6.PEDS1711

Rosazza, C., Deleo, F., D'Incerti, L., Antelmi, L., Tringali, G., Didato, G., et al. (2018). Tracking the re-organization of motor functions after disconnective surgery: a longitudinal fMRI and DTI study. *Front. Neurol.* 9:400. doi: 10.3389/fneur.2018.00400

Rosazza, C., Ghielmetti, F., Minati, L., Vitali, P., Giovagnoli, A. R., Deleo, F., et al. (2013). Preoperative language lateralization in temporal lobe epilepsy (TLE) predicts peri-ictal, pre and post-operative language performance: an fMRI study. *NeuroImage Clin.* 3, 73–83. doi: 10.1016/j.nicl.2013.07.001

Rosenow, F., and Lüders, H. (2001). Presurgical evaluation of epilepsy. *Brain* 124, 1683–1700. doi: 10.1093/brain/124.9.1683

Salamon, N., Kung, J., Shaw, S. J., Koo, J., Koh, S., Wu, J. Y., et al. (2008). FDG-PET/MRI co-registration improves detection of cortical dysplasia in epilepsy patients. *Neurology* 71, 1594–1601. doi: 10.1212/01.wnl.0000334752.41807.2f

San Martín Molina, I. S., Salo, R. A., Abdollahzadeh, A., Tohka, J., Gröhn, O., and Sierra, A. (2020). In vivo diffusion tensor imaging in acute and subacute phases of mild traumatic brain injury in rats. *eNeuro* 7, 1–18. doi: 10.1523/ENEURO.0476-19.2020

Shah, A. K., and Mittal, S. (2014). Evaluation of magnetic resonance imaging-negative drug-resistant epilepsy. *Ann. Indian Acad. Neurol.* 17(Suppl. 1), S80–S88. doi: 10.4103/0972-2327.128667

Stamoulis, C., Verma, N., Kaulas, H., Halford, J. J., Duffy, F. H., Pearl, P. L., et al. (2017). The promise of subtraction ictal SPECT co-registered to MRI for improved seizure localization in pediatric epilepsies: affecting factors and relationship to the surgical outcome. *Epilepsy Res.* 129, 59–66. doi: 10.1016/j.eplepsyres.2016.11.020

Szaflarski, J. P., Gloss, D., Binder, J. R., Gaillard, W. D., Golby, A. J., Holland, S. K., et al. (2017). Practice guideline summary: use of fMRI in the presurgical evaluation of patients with epilepsy. Report of the Guideline Development, Dissemination, and Implementation Subcommittee of the American Academy of Neurology. *Neurology* 88, 395–402. doi: 10.1212/WNL.0000000000003532

Tsai, M. H., Vaughan, D. N., Perchyonok, Y., Fitt, G. J., Scheffer, I. E., Berkovic, S. F., et al. (2016). Hippocampal malrotation is an anatomic variant and has no clinical significance in MRI-negative temporal lobe epilepsy. *Epilepsia* 57, 1719–1728. doi: 10.1111/epi.13505

Valmier, J., Touchon, J., and Baldy-Moulinier, M. (1989). Interictal regional cerebral blood flow during nonspecific activation test in partial epilepsy. *J. Neurol. Neurosurg. Psychiatry* 52, 364–371. doi: 10.1136/jnnp.52.3.364

Vitali, P., Dronkers, N., Pincherle, A., Giovagnoli, A. R., Marras, C., D'Incerti, L., et al. (2011). Accuracy of pre-surgical fMRI confirmed by subsequent crossed aphasia. *Neurol. Sci.* 32, 175–180. doi: 10.1007/s10072-010-0426-y

Yerys, B. E., Jankowski, K. F., Shook, D., Rosenberger, L. R., Barnes, K. A., Berl, M. M., et al. (2009). The fMRI success rate of children and adolescents: typical development, epilepsy, attention deficit/hyperactivity disorder, and autism spectrum disorders. *Hum. Brain Mapp.* 30, 3426–3435. doi: 10.1002/hbm.20767

Yogarajah, M., Focke, N. K., Bonelli, S., Cercignani, M., Acheson, J., Parker, G. J., et al. (2009). Defining Meyer's loop-temporal lobe resections, visual field deficits and diffusion tensor tractography. *Brain* 132, 1656–1668. doi: 10.1093/brain/awp114

Conflict of Interest: The authors declare that the research was conducted in the absence of any commercial or financial relationships that could be construed as a potential conflict of interest.

Publisher's Note: All claims expressed in this article are solely those of the authors and do not necessarily represent those of their affiliated organizations, or those of the publisher, the editors and the reviewers. Any product that may be evaluated in this article, or claim that may be made by its manufacturer, is not guaranteed or endorsed by the publisher.

frontiers in Neuroscience

ORIGINAL RESEARCH
published: 23 August 2021
doi: 10.3389/fnins.2021.651710

Abnormal Topological Network in Parkinson's Disease With Impulse Control Disorders: A Resting-State Functional Magnetic Resonance Imaging Study

Xiaopeng Zhu[1†], Langsha Liu[2†], Yan Xiao[3], Fan Li[1], Yongkai Huang[1], Deqing Han[1], Chun Yang[1] and Sian Pan[4*]*

[1] Department of Neurosurgery, Zhuzhou Central Hospital, Zhuzhou, China, [2] Department of Cardiac Surgery, Xiangya Hospital, Central South University, Changsha, China, [3] Department of Day Surgery Center, Zhuzhou Central Hospital, Zhuzhou, China, [4] Department of Rehabilitation Medicine, Zhuzhou Central Hospital, Zhuzhou, China

OPEN ACCESS

Edited by:
Ahmad Raza Khan, Centre of Bio-Medical Research (CBMR), India

Reviewed by:
Nicola Modugno, University of L'Aquila, Italy
Simona Raimo, University of Campania Luigi Vanvitelli, Italy

***Correspondence:**
Chun Yang
chun2007yang@163.com
Sian Pan
738469325@qq.com

[†] These authors have contributed equally to this work and share first authorship

Specialty section:
This article was submitted to Neurodegeneration, a section of the journal Frontiers in Neuroscience

Received: *10 January 2021*
Accepted: *23 July 2021*
Published: *23 August 2021*

Citation:
Zhu X, Liu L, Xiao Y, Li F, Huang Y, Han D, Yang C and Pan S (2021) Abnormal Topological Network in Parkinson's Disease With Impulse Control Disorders: A Resting-State Functional Magnetic Resonance Imaging Study. Front. Neurosci. 15:651710. doi: 10.3389/fnins.2021.651710

In recent years, neuroimaging evidence shows that the brains of Parkinson disease (PD) with impulse control disorders (ICDs) patients have functional disconnection changes. However, so far, it is still unclear whether the topological organization is damaged in PD patients with ICD. In this study, we aimed to explore the functional brain network in 18 patients with PD with ICDs (PD-ICD) and 18 patients with PD without ICDs (PD-nICD) by using functional magnetic resonance imaging and graph theory approach. We found that the PD-ICD patients had increased clustering coefficient and characteristic path length, while decreased small-world index compared with PD-nICD patients. Furthermore, we explored the hypothesis whether the abnormality of the small-world network parameters of PD-ICD patients is accompanied by the change of nodal centrality. As we hypothesized, the nodal centralities of the default mode network, control network, and dorsal attention network were found to be significantly damaged in the PD-ICD group compared with the PD-nICD group. Our study provides more evidence for PD-ICD patients' brain network abnormalities from the perspective of information exchange, which may be the underlying pathophysiological basis of brain abnormalities in PD-ICD patients.

Keywords: Parkinson's disease, impulse control disorders, fMRI, topological network, graph theory

INTRODUCTION

Parkinson disease (PD) is a common neurodegenerative disease in middle-aged and elderly people. Its main clinical manifestations are motor symptoms such as resting tremor, bradykinesia, muscle rigidity, and abnormal posture, as well as non-motor symptoms such as impulse control disorders (ICDs). ICD refers to a mental disorder in which patients are driven by a strong desire to adopt improper behaviors to obtain self-satisfaction. Fifteen percent of PD patients have one or more clinical symptoms of ICD (Vriend, 2018), which mainly include pathological gambling, compulsive eating, hypersexuality, compulsive shopping, and so on (Vargas and Cardoso, 2018). Once PD

patients suffer from ICD, clinical management and intervention will become more difficult. Therefore, in the early stage of PD with ICDs (PD-ICD), it is very important to understand the corresponding specific changes of PD-ICD.

Many previous neuroimaging studies, involving brain metabolism by using single-photon emission tomography (SPECT) (Cilia et al., 2011) and positron emission tomography (Thiel et al., 2003) and morphometric and functional imaging by using magnetic resonance imaging (MRI) (Frosini et al., 2010; Carriere et al., 2015; Tessitore et al., 2016), have made a lot of contributions in exploring the abnormal changes related to PD-ICD. They have consistently demonstrated dysfunction in both cortical and subcortical areas, which are important in the reward system, such as the striatum, anterior cingulate cortex (ACC), and insula. For example, in the SPECT study, PD patients with pathological gambling were found to be associated with ACC–striatal disconnection, which may indicate a specific abnormality of behavior control and explain why PD gamblers used to persist in gambling despite the self-destructive consequences (Cilia et al., 2011). A recent review of functional studies revealed decreased activity in ACC and increased activity in the ventral striatum and orbitofrontal cortex (Santangelo et al., 2019). Evidence from one of the resting-state functional MRI (rs-fMRI) studies showed that PD with ICD symptoms was associated with the functional disconnection between the left anterior putamen (an associative striatal area) and the left inferior temporal gyrus and the left ACC (limbic cortical regions) (Carriere et al., 2015). In addition, PD-ICD patients have been shown through several diffusion tensor imaging tractography to have widespread white matter tract damage (Yoo et al., 2015; Canu et al., 2017; Zadeh et al., 2018), which further confirm the impaired network connection in PD patients with ICD.

In recent years, as a new network analysis method, graph theory analysis has been widely used in the research of many neurological and psychiatric diseases including PD. This method models the brain regions and the connections between regions as nodes and edges, such that the brain is modeled as a topological network composed of many points and edges, which can be studied for network parameters and network efficiency. However, so far, it is still unclear whether the topographic organization is damaged in PD patients with ICD. Given the disconnected brain in PD with ICD, as well as the disruption of topological organization in PD, it is plausible that the whole-brain topological network of PD-MCI may also be damaged in a diseased state. Therefore, in the current study, we aimed to explore whether the presence of ICD in PD patients may determine abnormalities in the topological network by using rs-fMRI and graph theory methods.

MATERIALS AND METHODS

Study Population

All MRI and experimental data used in this study were obtained from the Parkinson's Progression Markers Initiative,[1] which is a large-scale, comprehensive observational, multicenter project of PD progression biomarkers (Marek et al., 2011). A total of 52 participants were analyzed, including 18 participants in the PD-ICD group, 18 in the PD without ICDs (PD-nICD) group, and 16 age- and sex-matched health control (HC) group (**Table 1**). All PD patients were diagnosed according to the criteria of the United Kingdom Brain Bank (Hughes et al., 1992). The study was approved by the Institutional Review Boards/Independent Ethics Committees. Written informed consent was obtained from all subjects. For more details on the study, see http://www.ppmi-info.org/wp-content/uploads/2013/02/PPMI-Protocol-AM5-Final-27Nov2012v6-2.pdf.

MRI Parameters

The imaging data were acquired on the Siemens 3-T MRI scanner. T1-weighted gradient-echo 3D MPRAGE sequence was used [repetition time (TR) = 2,300 ms, time to echo (TE) = 2.98 ms, fractional anisotropy (FA) = 9°, 1-mm^3 isotropic voxel] to obtain high-resolution structural images. rs-fMRI scan is obtained by echo plane sequence (TR = 2,400 ms, TE = 25 ms, FA = 80, voxel size = 3.3 mm^3, total 210 volumes, 40 axial slices). It is recommended that the subjects open their eyes and relax quietly to perform a functional scan of the resting state and try not to fall asleep.

Data Preprocessing and Statistical Analysis

Results included in this manuscript come from preprocessing performed using fMRIPrep 1.4.1 (Esteban et al., 2019), which is based on Nipype 1.2.0 (Gorgolewski et al., 2011). More method details are shown in the **Supplementary Material**.

RESULTS

The Small-World Topology in PD-ICD, PD-nICD, and HC Patients

The topological brain networks at all three groups had the characteristics of "small-world" networks. For example, over an entire range of density thresholds, the small-world indexes of these three groups were larger than one ($\sigma > 1$) (**Figure 1C**).

PD-ICD Group Versus PD-nICD Group

Compared to the PD-nICD group, the PD-ICD group showed significantly increased clustering coefficient Cp (density thresholds: 36–38, 40, 42–50%, $p < 0.05$, two-tailed) (**Figure 1A**), characteristic path length Lp (density thresholds: 25–39%, $p < 0.05$, two-tailed) (**Figure 1B**), and significantly decreased small-world index σ (density thresholds: 10, 23, 26–27%, $p < 0.05$, two-tailed) (**Figure 1C**). Furthermore, we explored the hypothesis whether the abnormality of the small-world network parameters of PD-ICD patients is accompanied by the change of nodal centrality. Compared with the PD-nICD group, the brain regions with significantly increased node centrality in PD-ICD patients are located in default mode network (DMN), control

[1] http://www.ppmi-info.org

TABLE 1 | Demographic and clinical features of HC, PD-nICD, and PD-ICD.

	HC (n = 16)	PD-nICD (n = 18)	PD-ICD (n = 18)	p-Value
Age (years)	64.75 ± 9.28	59.69 ± 11.64	62.13 ± 12.53	0.44
Gender (male:female)	13:3	12:6	12:6	0.56
Disease duration (years)	–	1.90 ± 0.81	2.62 ± 1.33	0.06
UPDRS-III	–	19.67 ± 8.22	22.39 ± 10.72	0.40
Hoehn and Yahr stage	–	1.78 ± 0.43	1.83 ± 0.51	0.73
Montreal cognitive assessment	27.75 ± 1.25	27.44 ± 2.25	25.67 ± 4.39	0.10
Education (years)	16.88 ± 2.66	15.56 ± 2.91	15.78 ± 2.96	0.37
Depression (Geriatric Depression Scale 15)	2.19 ± 2.95	2.06 ± 1.92	3.11 ± 2.61	0.40
ICD (Questionnaire for Impulsive–Compulsive Disorders in Parkinson Disease–Current Short)	0 ± 0	0 ± 0	1.22 ± 0.55	<0.00001

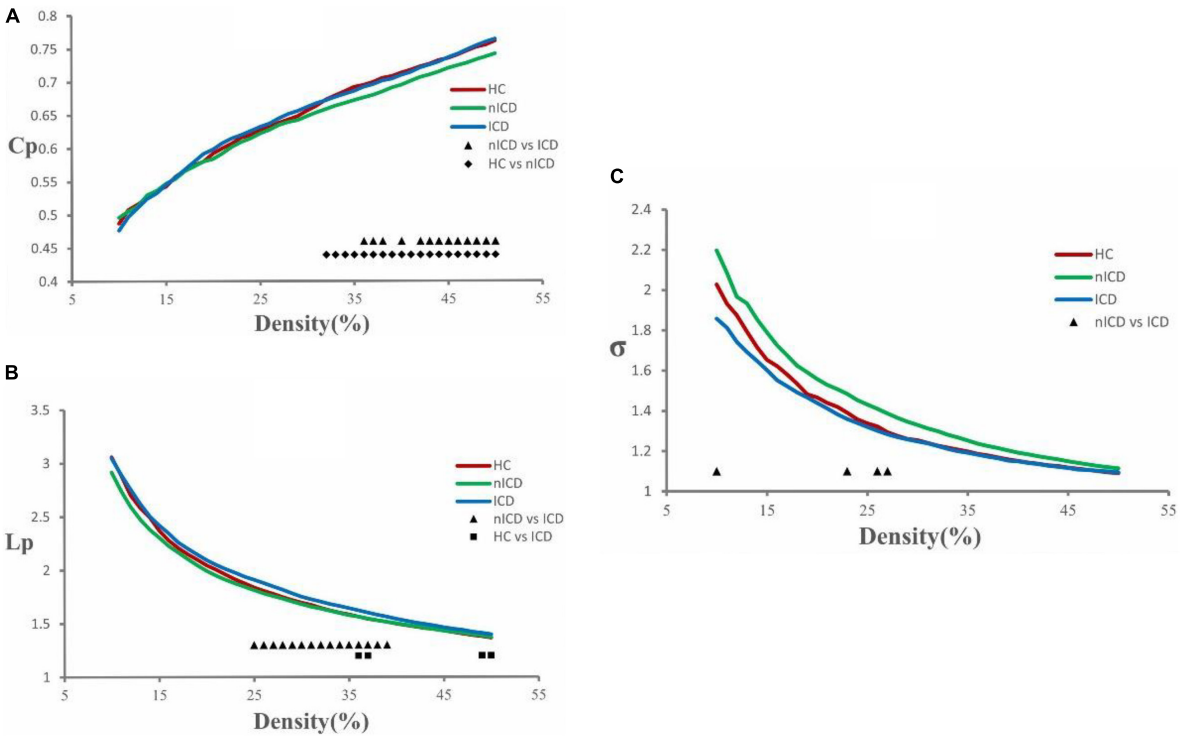

FIGURE 1 | Cluster coefficient (Cp), characteristic path length (Lp), and small-world index (σ) in PD-nICD, PD-ICD, and HC. **(A)** The Cp from three groups. Black triangle means significant differences between PD-nICD and PD-ICD (36–38, 40, 42–50%, $p < 0.05$). Black diamond means significant differences between HC and PD-nICD (density thresholds: 32–50%, $p < 0.05$). **(B)** The Lp from three groups. Black triangle means significant differences between PD-nICD and PD-ICD (density thresholds: 25–39%, $p < 0.05$). Black square means significant differences between HC and PD-ICD (density thresholds: 36–37, 49–50% $p < 0.05$). **(C)** The σ from three groups. Black triangle means significant differences between PD-nICD and PD-ICD (density thresholds: 10, 23, 26–27%, $p < 0.05$).

network (CN), and dorsal attention network (DAN), and the significantly reduced regions are located in DAN (**Table 2**).

PD-nICD Group Versus HC Group

Compared to the HC group, the PD-nICD group showed a significantly decreased clustering coefficient Cp (density thresholds: 32–50%, $p < 0.05$, two-tailed) (**Figure 1A**).

PD-ICD Group Versus HC Group

Compared to the HC group, the PD-ICD group showed significantly increased characteristic path length Lp (density thresholds: 36–37, 49–50% $p < 0.05$, two-tailed) (**Figure 1B**).

DISCUSSION

As far as we know, this is the first time to explore the changes of the brains from the perspective of topological networks in PD patients with ICD by using fMRI and graph theory analysis. We found that the PD-ICD patients had increased clustering coefficient and characteristic path length, while decreased small-world index compared with PD-nICD patients. Furthermore, we explored the hypothesis whether the abnormality of the small-world network parameters of PD-ICD patients is accompanied by the change of nodal centrality. As we hypothesized, the nodal centralities of DMN, CN, and DAN were found to be significantly

TABLE 2 | Nodal centrality differences between PD-ICD and PD-nICD.

	ROI label	ROI name	ROI network	*p*-Value
PD-ICD larger than PD-nICD	36	7Networks_LH_Cont_pCun_1	CN	0.001
	49	7Networks_LH_Default_pCunPCC_1	DMN	0.004
	67	7Networks_RH_DorsAttn_Post_1	DAN	0.037
PD-ICD smaller than PD-nICD	71	7Networks_RH_DorsAttn_Post_5	DAN	0.049

damaged in the PD-ICD group compared with the PD-nICD group. As the pathogenesis of PD-ICD is not yet fully understood, we will further discuss our findings from the perspective of the topological network and the underlying pathophysiological basis that may arise.

Our results showed that whether it is NC group's, PD-nICD group's, or PD-ICD group's brain functional network, they are all in line with the characteristics of small-world networks. This is similar to the studies of topological networks in other brain diseases, such as Alzheimer disease, schizophrenia, and so on (Liu et al., 2008; Zhao et al., 2012; Seo et al., 2013). Especially in the recent related research of topological networks in PD patients, the small-world network characteristics of the PD brain are also consistently presented (Luo et al., 2014; Berman et al., 2016; Chen et al., 2020). A small-world network is a relatively high-efficiency network model, with a high clustering coefficient and low characteristic shortest path length (Bullmore and Sporns, 2009). The brains of PD-ICD patients also have the characteristics of a small-world network, indicating that even in a disease state, the brain network is still a relatively efficient network model, which may be necessary for their daily activities, such as recalling, thinking, or decision making.

Although the brain network of PD-ICD patients presented a small-world characteristic, the network parameters were significantly different from those of the PD-nICD group. In our study, the clustering coefficient and characteristic shortest path length of the functional network in PD-ICD were significantly higher than in PD-nICD. In a topological network, the clustering coefficient reflects the efficiency of information transfer between local areas, and the higher the clustering coefficient, the more efficient the integration of information in the local area. The characteristic shortest path length reflects the overall information transmission, and the shorter the characteristic shortest path, the higher the efficiency of information transmission between long-distance areas (Bullmore and Sporns, 2009). Therefore, the increase in the clustering coefficient of the functional network of PD-ICD patients may indicate that the communication between the local brain regions related to impulsive behaviors is enhanced, leading to the occurrence of impulsive behaviors. The increase in the patient's characteristic path length may indicate that the information exchange in the remote brain regions that inhibit impulsive behavior has also become slower, making it more difficult for patients to control and stop these impulsive behaviors.

We also explored the hypothesis whether the abnormality of clustering coefficient and characteristic shortest path length in PD-ICD patients is accompanied by the change of nodal centrality. Our results show that, compared with PD-nICD, the brain regions with significantly increased node centrality in PD-ICD patients are located in DMN, CN, and DAN, and the significantly reduced regions are located in DAN.

Default mode network, CN, and DAN are three networks that play an important role in cognition, behavior, and attention, which are inseparable from the brain's information exchange and processing (Petrides, 2005; Fox et al., 2006; Koechlin and Summerfield, 2007; Buckner et al., 2008; Spreng et al., 2009). The DMN is considered to be related to ruminations, mind-wandering, and cognitive processing (Buckner et al., 2008; Spreng et al., 2009). The CEN is involved in the process of external stimuli, decision-making, and executive behaviors (Petrides, 2005; Koechlin and Summerfield, 2007). DAN is one of the sensory orientation systems in the human brain. It involves voluntary top-down orientation and indicates when, where, or in what direction the subject should perform behavioral activities (Fox et al., 2006). When it comes to PD with ICD symptoms, there are a few previous articles about these networks. As far as we know, there are currently only two related articles. One of them found that PD-ICD was related to increased connectivity within the salience network (SN) and DMN, as well as with a decreased connectivity within CN (Tessitore et al., 2017b). The other found decreased connectivity in DMN and CN, and increased connectivity in SN in PD-ICD when compared with PD-nICD patients (Tessitore et al., 2017a). Similar to previous studies, the current article also found that the DMN and CN network in the brain of PD-ICD patients are significantly abnormal compared with PD-nICD. The difference is that our research did not find significant changes in the SN network but found that the DAN network was damaged. This may be because our research method used a large-scale topological network, the information flow related to the centrality of the node needs to calculate the flow of information in the whole brain, rather than the functional connection between several brain regions. However, it is worth noting that our research also found DMN and CN in the brains of PD-ICD patients from the perspective of the topological network. This may indicate that DMN and CN network abnormalities are related to the pathogenesis and development of ICD symptoms in PD, and whether there are related abnormalities in DAN network still needs more research to confirm.

This study still has some limitations. The most important aspect is that the sample size is relatively small. Although our research found significant topological network differences between PD-ICD and PD-nICD, the small sample size prevented us from obtaining multiple comparisons corrected results. Second, we control the influence of confusion factors

(such as age, gender, and so on) between groups on the topological network, but we cannot control the influence of these factors within the group. Third, the neural network mechanisms of different subtypes of ICD may be different. This study also did not distinguish the impact of ICD subtypes on topological networks. We hope that sufficient samples can be obtained in future studies for further research.

CONCLUSION

In summary, by using the topological network analysis method, we found that the clustering coefficient and characteristic path length of the brain function network of PD-ICD patients increased, accompanied by damage to the DMN, CN, and DAN network nodes. This may be the underlying pathophysiological basis of brain abnormalities in PD-ICD patients. At the same time, the current study also provides more evidence for PD-ICD patients' brain network abnormalities from the perspective of information exchange.

DATA AVAILABILITY STATEMENT

The original contributions presented in the study are included in the article/**Supplementary Material**, further inquiries can be directed to the corresponding author/s.

ETHICS STATEMENT

The studies involving human participants were reviewed and approved by the Zhuzhou Central Hospital. The patients/participants provided their written informed consent to participate in this study.

AUTHOR CONTRIBUTIONS

CY and SP proposed this study idea concept, designed the experiments, and modified the manuscript. XZ and LL were responsible for performing the experiments and writing the original manuscript. YX, FL, YH, and DH were responsible for finding relevant literature and materials. All authors contributed to the article and approved the submitted version.

ACKNOWLEDGMENTS

Data used in the preparation of this article were obtained from the Parkinson's Progression Markers Initiative database (www.ppmi-info.org/data). For up-to-date information on the study, visit www.ppmi-info.org. Parkinson's Progression Markers Initiative – a public–private partnership – is sponsored by the Michael J. Fox Foundation for Parkinson's Research (MJFF) and is co-funded by MJFF, AbbVie, Avid Radiopharmaceuticals, Biogen Idec, Bristol Myers Squibb, Covance, Eli Lilly & Co., F. Hoffmann-La Roche, Ltd., GE Healthcare, Genentech, GlaxoSmithKline, Lundbeck, Merck, MesoScale, Piramal, Pfizer, and UCB.

SUPPLEMENTARY MATERIAL

The Supplementary Material for this article can be found online at: https://www.frontiersin.org/articles/10.3389/fnins.2021.651710/full#supplementary-material

REFERENCES

Berman, B. D., Smucny, J., Wylie, K. P., Shelton, E., Kronberg, E., Leehey, M., et al. (2016). Levodopa modulates small-world architecture of functional brain networks in Parkinson's disease. *Mov. Disord.* 31, 1676–1684. doi: 10.1002/mds.26713

Buckner, R. L., Andrews-Hanna, J. R., and Schacter, D. L. (2008). The brain's default network: anatomy, function, and relevance to disease. *Ann. N. Y. Acad. Sci.* 1124, 1–38. doi: 10.1196/annals.1440.011

Bullmore, E., and Sporns, O. (2009). Complex brain networks: graph theoretical analysis of structural and functional systems. *Nat. Rev. Neurosci.* 10, 186–198. doi: 10.1038/nrn2575

Canu, E., Agosta, F., Markovic, V., Petrovic, I., Stankovic, I., Imperiale, F., et al. (2017). White matter tract alterations in Parkinson's disease patients with punding. *Park Relat. Disord.* 43, 85–91. doi: 10.1016/j.parkreldis.2017.07.025

Carriere, N., Lopes, R., Defebvre, L., Delmaire, C., and Dujardin, K. (2015). Impaired corticostriatal connectivity in impulse control disorders in Parkinson disease. *Neurology* 84, 2116–2112. doi: 10.1212/wnl.0000000000001619

Chen, X., Liu, M., Wu, Z., and Cheng, H. (2020). Topological abnormalities of functional brain network in early-stage Parkinson's disease patients with mild cognitive impairment. *Front. Neurosci.* 14:616872.

Cilia, R., Cho, S. S., van Eimeren, T., Marotta, G., Siri, C., Ko, J. H., et al. (2011). Pathological gambling in patients with Parkinson's disease is associated with fronto-striatal disconnection: a path modeling analysis. *Mov. Disord.* 26, 225–233. doi: 10.1002/mds.23480

Esteban, O., Markiewicz, C. J., Blair, R. W., Moodie, C. A., Isik, A. I., Erramuzpe, A., et al. (2019). fMRIPrep: a robust preprocessing pipeline for functional MRI. *Nat. Methods.* 16, 111–116. doi: 10.1038/s41592-018-0235-4

Fox, M. D., Corbetta, M., Snyder, A. Z., Vincent, J. L., and Raichle, M. E. (2006). Spontaneous neuronal activity distinguishes human dorsal and ventral attention systems. *Proc. Natl. Acad. Sci. U.S.A.* 103, 10046–10051. doi: 10.1073/pnas.0604187103

Frosini, D., Pesaresi, I., Cosottini, M., Belmonte, G., Rossi, C., Dell'Osso, L., et al. (2010). Parkinson's disease and pathological gambling: results from a functional MRI study. *Mov. Disord.* 25, 2449–2453. doi: 10.1002/mds.23369

Gorgolewski, K., Burns, C. D., Madison, C., Clark, D., Halchenko, Y. O., Waskom, M. L., et al. (2011). Nipype: a flexible, lightweight and extensible neuroimaging data processing framework in Python. *Front Neuroinform.* 5:13. doi: 10.3389/fninf.2011.00013

Hughes, A. J., Daniel, S. E., Kilford, L., and Lees, A. J. (1992). Accuracy of clinical diagnosis of idiopathic Parkinson's disease: a clinico-pathological study of 100 cases. *J. Neurol. Neurosurg. Psychiatry.* 55, 181–184. doi: 10.1136/jnnp.55.3.181

Koechlin, E., and Summerfield, C. (2007). An information theoretical approach to prefrontal executive function. *Trends Cogn. Sci.* 11, 229–235. doi: 10.1016/j.tics.2007.04.005

Liu, Y., Liang, M., Zhou, Y., He, Y., Hao, Y., Song, M., et al. (2008). Disrupted small-world networks in schizophrenia. *Brain* 131(Pt 4), 945–961. doi: 10.1093/brain/awn018

Luo, C. Y., Chen, Q., Song, W., Chen, K., Guo, X. Y., Yang, J., et al. (2014). Resting-state fMRI study on drug-naive patients with Parkinson's disease and with depression. *J. Neurol. Neurosurg. Psychiatry* 85, 675–683. doi: 10.1136/jnnp-2013-306237

Marek, K., Jennings, D., Lasch, S., Siderowf, A., Tanner, C., Simuni, T., et al. (2011). The Parkinson progression marker initiative (PPMI). *Prog Neurobiol.* 95, 629–635.

Petrides, M. (2005). Lateral prefrontal cortex: architectonic and functional organization. *Philos. Trans. R Soc. B Biol. Sci.* 360, 781–795. doi: 10.1098/rstb.2005.1631

Santangelo, G., Raimo, S., Cropano, M., Vitale, C., Barone, P., and Trojano, L. (2019). Neural bases of impulse control disorders in Parkinson's disease: a systematic review and an ALE meta-analysis. *Neurosci. Biobehav. Rev.* 107, 672–685. doi: 10.1016/j.neubiorev.2019.09.041

Seo, E. H., Lee, D. Y., Lee, J. M., Park, J. S., Sohn, B. K., Lee, D. S., et al. (2013). Whole-brain functional networks in cognitively normal, mild cognitive impairment, and Alzheimer's disease. *PLoS One* 8:e53922. doi: 10.1371/journal.pone.0053922

Spreng, R. N., Mar, R. A., and Kim, A. S. N. (2009). The common neural basis of autobiographical memory, prospection, navigation, theory of mind, and the default mode: a quantitative meta-analysis. *J. Cogn. Neurosci.* 21, 489–510. doi: 10.1162/jocn.2008.21029

Tessitore, A., De Micco, R., Giordano, A., di Nardo, F., Caiazzo, G., Siciliano, M., et al. (2017a). Intrinsic brain connectivity predicts impulse control disorders in patients with Parkinson's disease. *Mov. Disord.* 32, 1710–1719. doi: 10.1002/mds.27139

Tessitore, A., Santangelo, G., De Micco, R., Giordano, A., Raimo, S., Amboni, M., et al. (2017b). Resting-state brain networks in patients with Parkinson's disease and impulse control disorders. *Cortex* 94, 63–72. doi: 10.1016/j.cortex.2017.06.008

Tessitore, A., Santangelo, G., De Micco, R., Vitale, C., Giordano, A., Raimo, S., et al. (2016). Cortical thickness changes in patients with Parkinson's disease and impulse control disorders. *Park Relat. Disord.* 24, 119–125. doi: 10.1016/j.parkreldis.2015.10.013

Thiel, A., Hilker, R., Kessler, J., Habedank, B., Herholz, K., and Heiss, W. D. (2003). Activation of basal ganglia loops in idiopathic Parkinson's disease: A PET study. *J. Neural Transm.* 110, 1289–1301. doi: 10.1007/s00702-003-0041-7

Vargas, A. P., and Cardoso, F. E. C. (2018). Impulse control and related disorders in Parkinson's disease. *Arq. Neuropsiquiatr.* 76, 399–410.

Vriend, C. (2018). The neurobiology of impulse control disorders in Parkinson's disease: from neurotransmitters to neural networks. *Cell Tissue Res.* 373, 327–336. doi: 10.1007/s00441-017-2771-0

Yoo, H. B., Lee, J. Y., Lee, J. S., Kang, H., Kim, Y. K., et al. (2015). Whole-brain diffusion-tensor changes in parkinsonian patients with impulse control disorders. *J. Clin. Neurol.* 11, 42–47. doi: 10.3988/jcn.2015.11.1.42

Zadeh, M. M., Ashraf-Ganjouei, A., Sherbaf, F. G., Haghshomar, M., and Aarabi, M. H. (2018). White matter tract alterations in drug-Naïve Parkinson's disease patients with impulse control disorders. *Front Neurol.* 9:163. doi: 10.3389/fneur.2018.00163

Zhao, X., Liu, Y., Wang, X., Liu, B., Xi, Q., Guo, Q., et al. (2012). Disrupted small-world brain networks in moderate Alzheimer's disease: a resting-state fMRI study. *PLoS One* 7:e33540. doi: 10.1371/journal.pone.0033540

Conflict of Interest: The authors declare that the research was conducted in the absence of any commercial or financial relationships that could be construed as a potential conflict of interest.

Publisher's Note: All claims expressed in this article are solely those of the authors and do not necessarily represent those of their affiliated organizations, or those of the publisher, the editors and the reviewers. Any product that may be evaluated in this article, or claim that may be made by its manufacturer, is not guaranteed or endorsed by the publisher.

frontiers in Neuroscience

ORIGINAL RESEARCH
published: 16 September 2021
doi: 10.3389/fnins.2021.730879

FLAIR and ADC Image-Based Radiomics Features as Predictive Biomarkers of Unfavorable Outcome in Patients With Acute Ischemic Stroke

Guanmin Quan[1†], Ranran Ban[1†], Jia-Liang Ren[2], Yawu Liu[3], Weiwei Wang[4], Shipeng Dai[5] and Tao Yuan[1]*

[1] Department of Medical Imaging, The Second Hospital of Hebei Medical University, Shijiazhuang, China, [2] GE Healthcare China, Beijing, China, [3] Department of Clinical Radiology, Kuopio University Hospital, Kuopio, Finland, [4] Department of Radiology, Handan Central Hospital, Handan, China, [5] Department of Radiology, Cangzhou City Hospital, Cangzhou, China

OPEN ACCESS

Edited by:
Maryam Ardalan, University of Gothenburg, Sweden

Reviewed by:
Alexandre Rosa Franco, Nathan Kline Institute for Psychiatric Research, United States
Tobias Greve, Ludwig Maximilian University of Munich, Germany

***Correspondence:**
Tao Yuan
420490790@qq.com

[†]These authors have contributed equally to this work and share first authorship

Specialty section:
This article was submitted to Brain Imaging Methods, a section of the journal Frontiers in Neuroscience

Received: *25 June 2021*
Accepted: *13 August 2021*
Published: *16 September 2021*

Citation:
Quan G, Ban R, Ren J-L, Liu Y, Wang W, Dai S and Yuan T (2021) FLAIR and ADC Image-Based Radiomics Features as Predictive Biomarkers of Unfavorable Outcome in Patients With Acute Ischemic Stroke. Front. Neurosci. 15:730879. doi: 10.3389/fnins.2021.730879

At present, it is still challenging to predict the clinical outcome of acute ischemic stroke (AIS). In this retrospective study, we explored whether radiomics features extracted from fluid-attenuated inversion recovery (FLAIR) and apparent diffusion coefficient (ADC) images can predict clinical outcome of patients with AIS. Patients with AIS were divided into a training (n = 110) and an external validation (n = 80) sets. A total of 753 radiomics features were extracted from each FLAIR and ADC image of the 190 patients. Interquartile range (IQR), Wilcoxon rank sum test, and least absolute shrinkage and selection operator (LASSO) were used to reduce the feature dimension. The six strongest radiomics features were related to an unfavorable outcome of AIS. A logistic regression analysis was employed for selection of potential predominating clinical and conventional magnetic resonance imaging (MRI) factors. Subsequently, we developed several models based on clinical and conventional MRI factors and radiomics features to predict the outcome of AIS patients. For predicting unfavorable outcome [modified Rankin scale (mRS) > 2] in the training set, the area under the receiver operating characteristic curve (AUC) of ADC radiomics model was 0.772, FLAIR radiomics model 0.731, ADC and FLAIR radiomics model 0.815, clinical model 0.791, and clinical and conventional MRI model 0.782. In the external validation set, the AUCs for the prediction with ADC radiomics model was 0.792, FLAIR radiomics model 0.707, ADC and FLAIR radiomics model 0.825, clinical model 0.763, and clinical and conventional MRI model 0.751. When adding radiomics features to the combined model, the AUCs for predicting unfavorable outcome in the training and external validation sets were 0.926 and 0.864, respectively. Our results indicate that the radiomics features extracted from FLAIR and ADC can be instrumental biomarkers to predict unfavorable clinical outcome of AIS and would additionally improve predictive performance when adding to combined model.

Keywords: acute ischemic stroke, outcome, magnetic resonance imaging, apparent diffusion coefficient, radiomics

INTRODUCTION

Acute ischemic stroke (AIS) is a critical cerebrovascular disorder worldwide with high morbidity and disability and accounts for 60–80% of all strokes (Darwish et al., 2020). The cerebral infarct in the middle cerebral artery (MCA) territory represents the most frequent AIS (Sommer et al., 2018). Early diagnosis and prognosis assessment are crucial in the management of AIS. At present, the National Institute of Health Stroke Scale (NIHSS) is the most commonly used clinical score for the evaluation of functional impairment (Choi et al., 2015). Most of the clinical trials on AIS are based on computed tomography (CT), CT angiography (CTA), and CT perfusion (CTP), which provide several and fast information about cerebral ischemic tissue. However, contrast-enhanced CT techniques are not universally accepted methods in the routine workup in AIS patients in some institutions due to the possible risk of intravenous injection of iodinated contrast agent and technical complex. Instead, non-contrast CT and multimodality magnetic resonance imaging (MRI) are used as substitute imaging modalities for clinical evaluation in AIS patients. Conventional MR stroke protocol, even without contrast injection, could be an alternative tool for providing both anatomic and functional information, including the lesion location and size, occluded vessels, diffusion characteristics, and cerebral blood perfusion obtained by arterial spin label (ASL) technique. Thus, the objective MRI markers would be useful to assist in predicting prognosis for an individual AIS patient.

By intravenous injection of contrast agent, enhanced MRI can provide further information, and the lesion mismatch on perfusion-weighted imaging (PWI) and diffusion-weighted imaging (DWI) has been employed to estimate the ischemic penumbra (Darwish et al., 2020). Whereas, enhanced MRI is not a universally accepted method in the routine workup in AIS patients due to an intravenous injection of gadolinium agent, it is time consuming, and the patient's cooperation. Evidences have also shown its possibility to improve prognostic estimation with other non-enhanced MRI features, including fluid-attenuated inversion recovery (FLAIR) vascular hyperintensity (FVH) (Jiang et al., 2019), susceptibility vessel sign (SVS) (Rudilosso et al., 2021), cerebral artery laterality (Ichijo et al., 2013), and lesion volume (Bucker et al., 2017). Nevertheless, most of these studies are based only on morphologic information. Therefore, we will focus on FLAIR and apparent diffusion coefficient (ADC) as our research sequences in the setup of prognosis prediction models in this study.

As a novel developed data analysis technique, radiomics can extract great many quantitative features from medical images. Radiomics features would reflect subtle pathophysiologic features and heterogeneity of lesions. Radiomics has been employed in the diagnosis, prognostic estimation, and treatment evaluation of varied diseases. A recent study presented a promising result by using texture analysis with FLAIR and DWI images in AIS patients (Wang et al., 2020). They found that the texture features could be used as biomarkers to assess stroke severity. In other studies, radiomics features were extracted from CT angiography, enhanced T1WI, and ADC map. It has been proven that radiomics is an effective image analysis tool in the depiction of ischemic penumbra (Tang et al., 2020), evaluation of collateral circulation (Dolotova et al., 2020), prediction of hemorrhagic transformation (Kassner et al., 2009), prediction of malignant infarct (Wen et al., 2020), and forecasting clinical outcome in AIS patients. However, prognosis estimation was often made only based on radiomics features without clinical factors. So far, few studies have been performed to setup a prognostic model based on radiomics to predict clinical outcome individually. We hypothesized that the radiomics features extracted from FLAIR and ADC could be a prognostic biomarker for predicting clinical outcome in AIS patients.

Thus, the aim of this study was to explore radiomics based on FLAIR and ADC to predict the clinical outcome after 90 days of AIS onset. In addition, we tested the diagnostic performance of this model in an external validation set.

MATERIALS AND METHODS

Patients

This study was approved by the ethics committee of The Second Hospital of Hebei Medical University. Due to its retrospective nature, informed consent from patients was waived. AIS patients were retrospectively collected from three hospitals during January 2018 to June 2020. AIS was defined as the presence of acute clinical vascular syndromes and infarction DWI in MCA territory. Inclusion criteria included the following: (1) a first-ever AIS in unilateral MCA territory; (2) acute ictus of stroke $\leq$ 72 h before MR examination; (3) the maximum diameter of AIS lesions $\geq$ 1 cm; and (4) modified Rankin scale (mRS) at 90 days after ictus was available. Exclusion criteria included the following: (1) lacunar cerebral infarct; (2) secondary hemorrhagic transformation of AIS lesions; (3) coexisting other diseases that affect neurologic function, such as brain tumor, cerebral hemorrhage, trauma, and demyelinating disease; (4) age less than 18 years old; and (5) severe artifact on FLAIR or ADC images.

During the study period, 344 AIS patients were collected. There were 154 patients excluded due to bilateral cerebral infarction of anterior circulation or combined with posterior circulation cerebral infarction (n = 77); neurological dysfunction left by previous history of AIS (n = 21); complicated with other diseases causing neurological dysfunction, including brain tumor, hemorrhagic stroke, demyelinating disease, and brain trauma (n = 15); incomplete imaging and clinical data or poor image quality (n = 13); and the maximum diameter of DWI high signal < 1 cm (n = 28). Finally, 190 patients were enrolled into the present study (**Figure 1**). According to the Transparent Reporting of a multivariable prediction model for Individual Prognosis or Diagnosis (TRIPOD) (Collins et al., 2015), 110 patients who came from one hospital were assigned as training set. Eighty patients who came from the other two hospitals were assigned as external validation set. There was no significant difference in the baseline clinical and MRI variables between two sets (**Table 1**). A comparison of population characteristics of anterior circulation AIS patients with different outcomes is shown in **Table 2**.

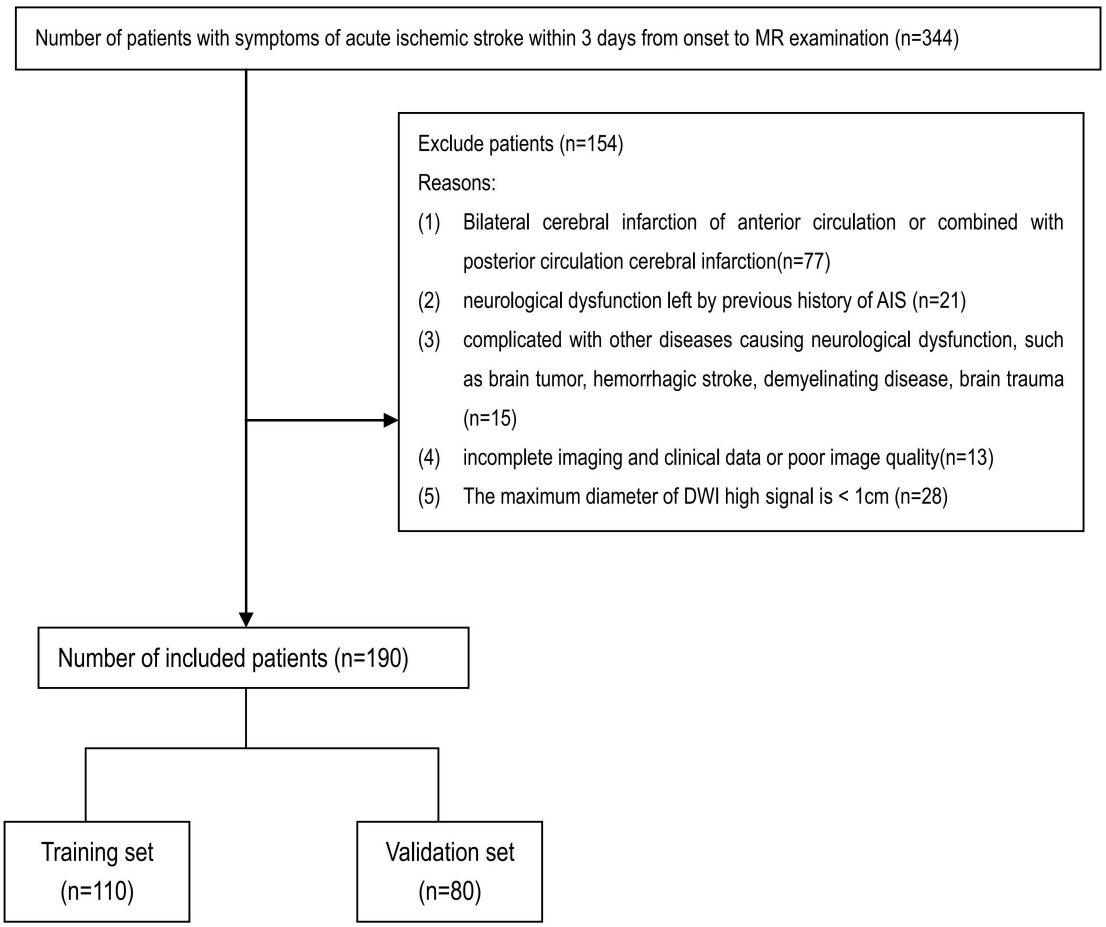

FIGURE 1 | Flowchart of the collection of patients.

The demographic and clinical data (Liu et al., 2018) included gender, age, history of hypertension, diabetes mellitus, hyperlipidemia, coronary heart disease, smoking, alcohol consumption, previous cerebral infarct attack, time from ictus to MR examination (in hours), baseline NIHSS score on admission, and mRS score at 90 days. The orthogonal diameters (ODs) of infarct lesion (Yuan et al., 2019), admission addressStreetDiffusion-Weighted Imaging-Alberta Stroke Program Early CT (DWI-ASPECT) score, and Fazekas score (Fazekas et al., 2002) were measured for each patient. Unfavorable clinical outcome was defined as mRS > 2 at 90 days (Jiang et al., 2019). The treatment strategy included intravenous thrombolytic therapy, anti-thrombotic therapy, anticoagulant, oral statins, and antiplatelet. Arterial thrombectomy was performed in 12 patients in this cohort.

Image Analysis

Acute ischemic stroke patients underwent MR examination with a 3T Philips MR scanner (Achieva, Netherlands; in The Second Hospital of Hebei Medical University) or a GE MR System (Signa, United States; in Handan Central Hospital and Cangzhou City Hospital). The MRI protocol included FLAIR, DWI, and magnetic resonance angiography (MRA). The imaging protocol parameters at the Philips MR system were as follows: (1) FLAIR: repetition time (TR)/echo time (TE) = 9,000 ms/140 ms, inversion time (TI) = 2,600 ms; (2) DWI: single-shot echo planar imaging, b = 1,000 s/mm^2, TR/TE = 2,208 ms/96 ms; and (3) MRA: time of flight sequence, 3D acquisition, TR/TE = 20 ms/3.5 ms. Imaging parameters at the GE MR system were as follows: (1) FLAIR: TR/TE = 8,000 ms/126 ms, TI = 2,400 ms; (2) DWI: single-shot echo planar imaging, b = 1,000 s/mm^2, TR/TE = 4,500 ms/72.5 ms; and (3) MRA: time of flight sequence, 3D acquisition, TR/TE = 20 ms/3.2 ms.

The conventional MRI factors, including ODs of the lesion, Fazekas scores, and admission DWI-ASPECTS, were analyzed by two neuroradiologists (with 10 and 21 years of experience separately) independently. When a disagreement existed, consensus was reached after consulting another radiologist with a 26-year experience in neuroradiology. The ODs were measured on the DWI slice with the largest lesion diameter (Yuan et al., 2019). If there were multiple infarct lesions, the ODs of the first three largest lesions were summed up. We recorded the DWI-ASPECTS, in which a score of 0 indicates diffuse infarct throughout the MCA territory and a score of 10 represents no

lesion (Tei et al., 2011). The white matter lesions were evaluated with Fazekas score (Fazekas et al., 2002), in which a score of 3 indicates confluent lesions and a score of 0 represents no lesions.

Feature Extraction

The FLAIR and ADC images of all eligible AIS patients were imported into the software Insight Segmentation and Registration Toolkit-ANAP (ITK-SNAP, version 3.8.0[1]). Two neuroradiologists manually delineated the lesions on the ADC, then the region of interest (ROI) on ADC was copied to the corresponding FLAIR slice by using a free available software[2] (**Figure 2**). In the areas of infarction, the FLAIR and ADC images were consequently segmented and were loaded into the open-source platform, PyRadiomics[3], to extract radiomics features (van Griethuysen et al., 2017). Logistic regression analysis was employed for further selection of significant

[1]http://www.itk-snap.org

[2]http://download.slicer.org

[3]http://www.radiomicss.io

TABLE 1 | Population characteristics of patients with AIS in the training and validation sets.

Characteristics	Training (*n* = 110)	Validation (*n* = 80)	*p*-value
Age (years), median (IQR)	62 (50.75, 70.25)	58 (50, 68)	0.586
Male sex, *n* (%)	78 (70.9%)	61 (76.3%)	0.412
Risk factors, *n* (%)			
Hypertension	69 (62.7%)	52 (65.0%)	0.748
Diabetes mellitus	28 (25.5%)	15 (18.8%)	0.276
Hyperlipidemia	6 (5.5%)	6 (7.5%)	0.567
Coronary heart disease	9 (8.2%)	7 (8.8%)	0.889
Smoking	35 (31.8%)	28 (35.0%)	0.646
Alcohol consumption	29 (26.4%)	14 (17.5%)	0.149
Previous stroke attack, *n* (%)	16 (14.5%)	11 (13.8%)	0.877
Interval from ictus to MR (hours)	26.50 ± 15.77	28.69 ± 14.36	0.627
Orthogonal diameter of the lesion, median (IQR)	2.47 (1.14, 6.66)	3.82 (1.51, 8.73)	0.107
Admission NIHSS, median (IQR)	3 (2, 6.25)	4 (2, 8)	0.077
Fazekas scores, median (IQR)	2.5 (1, 4)	2 (1, 3)	0.305
Admission DWI-ASPECTS, median (IQR)	9 (8, 9)	8 (7, 9)	0.105
mRS at 90 days, median (IQR)	2 (1,3)	1 (1,3)	0.200
mRS > 2, *n* (%)	30 (27.27%)	21 (26.25%)	0.875

DWI-ASPECTS, diffusion-weighted imaging-Alberta Stroke Program Early CT Score; mRS, modified Rankin score; n, number; NIHSS, National Institute of Health Stroke Scale.

TABLE 2 | Population characteristics of AIS patients with favorable and unfavorable outcome.

Characteristics	Favorable (*n* = 139)	Unfavorable (*n* = 51)	*p*-value
Age (years), median (IQR)	56 (48, 65.5)	69(59, 75)	<0.001*
Male sex, *n* (%)	110 (79.1%)	29 (56.9%)	0.002*
Risk factors, *n* (%)			
Hypertension	91 (65.5%)	30 (58.8%)	0.399
Diabetes mellitus	31 (22.3%)	12 (23.5%)	0.858
Hyperlipidemia	11 (7.9%)	1 (2%)	0.153
Coronary heart disease	9 (6.5%)	7 (13.7%)	0.111
Smoking	45 (32.4%)	18 (35.3%)	0.705
Alcohol consumption	33 (23.7%)	10 (19.6%)	0.546
Previous stroke ictus, *n* (%)	17 (12.2%)	10 (19.6%)	0.197
Interval from ictus to MR (hours)	26.85 ± 13.65	29.26 ± 15.75	0.268
Orthogonal diameter of the lesion, median (IQR)	2.32 (1.12, 5.28)	7.99 (15.05, 2.67)	<0.001*
Admission NIHSS, median (IQR)	3 (2, 5)	7 (5, 10.5)	<0.001*
Fazekas scores, median (IQR)	2 (1, 3)	2 (1, 4)	0.369
Admission DWI-ASPECTS, median (IQR)	9 (8, 9)	8 (6, 9)	<0.001*
mRS at 90 days, median (IQR)	1 (0, 2)	3 (3, 4)	<0.001*

*DWI-ASPECTS, diffusion-weighted imaging-Alberta Stroke Program Early CT Score; mRS, modified Rankin score; n, number; NIHSS, National Institute of Health Stroke Scale. *, with signifcant difference.*

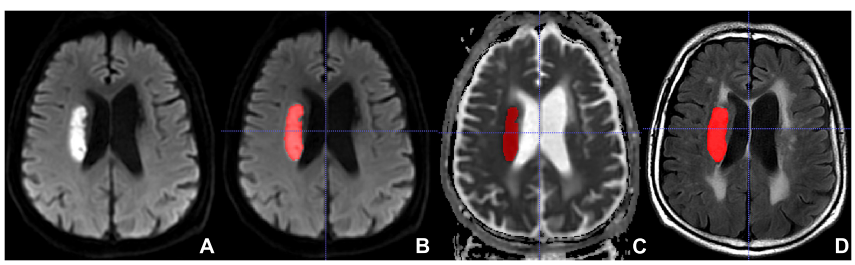

FIGURE 2 | Lesion segmentation with the Insight Segmentation and Registration Toolkit-ANAP (ITK-SNAP). **(A)** Non-segmented diffusion-weighted imaging (DWI). **(B)** Segmented DWI. **(C)** Segmented apparent diffusion coefficient (ADC). **(D)** Segmented fluid-attenuated inversion recovery (FLAIR).

features. These selected significant features were used to calculate radscore.

Development and Validation of Prediction Models

To develop prediction models, we performed a univariate logistic regression analysis for each potential factor (age, gender, various risk factors of cerebral vascular disease, interval from ictus to MR, ODs of infarct, admission NIHSS, Fazekas score, and admission DWI-ASPECTS) in the training set to select demographic, clinical, and conventional MRI predictors associated with unfavorable outcome. Then, the factors showing significant in the univariate logistic regression analysis and the radiomics features were used to develop six prognosis prediction models by using multivariable logistic regression analysis: ADC radiomics model, FLAIR radiomics model, ADC + FLAIR radiomics model, clinical model, clinical + conventional MRI factors model, and a combination model (all radiomics features and clinical and conventional MRI factors). The fitting formulas that were constructed with the training set were applied to the patients in the validation set.

Statistical Analysis

Statistical analyses were performed with IBM SPSS Statistics (version 21.0). The consistency between observers for estimating ODs of infarct lesions, the DWI-ASPECTS score, Fazekas score, admission NIHSS, and the reliability of extracted radiomics features were evaluated by the inter-class correlation coefficient. An ICC value more than 0.75 was considered as good consistency.

A logistic regression was used (1) to compare the difference in each potential variable between the training and validation sets and (2) to select the significant demographic, clinical, and conventional MRI variables that associated with unfavorable outcome. A *P*-value less than 0.05 was considered statistically significant.

A receiver operating characteristic (ROC) curve was employed to assess the performance of the six prediction models for discriminating unfavorable outcome from favorable outcome both in the training and validation sets. The performance of a model was considered good when the value of area under the ROC curve (AUC) was larger than 0.75.

TABLE 3 | Logistic analyses for the predictors of unfavorable outcome of AIS patients.

Characteristics	Univariate analysis		Multivariate analysis	
	OR (95% CI)	*p*-value	OR (95% CI)	*p*-value
Age (>60.5 years)	1.067 (1.035, 1.099)	<0.001	1.070 (1.034, 1.107)	<0.001
Sex (male)	0.348 (0.175, 0.692)	0.003	0.336 (0.147, 0.770)	0.010
Admission NIHSS	1.244 (1.142, 1.356)	<0.001	1.270 (1.156, 1.394)	<0.001
Admission DWI-ASPECTS	0.627 (0.493, 0.789)	<0.001		
OD values of the lesion	1.037 (1.011, 1.065)	0.006		

CI, confidence interval; DWI-ASPECTS, diffusion-weighted imaging-Alberta Stroke Program Early CT Score; NIHSS, National Institute of Health Stroke Scale; OD, orthogonal diameter; OR, odds ratio.

RESULTS

Patients' Characteristics

Due to imbalance of the data, we balanced them in both training and validation sets with Synthetic Minority Oversampling Technique (SMOTE) at first.

The basic characteristics of training and validation AIS patients are shown and compared in **Table 1**. There was no significant difference of outcome distribution between the two sets. The incidences of unfavorable outcome (mRS > 2 at 90 days) in the training and validation sets were 27.7% and 26.25% separately ($P = 0.875$). A univariate analysis showed that the following variables were significantly associated with the unfavorable outcome: age ($P < 0.001$), gender ($P = 0.003$), ODs ($P = 0.006$), admission NIHSS ($P < 0.001$), and DWI-ASPECTS ($P < 0.001$). Whereas, the time interval from stroke attack to MR examination ($P = 0.119$), hypertension ($P = 0.748$), diabetes mellitus ($P = 0.276$), hyperlipidemia ($P = 0.567$), coronary heart disease ($P = 0.889$), smoking ($P = 0.646$), alcohol consumption ($P = 0.149$), previous ictus ($P = 0.877$), and admission Fazekas score ($P = 0.305$) were not related to unfavorable outcome (**Table 2**). The average Fazekas score of the patients in the present study was 2.32. A multivariate analysis showed that the following variables were significantly associated with the unfavorable outcome: age ($P < 0.001$), gender ($P = 0.010$), admission NIHSS ($P < 0.001$) (**Table 3**).

Assessment of Radiomics Features

The extracted features included three categories: shape features; first-order statistic features (histogram); and second-order statistic features, including gray level co-occurrence matrix (GLCM), gray level run-length matrix (GLRLM), gray level size zone matrix (GLSZM), gray level-dependent matrix (GLDM), and neighborhood gray-tone difference matrix (NGTDM). A total of 753 radiomics features were extracted from FLAIR and ADC images. Dimension reduction of data redundancy was performed with the Wilcoxon rank sum test, Spearman correlation analysis, and least absolute shrinkage and selection operator (LASSO). In brief, we employed cross-validation to determine an optimized tuning parameter λ when coefficients of indistinctive covariates were non-zero results. Then, this optimized λ was used for feature selection in the LASSO method (Li et al., 2018). At last, we used the selected features to setup a LASSO Cox regression model. After cutting off irrelevant and redundant features, the final six features were used as ultimate radiomics signatures: (1) DWI_wavelet. LH_first order_Interquartile Range; (2) DWI_wavelet. HL_GLCM_Idmn; (3) DWI_wavelet. HL_GLRLM_LongRun Emphasis; (4) FLAIR_original_GLSZM_ SmallArea Low GrayLevel Emphasis; (5) FLAIR_log. sigma. 5.0.mm. 3D_GLRLM_RunLength NonUniformity; and (6) FLAIR_wavelet. LL_GLDM_Low

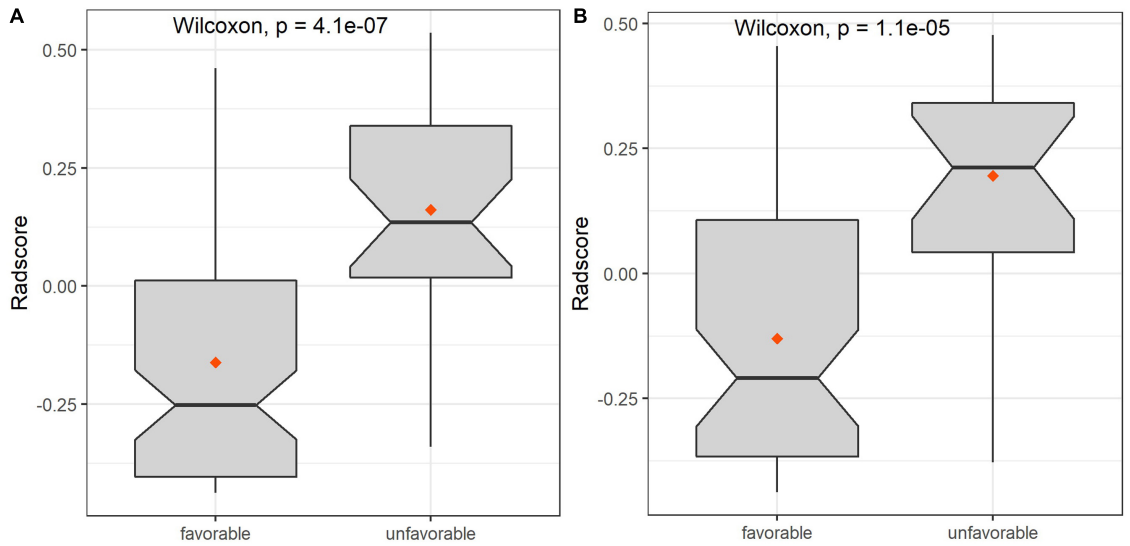

FIGURE 3 | The box diagrams of radscore for discriminating favorable and unfavorable outcomes with combined model in the training and validation sets. **(A)** Training set. **(B)** Validation set.

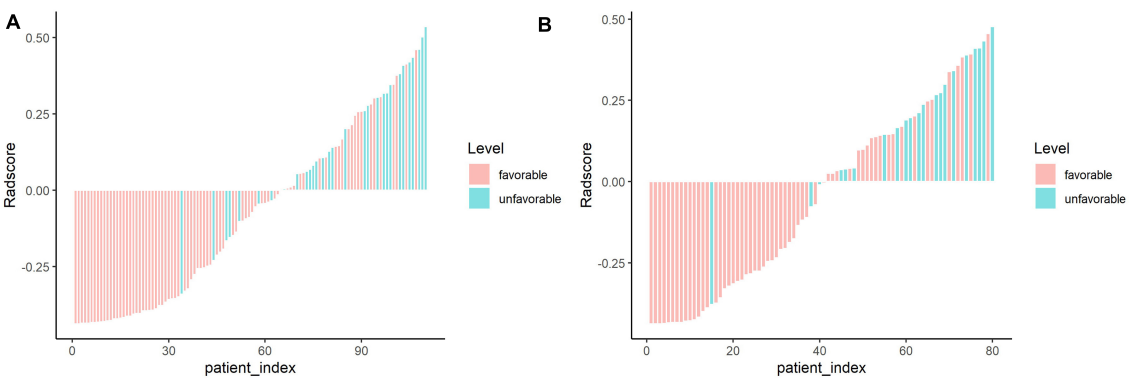

FIGURE 4 | Waterfall chart showing radscores for each patient in the training and validation sets. The red columns represent patients with favorable outcome, whereas the green columns represent those with unfavorable outcome. **(A)** Training set. **(B)** Validation set.

GrayLevel Emphasis. The detailed explanation of these features is shown in **Supplementary Material 1**. There was a significant difference of radscore between favorable and unfavorable outcome patients both in training and validation sets (**Figures 3**, **4** and **Tables 4**, **5**).

Comparison of Performance of the Prediction Models

The AUC values and other diagnostic performance indexes, including specificity, sensitivity, accuracy, positive and negative predictive values (PPV and NPV), and the comparison of AUCs among these models for predicting unfavorable outcome in the training and testing sets, are shown in **Figure 5** and **Tables 4**, **5**.

In the training set for predicting unfavorable outcome, the AUCs were as follows: ADC radiomics model 0.772, FLAIR radiomics model 0.731, ADC + FLAIR radiomics model 0.815, clinical model 0.791, and clinical and conventional MRI model 0.782. When combining clinical and conventional MRI factors and radiomics signatures, the AUC was significantly increased, reaching to 0.926 (**Table 4** and **Figure 5**). In comparison, the combined model (all factors) had significantly better performance than any other model ($P < 0.05$) in the training set, so did the ADC + FLAIR model comparing with the FLAIR model ($P = 0.041$). However, there was no significant difference between the AUCs of other models (**Table 5**).

In the validation set for predicting unfavorable outcome, the AUCs were as follows: ADC radiomics model 0.795, FLAIR radiomics model 0.707, ADC + FLAIR radiomics model 0.825, clinical model 0.763, and clinical and conventional MRI model 0.751. When combining clinical and conventional MRI factors and radiomics signatures, the AUC value was increased to 0.864 (**Table 4** and **Figure 5**). The PPV was relatively lower (0.531) and the NPV was relatively higher (0.917) in the validation

TABLE 4 | The diagnostic performance of the prediction models.

	Models	AUC	95% CI	Sensitivity	Specificity	Accuracy	PPV	NPV
Training (*n* = 110)	ADC	0.772	(0.681–0.864)	0.833	0.662	0.709	0.481	0.914
	FLAIR	0.731	(0.629, 0.834)	0.700	0.637	0.655	0.420	0.850
	ADC + FLAIR	0.815	(0.734, 0.895)	0.767	0.725	0.736	0.511	0.892
	Clin	0.791	(0.687, 0.894)	0.733	0.787	0.773	0.564	0.887
	Clin + Con MR	0.782	(0.684, 0.881)	0.800	0.637	0.682	0.453	0.895
	Combined all	0.926	(0.878, 0.974)	0.867	0.875	0.873	0.722	0.946
Validation (*n* = 80)	ADC	0.795	(0.687, 0.903)	0.810	0.525	0.600	0.378	0.886
	FLAIR	0.707	(0.583, 0.831)	0.857	0.576	0.650	0.419	0.919
	ADC + FLAIR	0.825	(0.726, 0.923)	0.857	0.644	0.700	0.462	0.927
	Clin	0.763	(0.632, 0.894)	0.667	0.763	0.738	0.500	0.896
	Clin + Con MR	0.751	(0.619, 0.883)	0.762	0.729	0.738	0.500	0.896
	Combined all	0.864	(0.773, 0.954)	0.810	0.746	0.762	0.531	0.917

Combined all indicates all factors, including clinical and conventional MRI factors and radiomics features. AUC, area under the curves; ADC, apparent diffusion coefficient; Clin, clinical variables; Con MRI, conventional MRI factors; CI, confidence interval; FLAIR, fluid-attenuated inversion recovery; PPV, positive predictive value; NPV, negative predictive value.

set. In comparison, the combined model (all factors) had significantly better performance than FLAIR, clinical (Clin), and Clin + conventional (Con) MRI models ($P < 0.05$) in the validation set, so did the ADC + FLAIR model comparing with the FLAIR model ($P = 0.036$). However, there was no significant difference between the AUCs of other models (**Table 5**).

The diagnostic performance of the prediction models was tested with a precision–recall (PR) curve. The areas under curve of the "all" model (combined model) were largest both for ROCs and PR curves in training and validation sets (the areas under curve of PR was 0.79 in the training set and 0.71 in the validation set) (**Figure 5**). This indicated that the combined model could attain better diagnostic performance than any other models.

In the combined model ("all" model), the ORs for various factors were as follows: radioscore (ADC + FLAIR), 2.08; age (>60.5 years), 1.07; sex (male), 0.22; DWI-ASPECTS ≥ 7, 1.25; and admission NIHSS, 1.18 (**Supplementary Material 2**). Thus, radioscore, age, DWI-ASPECTS ≥ 7, and admission NIHSS were the risk factors of unfavorable outcome in AIS patients.

TABLE 5 | Comparison the AUCs among different prediction models (*P*-value).

Training set					
Training sets	**FLAIR**	**ADC + FLAIR**	**Clin**	**Clin + Con MRI**	**All (combined model)**
ADC	0.458	0.190	0.795	0.877	<0.001*
FLAIR	–	0.041*	0.477	0.523	<0.001*
ADC + FLAIR	–	–	0.732	0.621	0.001*
Clin	–	–	–	0.555	0.003*
Clin + Con MRI	–	–	–	–	0.001*
Validation Set					
Validation sets	**FLAIR**	**ADC + FLAIR**	**Clin**	**Clin + Con MRI**	**All (combined model)**
ADC	0.210	0.609	0.693	0.586	0.221
FLAIR	–	0.036*	0.532	0.616	0.011*
ADC + FLAIR	–	–	0.471	0.393	0.446
Clin	–	–	–	0.323	0.031*
Clin + Con MRI	–	–	–	–	0.021*

*All indicates all factors, including clinical and conventional MRI factors and radiomics features. AUC, area under the curves; ADC, apparent diffusion coefficient; Clin, clinical variables; Con MRI, conventional MRI factors; FLAIR, fluid-attenuated inversion recovery. *P < 0.05.*

DISCUSSION

In this study, we extracted radiomics features based on FLAIR and ADC images and developed a combination model for predicting the functional outcome in AIS patients. We found that the radiomics signatures, especially those extracted from ADC image, were associated with unfavorable outcome (mRS > 2) and was a value risk factor. Moreover, radiomics based on FLAIR and ADC can improve the diagnostic performance of the combination prediction model.

Conventional MRI, including FLAIR and DWI, had been proven a useful tool in predicting AIS outcome. The location, volume, as well as signal intensity of infarct lesions are the effective markers of prognosis. Boss et al. (2019) explored the influence of visual DWI lesion homogeneity on clinical outcome in 30 AIS patients. A significant difference of mRS scores was found between patients with homogenous and non-homogeneous DWI lesions. However, they did not offer a quantization parameter of lesion homogeneity, and the finding has not been verified in other studies. In another study that included 65 AIS patients treated with thrombolysis, Tanriverdi et al. (2016) assessed the relationship between FLAIR hyperintensity and functional outcome. They suggested that a rise of FLAIR intensity ratio is a marker of favorable outcome. Whereas, the setup of prediction model and validation in other medical centers had not been made. Radiomics capture subtle

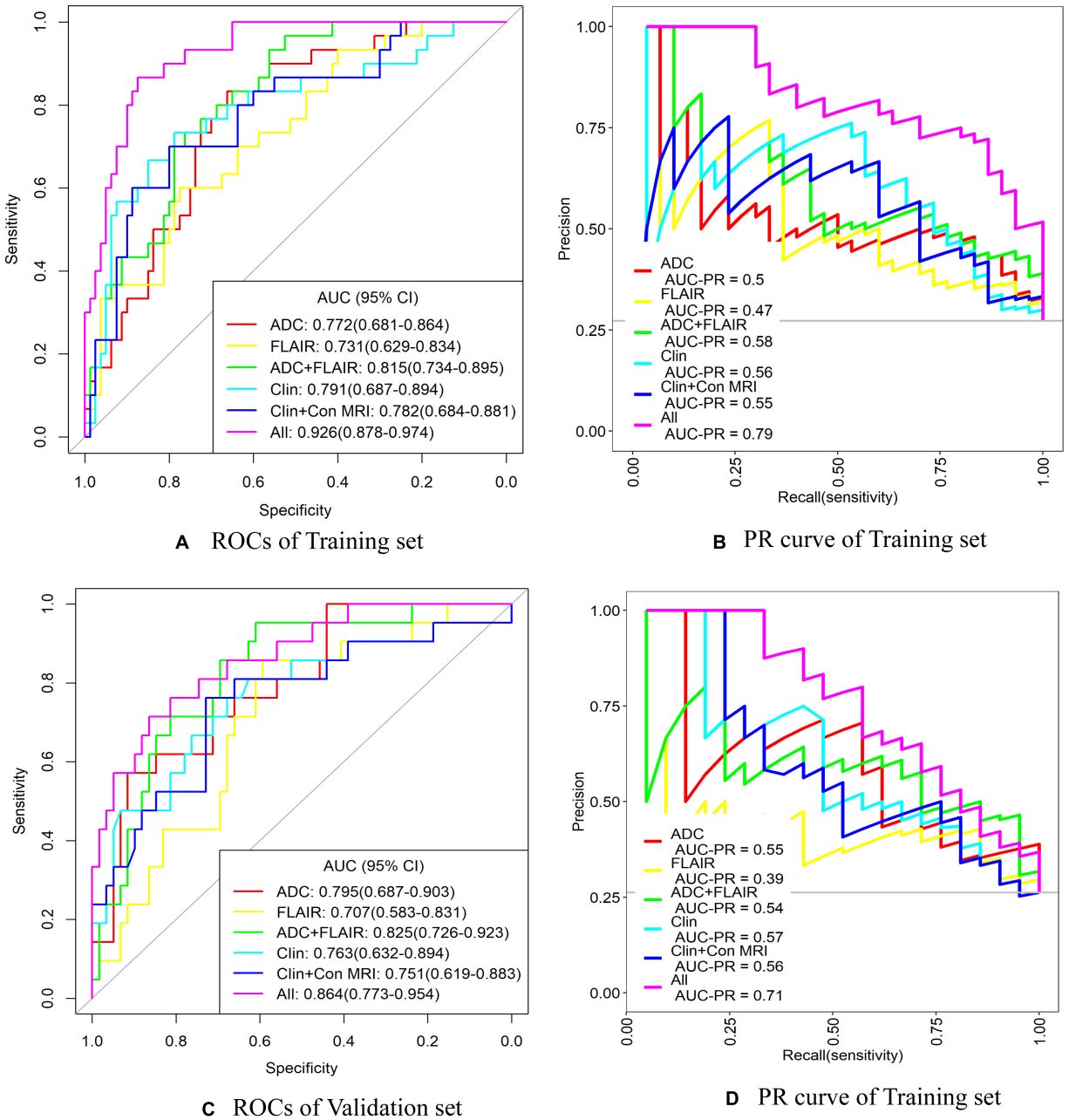

FIGURE 5 | ROC and precision–recall (PR) curve analysis of the six models for predicting unfavorable outcome in training and validation sets. ADC, apparent diffusion coefficient; AUC, area under the curve; Clin + Con MRI, clinical + conventional MRI variables; CI, confidence interval; FLAIR, fluid-attenuated inversion recovery; ROC, receiver operating characteristic curve. **(A,B)** ROC and PR curves of the training set. **(C,D)** ROC and PR curves of the validation set.

variation within medical images. After extraction of radiomics features and dimension reduction of data redundancy, the strongest features could be used to analyze the heterogeneity of lesions and thus to predict patient outcome (Qiu et al., 2019; Tomaszewski and Gillies, 2021). Radiomics is superior to conventional imaging visual analysis in identifying the heterogeneity of AIS lesions (Wen et al., 2020). Qiu et al. (2019) also found that the radiomics features extracted from non-contrast CT and CT angiography were useful to predict the recanalization of cerebral arteries with intravenous injection of alteplase in AIS patients. Therefore, we selected FLAIR and DWI images to develop radiomics signatures and explore their prognostic role of clinical outcome in AIS patients.

Our results suggested that radiomics signatures extracted from FLAIR and DWI can be correlated with mRS scores. The diagnostic odds ratio (OR) analysis also showed that the

weight of radioscore (2.08) was higher than any other clinical and conventional MRI factors (from 0.22 to 1.25). This result indicated that radioscore is the most important risk factor for predicting unfavorable outcome of AIS patients. It confirms our hypothesis that these features could be used as a biomarker to predict AIS outcome. In the study conducted by Tozer et al. (2018), texture features were extracted from FLAIR images. They found that these texture features were correlated with executive dysfunction and cognition in patients with cerebral small vessel disease instead of AIS. Wang et al. (2020) also confirmed that texture features extracted from FLAIR images and ADC maps could serve as a biomarker of stroke severity. While these features were not predictive of mRS scores in their study, on the other hand, they only enrolled ischemic stroke patients in subacute phase and did not test their results in an external validation set. In contrast, in the present study, we enrolled the AIS patients from three hospitals who suffered from ischemic attack less than 72 h and extracted radiomics signatures based both on FLAIR and ADC images.

Although radiomics features capture subtle heterogeneity beyond the perception of the human eye, our study showed that the AUCs of ADC + FLAIR radiomics feature model were slightly superior to those of pure Clin or Clin + Con MRI model both in the training and validation sets. But, other diagnostic performance indexes of ADC + FLAIR radiomics feature model were similar or even slightly lower than those of pure Clin or Clin + Con MRI model both in the training and validation sets. Thus, the direct usefulness of models only based on ADC and FLAIR radiomics features to predict unfavorable outcome of AIS may cause bias or errors. On the other hand, the multi-parameter analysis has been proven to attain better diagnostic performance. Therefore, the model integrating clinical and conventional MRI factors could be used in predicting outcome in AIS patients. The ability for predicting AIS outcome was improved significantly for this combination. In our study, the AUC and PPV of predicting unfavorable outcome in the training set with combined model were improved significantly (0.926 and 0.722, separately). Previous studies have also reported diagnostic performance improvement when this methodology was combined to clinical and conventional imaging variables. In one retrospective study of 38 pathologically confirmed intraductal papillary mucinous neoplasms (IPMN) of the pancreas, Permuth et al. (2016) found that the combined radiogenomic model attained more accurate prediction of the IPMN malignancy (AUC = 0.92). Wen et al. (2020) extracted radiomics features from non-contrast CT and CTA images of 126 patients with MCA infarct. They developed a combined prediction model based on radiomics and ASPECTS and showed a good performance of this model in predicting malignant MCA infarct both in the training and validation sets (with AUC of 0.917 and 0.913, respectively). These results confirmed the superiority of a combined model, indicating that clinical and conventional imaging factors and radiomics features have an intercrossing incremental effect on each other, adding up to a more satisfactory outcome prediction model for AIS patients. Thus, radiomics features should be combined to multi-parameter analysis with clinical variables as well as conventional visual factors to form a comprehensive marker panel with better performance. However, the PPV was relatively lower (0.531) and the NPV was relatively higher (0.917) in the validation set. This means four participants in the validation set will be incorrectly labeled as unfavorable outcome. The phenomena of relatively lower PPV and higher NPV in the validation set of the present study is probably because the data of the validation set come from the other two institutes. The heterogeneity of MR data and clinical factors could reduce the efficiency of the combined model.

Clinical and MR factors also play an important role in outcome prediction of AIS. Previous studies have reported that the clinical variables, such as gender, age, and admission NIHSS, could be used as factors for predicting the outcome of AIS patients (Kim and Vemuganti, 2015; Wu et al., 2019). To validate these results, we used the 90-day mRS $>$ 2 as an unfavorable outcome criteria. In our study, multivariate logistic analysis confirmed that higher admission NIHSS scores, age ($>$60.5 years old), and gender (female) were independent predictors of unfavorable outcome. Both the above studies and the present study proved that the selected clinical variables have the potential in predicting long-term outcome of AIS. Along with clinical predictors, our findings also indicated that conventional MRI variables, including infarct volume and DWI-ASPECTS score, seem to be independent markers for predicting functional outcome. In previous studies, certain conventional MRI factors, especially those based on FLAIR and DWI images, have been proven to be associated with the outcome of AIS patients (Bucker et al., 2017; Liu et al., 2018; Tozer et al., 2018). Similarly, our earlier study also proved that with a cut-off value of 57.3 ml, the infarct volume could predict unfavorable patient outcome (Yuan et al., 2019). In the present study, we did not find an association between Fazekas score and 90-day mRS. This phenomena could ascribed to the lower Fazekas score of the patients in this study. The patients with lower Fazekas score experienced a less severe cerebral vascular disease (Liu et al., 2018). Otherwise, only moderate to severe leukoaraiosis (with higher Fazekas score) was the independent predictor of unfavorable outcome. Therefore, the use of clinical and conventional MR factors alone for predicting the outcome accurately has been challenged (Boss et al., 2019).

Limitations

It should be noted that there are several limitations in the present study. The main limitation is the relatively small sample size, which might cause an overfitting problem for developing radscore. However, to address this limitation, we used the external validation analysis to minimize this bias. Second, we collected the imaging data of AIS retrospectively. This might lead to selection bias. The results obtained from the consecutive AIS patients enabled the development of tentative outcome prediction model. Third, our current study did not include functional MR imaging. In the future, the data of perfusion imaging, amide proton transfer imaging, and other functional imaging could be added to a comprehensive model. Finally, only patients who had a stroke in the MCA territory are included, and this analysis cannot be generalized to strokes in other

areas of the brain. However, infarction in the MCA territory is a most common ischemic stroke with high prevalence of sequelae and mortality (Yuan et al., 2019; Wen et al., 2020). Thus, the prediction model combining radiomics features and clinical and conventional MRI factors may still facilitate the early and accurate prediction of stroke. We deduce that the radiomics features extracted from ADC and FLAIR can be helpful in the development of clinical decisions of AIS patients, especially for those patients with stroke in the MCA territory.

CONCLUSION

Our results showed the usefulness of radiomics based on FLAIR and ADC in predicting unfavorable functional outcome in patients with AIS. Radiomics can be added as an independent predictor along with clinical and conventional MRI factors. The results proved that the combination model, which incorporates clinical variables, conventional MRI information, and radiomics, demonstrated the highest efficiency in the prediction of functional outcomes after AIS attack. This model can facilitate prediction of AIS evolution in acute phase and would contribute more to clinical evaluation process.

DATA AVAILABILITY STATEMENT

The raw data supporting the conclusions of this article will be made available by the authors, without undue reservation.

ETHICS STATEMENT

The studies involving human participants were reviewed and approved by The Ethics Committees of The Second Hospital of Hebei Medical University. The ethics committee waived the requirement of written informed consent for participation.

AUTHOR CONTRIBUTIONS

GQ, RB, J-LR, WW, SD, and TY made a substantial contribution to the concept and design, acquisition of data or analysis, and interpretation of data. GQ, YL, and TY drafted the manuscript and revised it critically for relevant intellectual content. GQ, RB, and SD performed the MR examination and follow-up of patients. All the authors approved the final version of the manuscript.

FUNDING

This study was supported by the Specialist Leadership Project of Hebei Province (Grant Number: 361004) and the Technology tracking program for medical application of Hebei Province (Grant Number: G201725).

SUPPLEMENTARY MATERIAL

The Supplementary Material for this article can be found online at: https://www.frontiersin.org/articles/10.3389/fnins.2021.730879/full#supplementary-material

REFERENCES

Boss, S. M., Moustafa, R. R., Moustafa, M. A., Sadek, A. E., Mostafa, M. M., Aref, H. M., et al. (2019). Lesion homogeneity on diffusion-weighted imaging is a marker of outcome in acute ischemic stroke. *Egyptian J. Neurol. Psychiatry Neurosurg.* 55:59. doi: 10.1186/s41983-019-0101-z

Bucker, A., Boers, A. M., Bot, J. C. J., Berkhemer, O. A., Lingsma, H. F., Yoo, A. J., et al. (2017). Associations of ischemic lesion volume with functional outcome in patients with acute ischemic stroke : 24-hour versus 1-week imaging. *Stroke* 48, 1233–1240. doi: 10.1161/STROKEAHA.116.015156

Choi, V., Kate, M., Kosior, J. C., Buck, B., Steve, T., McCourt, R., et al. (2015). National Institutes of Health Stroke Scale score is an unreliable predictor of perfusion deficits in acute stroke. *Int . J. Stroke* 10, 582–588. doi: 10.1111/ijs.12438

Collins, G. S., Reitsma, J. B., Altman, D. G., and Moons, K. G. M. (2015). Transparent Reporting of a multivariable prediction model for Individual Prognosis Or Diagnosis (TRIPOD): the TRIPOD Statement. *Br. J. Surg.* 102, 148–158. doi: 10.1016/j.eururo.2014.11.025

Darwish, E. A., Abdelhameed-El-Nouby, M., and Geneidy, E. (2020). Mapping the ischemic penumbra and predicting stroke progression in acute ischemic stroke: the overlooked role of susceptibility weighted imaging. *Insights Imaging* 11, 6–17. doi: 10.1186/s13244-019-0810-y

Dolotova, D., Arkhipov, I., Blagosklonova, E., Donitova, V., Barmina, T., Sharifullin, F., et al. (2020). Application of radiomics in vesselness analysis of CT angiography images of stroke patients. *Stud. Health Technol. Inform.* 270, 33–37. doi: 10.3233/SHTI200117

Fazekas, F., Barkhof, F., Wahlund, L. O., Pantoni, L., Erkinjuntti, T., Scheltens, P., et al. (2002). CT and MRI rating of white matter lesions. *Cerebrovasc. Dis.* 13, 31–36. doi: 10.1159/000049147

Ichijo, M., Miki, K., Ishibashi, S., Tomita, M., Kamata, T., Fujigasaki, H., et al. (2013). Posterior cerebral artery laterality on magnetic resonance angiography predicts long-term functional outcome in middle cerebral artery occlusion. *Stroke* 44, 512–515. doi: 10.1161/STROKEAHA.112.674101

Jiang, L., Chen, Y. C., Zhang, H., Peng, M. Y., and Chen, H. Y. (2019). FLAIR vascular hyperintensity in acute stroke is associated with collateralization and functional outcome. *Eur. Radiol.* 29, 4879–4888. doi: 10.1007/s00330-019-06022-0

Kassner, A., Liu, F., Thornhill, R. E., Tomlinson, G., and Mikulis, D. J. (2009). Prediction of hemorrhagic transformation in acute ischemic stroke using texture analysis of postcontrast T1-weighted MR images. *J. MagnReson. Imaging* 30, 933–941. doi: 10.1002/jmri.21940

Kim, T. H., and Vemuganti, R. (2015). Effect of sex and age interactions on functional outcome after stroke. *CNS Neurosci. Ther.* 21, 327–336. doi: 10.1111/cns.12346

Li, W., Zhang, L., Tian, C., Song, H., Fang, M., Hu, C., et al. (2018). Prognostic value of computed tomography radiomics features in patients with gastric cancer following curative resection. *Eur. Radiol.* 29, 3079–3089. doi: 10.1007/s00330-018-5861-9

Liu, Y. Y., Zhang, M., Chen, Y., Gao, T., Yun, W. W., and Zhou, X. J. (2018). The degree of leukoaraiosis predicts clinical outcomes and prognosis in patients with middle cerebral artery occlusion after intravenous thrombolysis. *Brain Res.* 1681, 28–33. doi: 10.1016/j.brainres.2017.12.033

Permuth, J. B., Choi, J., Balarunathan, Y., Kim, J., Chen, D. T., Chen, L., et al. (2016). Combining radiomic features with a miRNA classifier may

improve prediction of malignant pathology for pancreatic intraductal papillary mucinous neoplasms. *Oncotarget* 7, 85785–85797. doi: 10.18632/oncotarget.11768

Qiu, W., Kuang, H., Nair, J., Assis, Z., Najm, M., McDougall, C., et al. (2019). Radiomics-based intracranial thrombus features on CT and CTA predict recanalization with intravenous alteplase in patients with acute ischemic stroke. *AJNR Am. J. Neuroradiol.* 40, 39–44. doi: 10.3174/ajnr.A5918

Rudilosso, S., Olivera, M., Esteller, D., Laredo, C., Amaro, S., Llull, L., et al. (2021). Susceptibility vessel sign in deep perforating arteries in patients with recent small subcortical infarcts. *J. Stroke Cerebrovasc. Dis.* 30:105415. doi: 10.1016/j.jstrokecerebrovasdis.2020.105415

Sommer, P., Posekany, A., Serles, W., Marko, M., Scharer, S., Fertl, E., et al. (2018). Is functional outcome different in posterior and anterior circulation stroke? *Stroke* 49, 2728–2732. doi: 10.1161/STROKEAHA.118.021785

Tang, T. T., Jiao, Y., Cui, Y., Zhao, D. L., Zhang, Y., Wang, Z., et al. (2020). Penumbra-based radiomics signature as prognostic biomarkers for thrombolysis of acute ischemic stroke patients: a multicenter cohort study. *J. Neurol.* 267, 1454–1463. doi: 10.1007/s00415-020-09713-7

Tanriverdi, Z., Gocmen, R., Oguz, K. K., Topcuoglu, M. A., and Arsava, E. M. (2016). Elevations in tissue fluid-attenuated inversion recovery signal are related to good functional outcome after thrombolytic treatment. *J. Stroke Cerebrovasc. Dis.* 25, 480–483. doi: 10.1016/j.jstrokecerebrovasdis.2015.10.024

Tei, H., Uchiyama, S., Usui, T., and Ohara, K. (2011). Diffusion-weighted ASPECTS as an independent marker for predicting functional outcome. *J. Neurol.* 258, 559–565. doi: 10.1007/s00415-010-5787-x

Tomaszewski, M. R., and Gillies, R. J. (2021). The biological meaning of radiomic features. *Radiology* 2021:202553. doi: 10.1148/radiol.2021202553

Tozer, D. J., Zeestraten, E., Lawrence, A. J., Barrick, T. R., and Markus, H. S. (2018). Texture analysis of T1-weighted and fluid-attenuated inversion recovery images detects abnormalities that correlate with cognitive decline in small vessel disease. *Stroke* 49, 1656–1661.

van Griethuysen, J. J. M., Fedorov, A., Parmar, C., Hosny, A., Aucoin, N., Narayan, V., et al. (2017). Computational radiomics system to decode the radiographic phenotype. *Cancer Res.* 77, e104–e107. doi: 10.1158/0008-5472.CAN-17-0339

Wang, H., Lin, J., Zheng, L., Zhao, J., Song, B., and Dai, Y. M. (2020). Texture analysis based on ADC maps and T2-FLAIR images for the assessment of the severity and prognosis of ischaemic stroke. *Clin. Imaging* 67, 152–159. doi: 10.1016/j.clinimag.2020.06.013

Wen, X., Li, Y., He, X., Xu, Y., Shu, Z., Hu, X., et al. (2020). Prediction of malignant acute middle cerebral artery infarct via computed tomography radiomics. *Front. Neurosci.* 14:708. doi: 10.3389/fnins.2020.00708

Wu, X., Liu, G., Zhou, W., Ou, A. H., Liu, X., Wang, Y. H., et al. (2019). Outcome prediction for patients with anterior circulation acute ischemic stroke following endovascular treatment: a single-center study. *Exp. Ther. Med.* 18, 3869–3876. doi: 10.3892/etm.2019.8054

Yuan, T., Ren, G., Quan, G., and Liu, Y. (2019). Maximum lesions area and orthogonal values accessed from DWI images would be alternative imaging markers for predicting the outcome of acute ischemia in the middle cerebral artery territory. *Acta Radiol.* 60, 628–633. doi: 10.1177/0284185118795330

Conflict of Interest: J-LR was employed by GE Healthcare China.

The remaining authors declare that the research was conducted in the absence of any commercial or financial relationships that could be construed as a potential conflict of interest.

Publisher's Note: All claims expressed in this article are solely those of the authors and do not necessarily represent those of their affiliated organizations, or those of the publisher, the editors and the reviewers. Any product that may be evaluated in this article, or claim that may be made by its manufacturer, is not guaranteed or endorsed by the publisher.

frontiers in Neuroscience

ORIGINAL RESEARCH
published: 05 October 2021
doi: 10.3389/fnins.2021.744429

Genetic Factors in Rasmussen's Encephalitis Characterized by Whole-Exome Sequencing

Junhong Ai[1], Yisong Wang[1], Dong Liu[2,3], Dongying Fan[1], Qiqi Wang[2], Tianfu Li[2,4], Guoming Luan[2,4], Peigang Wang[1]* and Jing An[1,4]**

[1] Department of Microbiology, School of Basic Medical Science, Capital Medical University, Beijing, China, [2] Department of Neurosurgery, Sanbo Brain Hospital, Capital Medical University, Beijing, China, [3] Department of Neurology, Beijing Tiantan Hospital, Capital Medical University, Beijing, China, [4] Center of Epilepsy, Beijing Institute for Brain Disorders, Beijing, China

Rasmussen's encephalitis (RE) is a rare chronic neurological disorder characterized by unihemispheric brain atrophy and epileptic seizures. The mechanisms of RE are complex. Adaptive immunity, innate immunity and viral infection are all involved in the development of RE. However, there are few studies on the role of genetic factors in the mechanisms of RE. Thus, the objective of this study was to reveal the genetic factors in the mechanisms of RE. Whole-exome sequencing (WES) was performed in 15 RE patients. Ten patients with temporal lobe epilepsy (TLE), which is a common and frequently intractable seizure disorder, were used as the controls. Thirty-one non-silent single nucleotide variants (SNVs) affecting 16 genes were identified in the RE cases. The functions of the genes with SNVs were associated with antigen presentation, antiviral infection, epilepsy, schizophrenia and nerve cell regeneration. Genetic factors of RE were found first in this study. These results suggest that RE patients have congenital abnormalities in adaptive immunity and are susceptible to some harmful factors, which lead to polygenic abnormal disease.

Keywords: Rasmussen's encephalitis (RE), seizure, genetic factors, whole-exome sequencing, singe nucleotide variants

OPEN ACCESS

Edited by:
Ahmad Raza Khan, Centre of Bio-Medical Research (CBMR), India

Reviewed by:
Binglin Zhu, University at Buffalo, United States
Carmen Rubio, Manuel Velasco Suárez Instituto Nacional de Neurología y Neurocirugía, Mexico

***Correspondence:**
Guoming Luan
luangm3@163.com
Peigang Wang
pgwang@ccmu.edu.cn
Jing An
anjing@ccmu.edu.cn

Specialty section:
This article was submitted to Neurodegeneration, a section of the journal Frontiers in Neuroscience

Received: *20 July 2021*
Accepted: *13 September 2021*
Published: *05 October 2021*

Citation:
Ai J, Wang Y, Liu D, Fan D, Wang Q, Li T, Luan G, Wang P and An J (2021) Genetic Factors in Rasmussen's Encephalitis Characterized by Whole-Exome Sequencing. Front. Neurosci. 15:744429. doi: 10.3389/fnins.2021.744429

INTRODUCTION

Rasmussen encephalitis (RE) is a rare chronic neurological disorder characterized by unihemispheric inflammation, refractory seizures, and progressive neurological deficits (Varadkar et al., 2014). It was first reported by the neurosurgeon Theodore Rasmussen in 1958 (Rasmussen et al., 1958). An epidemiological study from Germany estimated that the annual incidence of RE was 2.4 cases/10^7 persons aged $\leq$ 8 years (Bien et al., 2013). The disease mainly affects children, with an average age of onset of 6–7 years (Andermann and Farrell, 2006). However, there have also been reports that adolescents and adults account for 10% of all RE cases (Villani et al., 2006). Histopathological analysis of brain specimens revealed inflammation with microglial nodules, perivascular and parenchymal infiltration of T cells, loss of neurons and astrocytes, and gliosis in the affected hemisphere (Farrell et al., 1995; Bien et al., 2005). Immunomodulatory therapy seems to slow the progression of RE but cannot stop it or change the eventual outcome (Rasmussen et al., 1958). Cerebral hemispherectomy is still the only treatment for associated seizures, but it is related to inevitable dysfunction impairment (Kossoff et al., 2003).

There are various mechanisms related to RE. Adaptive immunity, innate immunity and viral infection are all involved in the development of RE. Immunopathological studies have shown that cytotoxic $CD8^+$ T lymphocytes are the most common T lymphocyte subgroup in the brains of patients with RE (Pardo et al., 2014). The intensity of peripheral $CD8^+$ T cell expansion is related to the severity of the disease (Schneider-Hohendorf et al., 2016). Although the adaptive immune response is an important effector of central nervous system (CNS) damage, the innate immune response mediated by the activation of microglia and astrocytes is also the core of the pathogenesis of RE. The degree of microglial activation follows the progression pattern of RE, parallels the degree of T lymphocyte infiltration, and is observed in the early stages of cortical involvement (Pardo et al., 2004; Troscher et al., 2019).

The pathological changes observed in RE brains are similar to those in viral encephalitis, which has promoted the study of pathogen infection in the damaged cerebral cortex. Human cytomegalovirus (HCMV) and Epstein-Barr virus (EBV) infections were originally proposed by Theodore Rasmussen (Walter and Renella, 1989; Farrell et al., 1991). Other viruses were also found in RE brain samples, such as herpes simplex virus (Vinters et al., 1993; Atkins et al., 1995). The localized and slowly progressing viral infection may explain the changes in monohemispheric encephalitis in RE. However, human herpesvirus infections are very common in humans. In all these studies, the causal relationship between viruses and RE pathogenesis has not been proven.

While RE is a rare chronic brain disorder, there are few studies on the role of genetic factors in the mechanism of RE. Early reports about genetic tests in RE came from case reports and found mutations in the *NOD2/CARD15* and *SCN1A* genes (Goyal et al., 2007; Ohmori et al., 2008). Subsequently, researchers found SNPs in the *CTLA4* and *PDCD1* genes and elucidated genetic predisposition in immunoregulatory genes (Takahashi et al., 2013). However, because of the small case number or limited number of genes detected, limitations existed for the above studies. To reveal the genetic factors in the mechanisms of RE, whole-exome sequencing (WES) in 15 RE patients was performed in this study. As a result, single nucleotide variants (SNVs) were found in genes with functions in antigen presentation, antiviral infection, epilepsy, schizophrenia and nerve cell regeneration.

MATERIALS AND METHODS

Rasmussen's Encephalitis Patients and Controls

Between 2008 and 2016, 34 patients with RE were admitted to Sanbo Brain Hospital (Beijing, China). Clinical diagnosis was made according to the "European consensus statement" (Bien et al., 2005). Among them, 15 patients were selected and enrolled in this study. Each patient was subjected to magnetic resonance imaging (MRI) examination using an MRI scanner (Siemens 3.0T TIM Trio MRI; Munich, Germany) for diagnosis before undergoing craniotomy.

Temporal lobe epilepsy (TLE) is a common refractory epilepsy in adolescents and adults (Tellez-Zenteno et al., 2012). There were partial similarities between RE and TLE in clinical manifestations and age of onset. However, their prognoses are greatly different. Cerebral hemispherectomy is the only treatment for associated seizures in RE, but it is related to inevitable dysfunction and impairment. Surgical resection of the temporal lobe has a good outcome in TLE. Thus, TLE was used as the control group in this study.

A total of 10 temporal lobe epilepsy (TLE) patients admitted to Sanbo Brain Hospital who underwent surgical treatment were used as a control group; they were generally matched with the RE group with respect to age. Patients with other nervous system diseases were excluded.

For RE and TLE patients, at least two blocks ($0.5 \times 0.5 \times 0.5$ cm each) of brain biopsies from different areas were collected for WES after the operations.

Whole-Exome Sequencing

WES was performed by GrandOmics (Beijing, China). Generally, the brain tissue collected during the operation was homogenized using a tissue disruptor. Then, genomic DNA was extracted with a TIANamp Genomic DNA Kit (DP304) (TIANGEN, China). DNA samples were quantified using a NanoDrop 2000. An exome-captured sequencing library was produced from the xGen Exome Research Panel v1.0 kit. The libraries were subsequently sequenced on an Illumina HiSeq X-ten sequencing instrument according to the manufacturer's instructions with a read depth greater than 100X, and more than 95% of the area covered more than 20X.

After sequencing, the original data were obtained in FASTQ format, and then the short reads were compared with Genome Reference Consortium Human genome build 37 (GRCh37) by Burrows-Wheeler Aligner (BWA) software (v0.7–6a) (Li and Durbin, 2009) to determine the position of the short sequence on the genome. Sequence Alignment/Map (SAM) tools software (v0.1.18) was used to align these short sequences and convert the data format. The removal of redundant information and noise generated in the process of sequencing was conducted by Picard software (v1.91). Genome Analysis Toolkit (GATK) software (v2.6–4) (McKenna et al., 2010) was used to analyze sample sequencing data and the difference loci (SNPs and InDels) of the referred genome, while Annovar software (2013Aug23 version) was used for functional annotation of these mutation sites.

Variant Filters

We considered only canonical transcripts for each variant, assuming the most deleterious predicted effect for each transcript according to VEP software. In gene-based analyses, only non-silent SNVs were considered (that is, transcript ablations, splice donor/acceptors, splice region, stop gain, frameshift, stop lost, initiator codon variants, transcript amplifications, in-frame insertion/deletions and missense) (**Figure 1**).

Statistical Analysis

The frequencies of selected non-silent SNVs in all RE and TLE cases were calculated. SNVs that had a high frequency in RE cases

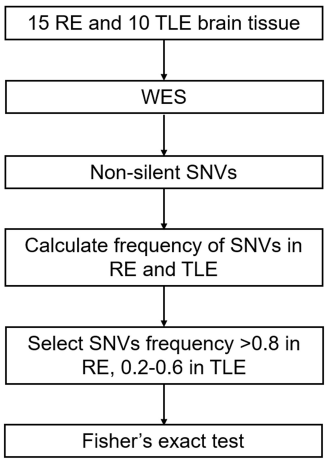

FIGURE 1 | Screening process of SNVs in RE. RE, Rasmussen's Encephalitis. TLE, temporal lobe epilepsy. WES, whole-exome sequencing. SNVs, single nucleotide variants.

(> 0.8) and low frequency in TLE and normal populations (0.2–0.6) were considered to be associated with the pathogenesis of RE (**Figure 1**).

Fisher's exact test was used for statistical analysis by SPSS 19.0 software. *P*-values less than 0.05 were considered to be significant.

RESULTS

Clinical Features of Patients With Rasmussen's Encephalitis

There were six males and nine females in the RE group, with a mean age of seizure onset of 7.7 years and a mean age at surgery of 11.0 years. The 10 TLE patients in the control group were generally matched with the RE patient group. There were four males and six females with a mean age of seizure onset of 7.3 years and a mean age at surgery of 9.4 years.

Single Nucleotide Variants in Rasmussen's Encephalitis

In total, 31 non-silent SNVs affecting 16 genes were identified in this study (**Figure 2**). Detailed information on all genes and mutations is shown in **Table 1**. Most of the SNVs (29/31) had a frequency of 0.2–0.6 in normal populations, while two in the *MUC2* gene had a low frequency (<0.1). No rare SNVs (<0.01) associated with specific functions were found. The frequency of these SNVs in the TLE group was nearly the same as that in the normal population. However, almost all of them were carried in the RE group, with a minimum frequency of 0.8.

Among the 16 genes with SNVs, half were related to antigen presentation, antiviral infection, epilepsy, schizophrenia and nerve cell regeneration, five had unknown functions, and three had no obvious connection with RE (**Figure 3**).

Genes With Single Nucleotide Variants in Rasmussen's Encephalitis Are Related to Antigen Presentation and Antiviral Infection

SNVs in four genes related to antigen presentation and one gene related to antiviral infection were found in RE cases (**Figure 3**). Genes related to antigen presentation were *HLA-DQA1, HLA-DQB1, HLA-DRB5,* and *CD1A*. The gene related to antiviral infection was *TRIM41*.

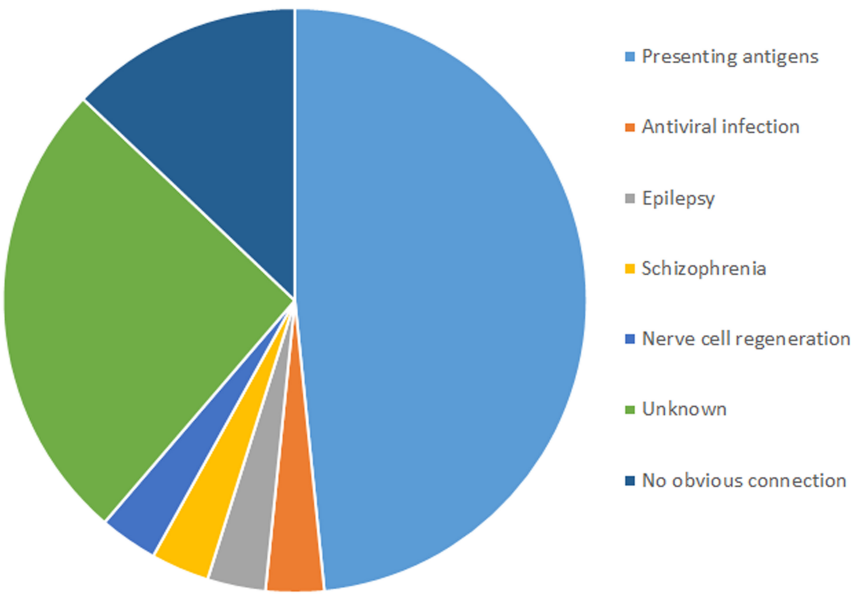

FIGURE 2 | Functions and numbers of SNVs associated with RE.

TABLE 1 | Single nucleotide variants obtained by WES in 15 RE cases and 10 TLE cases.

Gene	Genomic mutation	Mutation rate		cDNA	Protein	Gene function
		RE	TLE			
CD1A	chr1(hg19):g.158224904C > T	0.87	0.3	NM_001763.2:c.89C > T	p.Thr30Ile	Antigen presentation
HLA-DRB	chr6(hg19):g.32487390A > C	0.87	0.3	NM_002125.3:c.409A > C	p.Thr137Pro	Antigen presentation
HLA-DQA1	chr6(hg19):g.32610495A > G	1.0	0.6	NM_002122.4:c.722A > G	p.Gln241Arg	Antigen presentation
HLA-DQB1	chr6(hg19):g.32629137T > G	1.0	0.6	NM_002123.4:c.759A > C	p.Gln253His	Antigen presentation
	chr6(hg19):g.32629141C > T	1.0	0.6	NM_002123.4:c.755G > A	p.Arg252His	
	chr6(hg19):g.32629764C > T	1.0	0.4	NM_002123.3:c.514G > A	p.Ala172Thr	
	chr6(hg19):g.32629891C > T	1.0	0.4	NM_002123.3:c.514G > A	p.Ala172Thr	
	chr6(hg19):g.32629935C > G	1.0	0.6	NM_002123.3:c.470G > C	p.Gly157Ala	
	chr6(hg19):g.32632592C > G	0.93	0.4	NM_002123.2:c.362G > C	p.Gly121Ala	
	chr6(hg19):g.32632605C > A	0.93	0.4	NM_002123.2:c.349G > T	p.Val117Leu	
	chr6(hg19):g.32632694C > G	0.93	0.4	NM_002123.2:c.260G > C	p.Arg87Pro	
	chr6(hg19):g.32632700T > A	1.0	0.6	NM_002123.2:c.254A > T	p.Gln85Leu	
	chr6(hg19):g.32634306A > T	0.93	0.3	NM_002123.1:c.79T > A	p.Ser27Thr	
	chr6(hg19):g.32634350T > C	0.93	0.3	NM_002123.1:c.35A > G	p.Asp12Gly	
	chr1(hg19):g.158225019C > G	0.87	0.3	NM_001763.2:c.204C > G	p.Cys68Trp	
TRIM41	chr5(hg19):g.180651231G > A	0.8	0.2	NM_201627.1:c.232G > A	p.Ala78Thr	Antiviral infection
ADGRV1	chr5(hg19):g.90052289G > A	1.0	0.6	NM_032119.56:c.11599G > A	p.Glu3867Lys	Epilepsy
CMYA5	chr5(hg19):g.79028472C > T	1.0	0.5	NM_153610.2:c.3884C > T	p.Ala1295Val	Schizophrenia
TNR	chr1(hg19):g.175375469C > A	1.0	0.5	NM_003285.3:c.382G > T	p.Ala128Ser	Nerve cell regeneration
OR13C5	chr9(hg19):g.107361346C > T	1.0	0.6	NM_001004482.1:c.349G > A	p.Val117Met	No obvious connection
MUC2	chr11(hg19):g.1093610C > G	1.0	0.3	NM_002457.31:c.5429C > G	p.Thr1810Ser	No obvious connection
	chr11(hg19):g.1093612C > A	1.0	0.4	NM_002457.31:c.5431C > A	p.Pro1811Thr	
CPA4	chr7(hg19):g.129950740G > T	0.93	0.3	NM_016352.9:c.907G > T	p.Gly303Cys	No obvious connection
ARMCX4	chr2x(hg19):g.100749038C > T	0.87	0.3	NM_001256155.2:c.5462C > T	p.Ala1821Val	Unknown
TBC1D3K	chr17(hg19):g.36339584G > T	1.0	0.6	NM_001291464.13:c.1073C > A	p.Pro358Gln	Unknown
EFCAB13	chr17(hg19):g.45451894G > A	1.0	0.6	NM_152347.12:c.934G > A	p.Val312Ile	Unknown
RFPL4AL1	chr19(hg19):g.56284507T > G	1.0	0.6	NM_001277397.2:c.826T > G	p.Ser276Ala	Unknown
	chr19(hg19):g.56284511C > G	1.0	60.	NM_001277397.2:c.830C > G:	p.Thr277Ser	
	chr19(hg19):g.56284529C > A	1.0	0.6	NM_001277397.2:c.848C > A	p.Ser283Tyr	
	chr19(hg19):g.56284535A > G	1.0	0.6	NM_001277397.2:c.854A > G	p.Glu285Gly	
KRTAP10–6	chr21(hg19):g.46011468G > A	1.0	0.6	NM_198688.1:c.898C > T	p.Pro300Ser	Unknown

RE, Rasmussen's encephalitis; TLE, temporal lobe epilepsy; cDNA, complementary DNA.

HLA-DQA1, HLA-DQB1, and HLA-DRB5 belong to HLA class II. More than 11 SNVs were found in the *HLA-DQB1* gene, while one SNV was found in the *HLA-DQA1* and *HLA-DRB5* genes. One SNV was found in *CD1A*. In addition, there was one SNV in *TRIM41* gene in RE.

Genes With Single Nucleotide Variants in Rasmussen's Encephalitis Are Related to Epilepsy, Schizophrenia and Nerve Cell Regeneration

Three genes related to epilepsy, schizophrenia and nerve cell regeneration were found in RE in this study. *ADGRV1* plays a role in epilepsy. *CMYA5* was reported to have a connection to schizophrenia. *TNR* is related to nerve cell regeneration.

One SNV was found in the *ADGRV1, CMYA5,* and *TNR* genes in RE cases.

DISCUSSION

The mechanisms of RE are complex. Viral infection was originally proposed to be the possible cause of RE (Walter and Renella, 1989; Farrell et al., 1991). Over the years, several studies have reported the detection of a number of viruses, including enteroviruses, EBV, human HCMV, human papillomavirus and herpes simplex virus (HSV), in the brains of RE patients (Pardo et al., 2014). Furthermore, in our previous research, antigens of various human herpesviruses (HHVs), including HCMV, EBV and HHV6, were detected in RE brain tissues with positive rates ranging from 50 to 88.5% (Zhang et al., 2017; Liu et al., 2018). In addition, it was found that the interferon-induced transmembrane protein-3 (IFITM3) polymorphism rs12252-C is associated with the high detection rate of HCMV and rapid disease progression in RE patients with the IFITM3 rs12252-CC genotype. This result indicates that IFITM3 rs12252-C is related to the disease progression of RE patients by promoting persistent HCMV infection in brain tissue (Wang et al., 2021).

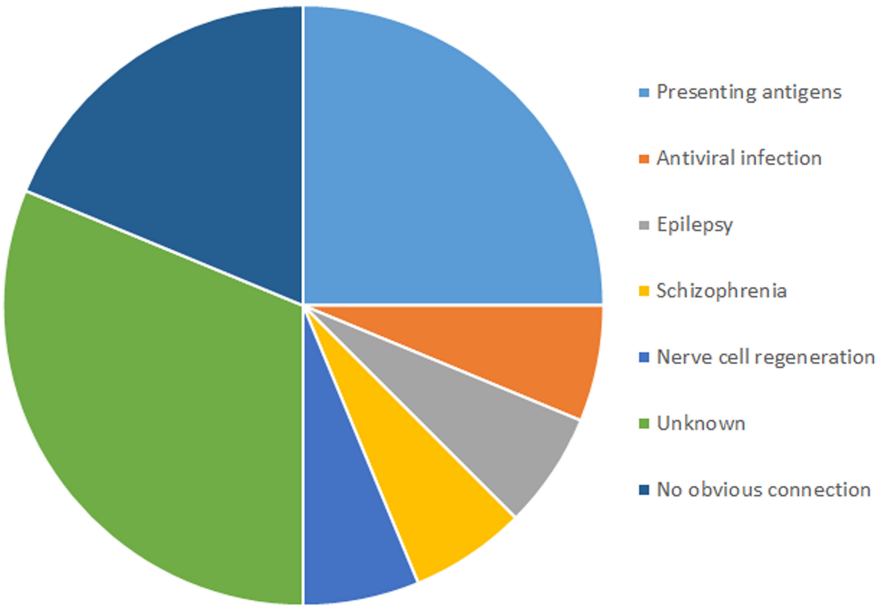

FIGURE 3 | Functions and numbers of genes carried SNVs associated with RE.

Drug-resistant epilepsy is one of the most important clinical features of RE (Bien et al., 2002; Pradeep et al., 2016). TLE is a common and frequently intractable seizure disorder. Both RE and TLE have complex pathogenesis and show similar syndromes. Thus, TLE was used as the control group in this study. Studies have shown that adaptive and innate immunity play an important role in the mechanisms of RE (Varadkar et al., 2014; Schneider-Hohendorf et al., 2016). However, the triggering factor of these immune responses remains unknown. In this study, WES was used to explore the genetic factors of RE. The results showed that SNVs related to antigen presentation and antiviral infection were found in RE cases. However, none of them were found in TLE cases. This suggested that unlike TLE patients, RE patients might have congenital abnormalities in adaptive immunity. Therefore, we speculated that the triggering factors of the adaptive immune response in brain tissue in RE cases may be SNVs related to antigen presentation and antiviral infection when facing the challenge of viral infection.

In addition to adaptive immune-related genes, SNVs were also found in genes involved in epilepsy, schizophrenia and nerve cell regeneration in RE brain tissue but not in TLE tissues. This result suggested that SNVs in genes with the function of epilepsy, schizophrenia and nerve cell regeneration may be responsible for neurological symptoms in RE cases. Although RE and TLE have similar clinical manifestations, the prognosis of them after surgical treatment is completely different. The outcome for most patients with TLE is good. However, the prognosis of RE is not satisfactory and is accompanied by progressive neurological dysfunction. Based on the results of this study, we speculate that it may be due to mutations in genes related to nerve cell regeneration in patients with RE, which inhibited the recovery of nervous system function. Simultaneously, due to mutations in genes related to antigen presentation and antiviral infection, the patient's adaptive immune function is dysregulated, and the antiviral effect is weakened, which in turn leads to aggravation of neurological diseases.

RE mainly affects children and is a pediatric epileptic syndrome in this population. Genetic factors and neurodevelopmental abnormalities were reported to be associated with age-specific epileptic syndromes, such as infantile spasms (IS). According to reports, approximately 7∼8% of infants with IS with unknown etiology have abnormal copy number variation (Osborne et al., 2010; Mefford et al., 2011). However, studies about the role of genetic factors in RE are lacking.

In this study, genetic factors of RE were explored. SNVs were found in genes with the functions of antigen presentation, antiviral infection, epilepsy, schizophrenia and nerve cell regeneration. We speculated that congenital abnormalities in adaptive immunity in RE would be the basis of neuron lesions, causing neurologic symptoms such as progressive neurological and cognitive deterioration and unihemispheric brain atrophy. Furthermore, SNVs in genes with functions in epilepsy, schizophrenia and nerve cell regeneration in RE cases may increase the degree of epilepsy.

In summary, genetic factors of RE were found in this study. We speculated that the triggering factors of the adaptive immune response against brain tissue in RE cases may be SNVs related to antigen presentation and antiviral infection when facing the challenge of viral infection. Congenital abnormalities in adaptive immunity increase neuropathy damage. Our results not only contribute to further understanding of the complex pathogenesis

of RE but also help further elucidate the etiology of the disease. In the future, a large number of RE samples and *in vitro* experiments are needed to verify the roles of these SNPs in the pathogenesis of RE.

DATA AVAILABILITY STATEMENT

The datasets presented in this study can be found in online repositories. The names of the repository/repositories and accession number(s) can be found below: NCBI SRA BioProject, accession no: PRJNA761444.

ETHICS STATEMENT

The studies involving human participants were reviewed and approved by the Ethics Committee of Sanbo Brain Hospital, Capital Medical University. Written informed consent to participate in this study was provided by the participants' legal guardian/next of kin.

AUTHOR CONTRIBUTIONS

JAi analyzed the data and wrote the manuscript. YW and DL collected data of the patients. DF contributed reagents and materials. TL and QW participated in analysis and discussion of the results. GL, PW, and JAn conceived and designed the experiments and the revision of the manuscript. All authors read and approve the final manuscript.

FUNDING

This work was supported by the National Natural Science Foundation of China (81972979 and U1902210) and the Support Project of High-level Teachers in Beijing Municipal Universities in the Period of 13th Five-year Plan (IDHT20190510).

REFERENCES

Andermann, F., and Farrell, K. (2006). Early onset Rasmussen's syndrome: a malignant, often bilateral form of the disorder. *Epilepsy Res.* 70(Suppl. 1), S259–S262. doi: 10.1016/j.eplepsyres.2006.02.011

Atkins, M. R., Terrell, W., and Hulette, C. M. (1995). Rasmussen's syndrome: a study of potential viral etiology. *Clin. Neuropathol.* 14, 7–12.

Bien, C. G., Widman, G., Urbach, H., Sassen, R., Kuczaty, S., Wiestler, O. D., et al. (2002). The natural history of Rasmussen's encephalitis. *Brain* 125, 1751–1759. doi: 10.1093/brain/awf176

Bien, C. G., Granata, T., Antozzi, C., Cross, J. H., Dulac, O., Kurthen, M., et al. (2005). Pathogenesis, diagnosis and treatment of Rasmussen encephalitis: a European consensus statement. *Brain* 128, 454–471. doi: 10.1093/brain/awh415

Bien, C. G., Tiemeier, H., Sassen, R., Kuczaty, S., Urbach, H., von Lehe, M., et al. (2013). Rasmussen encephalitis: incidence and course under randomized therapy with tacrolimus or intravenous immunoglobulins. *Epilepsia* 54, 543–550. doi: 10.1111/epi.12042

Farrell, M. A., Cheng, L., Cornford, M. E., Grody, W. W., and Vinters, H. V. (1991). Cytomegalovirus and Rasmussen's encephalitis. *Lancet* 337, 1551–1552. doi: 10.1016/0140-6736(91)93249-9

Farrell, M. A., Droogan, O., Secor, D. L., Poukens, V., Quinn, B., and Vinters, H. V. (1995). Chronic encephalitis associated with epilepsy: immunohistochemical and ultrastructural studies. *Acta Neuropathol.* 89, 313–321. doi: 10.1007/BF00309624

Goyal, M., Cohen, M. L., Bangert, B. A., Robinson, S., and Singer, N. G. (2007). Rasmussen syndrome and CNS granulomatous disease with NOD2/CARD15 mutations. *Neurology* 69, 640–643. doi: 10.1212/01.wnl.0000267429.89675.03

Kossoff, E. H., Vining, E. P., Pillas, D. J., Pyzik, P. L., Avellino, A. M., Carson, B. S., et al. (2003). Hemispherectomy for intractable unihemispheric epilepsy etiology vs outcome. *Neurology* 61, 887–890. doi: 10.1212/01.wnl.0000090107.04681.5b

Li, H., and Durbin, R. (2009). Fast and accurate short read alignment with Burrows-Wheeler transform. *Bioinformatics* 25, 1754–1760. doi: 10.1093/bioinformatics/btp324

Liu, D., Wang, X., Wang, Y., Wang, P., Fan, D., Chen, S., et al. (2018). Detection of EBV and HHV6 in the brain tissue of patients with Rasmussen's Encephalitis. *Virol. Sin.* 33, 402–409. doi: 10.1007/s12250-018-0063-9

McKenna, A., Hanna, M., Banks, E., Sivachenko, A., Cibulskis, K., Kernytsky, A., et al. (2010). The genome analysis toolkit: a mapreduce framework for analyzing next-generation DNA sequencing data. *Genome Res.* 20, 1297–1303. doi: 10.1101/gr.107524.110

Mefford, H. C., Yendle, S. C., Hsu, C., Cook, J., Geraghty, E., McMahon, J. M., et al. (2011). Rare copy number variants are an important cause of epileptic encephalopathies. *Ann. Neurol.* 70, 974–985. doi: 10.1002/ana.22645

Ohmori, I., Ouchida, M., Kobayashi, K., Jitsumori, Y., Inoue, T., Shimizu, K., et al. (2008). Rasmussen encephalitis associated with SCN 1 A mutation. *Epilepsia* 49, 521–526. doi: 10.1111/j.1528-1167.2007.01411.x

Osborne, J. P., Lux, A. L., Edwards, S. W., Hancock, E., Johnson, A. L., Kennedy, C. R., et al. (2010). The underlying etiology of infantile spasms (West syndrome): information from the United Kingdom Infantile Spasms Study (UKISS) on contemporary causes and their classification. *Epilepsia* 51, 2168–2174. doi: 10.1111/j.1528-1167.2010.02695.x

Pardo, C. A., Nabbout, R., and Galanopoulou, A. S. (2014). Mechanisms of epileptogenesis in pediatric epileptic syndromes: Rasmussen encephalitis, infantile spasms, and febrile infection-related epilepsy syndrome (FIRES). *Neurotherapeutics* 11, 297–310. doi: 10.1007/s13311-014-0265-2

Pardo, C. A., Vining, E. P., Guo, L., Skolasky, R. L., Carson, B. S., and Freeman, J. M. (2004). The pathology of Rasmussen syndrome: stages of cortical involvement and neuropathological studies in 45 hemispherectomies. *Epilepsia* 45, 516–526. doi: 10.1111/j.0013-9580.2004.33103.x

Pradeep, K., Sinha, S., Mahadevan, A., Saini, J., Arivazhagan, A., Bharath, R. D., et al. (2016). Clinical, electrophysiological, imaging, pathological and therapeutic observations among 18 patients with Rasmussen's encephalitis. *J. Clin. Neurosci.* 25, 96–104. doi: 10.1016/j.jocn.2015.05.062

Rasmussen, T., Olszewski, J., and Lloydsmith, D. (1958). Focal seizures due to chronic localized encephalitis. *Neurology* 8, 435–445. doi: 10.1212/wnl.8.6.435

Schneider-Hohendorf, T., Mohan, H., Bien, C. G., Breuer, J., Becker, A., Gorlich, D., et al. (2016). CD8(+) T-cell pathogenicity in Rasmussen encephalitis elucidated by large-scale T-cell receptor sequencing. *Nat. Commun.* 7:11153. doi: 10.1038/ncomms11153

Takahashi, Y., Mogami, Y., Mine, J., Imai, K., Koide, Y., Matsuda, K., et al. (2013). Genetic variations of immunoregulatory genes associated with Rasmussen syndrome. *Epilepsy Res.* 107, 238–243. doi: 10.1016/j.eplepsyres.2013.09.004

Tellez-Zenteno, J. F., Hernandez-Ronquillo, L., and Moien-Afshari, F. (2012). Discontinuation of antiepileptic drugs after successful surgery: who and when? *Epileptic Disord.* 14, 363–370. doi: 10.1684/epd.2012.0538

Troscher, A. R., Wimmer, I., Quemada-Garrido, L., Kock, U., Gessl, D., Verberk, S. G. S., et al. (2019). Microglial nodules provide the environment for

pathogenic T cells in human encephalitis. *Acta Neuropathol.* 137, 619–635. doi: 10.1007/s00401-019-01958-5

Varadkar, S., Bien, C. G., Kruse, C. A., Jensen, F. E., Bauer, J., Pardo, C. A., et al. (2014). Rasmussen's encephalitis: clinical features, pathobiology, and treatment advances. *Lancet Neurol.* 13, 195–205. doi: 10.1016/S1474-4422(13)70260-6

Villani, F., Pincherle, A., Antozzi, C., Chiapparini, L., Granata, T., Michelucci, R., et al. (2006). Adult-onset Rasmussen's encephalitis: anatomical-electrographic-clinical features of 7 Italian cases. *Epilepsia* 47(Suppl. 5), 41–46. doi: 10.1111/j.1528-1167.2006.00876.x

Vinters, H. V., Wang, R., and Wiley, C. A. (1993). Herpesviruses in chronic encephalitis associated with intractable childhood epilepsy. *Hum. Pathol.* 24, 871–879. doi: 10.1016/0046-8177(93)90137-6

Walter, G. F., and Renella, R. R. (1989). Epstein-Barr virus in brain and Rasmussen's encephalitis. *Lancet* 1, 279–280. doi: 10.1016/s0140-6736(89)91292-0

Wang, Y. S., Luo, Q. L., Guan, Y. G., Fan, D. Y., Luan, G. M., and Jing, A. (2021). HCMV infection and IFITM3 rs12252 are associated with Rasmussen's encephalitis disease progression. *Ann. Clin. Transl. Neurol.* 8, 558–570.

Zhang, Y., Wang, Y., Chen, S., Chen, S., Guan, Y., Liu, C., et al. (2017). Expression of human cytomegalovirus components in the brain tissues of patients with Rasmussen's encephalitis. *Virol. Sin.* 32, 115–121.

Conflict of Interest: The authors declare that the research was conducted in the absence of any commercial or financial relationships that could be construed as a potential conflict of interest.

Publisher's Note: All claims expressed in this article are solely those of the authors and do not necessarily represent those of their affiliated organizations, or those of the publisher, the editors and the reviewers. Any product that may be evaluated in this article, or claim that may be made by its manufacturer, is not guaranteed or endorsed by the publisher.

frontiers in Human Neuroscience

ORIGINAL RESEARCH
published: 26 November 2021
doi: 10.3389/fnhum.2021.739917

Neurometabolite Changes in Hyperthyroid Patients Before and After Antithyroid Treatment: An *in vivo* ^{1}H MRS Study

*Mukesh Kumar[1], Sadhana Singh[1,2], Poonam Rana[1], Pawan Kumar[1], Tarun Sekhri[3], Ratnesh Kanwar[3], Maria D'Souza[1] and Subash Khushu[1,2]**

[1] NMR Research Center, Institute of Nuclear Medicine and Allied Sciences (INMAS), New Delhi, India, [2] Centre for Ayurveda Biology and Holistic Nutrition (CABHN), The University of Trans-Disciplinary Health Sciences and Technology, Bengaluru, India, [3] Thyroid Research Center, Institute of Nuclear Medicine and Allied Sciences (INMAS), New Delhi, India

Purpose: Patients with hyperthyroidism have frequent neuropsychiatric symptoms such as lack of attention, concentration, poor memory, impaired executive functions, depression, and anxiety. These neurocognitive impairments such as memory, attention, and executive functions appear to be associated with dysfunction in brain regions. This study was conducted to investigate the metabolic changes in the brain subcortical regions, i.e., posterior parietal cortex and dorsolateral prefrontal cortex (DLPFC), in patients with hyperthyroidism before and after antithyroid treatment using proton magnetic resonance spectroscopy (^{1}H MRS).

Materials and Methods: We collected neuropsychological and ^{1}H MRS data from posterior parietal cortex and DLPFC, in both control (*N* = 30) and hyperthyroid (*N* = 30) patients. In addition, follow-up data were available for 19 patients treated with carbimazole for 30 weeks. The relative ratios of the neurometabolites were calculated using the Linear Combination Model (LCModel). Analysis of co-variance using Bonferroni correction was performed between healthy controls and hyperthyroid patients, and a paired *t*-test was applied in patients at baseline and follow-up. Spearman's rank-order correlation was used to analyze bivariate associations between thyroid hormone levels and metabolite ratios, and the partial correlation analysis was performed between neuropsychological scores and metabolite ratios, with age and sex as covariates, in the patients before and after treatment.

Results: Our results revealed a significant decrease in choline/creatine [glycerophosphocholine (GPC) + phosphocholine (PCh)/creatine (tCr)] in both the posterior parietal cortex and DLPFC in hyperthyroid patients, and these changes were reversible after antithyroid treatment. The posterior parietal cortex also showed significantly reduced glutamate/creatine (Glu/tCr), (glutamate + glutamine)/creatine (Glx/tCr), and increased glutathione/creatine (GSH/tCr) ratios in the hyperthyroid patients over control subjects. In DLPFC, only (*N*-acetyl aspartate + *N*-acetyl aspartyl-glutamate)/creatine (NAA + NAAG)/tCr was increased in the hyperthyroid patients.

OPEN ACCESS

Edited by:
Ahmad Raza Khan, Centre of Bio-Medical Research (CBMR), India

Reviewed by:
Maria Concepcion Garcia Otaduy, University of São Paulo, Brazil
Michael Albert Thomas, University of California, Los Angeles, United States

***Correspondence:**
Subash Khushu
skhushu@yahoo.com

Specialty section:
This article was submitted to Brain Imaging and Stimulation, a section of the journal Frontiers in Human Neuroscience

Received: *14 July 2021*
Accepted: *25 October 2021*
Published: *26 November 2021*

Citation:
Kumar M, Singh S, Rana P, Kumar P, Sekhri T, Kanwar R, D'Souza M and Khushu S (2021) Neurometabolite Changes in Hyperthyroid Patients Before and After Antithyroid Treatment: An in vivo ^{1}H MRS Study. Front. Hum. Neurosci. 15:739917. doi: 10.3389/fnhum.2021.739917

After antithyroid treatment, (GPC + PCh)/tCr increased, and Glx/tCr decreased in both brain regions in the patients at follow-up. Gln/tCr in the posterior parietal cortex was decreased in patients at follow-up. Interestingly, (GPC + PCh)/tCr in DLPFC showed a significantly inverse correlation with free tri-iodothyronine (fT3) in hyperthyroid patients at baseline, whereas NAA/tCr showed positive correlations with fT3 and free thyroxine (fT4) in hyperthyroid patients before and after antithyroid treatment, in the posterior parietal cortex. In DLPFC, only (NAA + NAAG)/tCr showed positive correlations with fT3 and fT4 in the patients before treatment.

Conclusion: The overall findings suggest that all the brain metabolite changes were not completely reversed in the hyperthyroid patients after antithyroid treatment, even after achieving euthyroidism.

Keywords: hyperthyroidism, magnetic resonance spectroscopy, neurometabolites, dorsolateral prefrontal cortex, posterior parietal cortex

INTRODUCTION

Thyroid hormones play an important role in the development and maturation of the brain and neuronal differentiation in humans (Zoeller and Rovet, 2004; Bernal, 2007). Dysfunction of these hormones may influence deficits in physiology, cognitive function, and emotional behavior (Bauer et al., 2008). Several studies have demonstrated that hyperthyroidism is commonly coupled with a range of neuropsychiatric symptoms, namely, nervousness, irritability, depression, anxiety, memory impairment, lack of concentration, and declined executive functions (Fahrenfort et al., 2000; Vogel et al., 2007; Yuan et al., 2019). The neurocognitive functions such as attention and concentration are associated with the cerebral cortex such as prefrontal and parietal cortices, which are highly sensitive to thyroid hormone concentration (Heuer, 2007). Although the effect of adult-onset hyperthyroidism on these brain regions is known, the underlying mechanism for the brain dysfunction and its reversibility remains unclear. We speculate that excess thyroid hormone not only influences brain function but may lead to metabolic abnormalities in the mature brain structures, namely, posterior parietal cortex and dorsolateral prefrontal cortex (DLPFC), critical for cognitive functions.

Magnetic-resonance-based imaging and spectroscopy have enormous potential for understanding structural, functional, and metabolic changes in various brain regions. Among non-invasive techniques, proton magnetic resonance spectroscopy (^{1}H MRS) provides an *in vivo* quantification of various neurochemicals/metabolites during pathological conditions in humans and animal models. Several studies have reported metabolic changes in different brain regions in hyperthyroid patients using ^{1}H MRS (Bhatara et al., 1998; Elberling et al., 2003; Danielsen et al., 2008). A previous ^{1}H MRS study demonstrated a decreased choline/creatine (Cho/Cr) ratio in the right prefrontal cortex in patients with hyperthyroidism (Bhatara et al., 1998). Elberling et al. (2003) have shown significantly reduced total choline and myoinositol (mI) in the acute phase of Graves' thyrotoxicosis compared with the healthy volunteers. Similarly, Danielsen et al. (2008) have reported significantly reduced *N*-acetyl aspartate (NAA), creatine (Cr), Cho, mI, and combined glutamate and glutamine (Glx) in both white matter (WM) and gray matter (GM) in parieto-occipital regions in patients with Graves' disease, and also found a reversal of Cho/Cr ratio in the patients at follow-up after the acute phase of the disease. However, there are limited studies that reveal the metabolic changes associated with hyperthyroidism in the posterior parietal cortex and DLPFC of the brain.

In this study, we aimed to examine the metabolic changes in the brain subcortical regions, i.e., posterior parietal cortex and DLPFC, in patients with hyperthyroidism before and after antithyroid treatment using ^{1}H MRS. Furthermore, the correlations of clinical indices, neuropsychological scores, and MRS data in the hyperthyroid patients were also carried out to understand the impact of clinical scores in these patients.

MATERIALS AND METHODS

Study Design

The hyperthyroid patients underwent thyroid hormone tests, neuropsychological assessments, and ^{1}H MRS scanning pre and post 30 weeks of carbimazole treatment (after achieving a euthyroid state). The dose of carbimazole for each patient was decided by the clinician according to the disease severity during the period of antithyroid treatment. A starting dose of carbimazole 0.5 mg/kg/day was given and patients were monitored every 6 weeks for free tri-iodothyronine (fT3), free thyroxine (fT4), and thyroid-stimulating hormone (TSH) levels. The dose was titrated to keep fT4 in the lower half of the normal range (12–22 pmol/l). After 30 weeks of antithyroid treatment, patients were ordered back to undergo comprehensive assessments to evaluate the therapeutic efficacy. The healthy control group underwent the same assessments one time only, at the beginning of the study.

Subjects

We recruited 30 healthy controls and 30 hyperthyroid patients for this study. Out of the original cohort of 30 patients, 19

TABLE 1 | Demographic, clinical and neuropsychological characteristics of all the subjects.

Characteristics	Controls (*N* = 30)	Hyperthyroid (*N* = 30)	Hyperthyroid (*n* = 19)		*p*- value	*p*- value
			Pre-therapy	Post-therapy		
Gender (Male/Female)	9/21	8/22			0.197	
Age (Years)	31.70 ± 8.24	34.28 ± 7.12			0.12	
Education (Years)	13.17 ± 3.30	12.37 ± 3.90			0.396	
BMI (Kg/m^2)	22.60 ± 3.39	22.51 ± 3.95	21.29 ± 2.79	22.58 ± 2.45	0.925	
TSH (μiU/ml)	2.41 ± 0.73	0.014 ± 0.017	0.010 ± 0.006	1.93 ± 1.75	0.000[a]	0.004[b]
fT4 (pmol/liter)	15.78 ± 4.93	44.28 ± 19.92	46.95 ± 19.88	16.44 ± 4.70	0.00[a]	0.000[b]
fT3 (pmol/liter)	5.83 ± 2.01	15.83 ± 6.63	17.56 ± 6.80	4.60 ± 1.98	0.000[a]	0.000[b]
Memory scale						
Long term episodic memory	5 ± 0	4.72 ± 0.65	4.74 ± 0.73	4.89 ± 0.32	0.10	0.47
Recent episodic memory	5 ± 0	4.93 ± 0.26	5.00 ± 0.00	4.95 ± 0.23	0.042[a]	0.12
Mental balance	4.48 ± 0.69	3.86 ± 1.33	3.84 ± 1.34	4.05 ± 1.31	0.05[a]	0.61
Working memory span (forward and backward)	4.72 ± 0.45	4.17 ± 1.20	4.16 ± 1.34	4.84 ± 0.69	0.029[a]	0.06
Delayed Recall	4.76 ± 0.44	4.55 ± 0.95	4.53 ± 0.96	4.68 ± 0.75	0.30	0.37
Immediate Recall	4.83 ± 0.38	4.62 ± 0.82	4.63 ± 0.76	4.84 ± 0.37	0.13	0.36
Immediate recall of semantically related word pairs	4.93 ± 0.26	4.59 ± 0.82	4.68 ± 0.75	4.95 ± 0.23	0.097	0.22
Immediate recall of arbitrarily related word pairs	4.69 ± 0.66	4.38 ± 1.05	4.00 ± 1.29	4.95 ± 0.23	0.16	0.02[b]
Visual retention	4.76 ± 0.44	4.21 ± 1.21	4.00 ± 1.29	4.95 ± 0.23	0.036[a]	0.009[b]
Recognition of objects	4.90 ± 0.31	4.17 ± 1.10	4.16 ± 1.21	4.74 ± 0.45	0.017[a]	0.04[b]
Performance Tests of intelligence						
Performance quotient	115.86 ± 20.02	104.34 ± 21.12	100.78 ± 17.23	121.21 ± 17.49	0.038[a]	0.001[b]
P/K × 100	133.92 ± 85.67	151.51 ± 104.69	171.54 ± 122.02	149.78 ± 67.70	0.528	0.36
Nahor-Benson Test	0.66 ± 1.01	1.71 ± 2.05	1.95 ± 2.07	0.53 ± 0.90	0.02[a]	0.002[b]
Bender Visual-Motor Gestal Test	1.31 ± 1.97	7.75 ± 8.61	8.84 ± 9.22	4.53 ± 3.64	0.004[a]	0.048[b]
MMSE	28.59 ± 1.68	26.62 ± 2.87	26.58 ± 2.76	27.11 ± 2.16	0.002[a]	0.44

Mean and standard deviation (SD) of demographic, thyroid hormone levels, neuropsychological tests scores. [a]Independent sample t-test between hyperthyroid and controls ($p < 0.05$);[b] Paired t-test between pre-therapy vs. post-therapy in 19 hyperthyroid patients ($p < 0.05$). BMI, body mass index; TSH, thyroid stimulating hormone; fT4, free thyroxine; fT3, free tri-iodothyronine; P/K, ratio of Pass-a-long and Koh's test; MMSE, Mini Mental State Examination.

were included in the follow-up study. Demographic, clinical, and neuropsychological data for all the subjects are summarized in **Table 1**. All the hyperthyroid patients were diagnosed with hyperthyroidism for the first time and were recruited from the Thyroid Research Centre of our Institute. All control subjects chosen for the study were recruited from the local community. Thyroid function tests [TSH, fT3, and fT4] were carried out in all the patients and control subjects.

The study was approved by the institutional research ethics committee, and informed consent was obtained for all the participants. Exclusion criteria for patients and controls were clinical evidence of stroke, head injury, cardiovascular diseases, history of smoking, alcohol or drug dependence, psychiatric disorders, or cognitive impairment.

Neuropsychological Data

The Mini Mental State Examination (Folstein et al., 1975) and the "Postgraduate Institute Battery of Brain Dysfunction (PGIBBD)" (Pershad and Verma, 1990) neuropsychological tests were performed in all the subjects. The memory scale, a part of PGIBBD, consists of a series of domain-specific cognitive function tests such as long-term episodic memory, recent episodic memory, mental balance, working memory span, delayed and immediate recall, immediate recall of semantically related word pairs, immediate recall of arbitrarily related word pairs, visual retention, and recognition of the objects (Pershad and Verma, 1990), were conducted for each subject. The higher raw score of each memory function test indicated better performance.

For executive function, Koh's block design (KBD) and pass-a-long test (PALT) tests were performed in both the controls and patients. The higher the raw scores of KBD and PALT, the better the performance of the individual. For visuospatial and motor functions, the Bender–Gestalt test (BGT) and Nahor–Benson test (NBT) were used. The higher raw dysfunction scores indicated poor performance.

The scoring of all neuropsychological data was done as per the procedure, which has been described in detail elsewhere (Pershad and Verma, 1990).

In vivo MRI/MRS Acquisition

We used 3T whole-body magnetic resonance (MR) system (Magnetom Skyra, Siemens, Germany) with a 20-channel head coil and a 45 mT/m actively shielded gradient system for brain studies. High-resolution T1-weighted images were collected using a Magnetization Prepared Rapid Acquisition Gradient-Echo (MPRAGE) pulse sequence [repetition time (TR) = 1,900 ms; echo time (TE) = 2.49 ms; matrix

size = 256 × 256; field of view (FOV) = 240 × 240 mm^2; slice thickness = 0.9 mm; and number of slices = 160]. Anatomical imaging was performed in all three orthogonal planes for the positioning of the MRS voxels. We collected T2-weighted multislice images [TR = 5,600 ms, TE = 100 ms, number of excitations (NEX) = 2, matrix size = 312 × 512, FOV = 220 mm, 25 slices, slice thickness = 4.0 mm, and distance factor = 1.2 mm] covering the entire brain, to rule out the presence of any focal brain lesions.

The MRS was acquired using the single volume point resolved spectroscopy sequence (PRESS) with acquisition parameters: TR/TE = 2,000/30 ms; spectral points = 1,024; spectral bandwidth = 1,200 Hz; and averages = 256). Water suppression was achieved with a chemically selective suppression (CHESS) pulse sequence. Automated global shimming was used to minimize the B_0 inhomogeneities and localized shimming was done to further minimize B_0 field variations over the voxel of interest. Water unsuppressed spectra with 10 averages were also acquired for reference purposes. The line width of spectra in all subjects was less than 0.156 ppm (20 Hz) at full-width at half maximum (FWHM). For the right posterior parietal cortex, a voxel of 12 × 12 × 12 mm^3 was placed in a sagittal slice and visually inspected on axial and coronal MR images. The visual cortex at the caudal pole of the brain and the somatosensory cortex just behind the central sulcus were used as anatomical boundaries for the voxel placement (**Figure 1A**). Similarly, a voxel of 12 × 12 × 12 mm^3 was placed in the right DLPFC, which was identified on the sagittal and coronal MR images (**Figure 1C**). For the right DLPFC, the superior frontal sulcus, the lateral fissure, and the genu of the corpus callosum were used as anatomical boundaries for the voxel placement. The position of the voxels was visually inspected and adjusted based on identifiable anatomical landmarks about standard brain atlases (Jackson and Duncan, 1996).

Magnetic Resonance Spectroscopy Data Analysis

The MRS raw data were processed using LCModel Version 6.3 for quantitative assessment of the brain metabolites (Provencher, 1993, 2001). To determine the detectability and quantitative reliability of each metabolite from the measured spectra, the % SD of each metabolite, defined as the Cramer–Rao lower bound (CRLB) criteria, was derived as a measurable index for quantitative reliability (Provencher, 1993). CRLB ≤ 20% was considered as an acceptable level of quantitative reliability. Metabolite ratios were used to reduce the variability in absolute values for different metabolites as observed in the subjects. We used total creatine (tCr) values as the internal reference for relative quantification due to its relatively stable concentration in the brain (Provencher, 2001).

Statistical Analysis

All the statistical analyses were conducted using SPSS (version 20.0, SPSS Inc., Chicago, IL, United States) statistical software. Demographic, clinical, and neuropsychological parameters were assessed by independent samples *t*-tests, and categorical characteristics were compared using the chi-squared test. Analysis of co-variance using Bonferroni correction was performed to compare different metabolite ratios between the two groups with age and sex as covariates. A paired *t*-test was used to compare metabolite ratios in the patients at baseline and the follow-up. MRS voxel GM, WM, and cerebrospinal fluid (CSF) were calculated using the Matlab script (Quadrelli et al., 2016).

Spearman's rank-order correlation was used to analyze bivariate associations between clinical indices (fT3, fT4, and TSH) and metabolite ratios, and the partial correlation analysis was performed between neuropsychological scores and metabolite ratios, with age and sex as covariates, in the healthy controls and patients before and after treatment. A p value ≤ 0.05 was considered to be statistically significant.

RESULTS

Demographic, Clinical, and Neuropsychological Variables

Demographic, clinical, and neuropsychological data of hyperthyroid patients and control subjects are summarized in **Table 1**. No significant differences in age (p = 0.120), sex (p = 0.197), education (p = 0.396), or BMI (p = 0.925) appeared between the groups. In hyperthyroid patients, suppressed TSH (≤0.01 μIU/ml), elevated fT3 (≥7 pmol/l) and fT4 (≥22 pmol/l) levels were observed. However, the thyroid hormones of the control subjects were within normal ranges (TSH = 0.27–4.2 μIU/ml, fT3 = 2.6–6.8 pmol/l, and fT4 = 12.0–22.0 pmol/l). After antithyroid treatment, a significant increase in TSH levels (1.93 ± 1.75 μIU/ml), and reduced fT3 (4.60 ± 1.98 pmol/l) and fT4 (16.44 ± 4.70 pmol/l) values, were found in the patients at follow-up.

Significantly decreased scores were observed in recent episodic memory, mental balance, working memory span, visual retention, recognition of objects, performance quotient, and increased scores in NBT and BGT, in hyperthyroid patients over healthy controls (**Table 1**). After antithyroid treatment, patients at follow-up showed improvement in working memory span, immediate recall of arbitrarily related word pairs, visual retention, recognition of objects, performance quotient, and NBT and BGT scores (**Table 1**).

Magnetic Resonance Spectroscopy Results

The quality of the spectra between the groups was not significantly different as judged by FWHM and signal-to-noise ratio (SNR). The FWHM and SNR of the healthy controls and hyperthyroid patients before and after treatment are summarized in **Table 2**. No significant differences for GM, WM, and CSF in voxel tissue components were found between healthy controls, hyperthyroid patients before and after thyroxine treatment in both the brain regions (**Table 2**). There was no significant difference in tCr concentration between healthy controls and hyperthyroid patients in the right posterior parietal cortex (p = 0.96) and right DLPFC (p = 0.39). In the posterior

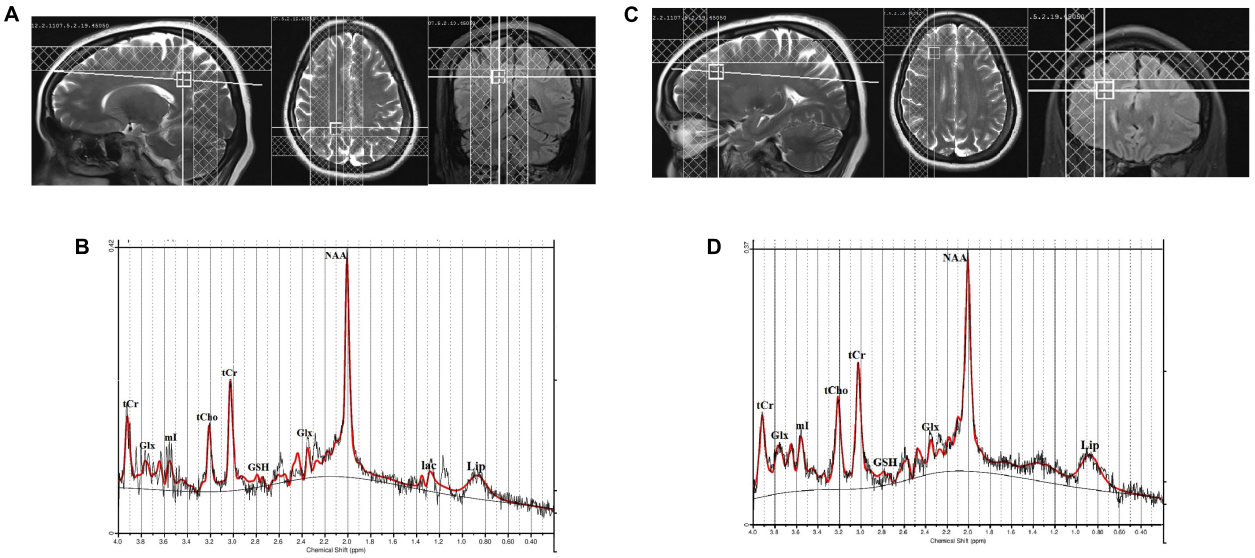

FIGURE 1 | (A) Location of 12 × 12 × 12 mm^3 voxel in the right posterior parietal cortex, **(B)** a representative spectrum analyzed by LCModel, **(C)** location of 12 × 12 × 12 mm^3 voxel in the right dorsolateral prefrontal cortex (DLPFC), and **(D)** a representative spectrum analyzed by LCModel.

parietal cortex, significantly decreased Glu/tCr (p = 0.001), [glycerophosphocholine (GPC) + phosphocholine (PCh)]/tCr (p = 0.004), and Glx/tCr (p = 0.011), and increased GSH/tCr (p = 0.035) metabolite ratios were found in hyperthyroid patients over healthy controls (**Table 2**). In addition, NAA/tCr (p = 0.075) showed an increasing trend in hyperthyroid patients compared to healthy controls, but it did not reach the level of statistical significance. In DLPFC, significantly reduced (GPC + PCh)/tCr (p = 0.005) and increased (NAA + NAAG)/tCr (p = 0.030) were observed in hyperthyroid patients compared to healthy controls (**Table 2**). The representative spectra acquired from the right posterior parietal cortex and right DLPFC regions of a control subject are shown in **Figures 1B,D**.

After treatment, (GPC + PCh)/tCr metabolite ratio reversal (p = 0.006 for right posterior parietal cortex; p = 0.001 for right DLPFC) in both the brain regions studies. Patients at follow-up showed significantly decreased Gln/tCr (p = 0.020), Glx/tCr (p = 0.035) in the posterior parietal cortex, and Glx/tCr (p = 0.037) in DLPFC. Also, GSH/tCr (p = 0.058) showed an increasing trend in the patients at follow-up (**Table 2**).

Correlation Analysis Among Thyroid Indices, Neuropsychological Scores, and Neurometabolites

After controlling for age and sex, hyperthyroid patients had positive correlations between (GPC + PCh)/tCr in the posterior parietal cortex and immediate recall of arbitrarily related word pairs (r = 0.584 and p = 0.002) (**Figure 2A**). In hyperthyroid patients, (GPC + PCh)/tCr in DLPFC positively correlated with delayed recall memory scores (r = 0.405 and p = 0.041) (**Figure 2B**), and negatively with Bender Visual-Motor Gestal test (r = −0.416 and p = 0.04) (**Figure 2C**) and Nahor–Benson test (r = −0.538 and p = 0.005) scores (**Figure 2D**).

Furthermore, in hyperthyroid patients at baseline, NAA/tCr in the posterior parietal cortex showed a significantly positive correlation with fT3 (r = 0.412 and p = 0.026) (**Figure 2E**) and fT4 (r = 0.400 and p = 0.031) (**Figure 2F**). GPC + PCh/tCr in DLPFC showed an inverse correlation with fT3 (r = −0.387 and p = 0.042) (**Figure 2G**), and positive correlations between (NAA + NAAG)/tCr and fT3 (r = 0.417 and p = 0.027) (**Figure 2H**) and fT4 (r = 0.389 and p = 0.045) (**Figure 2I**) in hyperthyroid patients at baseline. At follow-up, only NAA/tCr showed a significantly positive correlation with fT3 (r = 0.489 and p = 0.05) (**Figure 3A**) and fT4 (r = 0.603 and p = 0.01) (**Figure 3B**) in the posterior parietal cortex in patients after antithyroid treatment. In healthy controls, no significant correlations were observed among clinical parameters, neuropsychological scores and metabolite ratios.

DISCUSSION

This study investigated the metabolic changes in the posterior parietal cortex and DLPFC brain regions in hyperthyroid patients before and after antithyroid treatment using ^{1}H MRS. Our results showed significant changes in the major brain metabolites, mainly in the posterior parietal cortex region due to thyroid hormone dysfunction in hyperthyroid patients, which include (GPC + PCh) as a marker of cellular membrane turnover, Glu as a measure of glutamate metabolism, GSH as an oxidative stress marker and NAA as a neuronal cell marker (Fonnum, 1984).

It is known that thyroid hormones regulate the processes of terminal brain differentiation such as neurogenesis, neuronal migration, neuronal and glial cell differentiation, myelination, and synaptogenesis (Chan and Kilby, 2000; Bernal, 2007). Thyroid hormones mediate central nervous system effects primarily through interaction of the active hormone T3 with nuclear receptors and regulation of gene expression (Heuer, 2007;

TABLE 2 | Relative values of neuro-metabolites and spectral quality measures for the 30 controls, and 30 hyperthyroid and 19 hyperthyroid patients at baseline and at follow-up in posterior parietal cortex and dorsolateral prefrontal cortex (DLPFC).

(Metabolites) Posterior parietal cortex (PP)	Control (n = 30) (Mean ± SD)	Hyperthyroidism (n = 30) (Mean ± SD)	Hyperthyroidism (n = 19)		p-value	p-value	CRLB
			Pre-therapy (Mean ± SD)	Post-therapy (Mean ± SD)			
Gln/tCr	1.495 ± 0.33	1.354 ± 0.38	1.452 ± 0.399	1.107 ± 0.346	0.162	0.020[b]	≤20 %
Glu/tCr	1.156 ± 0.29	0.897 ± 0.21	0.940 ± 0.227	1.021 ± 0.177	0.001[a]	0.225	≤20 %
GSH/tCr	0.257 ± 0.05	0.287 ± 0.074	0.278 ± 0.071	0.333 ± 0.087	0.033[a]	0.058[b]	≤20 %
mI/tCr	1.439 ± 0.27	1.364 ± 0.32	1.334 ± 0.262	1.193 ± 0.467	0.303	0.149	≤11 %
NAA/tCr	1.431 ± 0.20	1.484 ± 0.20	1.480 ± 0.168	1.469 ± 0.202	0.077[a]	0.831	≤10 %
GPC+PCh/tCr	0.283 ± 0.04	0.249 ± 0.03	0.258 ± 0.043	0.302 ± 0.038	0.004[a]	0.006[b]	≤8 %
NAA+NAAG/tCr	1.652 ± 0.16	1.664 ± 0.17	1.700 ± 0.194	1.762 ± 0.195	0.441	0.111	≤5 %
Glu+Gln/tCr	2.585 ± 0.46	2.225 ± 0.45	2.356 ± 0.499	1.856 ± 0.477	0.011[a]	0.035[b]	≤12 %
Dorsolateral prefrontal cortex (DLPFC)							
Gln/tCr	1.259 ± 0.235	1.171 ± 0.355	1.377 ± 0.404	1.324 ± 0.340	0.174	0.610	≤20 %
Glu/tCr	0.930 ± 0.222	0.992 ± 0.251	0.985 ± 0.232	1.076 ± 0.198	0.124	0.155	≤20 %
GSH/tCr	0.312 ± 0.058	0.303 ± 0.082	0.300 ± 0.074	0.329 ± 0.086	0.580	0.323	≤20 %
mI/tCr	1.381 ± 0.260	1.311 ± 0.310	1.245 ± 0.249	1.211 ± 0.414	0.266	0.661	≤10 %
NAA/tCr	1.346 ± 0.220	1.305 ± 0.242	1.323 ± 0.213	1.329 ± 0.255	0.973	0.914	≤10 %
GPC+PCh/tCr	0.290 ± 0.047	0.249 ± 0.036	0.251 ± 0.033	0.309 ± 0.039	0.005[a]	0.001[b]	≤7 %
NAA+NAAG/tCr	1.519 ± 0.127	1.574 ± 0.176	1.553 ± 0.176	1.551 ± 0.187	0.028[a]	0.943	≤5 %
Glu+Gln/tCr	2.138 ± 0.302	2.118 ± 0.444	2.299 ± 0.447	2.006 ± 0.520	0.730	0.037[b]	≤14 %
Spectral Quality Measures							
Posterior parietal cortex (PP)							
FWHM (in ppm)	0.059 ± 0.02	0.062 ± 0.02	0.063 ± 0.025	0.057 ± 0.02	0.48	0.52	
SNR	12.13 ± 2.43	11.77 ± 1.19	12 ± 2.09	12.53 ± 2.48	0.52	0.36	
GM	0.376 ± 0.11	0.416 ± 0.14	0.438 ± 0.15	0.377 ± 0.13	0.21	0.20	
WM	0.598 ± 0.13	0.553 ± 0.17	0.531 ± 0.19	0.594 ± 0.15	0.21	0.25	
CSF	0.031 ± 0.05	0.031 ± 0.04	0.033 ± 0.04	0.030 ± 0.02	0.5	0.81	
DLPFC							
FWHM (in ppm)	0.064 ± 0.02	0.065 ± 0.026	0.059 ± 0.027	0.069 ± 0.02	0.96	0.183	
SNR	12.56 ± 1.95	12.41 ± 2.03	12.89 ± 2.07	11.79 ± 2.46	0.79	0.074	
GM	0.385 ± 0.12	0.416 ± 0.14	0.394 ± 0.16	0.371 ± 0.13	0.37	0.61	
WM	0.591 ± 0.13	0.553 ± 0.17	0.583 ± 0.20	0.595 ± 0.15	0.34	0.82	
CSF	0.024 ± 0.02	0.031 ± 0.04	0.024 ± 0.04	0.030 ± 0.02	0.42	0.55	

[a]*Indicates $p < 0.05$ (Bonferroni correction for multiple comparison between control and hyperthyroid patients);* [b]*indicates $p < 0.05$ (paired t-test in hyperthyroid patients at baseline and at follow-up). SD, standard deviation; CRLB, Cramer-Rao lower bound; FWHM, full width at half maximum; SNR, signal to noise ratio; GM, gray matter; WM, white matter; CSF, cerebrospinal fluid.*

Bauer et al., 2008). In adult humans, thyroid hormone deficiency or excess may lead to brain metabolism changes that cause clinical manifestations, namely, neurological and psychiatric symptoms (Joffe and Sokolov, 1994; Bernal, 2007), which are usually reversible with proper treatment. Our findings have shown the metabolic changes in total choline, combined peak of Glu and Gln, and NAA or (NAA + NAAG) in the posterior parietal cortex and DLPFC in hyperthyroid patients.

In the current study, hyperthyroid patients had significantly lower (GPC + PCh)/tCr in both the posterior parietal cortex and DLPFC, compared to healthy controls, which reversed in both brain regions after antithyroid treatment. Choline acts as a precursor for major components of cellular membrane phospholipids such as phosphatidylcholine and sphingomyelin, and it affects cholinergic neurotransmission *via* the synthesis of the neurotransmitter acetylcholine (Bekdash, 2016). Choline also has pivotal functions, namely, the maintenance of structural integrity of membranes and modulation of cholinergic neurotransmission, functions that are often dysregulated in some neurodegenerative disorders (Bekdash, 2016). Thus, the reduced (GPC + PCh)/tCr might be due to reduced cholinergic neurotransmission as mediated by acetylcholine. Several studies have suggested that choline may attenuate age-related memory decline or memory impairments that may be induced during adulthood (Klein, 2000; Bekdash, 2016). We also found a positive correlation between (GPC + PCh)/tCr and memory and motor functions in the brain regions of hyperthyroid patients. Our study is in support of a previous study that has shown that the Cho/Cr ratio decreases when patients have thyrotoxicosis and increases after treatment when the conditions of patients change

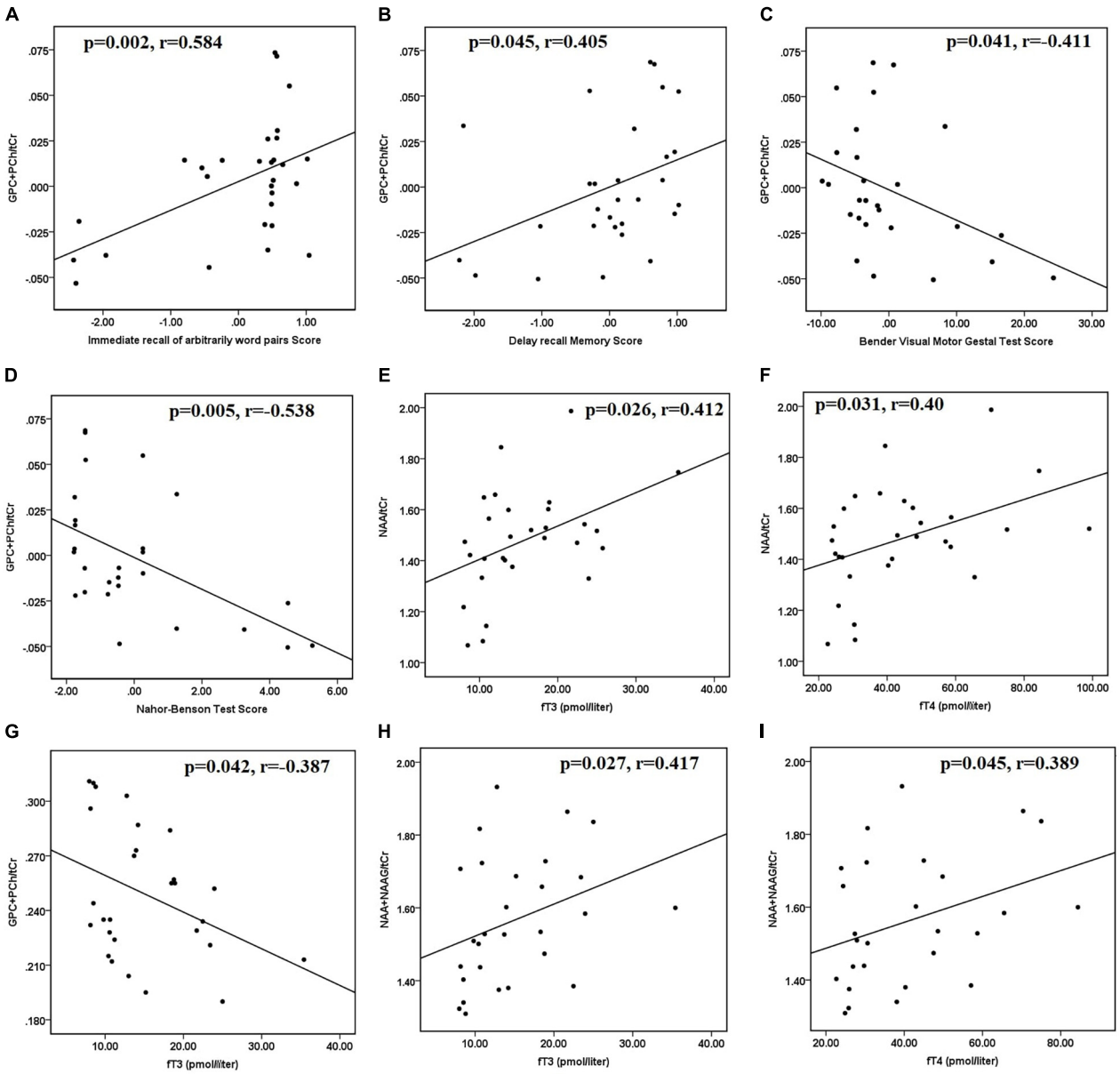

FIGURE 2 | Scatter plots showing significant correlations between clinical data, neuropsychological scores, and metabolite ratios in hyperthyroid patients at baseline. **(A)** Positive correlation between (GPC + PCh)/tCr in posterior parietal cortex and immediate recall of arbitrarily related word pairs scores, **(B)** positive correlation between (GPC + PCh)/tCr in DLPFC and delayed recall memory scores, negative correlations between **(C)** (GPC + PCh)/tCr in DLPFC and Bender Visual-Motor Gestal test scores, **(D)** (GPC + PCh)/tCr in DLPFC and Nahor–Benson test scores, in hyperthyroid patients at baseline. Positive correlations between **(E)** NAA/tCr in posterior parietal cortex and fT3 and **(F)** NAA/tCr in posterior parietal cortex and fT4. **(G)** Negative correlation between (GPC + PCh)/tCr in DLPFC and fT3, positive correlations between **(H)** (NAA + NAAG)/tCr in DLPFC and fT3, and **(I)** (NAA + NAAG)/tCr in DLPFC and fT4, in hyperthyroid patients at baseline. DLPFC, right dorsolateral prefrontal cortex; GPC, glycerophosphocholine; NAA, *N*-acetyl aspartate; NAAG, *N*-acetyl aspartyl-glutamate; PCh, phosphocholine; tCr, total creatine.

to euthyroidism (Bhatara et al., 1998). In addition, our study also showed a positive correlation of (GPC + PCh)/tCr in both the brain regions with certain memory and motor functions, and a negative correlation of (GPC + PCh)/tCr in DLPFC with fT3 in the hyperthyroid patients.

Our findings showed significantly reduced Glu/tCr and Glx/tCr ratios in the posterior parietal cortex in hyperthyroid patients compared to healthy controls. Glu is the principal excitatory neurotransmitter, whereas Gln is a precursor of Glu and GABA in the brain, and its metabolism depends on astrocytes (Fonnum, 1984; Erecinska and Silver, 1990). During neurotransmission, Glu is released from the presynaptic terminals and converted to Gln *via* the Gln synthetase, an astrocyte-specific enzyme, in astrocytes. The Gln travels back to the neuron, where it is reconverted to Glu by a phosphate-dependent glutaminase enzyme (Meldrum, 2000). Therefore, the

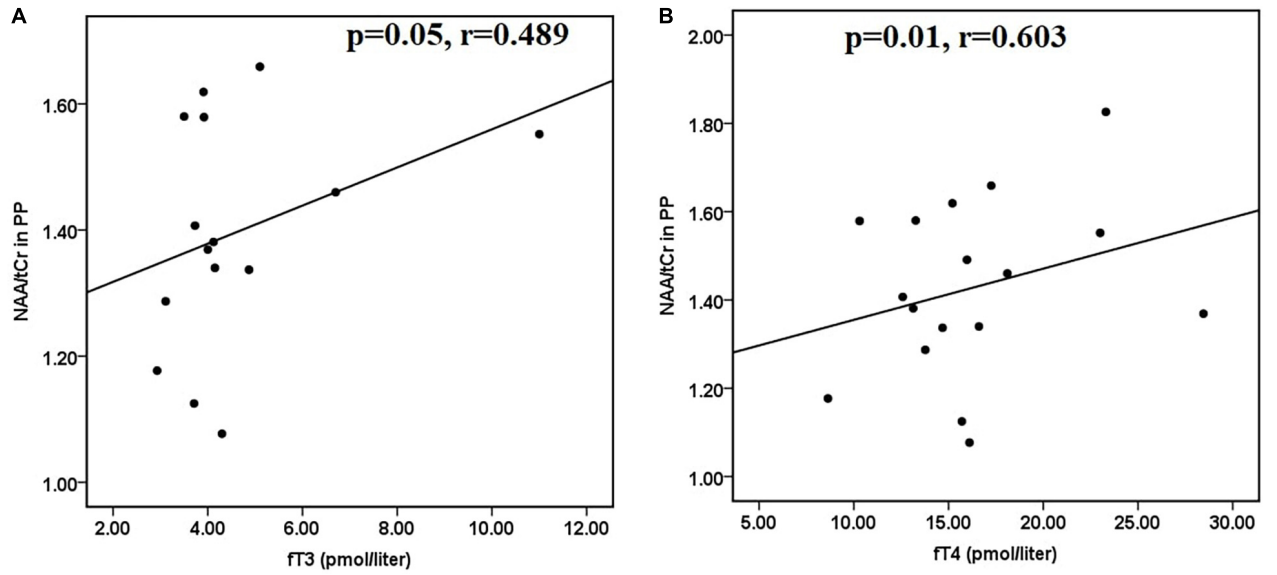

FIGURE 3 | Scatter plots showing significant positive correlations between **(A)** NAA/tCr in posterior parietal cortex and fT3 and **(B)** NAA/tCr in posterior parietal cortex and fT4, in hyperthyroid patients at follow-up. NAA, *N*-acetyl aspartate; tCr, total creatine.

decreased Glu/tCr, and Glx/tCr ratios as observed in our study might be due to abnormal Glu-Gln cycling or decreased Glu activity in hyperthyroid patients. After antithyroid treatment, a significantly decreased Glx/tCr ratio in both brain regions was found in the patients at follow-up. These results might indicate that the metabolite alterations persisted even after the patients returned to the euthyroid state following antithyroid treatment. A previous study has shown that reduced Glu and Gln in the parieto-occipital WM in patients with Graves' thyrotoxicosis persistently decreased even after antithyroid treatment (Danielsen et al., 2008). Different responses in terms of metabolite changes were observed in the two cortical regions studied, wherein metabolites associated with Glu metabolism were altered only in the posterior parietal cortex region, depicting compartmentalization of thyroid hormone influence on astrocytic Glu metabolism in the brain. However, the disparity in Glu metabolism in different regions is still a question of research.

In addition, there was a significant increase in (NAA + NAAG)/tCr in DLPFC in the hyperthyroid patients as compared with controls. In the posterior parietal cortex, an increasing trend was observed in NAA/tCr in hyperthyroid patients. After antithyroid treatment, both NAA/tCr in the posterior parietal cortex and (NAA + NAAG)/tCr in DLPFC decreased but were not statistically significant. NAA is an essential amino acid that is released from the breakdown of NAAG and is mainly synthesized in the mitochondria. NAA takes part in many processes, like regulation of protein synthesis, lipid production, and the metabolism of aspartate and NAAG in the brain. Increased NAA/tCr and NAA + NAAG/tCr may suggest impaired catabolism of NAA, as NAA is catabolized in astrocytes and oligodendrocytes, and may be affected by astrogliosis (Baslow, 2003; Aston et al., 2005). Besides cellular alterations, studies have reported higher NAA indicating oxidative stress (Surendran and Bhatnagar, 2011; Khan et al., 2018). We also found a positive correlation between NAA/tCr and fT3 and fT4 in the posterior parietal cortex in patients at baseline and follow-up, and positive correlations between (NAA + NAAG)/tCr and fT3 and fT4 in DLPFC in patients at baseline only.

In our study, we found an increased GSH/tCr ratio, an important antioxidant of the cells in the hyperthyroid patients, which further showed an increasing trend in the patients at follow-up. It is reported that elevated thyroid hormones levels (hyperthyroidism) induce oxidative stress (Villanueva et al., 2013). An increase in GSH could possibly reflect either an upregulation of local GSH production or downregulation in GSH breakdown to counterbalance increased oxidative stress (Duffy et al., 2014). An MRS study has shown that patients with mild cognitive impairment (MCI) had elevated GSH levels in the anterior and posterior cingulate, and the higher levels of anterior cingulate GSH were associated with poorer cognitive performance in MCI patients (Duffy et al., 2014). This increase in GSH level was explained as an early compensatory or neuroprotective response in MCI (Duffy et al., 2014).

In this study, reduced mI/tCr was also observed in both the brain regions in hyperthyroid patients, but it was not statistically significant. Although a previous study has shown a significantly reduced mI/tCr ratio in the parieto-occipital WM and frontal GM in the acute phase of Graves' thyrotoxicosis compared with healthy volunteers (Elberling et al., 2003). Another study reported that the mI/tCr ratio was increased in the parieto-occipital WM, occipital GM, and frontal GM in hyperthyroid patients after antithyroid treatment (Danielsen et al., 2008).

Our study has provided information on metabolic changes in hyperthyroidism. However, there are certain limitations to this study. Our sample size is small for the follow-up study.

Future studies with a large number of subjects may improve the robustness of data. Secondly, a follow-up study at different time points is necessary to see if the complete reversal of brain metabolites after antithyroid treatment in hyperthyroid patients is possible. This information may be valuable in the management and therapeutic planning of hyperthyroid patients in the future. Thirdly, we have not assessed depression and anxiety scores, which may affect metabolite levels in hyperthyroid patients.

CONCLUSION

Our study provides evidence that hyperthyroidism results in changes of key metabolites in the posterior parietal cortex and DLPFC, possibly indicating alterations in astrocyte physiology, glutamate/glutamine cycle, and/or oxidative stress in the adult human brain. In this study, altered neurometabolite ratios were found in the brain regions which showed reversible changes after antithyroid treatment in hyperthyroid patients. In addition, a few metabolites showed a significant correlation with thyroid indices (fT3 and fT4) and neuropsychological scores in the brain regions. The overall findings suggest that all the brain metabolites were not completely reversed in the hyperthyroid patients after antithyroid treatment, even after achieving euthyroidism. This finding has great relevance for the proper treatment and management of these patients.

DATA AVAILABILITY STATEMENT

The original contributions presented in the study are included in the article/supplementary material, further inquiries can be directed to the corresponding author/s.

ETHICS STATEMENT

The studies involving human participants were reviewed and approved by INMAS-Institutional Human Ethics Committee. The patients/participants provided their written informed consent to participate in this study.

AUTHOR CONTRIBUTIONS

MK contributed to study design, protocol design, data acquisition, neuropsychological assessment, data processing, and approved the first draft manuscript. SS wrote and submitted the final manuscript. PR and SK contributed to manuscript review and study design. PK contributed to data acquisition. MD'S contributed to patient's report preparation. RK contributed to recruitment and clinical assessment of thyroid patients. TS contributed to recruitment and clinical assessment of thyroid patients and study design. All authors contributed to the article and approved the submitted version.

FUNDING

This work was supported by the DRDO R&D Project No. INM 311 (4.1).

ACKNOWLEDGMENTS

MK is grateful to the National DBT-RA Program Biotechnology and Life Sciences (DBT) for providing Research Associate Fellowship.

REFERENCES

Aston, C., Jiang, L., and Sokolov, B. P. (2005). Transcriptional profiling reveals evidence for signaling and oligodendroglial abnormalities in the temporal cortex from patients with major depressive disorder. *Mol. Psychiatry* 10, 309–322. doi: 10.1038/sj.mp.4001565

Baslow, M. H. (2003). N-acetylaspartate in the vertebrate brain: metabolism and function. *Neurochem. Res.* 28, 941–953. doi: 10.1023/a:1023250721185

Bauer, M., Goetz, T., Glenn, T., and Whybrow, P. C. (2008). The thyroid-brain interaction in thyroid disorders and mood disorders. *J. Neuroendocrinol.* 20, 1101–1114. doi: 10.1111/j.1365-2826.2008.01774.x

Bekdash, R. A. (2016). Choline and the brain: an epigenetic perspective. *Adv. Neurobiol.* 12, 381–399. doi: 10.1007/978-3-319-28383-8_21

Bernal, J. (2007). Thyroid hormone receptors in brain development and function. *Nat. Clin. Pract. Endocrinol. Metab.* 3, 249–259. doi: 10.1038/ncpendmet0424

Bhatara, V. S., Tripathi, R. P., Sankar, R., Gupta, A., and Khushu, S. (1998). Frontal lobe proton magnetic-resonance spectroscopy in Graves' disease: a pilot study. *Psychoneuroendocrinology* 23, 605–612. doi: 10.1016/s0306-4530(98)00028-26

Chan, S., and Kilby, M. D. (2000). Thyroid hormone and central nervous system development. *J. Endocrinol.* 165, 1–8.

Danielsen, E. R., Elberling, T. V., Rasmussen, A. K., Dock, J., Hording, M., Perrild, H., et al. (2008). Reduced parietooccipital white matter glutamine measured by proton magnetic resonance spectroscopy in treated graves' disease patients. *J. Clin. Endocrinol. Metab.* 93, 3192–3198. doi: 10.1210/jc.2007-2161

Duffy, S. L., Lagopoulos, J., Hickie, I. B., Diamond, K., Graeber, M. B., Lewis, S. J., et al. (2014). Glutathione relates to neuropsychological functioning in mild cognitive impairment. *Alzheimers Dement.* 10, 67–75. doi: 10.1016/j.jalz.2013.01.005

Elberling, T. V., Danielsen, E. R., Rasmussen, A. K., Feldt-Rasmussen, U., Waldemar, G., and Thomsen, C. (2003). Reduced myo-inositol and total choline measured with cerebral MRS in acute thyrotoxic Graves' disease. *Neurology* 60, 142–145. doi: 10.1212/01.wnl.0000038911.07643.bf

Erecinska, M., and Silver, I. A. (1990). Metabolism and role of glutamate in mammalian brain. *Prog. Neurobiol.* 35, 245–296. doi: 10.1016/0301-0082(90)90013-90017

Fahrenfort, J. J., Wilterdink, A. M., and van der Veen, E. A. (2000). Long-term residual complaints and psychosocial sequelae after remission of hyperthyroidism. *Psychoneuroendocrinology* 25, 201–211. doi: 10.1016/s0306-4530(99)00050-55

Folstein, M. F., Folstein, S. E., and McHugh, P. R. (1975). Mini-mental state. a practical method for grading the cognitive state of patients for the clinician. *J. Psychiatr. Res.* 12, 189–198. doi: 10.1016/0022-3956(75)90026-90026

Fonnum, F. (1984). Glutamate: a neurotransmitter in mammalian brain. *J. Neurochem.* 42, 1–11. doi: 10.1111/j.1471-4159.1984.tb09689.x

Heuer, H. (2007). The importance of thyroid hormone transporters for brain development and function. *Best Pract. Res. Clin. Endocrinol. Metab.* 21, 265–276. doi: 10.1016/j.beem.2007.03.003

Jackson, G. D., and Duncan, J. S. (1996). *MRI Neuroanatomy: A New Angle on the Brain*. Newyork, NY: Churchill Livingstone.

Joffe, R. T., and Sokolov, S. T. (1994). Thyroid hormones, the brain, and affective disorders. *Crit. Rev. Neurobiol.* 8, 45–63.

Khan, A. R., Hansen, B., Wiborg, O., Kroenke, C. D., and Jespersen, S. N. (2018). Diffusion MRI and MR spectroscopy reveal microstructural and metabolic

brain alterations in chronic mild stress exposed rats: a CMS recovery study. *Neuroimage* 167, 342–353. doi: 10.1016/j.neuroimage.2017.11.053

Klein, J. (2000). Membrane breakdown in acute and chronic neurodegeneration: focus on choline-containing phospholipids. *J. Neural. Transm.* 107, 1027–1063. doi: 10.1007/s007020070051

Meldrum, B. S. (2000). Glutamate as a neurotransmitter in the brain: review of physiology and pathology. *J. Nutr.* 130(4S Suppl.), 1007S–1015S. doi: 10.1093/jn/130.4.1007S

Pershad, D., and Verma, S. (1990). *Handbook of PGI Battery of Brain Dysfunction (PGI-BBD)*, 1st Edn. Agra: National Psychological Corporation.

Provencher, S. W. (1993). Estimation of metabolite concentrations from localized *in vivo* proton NMR spectra. *Magn. Reson. Med.* 30, 672–679. doi: 10.1002/mrm.1910300604

Provencher, S. W. (2001). Automatic quantitation of localized *in vivo* 1H spectra with LCModel. *NMR Biomed.* 14, 260–264. doi: 10.1002/nbm.698

Quadrelli, S., Mountford, C., and Ramadan, S. (2016). Hitchhiker's guide to voxel segmentation for partial volume correction of *in vivo* magnetic resonance spectroscopy. *Magn. Reson. Insights* 9, 1–8. doi: 10.4137/MRI.S32903

Surendran, S., and Bhatnagar, M. (2011). Upregulation of N-acetylaspartic acid induces oxidative stress to contribute in disease pathophysiology. *Int. J. Neurosci.* 121, 305–309. doi: 10.3109/00207454.2011.558225

Villanueva, I., Alva-Sanchez, C., and Pacheco-Rosado, J. (2013). The role of thyroid hormones as inductors of oxidative stress and neurodegeneration. *Oxid. Med. Cell Longev.* 2013:218145. doi: 10.1155/2013/218145

Vogel, A., Elberling, T. V., Hording, M., Dock, J., Rasmussen, A. K., Feldt-Rasmussen, U., et al. (2007). Affective symptoms and cognitive functions in the acute phase of Graves' thyrotoxicosis. *Psychoneuroendocrinology* 32, 36–43. doi: 10.1016/j.psyneuen.2006.09.012

Yuan, L., Zhang, Y., Luan, D., Xu, X., Yang, Q., Zhao, S., et al. (2019). Reversible affective symptoms and attention executive control network impairment following thyroid function normalization in hyperthyroidism. *Neuropsychiatr. Dis. Treat* 15, 3305–3312. doi: 10.2147/NDT.S227386

Zoeller, R. T., and Rovet, J. (2004). Timing of thyroid hormone action in the developing brain: clinical observations and experimental findings. *J. Neuroendocrinol.* 16, 809–818. doi: 10.1111/j.1365-2826.2004.01243.x

Conflict of Interest: The authors declare that the research was conducted in the absence of any commercial or financial relationships that could be construed as a potential conflict of interest.

Publisher's Note: All claims expressed in this article are solely those of the authors and do not necessarily represent those of their affiliated organizations, or those of the publisher, the editors and the reviewers. Any product that may be evaluated in this article, or claim that may be made by its manufacturer, is not guaranteed or endorsed by the publisher.

frontiers in Human Neuroscience

ORIGINAL RESEARCH
published: 10 December 2021
doi: 10.3389/fnhum.2021.774236

Reduced White Matter Integrity in Patients With End-Stage and Non-end-Stage Chronic Kidney Disease: A Tract-Based Spatial Statistics Study

Yuhan Jiang[1†], Qiuyi Gao[2†], Yangyingqiu Liu[1], Bingbing Gao[1], Yiwei Che[3], Liangjie Lin[4], Jian Jiang[1], Peipei Chang[1], Qingwei Song[1], Weiwei Wang[1], Nan Wang[2] and Yanwei Miao[1*]*

[1] Department of Radiology, The First Affiliated Hospital of Dalian Medical University, Dalian, China, [2] Department of Nephrology, The First Affiliated Hospital of Dalian Medical University, Dalian, China, [3] Department of Radiology, The Third People's Hospital of Dalian, Dalian, China, [4] Philips Healthcare China, Beijing, China

OPEN ACCESS

Edited by:
Ahmad Raza Khan,
Center of Bio-Medical Research (CBMR), India

Reviewed by:
Kourosh Sheibani,
Basir Eye Health Research Center, Iran
Mukesh Kumar,
All India Institute of Medical Sciences, India

***Correspondence:**
Nan Wang
pyran78@163.com
Yanwei Miao
ywmiao716@163.com

[†] These authors have contributed equally to this work

Specialty section:
This article was submitted to Brain Imaging and Stimulation, a section of the journal Frontiers in Human Neuroscience

Received: 16 September 2021
Accepted: 12 November 2021
Published: 10 December 2021

Citation:
Jiang Y, Gao Q, Liu Y, Gao B, Che Y, Lin L, Jiang J, Chang P, Song Q, Wang W, Wang N and Miao Y (2021) Reduced White Matter Integrity in Patients With End-Stage and Non-end-Stage Chronic Kidney Disease: A Tract-Based Spatial Statistics Study. Front. Hum. Neurosci. 15:774236. doi: 10.3389/fnhum.2021.774236

Background and Purpose: Reduced white matter (WM) integrity has been implicated in chronic kidney disease (CKD), especially in end-stage renal disease (ESRD). However, whether the differences in WM abnormalities exist in ESRD and non-end-stage CKD (NES-CKD) remains unclear. Hence, this study aimed to investigate the WM microstructural changes between the two stages using diffusion tensor imaging (DTI) and explore the related influencing factors.

Methods: Diffusion tensor imaging' images were prospectively acquired from 18 patients with ESRD, 22 patients with NES-CKD, and 19 healthy controls (HCs). Tract-based spatial statistics (TBSS) was performed to assess the voxel-wise differences in WM abnormalities among the three groups. The relationships between DTI parameters and biochemical data were also analyzed.

Results: Compared with NES-CKDs, FA value was significantly decreased, and AD value increased in ESRDs mainly in brain regions of bilateral anterior thalamic radiation (ATR), the genu and body of corpus callosum (CC), bilateral anterior corona radiata, superior corona radiata, and superior longitudinal fasciculus. Besides, extensive and symmetrical deep WM damages were observed in patients with ESRD, accompanied by increased MD and RD values. Multiple regression analysis revealed that uric acid and serum phosphorus level can be used as independent predictors of WM microstructural abnormalities in clusters with statistical differences in DTI parameters between ESRD and NES-CKD groups.

Conclusion: In the progression of CKD, patients with ESRD have more severe WM microstructural abnormalities than NES-CKDs, and this progressive deterioration may be related to uric acid and phosphate levels.

Keywords: tract-based spatial statistics, chronic kidney disease, end-stage renal disease, uric acid, phosphate

INTRODUCTION

Chronic kidney disease (CKD) is defined as decreased kidney function shown by an estimated glomerular filtration rate (eGFR) of less than 60 ml/min per 1.73 m^2 or the presence of albuminuria with at least 3-month duration (Zhang L. et al., 2012; Webster et al., 2017). End-stage renal disease (ESRD) occurs when CKD progresses to the eGFR of < 15 ml/min/1.73 m^2. Continuous renal replacement therapy is essential to maintain the health of patients with ESRD, and hemodialysis accounts for the largest proportion in China (Navva et al., 2015). About 10–40% of patients with CKD had impaired cognitive function (Sarnak et al., 2013) and gradually progresses with the decline of kidney function. Patients at stage 4 have almost two times the memory and attention deficits compared with stage 3 (Egbi et al., 2015). In addition, patients with ESRD treated with hemodialysis show a 26–60% prevalence of mild cognitive impairment. The neurocognitive decline is most likely to be related to brain structure damage, especially white matter (WM) abnormalities (Vogels et al., 2012). Many studies have shown that WM abnormalities may appear earlier than brain atrophy and are more sensitive to early marker (Bartzokis, 2011; Metzler-Baddeley et al., 2019). In addition, more severe CKD may lead to more severe WM damage, which is associated with cognitive impairment (Liu et al., 2020). Therefore, WM integrity may be a more suitable biomarker for brain changes in patients with CKD.

Diffusion tensor imaging (DTI), a non-invasive neuroimaging technique, measures the diffusion tensor of water molecules and provides a detailed assessment of fiber tracts, which has been widely applied in microstructural WM integrity assessment (Hagmann et al., 2006; Nucifora et al., 2007). Therefore, patients with CKD can apply DTI technology for regular follow-up to track the changes in WM microstructure and conduct a detailed assessment of cognitive-related microstructure impairment. Some other more advanced dMRI techniques, such as diffusion kurtosis imaging (DKI) (Fieremans et al., 2011), neurite orientation dispersion and density imaging (NODDI) (Zhang H. et al., 2012), and fixel-based analysis (FBA) (Raffelt et al., 2015), provide additional and richer indicators to detailed evaluate the microstructure characteristics of tissues.

Previous studies based on DTI have found that patients with ESRD have abnormal WM integrity in multiple regions of the brain (Kong et al., 2014; Zhang et al., 2015; Yin et al., 2018; Chou et al., 2019). However, studies on the changes in WM integrity of patients with non-end-stage CKD (NES-CDK) are still limited. So far, only one study by Liu et al. (Liu et al., 2020) revealed that adult patients with CKD at stage 4 have reduced integrity of WM tracts in the corpus callosum (CC), anterior thalamic radiation (ATR), inferior fronto-occipital fasciculus (IFOF), and inferior longitudinal fasciculus (ILF). To rule out the effects of long-term hemodialysis, their study only included patients with CKD at stages 3–4. In fact, a report of longitudinal WM alterations in patients with ESRD showed that the toxic effect of ESRD itself may be the major factor of poor WM integrity (Chou et al., 2019).

Although WM microstructural abnormality in patients with CKD has been suggested, no studies have yet reported the direct comparison of DTI parameters (fractional anisotropy [FA], mean diffusivity [MD], axial diffusivity [AD], and radial [RD] diffusivity) between patients with ESRD and NES-CKD using tract-based spatial statistics (TBSS) analysis, to the best of our knowledge. TBSS is an advanced hypothesis-free method for analyzing whole-brain WM fiber tracts, which has been widely used in studies of various neurological diseases (Smith et al., 2006; Chen et al., 2018; Lim et al., 2019; Mei et al., 2020; Yamada et al., 2020). Compared with voxel-based analysis (VBA) using statistical parametric mapping, TBSS improves the registration sensitivity and accuracy based on the diffusion data projected onto a single, averaged FA skeleton located at the center of major cerebral WM pathways. TBSS also overcomes the personal evaluation bias in methods based on regions of interest (Smith et al., 2006; Qi et al., 2013).

This study applies TBSS to examine the microstructural abnormalities of the whole-brain WM skeleton among participants with ESRD, NES-CDK, and healthy controls (HCs) to accurately explore the characterization of WM alterations during CKD progression. The DTI metrics used in this study include FA, MD, AD, and RD, which may provide an overall characterization of WM alterations in patients with CKD. We hypothesize that WM microstructural alterations existed differences in the patients with ESRD and NES-CKD. We also explored the relationships among these DTI parameters with the clinical and laboratory data, and also cognitive function in participants with ESRD.

MATERIALS AND METHODS

Participants

This study was approved by the Local Ethics Committee of the First Affiliated Hospital of Dalian Medical University. Informed consents were obtained from patients or legal guardians before the study. CKD diagnosis was confirmed by a nephrologist according to the kidney disease outcomes quality initiative (K/DOQI) classification, with < 15 and 15–59 ml/min/1.73 m^2 classified as ESRD and NES-CDK, respectively. Other inclusion criteria for patients with ESRD and NES-CDK were as follows: (1) maintenance hemodialysis (3–4 times per week) for at least 3 months and no dialysis, respectively; (2) age > 18 years; and (3) right-handedness. Exclusion criteria included the following: (1) had a history of traumatic brain injury, psychiatric diseases, or other neurological disorders (e.g., infarction); (2) recipient of renal transplant; and (3) contraindications for MRI examination (e.g., claustrophobia, pacemaker).

Abbreviations: AD, axial diffusivity; ATR, anterior thalamic radiation; CKD, chronic kidney disease; CST, corticospinal; ESRD, end-stage renal disease; FA, fractional anisotropy; FDR, false discovery rate; LDL, low-density lipoprotein; P, serum phosphorus; MD, mean diffusivity; MoCA, Montreal Cognitive Assessment; RD, radial diffusivity; TBSS, tract-based spatial statistics; NES-CKD, non-end-stage chronic kidney disease; Urea, serum urea; UA, uric acid.

Between April 2019 and May 2021, 45 patients diagnosed with CKD were prospectively recruited in this study. Patients with poor image quality (n = 3) and with claustrophobia (n = 2) were excluded. Therefore, 40 patients with CKD, including 18 patients with ESRD and 22 with NES-CKD at stages 1–4, were enrolled in the final analysis. Nineteen HCs (right-handedness) were recruited with similar age, sex, body mass index (BMI), and education level to the participants with CKD. The exclusion criteria for HCs were traumatic brain injury, mental disorder, and neurological disorders.

Neurocognitive Assessments

Among 40 patients with CKD, only 12 ESRD participants completed cognitive assessment [Beijing revised version Montreal Cognitive Assessment (MoCA)] before MR data acquisition. MoCA is a fast, comprehensive, deliberate, and sensitive neurocognitive assessment tool, which has previously been applied in the CKD population (Tiffin-Richards et al., 2014; Liu et al., 2020).

Clinical Data and Laboratory Tests

All patients with CKD underwent clinical data collection (course of disease, admission blood pressure) and several biochemical tests, including serum creatinine (Scr), creatinine (Cre), serum urea (Urea), uric acid (UA), cystatin C (Cys C), cholesterol (CHOL), homocysteine (HCY), low-density lipoprotein (LDH), high-density lipoprotein (HDL), triglyceride (TG), serum kalium (K), serum natrium (Na), serum calcium (Ca), serum phosphorus (P), and parathyroid hormone (PTH) levels before MR data acquisition. No biochemical test was performed on the participants in the HC group.

Diffusion Tensor Imaging

Diffusion Tensor Imaging Data Acquisition

Diffusion-weighted images were obtained with a 3.0T MRI scanner (Ingenia CX, Philips Healthcare, Best, Netherlands) equipped with a 32-channel phased-array head coil, using a single-shot echo-planar imaging (SS-EPI) sequence. The parameters were as follows: 64 non-collinear spatial directions at b value = 1,000 s/mm^2, one baseline image at b = 0 s/mm^2, TR/TE = 6,000 ms / 92 ms, voxel size = 2 mm × 2 mm × 2 mm, matrix size = 128 × 128, field of view = 256 mm × 256 mm, slice thickness = 2 mm, without a slice gap. A total of 68 axial slices were collected, covering the whole brain, and the duration of the DTI scan was 6 min and 46 s.

Diffusion Tensor Imaging Data Preprocessing

Diffusion tensor imaging data were processed using the Functional MRI of the Brain (FMRIB) Software Library (FSL) version 5.0.9[1] (Smith et al., 2004). Eddy current-induced distortions and motion artifacts were corrected by registering each diffusion-weighted image to the non-diffusion weighted volume (b0 image) using the affine alignment (Andersson and Sotiropoulos, 2016). All images were visually inspected before and after corrections. "Brain Extraction Tool (BET)" inside the FSL package was used to extract a brain mask from the eddy corrected image to remove the skull and non-brain tissue (Smith, 2002). Diffusion tensor at each voxel was fitted using the DTIFIT tool to generate FA, MD, and eigenvalue ($\lambda1$, $\lambda2$, $\lambda3$) maps. Axial (AD = $\lambda1$) and radial [RD = ($\lambda2 + \lambda3$)/2] diffusivity maps were then calculated from these eigenvalues.

[1] http://fsl.fmrib.ox.ac.uk/fsl/

Tract-Based Spatial Statistics Analysis

Voxel-wise statistical analysis of the FA maps was performed using the TBSS toolbox in FSL (Smith et al., 2004, 2006). All FA maps were spatially aligned to a 1 mm × 1 mm × 1 mm FMRIB58 FA standard space using a non-linear registration algorithm. The aligned FA maps were averaged to create a mean FA image and then skeletonized to generate a mean FA skeleton, which represents the center of all WM fiber tracts common to all participants. The FA threshold for the skeletonization was 0.20 to exclude gray matter and cerebrospinal fluid interference and also intersubject variability. Aligned FA maps for all subjects were then projected onto this skeleton. The same FA transformation was then also applied to MD, AD, and RD images for statistical analysis.

To estimate the voxel-wise FA, MD, AD, and RD differences among the three groups, individual skeleton images were inputted to the general linear model (GLM) analysis, adjusting for age, sex, years of education, and BMI as covariates. Non-parametric permutation-based testing was performed using randomize in FSL (Winkler et al., 2014). One-way analysis of covariance (ANOVA) was performed with one F-test for the overall group effect on diffusion parameters (FA, AD, RD, and MD) and six contrasts for the individual comparisons of voxel-wise diffusion parameters between the groups. Results are reported at the $p < 0.05$ level after 5,000 permutations using permutation-based non-parametric inference, with threshold-free cluster enhancement (TFCE) and family-wise error (FWE) rate correction for multiple comparisons (Smith and Nichols, 2009).

The FSL's cluster was used to identify statistically significant ($p < 0.05$) clusters followed by an atlas query to describe the localization of all the anatomical clusters using the John Hopkins University (JHU)—International Consortium of Brain Mapping DTI-81 WM labels and JHU white matter tractography atlas template. DTI parameters in each significant cluster were then extracted from the skeletonized TBSS image of each participant.

Statistical Analysis

Statistical analysis was carried out using IBM SPSS software, version 22.0. One-way ANOVA was used to compare the ages and BMI of the participants among the three groups. A Kruskal–Wallis test was used to compare the years of education. Data without normal distributions were analyzed using non-parametric tests. Categorical variable analyses were analyzed by chi-squared test. The clinical features between the ESRD and CKD groups were performed using the independent sample t-tests.

For normally distributed data, the partial correlation was used to assess the association between the extracted DTI parameters and clinical data, adjusting for the same covariates as above.

TABLE 1 | Demographic and clinical characteristics.

	ESRD (*n* = 18)	NES-CKD (*n* = 22)	HC (*n* = 19)	t/Z/F/χ2	*p*-value
Gender (M/F)	10 / 8	11 / 11	8 / 11	0.679	0.712
Age, years	57.28 ± 12.22	54.68 ± 13.62	56.05 ± 11.65	0.212	0.810
BMI, Kg/m^2	23.63 ± 2.78	25.57 ± 4.27	24.25 ± 2.42	1.799	0.175
Education, years, M (IQR)	13 (9.75, 15)	12 (9, 15)	12 (12, 15)	0.275	0.871
MoCA, M (IQR)	26 (25, 28)	–	23.5 (22, 24.25)	−2.894	**0.004***
Stage, *n* (%)	Stages 5, 18 (100)	Stages 1, 6 (27.27) Stages 2, 4 (18.18) Stages 3, 6 (27.27) Stages 4, 6 (27.27)	–		
Basic admissions					
Hypertension, *n* (%)	13 (72.2)	13 (59.1)	–	6.599	0.298
Diabetes Mellitus, *n* (%)	13 (72.2)	13 (59.1)	–	0.750	0.298
History of smoking, *n* (%)	4 (22.2)	7 (31.8)	–	0.457	0.377
History of drinking, *n* (%)	3 (16.7)	2 (22.0)	–	0.519	0.402
SBP, mmHg, M (IQR)	145 (130, 153.75)	130 (120, 140)	–	−1.468	0.155
DBP, mmHg, M (IQR)	80 (80, 80)	80 (76.25, 90)	–	−0.302	0.798
Biochemical parameters					
Glu, mmol/L, M (IQR)	4.58 (4.42, 5.54)	5.22 (4.76, 5.66)	–	−1.115	0.274
Cys C, mg/L, M (IQR)	7.15 (6.73, 7.81)	1.81 (1.16, 2.40)	–	−5.356	**0.000***
CHOL, mmol/L, M (IQR)	4.75 (4.38, 5.02)	5.2 (4.71, 6.08)	–	−1.713	0.089
TG, mmol/L, M (IQR)	1.48 (1.17, 1.91)	1.59 (1.14, 2.51)	–	−0.381	0.717
HDL, mmol/L	1.14 ± 0.28	1.05 ± 0.40	–	−0.856	0.397
LDL, mmol/L	2.62 ± 0.65	3.05 ± 0.81	–	1.785	0.082
Urea, mmol/L	24.67 ± 5.68	11.35 ± 6.22	–	−7.065	**0.000***
UA, μmol/L	403.33 ± 104.41	412.91 ± 120.26	–	0.266	0.792
K, mmol/L	4.95 ± 0.66	4.10 ± 0.53	–	−4.523	**0.000***
HCY, mmol/L, M (IQR)	23.41 (19.12, 27.47)	19.43 (13.25, 22.54)		−1.821	0.070
Cre, μmol/L, M (IQR)	1,008.5 (829.75, 1,121.5)	107.5 (79, 186.25)		−5.383	**0.000***
Na, mmol/L, M (IQR)	138 (136.25, 139)	141 (139.25, 141)		−3.520	**0.000***
Ca, mmol/L, M (IQR)	2.25 (2.21, 2.28)	2.22 (2.10, 2.26)		−1.415	0.163
P, mmol/L, M (IQR)	1.76 (1.29, 2.04)	1.28 (1.37)		−2.746	**0.005***
PTH, mmol/L, M (IQR)	191.75 (75.27, 478.18)	54.63 (32.33, 108.1)		−2.528	**0.011***

ESRD, end-stage renal disease; NES-CKD, non-end-stage chronic kidney disease; HC, health controls; n, number; BMI, body mass index; MoCA, Montreal Cognitive Assessment; SBP, systolic blood pressure; DBP, diastolic blood pressure; Glu, glucose; Cys C, cystatin C; CHOL, cholesterol; TG, triglyceride; HDL, high-density lipoprotein; LDH, low-density lipoprotein; Urea, serum urea; UA, uric acid; K, kalium; HCY, homocysteine; Cre, serum creatinine; Na, serum natrium; Ca, serum calcium; P, serum phosphorus; PTH, parathyroid hormone.

M, median; IQR, interquartile range; Values are presented as the mean ± standard deviation (SD), n (%), or M (IQR).

** and bold values indicates a statistical difference between groups, p < 0.05.*

Non-normally distributed data were analyzed using Spearman's correlation coefficient. Statistical significance was defined as two-tailed $p < 0.05$. Bonferroni's correction was applied for multiple testing.

RESULTS

Demographic and Clinical Characteristics

The demographic and clinical characteristics of the subjects from the ESRD, NES-CKD, and HC groups are presented in **Table 1**. There was no significant difference in gender, age, BMI, and years of education ($p > 0.05$). The ESRD group showed a significantly increased Cys C, Urea, Cre, K, Na, P, and PTH compared with the NES-CKD group ($p < 0.01$).

Tract-Based Spatial Statistics Results Between Groups

ANCOVA

An ANCOVA revealed a statistically significant effect for FA, MD, AD, and RD across ESRD, NES-CKD, and HC groups ($p < 0.05$, TFCE-corrected, **Supplementary Figure 1**).

ESRD vs. NES-CKD

We identified three independent clusters with statistically significant differences in FA and AD values and one independent cluster with a significant difference in MD and RD values between ESRD and NES-CKD groups. When compared to patients with NES-CKD, these clusters showed decreased FA or increased MD, AD, or RD in the ESRD group. Additionally, in these clusters, the

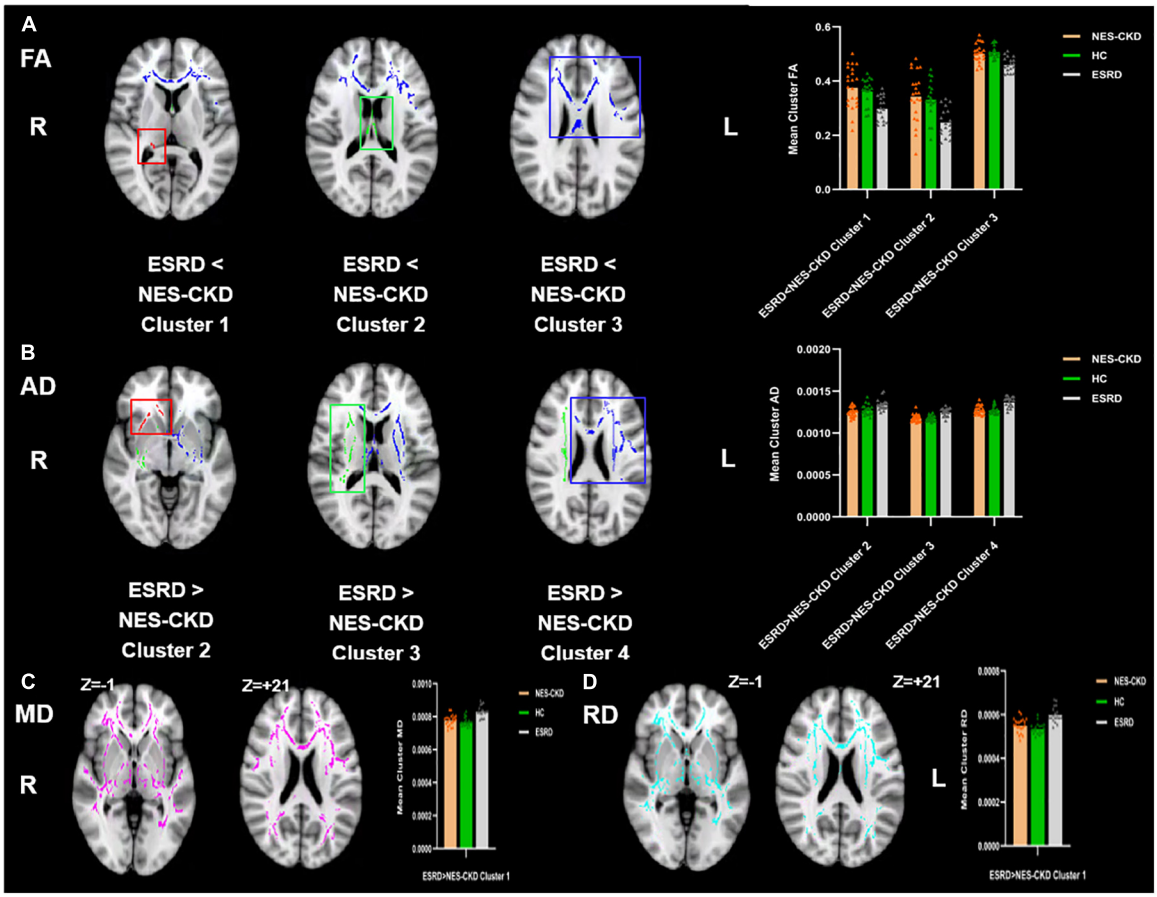

FIGURE 1 | Voxel clusters in which patients with ESRD exhibited decreased FA or increased AD, MD, or RD than NES-CKD. **(A)** Three independent clusters (red for Cluster 1; green for Cluster 2; blue for Cluster 3) with lower FA values in ESRD vs. NES-CKD. **(B)** Three independent clusters (red for Cluster 2; green for Cluster 3; blue for Cluster 4) with higher AD values in ESRD vs. NES-CKD. **(C)** One independent cluster (pink) with higher MD values in ESRD vs. NES-CKD. **(D)** One independent cluster (light blue) with higher RD values in ESRD vs. NES-CKD. The bar plots represent the corresponding mean diffusion metrics for each group. The triangle symbols indicate the data points of each participant in each group. ESRD, end-stage renal disease; NES-CKD, non-end-stage chronic kidney disease; HC, healthy control; FA, fractional anisotropy; MD, mean diffusivity; AD, axial diffusivity; RD, radial diffusivity.

average diffusion index values in the NES-CKD and HC groups were roughly similar (**Figure 1**).

Figure 2 showed the more detailed locations of *post hoc* analyses between ESRD and NES-CKD groups. We found significantly reduced FA values in the ESRD group compared to the NES-CKD group, mainly in bilateral ATR, the genu, and body of CC, bilateral anterior corona radiata (ACR), bilateral superior corona radiata, bilateral IFOF, and left superior longitudinal fasciculus (SLF) ($p < 0.05$, TFCE-corrected, **Table 2**). Besides, significantly increased AD values in patients with ESRD were confined to genu and body of CC, right ACR, bilateral ATR, right internal capsule, bilateral external capsule, bilateral corticospinal tract, bilateral corona radiata, left SLF, left IFOF, and left IFOF ($p < 0.05$, TFCE-corrected, **Table 3**). In addition, we observed extensive and symmetrical deep WM damage in patients with ESRD, accompanied by increased MD and RD values, including CC, bilateral corona radiata, bilateral ATR, bilateral IFOF, bilateral SLF, bilateral internal capsule, and bilateral external capsule (**Supplementary Tables 1**, **2**).

NES-CKD vs. HC

We identified two independent clusters with statistically significant differences in FA values between the NES-CKD and HC groups. When compared to HC patients, all of these clusters showed decreased FA in the NES-CKD group (**Figure 3**).

Figure 4 showed the detailed locations of *post hoc* analyses between NES-CKD and HC groups. We found lower FA and higher MD, AD, and RD values in patients with NES-CKD compared with HCs. FA decreased mainly in forceps major, middle cerebellar peduncle, right corticospinal tract, right SLF, left ATR, bilateral IFOF, left ACR, left anterior limb of the internal capsule, left posterior thalamic radiation, left external capsule, splenium of CC, and right posterior corona radiata. Refer to **Supplementary Table 3** for detailed information. Increased AD values are mainly located in the bilateral corona radiata, the body of CC, and bilateral corticospinal tracts (**Supplementary Table 4**). In addition, MD and RD values showed extensive and symmetrical increases in the deep WM. Detailed results were listed in **Supplementary Tables 5**, **6**.

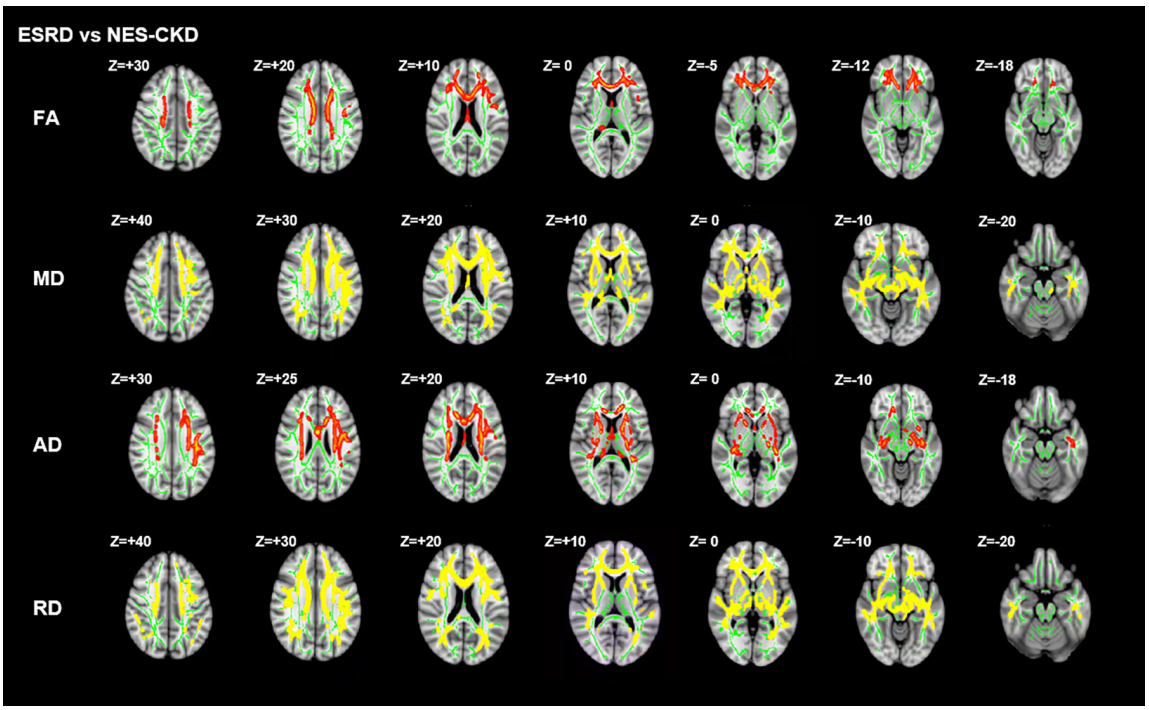

FIGURE 2 | *Post hoc* analyses result between patients with ESRD and NES-CKD. Green represents the mean FA skeleton of all subjects. Red–yellow represent regions with significant statistical values ($p < 0.05$, TFCE-corrected). ESRD, end-stage renal disease; NES-CKD, non-end-stage chronic kidney disease; FA, fractional anisotropy; MD, mean diffusivity; AD, axial diffusivity; RD, radial diffusivity.

TABLE 2 | Cluster sizes and locations for voxels with significantly reduced FA in ESRD vs. NES-CKD groups.

Cluster Number	JHU WM tractography atlas	JHU ICBM-DTI-81 WM labels	Voxel coordinates of Local maxima (MNI coordinates)			Voxels	Z-score	*p*-value
			X	Y	Z			
1	Anterior thalamic radiation R:4.38596	Fornix (cres) / Stria terminalis R:7.01754	18	−32	10	57	−1.69	0.046
2	Anterior thalamic radiation L:2.08997							
		Fornix (column and body of fornix):25.2595	1	−1	15	289	−1.80	0.036
	Anterior thalamic radiation R:3.62976							
3	Anterior thalamic radiation L:2.05252	Genu of CC:11.5581						
	Anterior thalamic radiation R:1.746	Body of CC:22.6704						
	Forceps minor:13.8569	Anterior corona radiata R:9.6662						
	Inferior fronto-occipital fasciculus L:2.35653	Anterior corona radiata L:11.7756	10	30	7	9,197	−3.10	0.001
	Inferior fronto-occipital fasciculus R:2.15581	Superior corona radiata R:3.84908						
	Superior longitudinal fasciculus L:1.18321	Superior corona radiata L:3.32717						
	Uncinate fasciculus L:1.42014	Superior longitudinal fasciculus L:1.90279						

MNI, Montreal Neurological Institute; L, abbreviation for the left hemisphere, R, abbreviation for the right hemisphere; JHU-WM tractography atlas, John Hopkins University white matter tractography atlas; JHU-ICBM-DTI-81 WM labels, John Hopkins University International Consortium of Brain Mapping DTI-81 WM labels; ESRD, end-stage renal disease; NES-CKD, non-end-stage chronic kidney disease; FA, fractional anisotropy.
The value after each region indicates the percentage probability of the cluster belonging to the given atlas label.
Any cluster with low voxels (<50) or region with low (<1%) probability has been excluded.

TABLE 3 | Cluster sizes and locations for voxels with significantly increased AD in ESRD vs. NES-CKD groups.

Cluster Number	JHU WM tractography atlas	JHU ICBM-DTI-81 WM labels	Voxel coordinates of Local maxima (MNI coordinates)			Voxels	Z-score	*p*-value
			X	Y	Z			
2	Forceps minor:15.1661	Genu of CC:28.9902	9	26	−5	307	−1.75	0.040
	Inferior fronto-occipital fasciculus R:15.5505	Anterior corona radiata R:19.544						
	Uncinate fasciculus R:8.3127	External capsule R:31.5961						
3	Anterior thalamic radiation R:5.10322	Anterior limb of internal capsule R:10.9053	25	−18	13	2,916	−2.41	0.008
	Corticospinal tract R:3.94753	Posterior limb of internal capsule R:7.13306						
	Inferior fronto-occipital fasciculus R:6.52092	Retrolenticular part of internal capsule R:10.3567						
		Anterior corona radiata R:11.2483						
		Superior corona radiata R:20.0274						
		Posterior corona radiata R:4.59534						
		Posterior thalamic radiation (include optic radiation) R:1.09739						
		External capsule R:10.8711						
4	Anterior thalamic radiation L:3.55331	Genu of CC:8.5528	−27	−30	16	7,822	−3.10	0.001
	Corticospinal tract L:2.61826	Body of CC:4.75582						
	Forceps minor:4.45513	Fornix (column and body of fornix):1.38072						
	Inferior fronto-occipital fasciculus L:3.18499	Anterior limb of internal capsule L:4.57683						
	Inferior longitudinal fasciculus L:1.10892	Posterior limb of internal capsule L:6.0854						
	Superior longitudinal fasciculus L:6.35093	Retrolenticular part of internal capsule L:3.15776						
	Superior longitudinal fasciculus (temporal part) L:2.93659	Anterior corona radiata L:6.28995						
		Superior corona radiata L:11.4804						
		External capsule L:8.09256						
		Superior longitudinal fasciculus L:7.60675						

MNI, Montreal Neurological Institute; L, abbreviation for the left hemisphere, R, abbreviation for the right hemisphere; JHU-WM tractography atlas, John Hopkins University white matter tractography atlas; JHU-ICBM-DTI-81 WM labels, John Hopkins University International Consortium of Brain Mapping DTI-81 WM labels; ESRD, end-stage renal disease; NES-CKD, non-end-stage chronic kidney disease; AD, axial diffusivity.
The value after each region indicates the percentage probability of the cluster belonging to the given atlas label.
Any cluster with low voxels (<50) or region with low (<1%) probability has been excluded.

Correlation Analysis

In the NES-CKD group, partial correlation analysis was conducted between the clusters (with statistically significant differences between the NES-CKD and HC groups) and biochemical tests, and we only found mean FA values in two independent clusters (Cluster 2 and Cluster 4) negatively correlated with TG ($r = -0.469$, $p = 0.049$) and LDL ($r = -0.476$, $p = 0.046$), respectively (**Figure 3**). Obviously, they did not survive Bonferroni's correction.

In the ESRD group, partial correlation analysis and multiple linear regression analysis revealed that UA level may serve as an independent predictor of mean FA changes in two clusters and mean AD changes in one cluster. Besides, LDL, P, and Urea levels may also be used as independent predictors of WM abnormalities in specific clusters with statistical differences in DTI parameters between ESRD and NES-CKD groups (**Table 4**). **Figure 5** showed the above-mentioned results of the partial correlation analysis. Detailed correlations were displayed in **Supplementary Figure 2**. We did not find any relationship between mean diffusion metrics clusters and MoCA ($p > 0.05$).

DISCUSSION

In this study, we applied the TBSS method to investigate the difference in WM microstructure changes between patients with ESRD and NES-CKD and also NES-CKD and HCs. The relationship between DTI parameters and biochemical tests was also explored. The main findings of this work were as follows: (1) compared with HCs, FA values reduced, and MD, AD, and RD values increased significantly in patients with NES-CKD and ESRD, indicating the microstructural damage in patients with both ESRD and NES-CKD; (2) In comparison with patients with NES-CKD, patients with ESRD also showed a significant decrease in FA values and an increase in MD, AD, and RD values, which suggests that patients with ESRD have more serious WM microstructure abnormalities; (3) DTI parameters in some clusters were significantly correlated with biochemical tests, such as UA, Urea, and P, showing that these indicators may induce the fragility of WM microstructure in patients with ESRD.

At present, the research on the WM microstructure changes of NES-CKD by TBSS is very minimal, and only one study involving

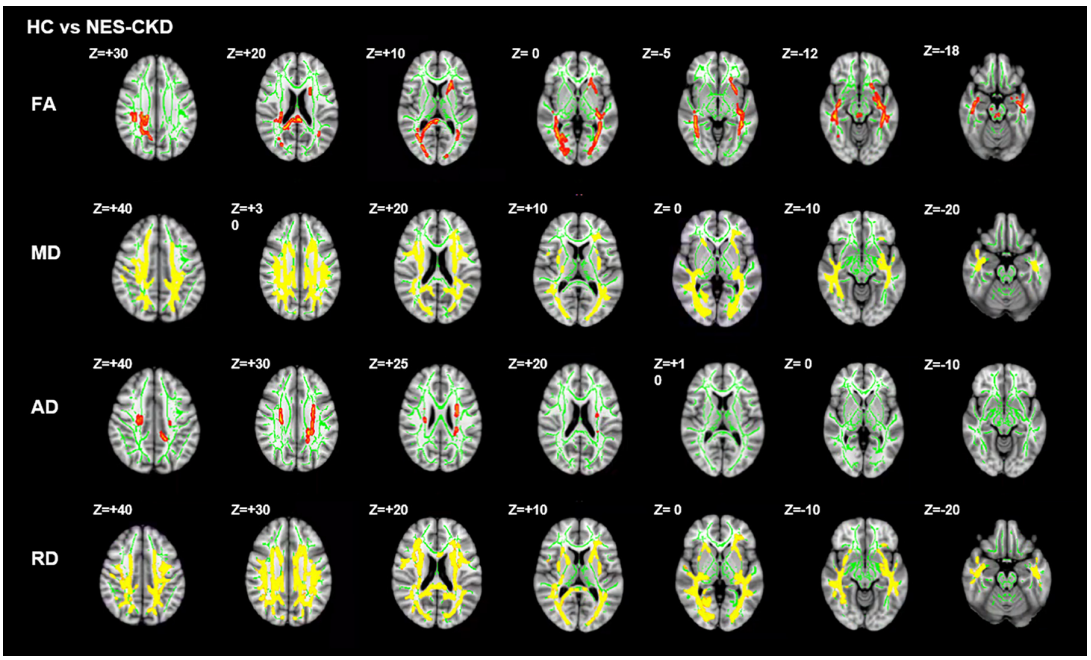

FIGURE 3 | *Post hoc* analyses result between patients with NES-CKD and HCs. Green represents the mean FA skeleton of all subjects. Red–yellow represent regions with significant statistical values ($p < 0.05$, TFCE-corrected). NES-CKD, non-end-stage chronic kidney disease; HC, healthy control; FA, fractional anisotropy; MD, mean diffusivity; AD, axial diffusivity; RD, radial diffusivity.

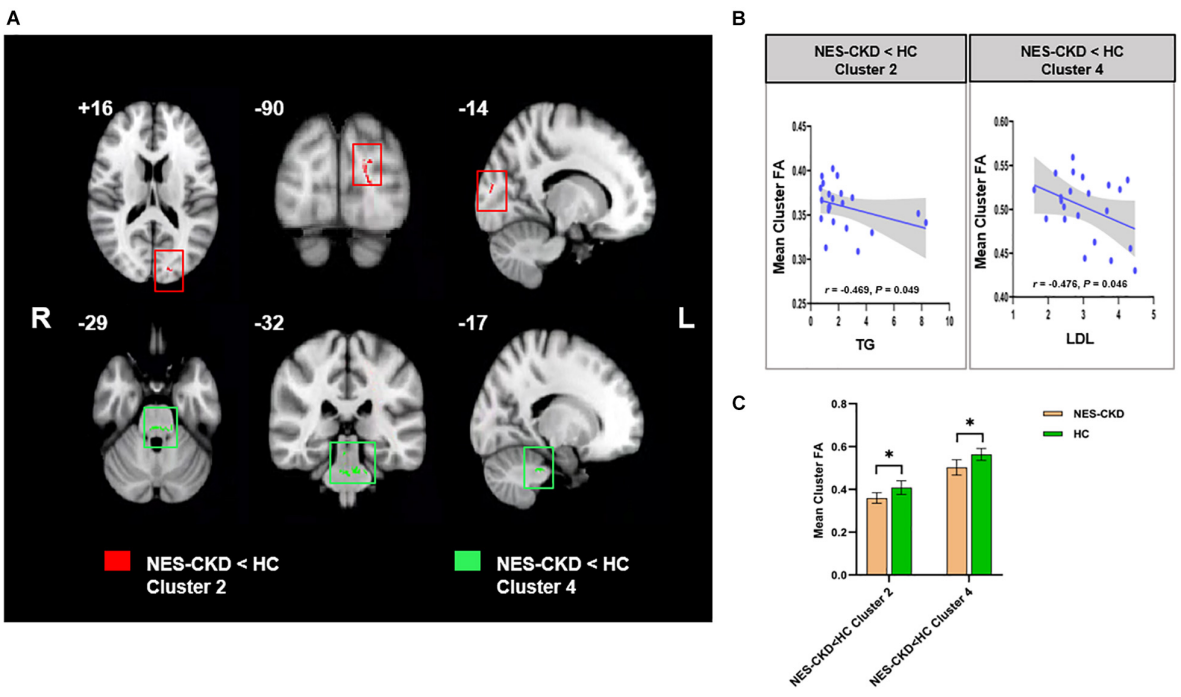

FIGURE 4 | (A) Biochemical tests relevant clusters with statistically significant FA differences obtained from the NES-CKD and HCs. Cluster 2 is marked in red and Cluster 4 in green. **(B)** Relationship between mean cluster FA and TG (left) and LDL (right). **(C)** The bar plots represent the corresponding mean FA for each group. NES-CKD, non-end-stage chronic kidney disease; HC, healthy control; FA, fractional anisotropy. * indicates a statistical difference between the two groups, $p < 0.05$.

TABLE 4 | Multiple linear regression analysis.

	Clusters	β	*P*
FA	ESRD < NES-CKD Cluster 1		
	UA	−0.622	0.006
	ESRD < NES-CKD Cluster 2		
	UA	−0.568	0.014
	ESRD < NES-CKD Cluster 3		
	LDL	−0.529	0.007
	P	−0.480	0.013
MD	ESRD > NES-CKD Cluster 1		
	Urea	0.679	0.002
AD	ESRD > NES-CKD Cluster 4		
	UA	0.766	<0.001
RD	ESRD > NES-CKD Cluster 1		
	P	0.536	0.022

UA, uric acid; LDH, low-density lipoprotein; P, serum phosphorus; Urea, serum urea. ESRD, end-stage renal disease; NES-CKD, non-end-stage chronic kidney disease; FA, fractional anisotropy; MD, mean diffusivity; AD, axial diffusivity; RD, radial diffusivity.

patients with stages 3 and 4 has been consulted (Liu et al., 2020). Similar to the results by Liu (Liu et al., 2020), our study also found decreased FA and increased MD values in multiple regions of patients with NES-CKD, especially in bilateral SLF, bilateral ILF, bilateral IFOF, CC, and bilateral corona radiata, in comparison with those of HCs.

Compared with the previous analyses based only on the FA and MD values, our study incorporated four diffusion metrics (FA, MD, AD, and RD), and thus the results can be more comprehensive. AD and RD indicate the degree of diffusion parallel to and perpendicular to the fiber orientation, respectively, and are sensitive to axon integrity and myelin damage. Our research showed that compared to healthy subjects, patients with NES-CKD have a broad and symmetrical increase in the RD value of WM microstructures, while the WM regions with increased AD values were relatively small. We speculate that in the progression of CKD, the reduction of FA is dominated by demyelination, and axonal injury only plays a small role. In addition, this study found that in regions where the MD values of patients with NES-CKD increased, the RD values also increased significantly. This finding has only been previously reported in ESRD (Chou et al., 2013). It is speculated that WM demyelination is the main neuropathy in patients with ESRD on long-term hemodialysis. But at present, changes in demyelination can also be observed in the progression of CKD. This also confirmed our above speculation.

In addition, in this study, reduced FA was observed in the middle cerebellar peduncle, which has not been mentioned previously. WM abnormalities in the infratentorial regions only have been reported in the study of ESRD after hemodialysis and were believed to be the results of transient edema and demyelination after hemodialysis (Tarhan et al., 2004; Lakadamyali and Ergün, 2011; Chou et al., 2013). However, the results of our study showed that there may also be changes in the microstructure of the subtentorial WM in patients with progressing CKD without dialysis, but the reason is still unclear and needs to be confirmed by larger samples or animal experiments.

Notably, in this study, we have found differences in WM characteristics between patients with ESRD and NES-CKD. To our knowledge, this is the first study applying TBSS to analyze the difference in WM microstructure between NES-CKDs and ESRDs.

In the ESRD group, although three independent clusters were identified with reduced FA values, and more than 96% voxels were located in Cluster 3, indicating that from non-end-stages to the end-stage, WM in patients with CKD has occurred large-scale alterations. Cluster 3 included voxels in the bilateral ATR, the genu and body of CC, bilateral ACR, bilateral superior corona radiata, bilateral IFOF, and left SLF. We found that most regions of this cluster were not shown in the different clusters between NES-CKD and HC groups, especially for genu and its extension radiating fibers (forceps minor) and body of CC and bilateral superior corona radiata, suggesting that the changes in WM characteristics in these regions only appear in the ESRD. As the largest WM tract, CC connects the bilateral hemispheres to realize their communication. *Post hoc* analysis showed decreased

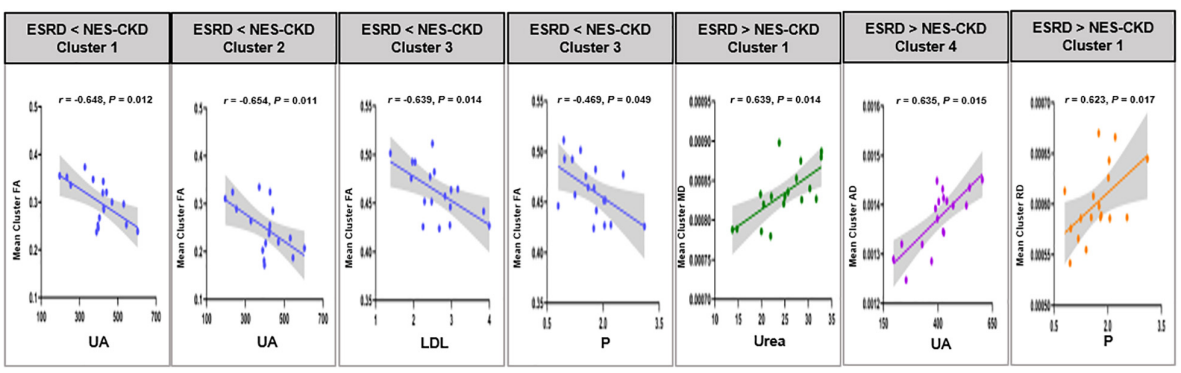

FIGURE 5 | Relationship between mean cluster diffusion metrics and biochemical tests. UA, uric acid; LDH, low-density lipoprotein; P, serum phosphorus; Urea, serum urea. ESRD, end-stage renal disease; NES-CKD, non-end-stage chronic kidney disease; FA, fractional anisotropy; MD, mean diffusivity; AD, axial diffusivity; RD, radial diffusivity.

FA in the splenium of CC in patients with NES-CKD, while WM abnormalities in the genu and body of CC appeared in patients with ESRD, indicating that with the progress of CKD, the abnormality in WM microstructure of the CC is gradually developing. We also identified that WM damages appear mainly in superior brain portions of the ESRD group. Corona radiata includes the ascending and descending fibers of the thalamus and cerebral cortex and participates in various functions such as emotion, execution, and cognition (Drevets et al., 2008; Cui et al., 2020). Studies have confirmed that the incidence of depressive symptoms in patients with CKD is significantly higher than that of ordinary people (Fischer et al., 2012; Al-Ali et al., 2021). Therefore, we suspect that the WM damage of CR may be related to a certain degree of depressive symptoms in the enrolled patients. However, it is a pity that the depression has not been evaluated due to patients' compliance, and follow-up studies are still needed.

Multiple regression analysis was conducted within the significant clusters and biochemical tests in the whole patients with ESRD to determine the impacts of biochemical indicators on WM microstructure. Excitingly, we identified the relationships between UA and mean FA or AD in three clusters demonstrating differences between ESRDs and NES-CKDs. Additionally, we also observed that these three clusters mainly include the region of ATR. ATR connects the mediodorsal and anterior thalamic nucleus with the frontal cortex and the anterior cingulate cortex and can also process information from the hippocampus (Setiadi et al., 2021), thus affecting cognitive function. Although there were literature supporting that UA can be beneficial to the pathological process of neurodegenerative diseases by reducing oxidative stress and free radicals (Kim et al., 2006; Lee et al., 2021), more and more studies have investigated the relationship between UA and cognitive impairment and found evidence about UA in exacerbating the deterioration of cognitive function (Beydoun et al., 2016; Li et al., 2021). Therefore, we speculate that UA may affect cognitive function through its effect on ATR. But this may be limited by the small sample size and the lack of correlation between UA and cognitive scores. Compared with the NES-CKD group, the phosphate and PTH levels in patients with ESRD were significantly higher, and the correlations observed in **Table 4** indicated that the serum phosphate level may serve as an independent influencing factor of diffusion parameters in some significant clusters. This suggests an association between phosphate and WM abnormalities; however, little is known about the mechanism. When renal function is impaired, an increase in phosphate will cause the secretion of PTH but reduce the active form of vitamin D, which will induce secondary hyperparathyroidism (Tsuchiya and Akihisa, 2021). However, high PTH can affect the neurotransmission of the central nervous system and induce neurotoxicity (Wilmskoetter et al., 2019).

Several limitations of this study should be noted. First, the small sample size in this study may limit the generality of the results. Second, the enrolled patients with ESRD were all undergoing regular hemodialysis, and the effect of hemodialysis on WM abnormalities cannot be ruled out. Third, due to patient compliance issues, most patients have not completed the cognitive tests, which also has a certain impact on our results regarding cognitive function in patients. Fourth, patients with CKD at stages 1–4 were combined into one group for analysis. In the future, dynamic research on CKD can be considered to further reveal the changes in WM at different stages.

CONCLUSION

In conclusion, the results of this study indicate that compared with patients in the progression of CKD, patients with ESRD have more severe WM microstructural abnormalities, and this progressive deterioration is related to uric acid and phosphate levels.

DATA AVAILABILITY STATEMENT

The original contributions presented in the study are included in the article/**Supplementary Material**, further inquiries can be directed to the corresponding author/s.

ETHICS STATEMENT

The studies involving human participants were reviewed and approved by the Local Ethics Committee of the First Affiliated Hospital of Dalian Medical University. The patients/participants provided their written informed consent to participate in this study. Written informed consent was obtained from the individual(s) for the publication of any potentially identifiable images or data included in this article.

AUTHOR CONTRIBUTIONS

YJ and QG were the guarantor of integrity of the entire study. YJ, QG, YL, BG, YC, JJ, and PC performed the literature research. YJ, QG, YL, BG, YC, JJ, PC, QS, LL, NW, WW, and YM performed the clinical studies. YJ, QG, NW, and YM performed experimental studies and manuscript editing. YJ, QG, and JJ performed statistical analysis. All authors contributed to study concepts, study design, data acquisition, data analysis/interpretation, involved in manuscript drafting and manuscript revision for important intellectual content, approved the final version of the submitted manuscript, and agreed to ensure that any questions related to the work are appropriately resolved.

FUNDING

This study was supported by the National Natural Science Foundation of China (Nos. 81671646 and 81801657).

SUPPLEMENTARY MATERIAL

The Supplementary Material for this article can be found online at: https://www.frontiersin.org/articles/10.3389/fnhum.2021.774236/full#supplementary-material

REFERENCES

Al-Ali, F., Elshirbeny, M., Hamad, A., Kaddourah, A., Ghonimi, T., Ibrahim, R., et al. (2021). Prevalence of depression and sleep disorders in patients on dialysis: a cross-sectional study in qatar. *Int. J. Nephrol.* 2021:5533416. doi: 10.1155/2021/5533416

Andersson, J. L. R., and Sotiropoulos, S. N. (2016). An integrated approach to correction for off-resonance effects and subject movement in diffusion MR imaging. *Neuroimage* 125, 1063–1078. doi: 10.1016/j.neuroimage.2015.10.019

Bartzokis, G. (2011). Alzheimer's disease as homeostatic responses to age-related myelin breakdown. *Neurobiol. Aging* 32, 1341–1371. doi: 10.1016/j.neurobiolaging.2009.08.007

Beydoun, M. A., Canas, J. A., Dore, G. A., Beydoun, H. A., Rostant, O. S., Fanelli-Kuczmarski, M. T., et al. (2016). Serum uric acid and its association with longitudinal cognitive change among urban adults. *J Alzheimers Dis.* 52, 1415–1430. doi: 10.3233/JAD-160028

Chen, H. J., Gao, Y. Q., Che, C. H., Lin, H., and Ruan, X. L. (2018). Diffusion tensor imaging with tract-based spatial statistics reveals white matter abnormalities in patients with vascular cognitive impairment. *Front. Neuroanat.* 12:53. doi: 10.3389/fnana.2018.00053

Chou, M. C., Hsieh, T. J., Lin, Y. L., Hsieh, Y. T., Li, W. Z., Chang, J. M., et al. (2013). Widespread white matter alterations in patients with end-stage renal disease: a voxelwise diffusion tensor imaging study. *AJNR Am. J. Neuroradiol.* 34, 1945–1951. doi: 10.3174/ajnr.A3511

Chou, M. C., Ko, C. H., Hsieh, T. J., Chang, J. M., and Chung, W. S. (2019). A preliminary report of longitudinal white matter alterations in patients with end-stage renal disease: a three-year diffusion tensor imaging study. *PLoS One* 14:e0215942. doi: 10.1371/journal.pone.0215942

Cui, Y., Dong, J., Yang, Y., Yu, H., Li, W., Liu, Y., et al. (2020). White matter microstructural differences across major depressive disorder, bipolar disorder and schizophrenia: a tract-based spatial statistics study. *J. Affect. Disord.* 260, 281–286. doi: 10.1016/j.jad.2019.09.029

Drevets, W. C., Price, J. L., and Furey, M. L. (2008). Brain structural and functional abnormalities in mood disorders: implications for neurocircuitry models of depression. *Brain Struct. Funct.* 213, 93–118. doi: 10.1007/s00429-008-0189-x

Egbi, O. G., Ogunrin, O., and Oviasu, E. (2015). Prevalence and determinants of cognitive impairment in patients with chronic kidney disease: a cross-sectional study in Benin City, Nigeria. *Ann. Afr. Med.* 14, 75–81. doi: 10.4103/1596-3519.149877

Fieremans, E., Jensen, J. H., and Helpern, J. A. (2011). White matter characterization with diffusional kurtosis imaging. *Neuroimage* 58, 177–188. doi: 10.1016/j.neuroimage.2011.06.006

Fischer, M. J., Xie, D., Jordan, N., Kop, W. J., Krousel-Wood, M., Kurella Tamura, M., et al. (2012). Factors associated with depressive symptoms and use of antidepressant medications among participants in the Chronic Renal Insufficiency Cohort (CRIC) and Hispanic-CRIC Studies. *Am. J. Kidney Dis.* 60, 27–38. doi: 10.1053/j.ajkd.2011.12.033

Hagmann, P., Jonasson, L., Maeder, P., Thiran, J. P., Wedeen, V. J., and Meuli, R. (2006). Understanding diffusion MR imaging techniques: from scalar diffusion-weighted imaging to diffusion tensor imaging and beyond. *Radiographics* 26 Suppl 1, S205–S223. doi: 10.1148/rg.26si065510

Kim, T. S., Pae, C. U., Yoon, S. J., Jang, W. Y., Lee, N. J., Kim, J. J., et al. (2006). Decreased plasma antioxidants in patients with Alzheimer's disease. *Int. J. Geriatr. Psychiatry* 21, 344–348. doi: 10.1002/gps.1469

Kong, X., Wen, J. Q., Qi, R. F., Luo, S., Zhong, J. H., Chen, H. J., et al. (2014). Diffuse interstitial brain edema in patients with end-stage renal disease undergoing hemodialysis: a tract-based spatial statistics study. *Medicine (Baltimore)* 93:e313. doi: 10.1097/MD.0000000000000313

Lakadamyali, H., and Ergün, T. (2011). MRI for acute neurologic complications in end-stage renal disease patients on hemodialysis. *Diagn. Interv. Radiol.* 17, 112–117. doi: 10.4261/1305-3825.DIR.3063-09.1

Lee, Y. G., Park, M., Jeong, S. H., Kang, S. W., Baik, K., Jung, J. H., et al. (2021). Effects of baseline serum uric acid and apolipoprotein E4 on longitudinal cognition and cerebral metabolism. *Neurobiol. Aging* 106, 223–231. doi: 10.1016/j.neurobiolaging.2021.05.003

Li, L. L., Ma, Y. H., Bi, Y. L., Sun, F. R., Hu, H., Hou, X. H., et al. (2021). Serum uric acid may aggravate Alzheimer's disease risk by affecting amyloidosis in cognitively intact older adults: the cable study. *J. Alzheimers Dis.* 81, 389–401. doi: 10.3233/JAD-201192

Lim, L., Hart, H., Howells, H., Mehta, M. A., Simmons, A., Mirza, K., et al. (2019). Altered white matter connectivity in young people exposed to childhood abuse: a tract-based spatial statistics (TBSS) and tractography study. *J. Psychiatry Neurosci.* 44, E11–E20. doi: 10.1503/jpn.170241

Liu, M., Wu, Y., Wu, X., Ma, X., Yin, Y., Fang, H., et al. (2020). White matter microstructure changes and cognitive impairment in the progression of chronic kidney disease. *Front. Neurosci.* 14:559117. doi: 10.3389/fnins.2020.559117

Mei, L., Li, X., Zhou, G., Ji, T., Chen, J., Xu, Z., et al. (2020). Effects of obstructive sleep apnoea severity on neurocognitive and brain white matter alterations in children according to sex: a tract-based spatial statistics study. *Sleep Med.* 82, 134–143. doi: 10.1016/j.sleep.2020.08.026

Metzler-Baddeley, C., Mole, J. P., Sims, R., Fasano, F., Evans, J., Jones, D. K., et al. (2019). Fornix white matter glia damage causes hippocampal gray matter damage during age-dependent limbic decline. *Sci. Rep.* 9:1060.

Navva, P. K., Venkata Sreepada, S., and Shivanand Nayak, K. (2015). Present status of renal replacement therapy in asian countries. *Blood Purif.* 40, 280–287. doi: 10.1159/000441574

Nucifora, P. G., Verma, R., Lee, S. K., and Melhem, E. R. (2007). Diffusion-tensor MR imaging and tractography: exploring brain microstructure and connectivity. *Radiology* 245, 367–384. doi: 10.1148/radiol.2452060445

Qi, R., Zhang, L. J., Zhong, J., Zhu, T., Zhang, Z., Xu, C., et al. (2013). Grey and white matter abnormalities in minimal hepatic encephalopathy: a study combining voxel-based morphometry and tract-based spatial statistics. *Eur. Radiol.* 23, 3370–3378. doi: 10.1007/s00330-013-2963-2

Raffelt, D. A., Smith, R. E., Ridgway, G. R., Tournier, J. D., Vaughan, D. N., Rose, S., et al. (2015). Connectivity-based fixel enhancement: whole-brain statistical analysis of diffusion MRI measures in the presence of crossing fibres. *Neuroimage* 117, 40–55. doi: 10.1016/j.neuroimage.2015.05.039

Sarnak, M. J., Tighiouart, H., Scott, T. M., Lou, K. V., Sorensen, E. P., Giang, L. M., et al. (2013). Frequency of and risk factors for poor cognitive performance in hemodialysis patients. *Neurology* 80, 471–480. doi: 10.1212/WNL.0b013e31827f0f7f

Setiadi, T. M., Martens, S., Opmeer, E. M., Marsman, J. C., Tumati, S., Reesink, F. E., et al. (2021). Widespread white matter aberration is associated with the severity of apathy in amnestic mild cognitive impairment: tract-based spatial statistics analysis. *Neuroimage Clin.* 29:102567. doi: 10.1016/j.nicl.2021.102567

Smith, S. M. (2002). Fast robust automated brain extraction. *Hum. Brain Mapp.* 17, 143–155.

Smith, S. M., and Nichols, T. E. (2009). Threshold-free cluster enhancement: addressing problems of smoothing, threshold dependence and localisation in cluster inference. *Neuroimage* 44, 83–98. doi: 10.1016/j.neuroimage.2008.03.061

Smith, S. M., Jenkinson, M., Johansen-Berg, H., Rueckert, D., Nichols, T. E., Mackay, C. E., et al. (2006). Tract-based spatial statistics: voxelwise analysis of multi-subject diffusion data. *Neuroimage* 31, 1487–1505.

Smith, S. M., Jenkinson, M., Woolrich, M. W., Beckmann, C. F., Behrens, T. E., Johansen-Berg, H., et al. (2004). Advances in functional and structural MR image analysis and implementation as FSL. *Neuroimage* 23 Suppl 1, S208–S219. doi: 10.1016/j.neuroimage.2004.07.051

Tarhan, N. C., Agildere, A. M., Benli, U. S., Ozdemir, F. N., Aytekin, C., and Can, U. (2004). Osmotic demyelination syndrome in end-stage renal disease after recent hemodialysis: MRI of the brain. *AJR Am. J. Roentgenol.* 182, 809–816. doi: 10.2214/ajr.182.3.1820809

Tiffin-Richards, F. E., Costa, A. S., Holschbach, B., Frank, R. D., Vassiliadou, A., Krüger, T., et al. (2014). The montreal cognitive assessment (MoCA) – a sensitive screening instrument for detecting cognitive impairment in chronic hemodialysis patients. *PLoS One* 9:e106700. doi: 10.1371/journal.pone.0106700

Tsuchiya, K., and Akihisa, T. (2021). The importance of phosphate control in chronic kidney disease. *Nutrients* 13:1670. doi: 10.3390/nu13051670

Vogels, S. C., Emmelot-Vonk, M. H., Verhaar, H. J., and Koek, H. L. (2012). The association of chronic kidney disease with brain lesions on MRI or CT: a systematic review. *Maturitas* 71, 331–336. doi: 10.1016/j.maturitas.2012.01.008

Webster, A. C., Nagler, E. V., Morton, R. L., and Masson, P. (2017). Chronic kidney disease. *Lancet* 389, 1238–1252.

Wilmskoetter, J., Fridriksson, J., Gleichgerrcht, E., Stark, B. C., Delgaizo, J., Hickok, G., et al. (2019). Neuroanatomical structures supporting lexical diversity, sophistication, and phonological word features during discourse. *Neuroimage Clin.* 24:101961. doi: 10.1016/j.nicl.2019.101961

Winkler, A. M., Ridgway, G. R., Webster, M. A., Smith, S. M., and Nichols, T. E. (2014). Permutation inference for the general linear model. *Neuroimage* 92, 381–397. doi: 10.1016/j.neuroimage.2014.01.060

Yamada, S., Takahashi, S., Ohoshi, Y., Ishida, T., Tsuji, T., Shinosaki, K., et al. (2020). Widespread white matter microstructural abnormalities and cognitive impairment in schizophrenia, bipolar disorder, and major depressive disorder: tract-based spatial statistics study. *Psychiatry Res. Neuroimaging* 298:111045. doi: 10.1016/j.pscychresns.2020.111045

Yin, Y., Li, M., Li, C., Ma, X., Yan, J., Wang, T., et al. (2018). Reduced white matter integrity with cognitive impairments in end stage renal disease. *Front. Psychiatry* 9:143. doi: 10.3389/fpsyt.2018.00143

Zhang, H., Schneider, T., Wheeler-Kingshott, C. A., and Alexander, D. C. (2012). NODDI: practical in vivo neurite orientation dispersion and density imaging of the human brain. *Neuroimage* 61, 1000–1016. doi: 10.1016/j.neuroimage.2012.03.072

Zhang, L., Wang, F., Wang, L., Wang, W., Liu, B., Liu, J., et al. (2012). Prevalence of chronic kidney disease in China: a cross-sectional survey. *Lancet* 379, 815–822.

Zhang, R., Liu, K., Yang, L., Zhou, T., Qian, S., Li, B., et al. (2015). Reduced white matter integrity and cognitive deficits in maintenance hemodialysis ESRD patients: a diffusion-tensor study. *Eur. Radiol.* 25, 661–668. doi: 10.1007/s00330-014-3466-5

Conflict of Interest: LL was employed by the company Philips Healthcare China.

The remaining authors declare that the research was conducted in the absence of any commercial or financial relationships that could be construed as a potential conflict of interest.

Publisher's Note: All claims expressed in this article are solely those of the authors and do not necessarily represent those of their affiliated organizations, or those of the publisher, the editors and the reviewers. Any product that may be evaluated in this article, or claim that may be made by its manufacturer, is not guaranteed or endorsed by the publisher.

frontiers in Neuroscience

ORIGINAL RESEARCH
published: 10 March 2022
doi: 10.3389/fnins.2022.849425

The Application of Diffusion Kurtosis Imaging on the Heterogeneous White Matter in Relapsing-Remitting Multiple Sclerosis

Qiyuan Zhu†, Qiao Zheng†, Dan Luo, Yuling Peng, Zichun Yan, Xiaohua Wang, Xiaoya Chen and Yongmei Li**

Department of Radiology, The First Affiliated Hospital of Chongqing Medical University, Chongqing, China

OPEN ACCESS

Edited by:
Brian Hansen,
Aarhus University, Denmark

Reviewed by:
Kouhei Kamiya,
Toho University, Japan
Christian Thaler,
University Medical Center Hamburg-Eppendorf, Germany

***Correspondence:**
Xiaoya Chen
xiaoya_c@163.com
Yongmei Li
lymzhang70@163.com

† These authors have contributed equally to this work

Specialty section:
This article was submitted to Brain Imaging Methods, a section of the journal Frontiers in Neuroscience

Received: *06 January 2022*
Accepted: *31 January 2022*
Published: *10 March 2022*

Citation:
Zhu Q, Zheng Q, Luo D, Peng Y, Yan Z, Wang X, Chen X and Li Y (2022) The Application of Diffusion Kurtosis Imaging on the Heterogeneous White Matter in Relapsing-Remitting Multiple Sclerosis. Front. Neurosci. 16:849425. doi: 10.3389/fnins.2022.849425

Objectives: To evaluate the microstructural damage in the heterogeneity of different white matter areas in relapsing-remitting multiple sclerosis (RRMS) patients by using diffusion kurtosis imaging (DKI) and its correlation with clinical and cognitive status.

Materials and Methods: Kurtosis fractional anisotropy (KFA), fractional anisotropy (FA), mean kurtosis (MK), and mean diffusivity (MD) in T1-hypointense lesions (T1Ls), pure T2-hyperintense lesions (pure-T2Ls), normal-appearing white matter (NAWM), and white matter in healthy controls (WM in HCs) were measured in 48 RRMS patients and 26 sex- and age-matched HCs. All the participants were assessed with the Mini-Mental State Examination (MMSE), the Montreal Cognitive Assessment (MoCA), and the Symbol Digit Modalities Test (SDMT) scores as the cognitive status. The Kurtzke Expanded Disability Status Scale (EDSS) scores were used to evaluate the clinical status in RRMS patients.

Results: The lowest KFA, FA, and MK values and the highest MD values were found in T1Ls, followed by pure-T2Ls, NAWM, and WM in HCs. The T1Ls and pure-T2Ls were significantly different in FA ($p = 0.002$) and MK ($p = 0.013$), while the NAWM and WM in HCs were significantly different in KFA, FA, and MK ($p < 0.001$; $p < 0.001$; $p = 0.001$). The KFA, FA, MK, and MD values in NAWM ($r = 0.360$, $p = 0.014$; $r = 0.415$, $p = 0.004$; $r = 0.369$, $p = 0.012$; $r = -0.531$, $p < 0.001$) were correlated with the MMSE scores and the FA, MK, and MD values in NAWM ($r = 0.423$, $p = 0.003$; $r = 0.427$, $p = 0.003$; $r = -0.359$, $p = 0.014$) were correlated with the SDMT scores.

Conclusion: Applying DKI to the imaging-based white matter classification has the potential to reflect the white matter damage and is correlated with cognitive impairment.

Keywords: multiple scleorsis (MS), magnetic resonance imaging (MRI), diffusion kurtosis imaging (DKI), normal-appearing white matter (NAWM), white matter lesions (WMLs), disease severity, cognitive impairment

Abbreviations: RRMS, Relapse-remitting multiple sclerosis; HCs, Healthy controls; WMLs, White matter lesions; T1Ls, T1-hypointense lesions; T2Ls, T2-hyperintense lesions; NAWM, Normal-appearing white matter; WM in HCs, White matter in healthy controls; DKI, Diffusion kurtosis imaging; KFA, Kurtosis fractional anisotropy; FA, Fractional anisotropy; MK, Mean kurtosis; MD, Mean diffusivity; MMSE, Mini-Mental State Examination; MoCA, Montreal Cognitive Assessment; SDMT, Symbol Digit Modalities Test; EDSS, Expanded Disability Status Scale.

INTRODUCTION

Multiple sclerosis (MS) is one of the most prevalent chronic inflammatory demyelinated diseases, which is characterized by edema, inflammation, demyelination, and axonal loss in the central nervous system (Evangelou et al., 2000; Reich et al., 2018). To better diagnose and evaluate MS in clinical practice, magnetic resonance imaging (MRI), as a highly sensitive tool, can provide disease information and monitor the disease progression (Polman et al., 2011). White matter lesions (WMLs) can be detected as areas of hyperintensity on T2-weighted images (T2WI) or fluid-attenuated inversion recovery (FLAIR) images. Those T2-hyperintense lesions (T2Ls) correspond to a broad spectrum of pathological changes, including edema, inflammation, demyelination, remyelination, gliosis, liquid necrosis, and axonal loss (MacKay et al., 2006). Compared to T2Ls, however, non-enhancing T1-hypointense lesions (T1Ls) indicate more severe damage reflecting demyelination, axonal loss, gliosis, and loss of intracellular matrix and are thought to provide a more accurate classification of the microstructural damage in MS patients (Barkhof et al., 2009; Wolinsky et al., 2013). Therefore, we hypothesize that those differences in intensities of WMLs on T1-weighted images (T1WI) and T2WI/FLAIR represent the different pathological changes in the white matter, which contribute differently to the progression of the disease.

The conventional MRI can be used to evaluate the number, volume, and distribution of lesions in MS patients but lack the specific information of microstructural damage (Filippi et al., 2018). Diffusion tensor imaging (DTI) is widely used to evaluate the microstructural changes in the WMLs and normal-appearing white matter (NAWM) either in clinical practice or research, which provides more sensitive measures for clinically related brain abnormalities. However, the diffusion of water molecules in brain tissue often follows non-Gaussian distribution, which is not entirely characterized by DTI (Tuch et al., 2003). To better evaluate such microstructure, diffusion kurtosis imaging (DKI) has been proposed as an extension of DTI, which can quantify the non-Gaussian diffusion characteristics of water molecules in tissues, and provides more real and accurate tissue microstructure information than DTI (Jensen et al., 2005). DKI provides both diffusivity and kurtosis parameters. The diffusivity parameters, such as fractional anisotropy (FA) and mean diffusivity (MD), are used to assess white matter integrity, and the kurtosis parameters mainly include kurtosis fractional anisotropy (KFA) and mean kurtosis (MK). The KFA value summarizes the directional change of kurtosis, reflecting the anisotropy of kurtosis that can be used to describe a more complex environment of the brain tissue (Glenn et al., 2015). The MK value can reflect the microstructural complexity and the density of the axons and myelin, which has shown the better potential value to detect the tissue microstructure alterations in neurological disorders (Steven et al., 2014). The decreased MK values were found in the chronic demyelinated lesions, which is believed to be linked to a loss of microstructure (Falangola et al., 2014) while the increased MK values were found in the early acute inflammatory demyelinating phase of the lesions, which was associated with microgliosis (Guglielmetti et al., 2016). Thus, DKI sequence has the potential to reflect the microstructural damages or pathological changes in the white matter tissues (whether WMLs or NAWM).

Previous studies have paid much attention on the heterogeneity of MS lesions and made the classifications based on imaging (Thaler et al., 2015; Lipp et al., 2019; Ye et al., 2020). Some researchers have applied the advanced MRI techniques, including diffusion MRI (dMRI), to evaluate the heterogeneity of MS lesions or tissue states of white matter (Thaler et al., 2021). Furthermore, seeking for the correlation between disease severity and imaging metrics would make the classification of lesions or white matter tissues meaningful. When combining the dMRI-derived parameters with clinical or cognitive status, researchers applied DTI and DKI based on the different brain regions analysis and found the correlation between the white matter integrity and the cognitive status (de Kouchkovsky et al., 2016; Margoni et al., 2019; Schiavi et al., 2021). Despite all that, few studies evaluated the correlation between the different heterogeneous white matter and clinical or cognitive status based on the severity of the microstructural damage of white matter. We therefore hypothesize that the sensitive DKI-derived parameters would reveal some correlations with the disease severity when evaluating the different types of white matter tissue, which could be served for clinical practice.

Hence, the aims of this study were to (i) apply DKI to quantitatively evaluate the degree of microstructural damage in different white matter tissue types in a cohort of relapsing-remitting multiple sclerosis (RRMS) patients and healthy controls (HCs) and (ii) combine the results of the DKI-derived parameters with the clinical and cognitive status to explore the potential imaging biomarker and (iii) its correlation with severity of the disease.

MATERIALS AND METHODS

Standard Protocol Approvals, Registrations, and Patient Consents

This retrospective study was approved by the Institutional Review Board of the First Affiliated Hospital of Chongqing Medical University, Chongqing, China, and written informed consent was obtained from each participant before MRI scans.

Subjects

Forty-eight RRMS patients and 26 sex- and age-matched HCs were enrolled from the Department of Radiology, the First Affiliated Hospital of Chongqing Medical University. All the participants were recruited between July 2019 and December 2020. Inclusion criteria for MS patients were as follows: (1) a confirmed diagnosis of RRMS according to the 2017 revised McDonald's diagnostic criteria (Thompson et al., 2018), (2) age 18–60 years, and (3) absence of neurological conditions other than MS. The exclusion criteria were as follows: (1) patients with contraindications for MRI scans, (2) history of intravenous corticosteroid treatment within 2 months before the imaging examinations, (3) image artifacts or incomplete

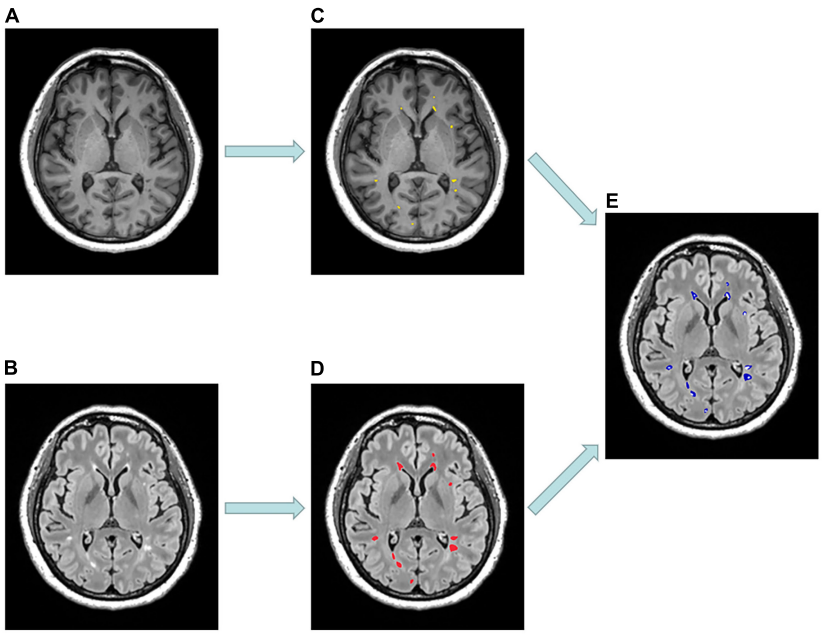

FIGURE 1 | Example of MR scans and lesion masks of a 53-year-old patient diagnosed with relapsing-remitting multiple sclerosis. **(A)** Selected axial MPRAGE image with hypointense lesions. **(B)** Selected axial FLAIR image with hyperintense lesions. **(C)** T1-hypointense lesions (T1Ls) mask (yellow). **(D)** T2-hyperintense lesions (T2Ls) mask (red). **(E)** Pure T2-hyperintense lesions (pure-T2Ls) mask (blue) was obtained by subtracting **(C)** from **(D)**.

clinical information, and (4) contrast-enhanced T1-MPRAGE hyperintense lesions. Among the 48 RRMS patients, only 10 of them were on the disease-modifying therapy (9 with teriflunomide and 1 with rituximab). The Mini-Mental State Examination (MMSE), the Montreal Cognitive Assessment (MoCA), and the Symbol Digit Modalities Test (SDMT) scores were used to assess the cognitive performance of all participants. The Kurtzke Expanded Disability Status Scale (EDSS) scores were used to assess the clinical status of the RRMS patients.

Magnetic Resonance Imaging Data Acquisitions

All MR scans were performed on a 3-T MR scanner (Magnetom Skyra, Siemens Healthcare GmbH, Erlangen, Germany) using a 32-channel head coil. A standard protocol for MS studies included a sagittal 3-dimensional T1-weighted magnetization prepared rapid gradient echo (MPRAGE) sequence [echo-time (TE) = 2.26 ms, repetition time (TR) = 2,300 ms, inversion time (TI) = 900 ms, 192 slices, field of view (FOV) = 256 mm, voxel size = 1.0 × 1.0 × 1.0 mm, acquisition time (TA) = 5:21 min] and a sagittal 3-dimensional FLAIR (TE = 388 ms, TR = 5,000 ms, TI = 1,800 ms, 192 slices, FOV = 256 mm, voxel size = 0.5 × 0.5 × 1.0 mm, TA = 7:07 min). DKI data were acquired using the following parameters: TE = 97 ms, TR = 5,000 ms, 25 slices, FOV = 220 mm, voxel size = 1.7 × 1.7 × 4.0 mm, TA = 6:04 min, integrated Parallel Acquisition Techniques (iPAT) acceleration factor = 2 (GRAPPA), Partial-Fourier = 6/8, and three b values (0, 1,000, and 2,000 s/mm^2) with diffusion encoding in 30 directions.

Imaging Analysis

In each RRMS patient, we purposely divided the white matter into three different areas, including T1-weighted hypointense lesions with corresponding T2-weighted hyperintensity defined as T1Ls, T2-weighted/FLAIR hyperintense lesions without T1-weighted hypointensity defined as pure-T2Ls, and normal-appearing white matter defined as NAWM (**Figures 1**, **2**). The total T2-hyperintense lesions volume (T2LV), T1Ls volume (T1LV), and pure-T2Ls volume (pure-T2LV) were calculated in each patient.

T1Ls were defined as areas with hypointense on T1-weighted images and hyperintense on a T2-weighted/FLAIR image. Thus, two independent raters (XC and DL) manually outlined the hypointense lesions according to the definition above on T1-weighted MPRAGE images using the ITK-SNAP 3.8.0 (accessed on June of 2019)[1] (Yushkevich et al., 2006). The resulting T1L masks of both raters were binarized and patient-wise multiplied to obtain a consensus mask.

As mentioned above, pure-T2Ls were defined as areas with only hyperintense on T2-weighted/FLAIR images and without hypointensity on T1-weighted images. The FLAIR image of each RRMS patient was registered to the T1-MPRAGE image. All the T2-hyperintense lesions were semi-automatically segmented on FLAIR images. Both the two steps mentioned above were using the Lesion Segmentation Tool (Schmidt et al., 2012). For accuracy, the semi-automatically segmented T2-hyperintense lesion masks were manually controlled and corrected to obtain the T2L masks. Since all T1Ls were shown as T2 hyperintense

[1]http://itksnap.org

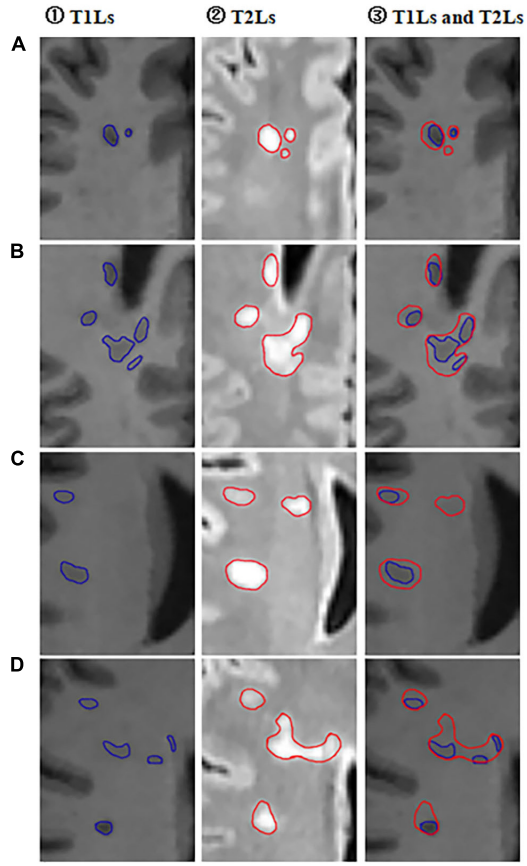

FIGURE 2 | Selected partial axial images of MPRAGE and FLAIR sequences. **(A–D)** Partial axial FLAIR/MPRAGE images of four different RRMS patients in our cohort. ① Outlined T1-hypointense lesions (T1Ls) on MPRAGE images; ② Outlined T2-hyperintese (T2Ls) lesions on FLAIR images; ③ Outlined both T2-hyperintense lesions (T1Ls) and T1-hypointense lesions (T2Ls) on MPRAGE images.

lesions in each patient, the T1L mask was subtracted from the T2L mask to obtain only the pure-T2L mask.

For the NAWM mask, we subtracted the T2L mask from the whole brain white matter mask, leaving those areas that are isointense both on T1-weighted and FLAIR/T2-weighted images. The whole-brain white matter mask was obtained from T1-weighted MPRAGE imaging by using Voxel-based morphometry (VBM) (Ashburner and Friston, 2000) in SPM8 software.[2]

Additionally, in the HCs cohort, we extracted the whole brain white matter (WM) mask in each subject. All the image binary subtraction steps mentioned above used the MATLAB R2013b software.

Diffusion Kurtosis Imaging Processing

DKI data were pre-processed, including denoising (Veraart et al., 2016), removal of Gibbs ringing artifacts (Kellner et al., 2016), correction of subject motion (Leemans and Jones, 2009) using the MRtrix3 package (Tournier et al., 2019), eddy-currents (Andersson et al., 2017), and susceptibility-induced distortions (Andersson et al., 2003) in FMRIB Software Library (FSL)[3] (Jenkinson et al., 2012). All the T1 images were registered to DKI b0 space individually using FSL. The diffusion kurtosis parametric maps, including the kurtosis fractional anisotropy (KFA), fractional anisotropy (FA), mean kurtosis (MK), and mean diffusivity (MD) (**Figure 3**), were calculated by the diffusion kurtosis estimator software (DKE),[4] using constrained linear least-squares quadratic programming (CLLS-QP) algorithm and applying standard parameters (spatial smoothing and strong median filtering) (Tabesh et al., 2011). The details of parameters used with DKE were as follows: the full width at half maximum (FWHM) of the Gaussian kernel was 3.375 mm; $Kmin = 0$, $NKmax = 3$ and $D > 0$ for constraint on directional kurtosis; $0 < K < 3$ for thresholds on output kurtosis maps. DKI tensor fitting was performed with constrained linear weighted fitting and DTI tensor fitting was performed with linear weighted fitting to, respectively, obtain the DKI- and DTI-based parametric maps. Finally, the binarized masks were multiplied with the corresponding KFA, FA, MK, and MD maps to obtain mean KFA, FA, MK, and MD values for each white matter tissue type of masks.

Statistical Analysis

Statistical analysis was performed using SPSS version 26.0 (IBM Corp., Armonk, NY, United States) and GraphPad Prism V5. Kolmogorov–Smirnov tests were applied to assess the normality of data distribution. Between RRMS patients and HCs, independent samples *t*-tests were used for age, MMSE, MoCA, and SDMT scores analysis and the Chi-square test was used for gender analysis. One-way ANOVA with the Bonferroni correction for multiple comparisons was used to compare the DKI parameter values in the four types of different white matter areas (T1Ls, pure-T2Ls, NAWM, and WM in HCs). *p*-values < 0.05 were considered statistically significant. Partial correlation analysis using age and education years as covariates was used to evaluate the relationship between T1LV, T2LV, pure-T2LV, and DKI parameter values with EDSS scores and the neuropsychological scores (MMSE, MoCA, and SDMT scores). To make the EDSS scores and the neuropsychological scores comparable with the imaging parameters, the *z*-scores of the four scores were calculated for each RRMS patient before the partial correlation analysis.

RESULTS

Demographic and Clinical Data

Demographic data and clinical characteristics of the participants are shown in **Table 1**. There were no significant differences in gender ($p = 0.945$) and age ($p = 0.075$) between RRMS patients and HCs. There were significant differences in MMSE ($p = 0.013$), MoCA ($p = 0.016$), and SDMT ($p < 0.001$) between RRMS patients and HCs.

[2]https://www.fil.ion.ucl.ac.uk/spm/

[3]https://fsl.fmrib.ox.ac.uk/fsl/fslwiki/

[4]https://www.nitrc.org/projects/dke

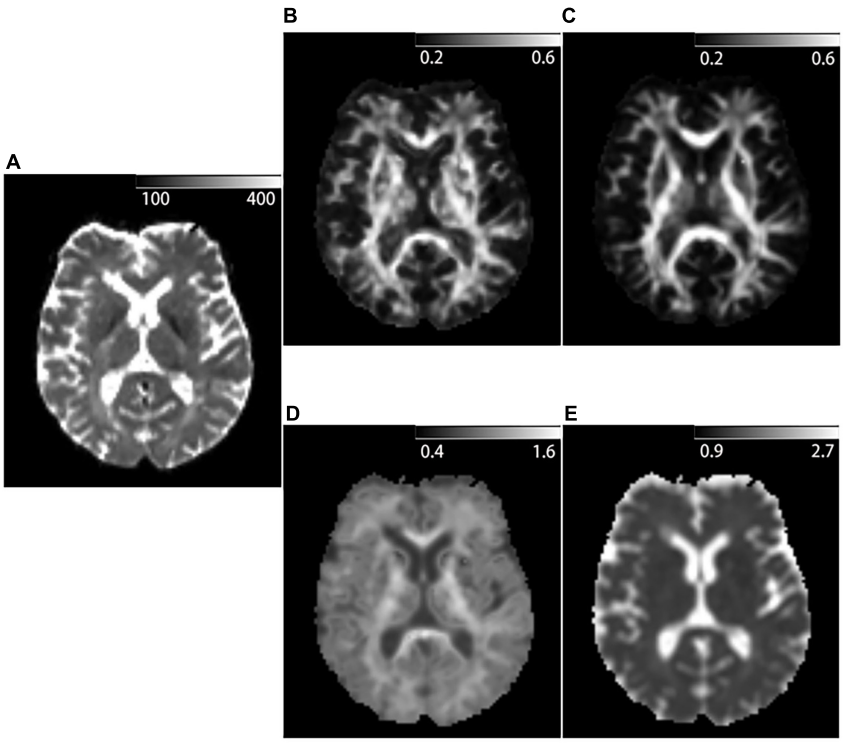

FIGURE 3 | Example of DKI-derived parametric maps of a 53-year-old patient diagnosed with Relapsing-remitting multiple sclerosis. **(A)** b = 0 mm^2/s image acquired with DKI sequence. **(B)** Kurtosis fractional anisotropy (KFA) parametric map acquired with DKI sequence. **(C)** Fractional anisotropy (FA) parametric map acquired with DKI sequence. **(D)** Mean kurtosis (MK) parametric map acquired with DKI sequence. **(E)** Mean diffusivity (MD) parametric map acquired with DKI sequence.

TABLE 1 | Demographic and clinical characteristics of the participants.

	RRMS patients	Healthy controls	*p*
No. of participants	48	26	
Age (years)	33.1 ± 9.2	37.0 ± 8.3	0.075[a]
Sex (male/female)	17/31	9/17	0.945[b]
DD (years)	5.4 ± 5.2	-	-
Education (years)	14.1 ± 2.9	14.3 ± 4.5	0.85[a]
EDSS scores	2.2 ± 1.3	-	-
MMSE scores	28.6 ± 1.6	29.3 ± 0.8	0.013[a]
MoCA scores	25.5 ± 3.5	27.4 ± 2.4	0.016[a]
SDMT scores	42.6 ± 17.3	53.2 ± 9.7	0.001[a]
T1LV (mm^3)	14,615.5 ± 11,939.4	-	-
T2LV (mm^3)	22,998.9 ± 19,421.2		-
Pure-T2LV (mm^3)	8,383.4 ± 8,571.3		-

[a]*p obtained using independent samples t-tests.*
[b]*p obtained using the Chi-square test.*
The data were shown as the mean values ± standard deviation.
DD, disease duration; EDSS, Expanded Disability Status Scale; MMSE, Mini-Mental State Examination; MoCA, Montreal Cognitive Assessment; SDMT, Symbol Digit Modalities Test.

Diffusion Kurtosis Imaging Parameter Analysis

The distribution of DKI parameter values in four tissue types is displayed in **Figure 4**. The four DKI parameter values were significantly different among the four tissue types, which are reported in **Table 2**. The *post hoc* analysis results are reported in **Table 3**. The lowest FA and MK values were shown in T1Ls, followed by pure-T2Ls, NAWM, and WM in HCs, and they were significant between each type of tissue ($p < 0.05$). Like the results of MK values, the lowest KFA and highest MD values were obtained in the T1Ls, followed by pure-T2Ls, NAWM, and WM in HCs. Except between T1Ls and pure-T2Ls in KFA ($p = 0.388$) and MD ($p = 1.000$) and between NAWM and WM in HCs in MD ($p = 0.671$), significant differences of KFA and MD values were found between every other two white matter tissue types ($p < 0.001$).

Correlations Between Imaging Parameters and Neuropsychological Scores

The MK values of pure-T2Ls ($r = 0.331$, $p = 0.024$) and the KFA, FA, MK, and MD values of NAWM ($r = 0.360$, $p = 0.014$; $r = 0.415$, $p = 0.004$; $r = 0.369$, $p = 0.012$; $r = -0.531$, $p < 0.001$) were correlated with the MMSE scores. The FA values of pure-T2Ls ($r = 0.309$, $p = 0.036$) were correlated with the MoCA scores. The FA and MK values of T1Ls ($r = 0.322$, $p = 0.029$; $r = 0.371$, $p = 0.011$), the FA and MK values of pure-T2Ls ($r = 0.355$, $p = 0.015$; $r = 0.400$, $p = 0.006$), and the FA, MK, and MD values of NAWM ($r = 0.423$, $p = 0.003$; $r = 0.427$, $p = 0.003$; $r = -0.359$, $p = 0.014$) were correlated with the SDMT scores.

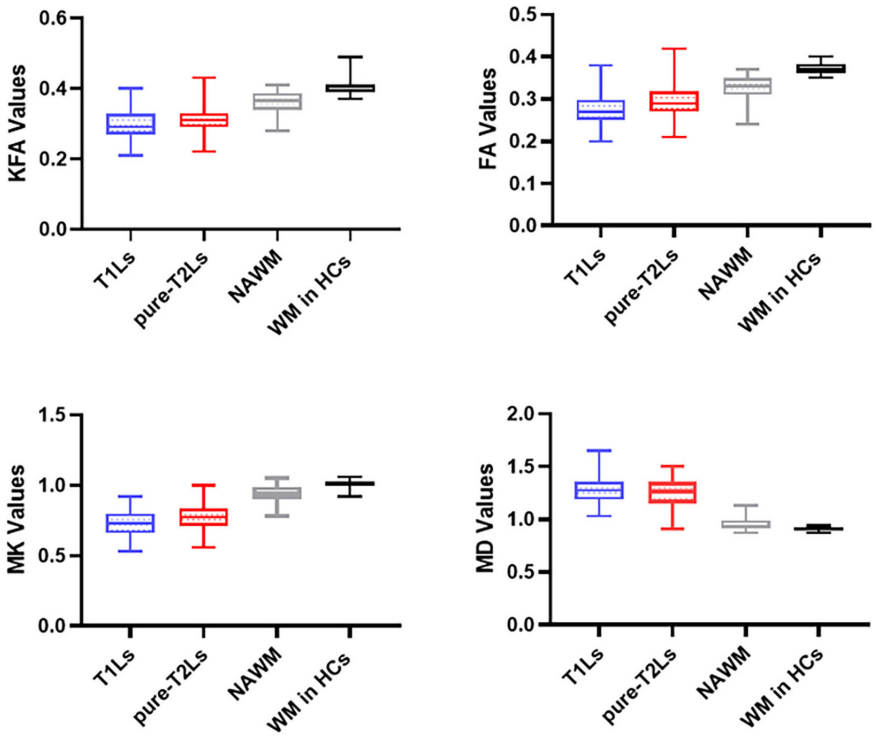

FIGURE 4 | Distribution of DKI parameters values in different white matter tissue types. T1Ls, T1-hypointense lesions; pure-T2Ls, pure T2-hyperintense lesions; NAWM, normal-appearing white matter; KFA, kurtosis fractional anisotropy; FA, fractional anisotropy; MK, mean kurtosis; MD, mean diffusivity.

TABLE 2 | The DKI parameter values analysis within the four white matter tissue types.

	KFA	FA	MK	MD
T1Ls (48)	0.295 ± 0.040	0.271 ± 0.039	0.727 ± 0.093	1.286 ± 0.142
Pure-T2Ls (48)	0.308 ± 0.036	0.295 ± 0.039	0.776 ± 0.090	1.256 ± 0.132
NAWM (48)	0.361 ± 0.030	0.327 ± 0.029	0.938 ± 0.064	0.949 ± 0.057
WM in HCs (26)	0.408 ± 0.027	0.372 ± 0.014	1.009 ± 0.029	0.907 ± 0.017
F	78.161	58.459	111.594	137.334
p	<0.001	<0.001	<0.001	<0.001

T1Ls, T1-hypointense lesions; pure-T2Ls, pure T2-hyperintense lesions; NAWM, normal-appearing white matter; WM in HCs, white matter in healthy controls; KFA, kurtosis fractional anisotropy; FA, fractional anisotropy; MK, mean kurtosis; MD, mean diffusivity.

TABLE 3 | *Post hoc* analysis between the DKI parameter values among the four white matter tissue types.

	KFA		FA		MK		MD	
	t	***p***	***t***	***p***	***t***	***p***	***t***	***p***
T1Ls vs. pure-T2Ls	−1.861	0.388	−3.620	0.002**	−3.112	0.013*	1.350	1
T1Ls vs. NAWM	−9.307	<0.001***	−8.194	<0.001***	−13.345	<0.001***	15.306	<0.001***
T1Ls vs. WM in HCs	−13.384	<0.001***	−12.386	<0.001***	−14.946	<0.001***	14.432	<0.001***
Pure-T2Ls vs. NAWM	−7.448	<0.001***	−4.575	<0.001***	−10.232	<0.001***	13.955	<0.001***
Pure-T2Ls vs. WM in HCs	−11.825	<0.001***	−9.352	<0.001***	−12.338	<0.001***	13.300	<0.001***
NAWM vs. WM in HCs	−5.582	<0.001***	−5.517	<0.001***	−3.763	<0.001***	1.599	0.671

*Statistical differences are *p < 0.05, **p < 0.01, ***p < 0.001.*
T1Ls, T1-hypointense lesions; pure-T2Ls, pure T2-hyperintense lesions; NAWM, normal-appearing white matter; WM in HCs, white matter in healthy controls; KFA, kurtosis fractional anisotropy; FA, fractional anisotropy; MK, mean kurtosis; MD, mean diffusivity.

TABLE 4 | Correlation between imaging parameters and clinical or cognitive assessment.

	EDSS(z)		MMSE(z)		MoCA(z)		SDMT(z)	
	r	*p*	*r*	*p*	*r*	*p*	*r*	*p*
T1LV	0.166	0.270	−0.178	0.238	−0.013	0.931	−0.360	0.014*
T2LV	0.185	0.21	−0.174	0.247	0.012	0.939	−0.409	0.005**
Pure-T2LV	0.119	0.433	−0.159	0.290	−0.046	0.761	−0.246	0.099
T1Ls_KFA	−0.115	0.445	0.056	0.712	0.093	0.538	0.000	1.000
T1Ls_FA	−0.167	0.266	0.148	0.325	0.076	0.617	0.322	0.029*
T1Ls_MK	−0.197	0.190	0.270	0.069	−0.070	0.643	0.371	0.011*
T1Ls_MD	−0.275	0.065	−0.237	0.113	0.124	0.411	−0.199	0.185
Pure-T2Ls_KFA	−0.062	0.680	0.097	0.522	0.278	0.061	0.740	0.627
Pure-T2Ls_FA	−0.112	0.458	0.218	0.146	0.309	0.036*	0.355	0.015*
Pure-T2Ls_MK	−0.099	0.513	0.331	0.024*	0.142	0.345	0.400	0.006**
Pure-T2Ls_MD	−0.150	0.321	−0.255	0.087	−0.086	0.570	−0.146	0.331
NAWM_KFA	−0.142	0.347	0.360	0.014*	0.267	0.073	0.261	0.080
NAWM_FA	−0.259	0.082	0.415	0.004**	0.176	0.241	0.423	0.003**
NAWM_MK	−0.157	0.296	0.369	0.012*	0.079	0.602	0.427	0.003**
NAWM_MD	−0.198	0.188	−0.531	<0.001***	−0.209	0.162	−0.359	0.014*

*Statistical differences are *p < 0.05, **p < 0.01, ***p < 0.001.*

T1LV, T1-hypointense lesions volume; T2LV, T2-hyperintense lesions volume; pure-T2LV, pure T2-hypointense lesions volume; T1Ls, T1-hypointense lesions; pure-T2Ls, pure T2-hyperintense lesions; NAWM, normal-appearing white matter; KFA, kurtosis fractional anisotropy; FA, fractional anisotropy; MK, mean kurtosis; MD, mean diffusivity; EDSS, Expanded Disability Status Scale; MMSE, Mini-Mental State Examination; MoCA, Montreal Cognitive Assessment; SDMT, Symbol Digit Modalities Test.

The T1LV ($r = -0.409$, $p = 0.005$) and T2LV ($r = -0.360$, $p = 0.014$) were correlated with the SDMT scores. There was no correlation between the DKI-derived parameters and the EDSS scores (**Table 4**).

DISCUSSION

In this study, we applied DKI to characterize the microstructural damage in the heterogeneity of different white matter areas and examine the correlations between the various degrees of DKI-derived parameter changes in different white matter types and the clinical or cognitive status. We found the lowest KFA, FA, and MK values, respectively, in T1Ls, followed by pure-T2Ls, NAWM, and WM in HCs. The highest MD values were found in T1Ls on the contrary, followed by pure-T2Ls, NAWM, and WM in HCs. We observed that the MK could be well-distinguished T1Ls and pure-T2Ls, as well as NAWM and WM in HCs. The results above indicated that the most severe microstructural damage occurred in T1Ls, which presented a different pathological state from pure-T2Ls. At the same time, NAWM was significantly different from WM in HCs, even if it had minor histopathological damage compared to focal lesions. Nevertheless, the damage degree reflected by DKI parameters in WMLs (T1Ls and pure-T2Ls) had little correlation with the clinical disability or cognitive impairment. Instead, DKI parameters in the NAWM were correlated with the cognitive status.

Previous studies have largely focused on the heterogeneity of different lesion types or tissue types in the white matter by using advanced MRI techniques. Faizy et al. (2016) have observed that different types of MS lesions showed significant differences by measuring myelin water fraction (MWF) values, presumably related to differences in the degree of tissue destruction. Lipp et al. (2019) quantified white matter damage *in vivo* by measuring fractional anisotropy (FA), radial diffusivity (RD), MWF, and magnetization transfer ratio (MTR) to differentiate the white matter tissue states in MS patients. Schiavi et al. (2021) used DBSI and DTI sequences of a 7-T scanner to investigate the pathology of different white matter tissue. Our present study was similar in lesion or white matter classifications with the previous studies above. However, the application of DKI based on ROI analysis in the different lesion or white matter categories is still rare.

DKI can characterize the non-Gaussian distribution of water molecules (Wu and Cheung, 2010). The diffusion kurtosis can reflect the deviation of water molecules from Gaussian distribution (Hui et al., 2008). The higher the diffusion kurtosis, the more the water molecule diffusion deviates from Gaussian distribution, indicating a more restricted diffusion and complex environment. KFA, one of the DKI-derived parameters, is similar to FA to some extent. However, KFA can better describe complex diffusion profiles due to the lesser non-isotropic diffusion effect and the high *b*-values of the DKI model (Lee et al., 2018; Li et al., 2021). Furthermore, it can also provide an essential complement for the poor performance of FA when the packing density of fiber bundles and axons increases (Karlsen et al., 2019). Notwithstanding, most studies did not use KFA values to evaluate white matter microstructure changes. Here, we utilized KFA values to investigate the varying degrees of microstructural damage in white matter and found that KFA values were the lowest in the most severe areas (T1Ls), just as FA values. However, FKA values are less sensitive in distinguishing the four types of white matter tissues than FA values in our

results. The difference in KFA values between T1Ls and pure-T2Ls did not reach significance. That may explain why only a few studies have used KFA values in detecting the white matter microstructure, even if KFA values can better describe the real biological tissue than FA values (Karlsen et al., 2019; Li et al., 2021). While the DKI-derived FA values in our study are in line with the previous studies (Yoshida et al., 2013; Lipp et al., 2019), the FA values were significantly different in each two types, respectively, between the four white matter tissue types.

Thaler et al. (2021) have emphasized the MK and MD values when applying DKI to the heterogeneity of MS lesions. Consistent with their findings, we found that the MK values offered a better discriminative effect than the MD values and might become a potential image biomarker in distinguishing the different lesion types. There was a significant difference in MK values between each two white matter tissue types, including between T1Ls and pure-T2Ls and between NAWM and WM in HCs. However, they did not observe a significant difference between NAWM and WM in HCs, which may be because they used a manually drawn ROIs-based approach to select eight regions of NAWM while we extracted the whole brain NAWM. Nevertheless, the MD values did not show good performance neither in distinguishing the two WMLs types nor in distinguishing NAWM and WM in HCs. Just as its name implies, MK values are the average kurtosis value in all directions, which can reflect the microstructure complexity and integrity (Grinberg et al., 2017). The decreased MK values indicated a shift of a diffusion kurtosis toward free water and compromised microstructure complexity (Coutu et al., 2014), which may be caused by axonal loss, myelin sheath damage, and the destruction of cellular components. Hence, the result of the lowest MK values in T1Ls showed the place where the most destructive white matter damage occurred. These findings demonstrated that DKI-derived parameters, especially the MK values, were closely linked to structural and intensity abnormalities seen on conventional MRI and were able to show abnormalities in NAWM that conventional MRI could not image for MS patients.

It is worth noting that most of the WMLs consist of T1Ls and pure-T2Ls in this work. T1Ls are in the center of these lesions, while pure-T2Ls are in the lesions' border. As previously mentioned, all the DKI-derived parameters were more altered in T1Ls, whether significantly or not, which means that the severe tissue damage and axon loss occurred in the center of the lesions while the white matter structure was more complex at the lesion's border. That relatively microstructure complexity in pure-T2Ls (WMLs' border) might result from activated microglia and macrophages at the rim of chronic active lesions (Dal-Bianco et al., 2017). This assumption was in line with the previous studies (Gillen et al., 2018; Schiavi et al., 2021) and could better explain the fact that the white matter areas of pure-T2Ls were presented differently on the two different sequences.

Furthermore, we sought to determine whether the DKI parameter values in the most severe areas (T1Ls) were related to the clinical or cognitive status. We used EDSS scores to reflect the clinical disability and neuropsychological scores such as MMSE, MoCA, and SDMT scores to reflect the cognitive functions. Disappointingly, the DKI parameter values were barely correlated with the clinical or cognitive status neither in T1Ls nor pure-T2Ls. These results might be explained by the experimental design. In this cross-sectional study, we only selected the image data at a certain time to draw the ROIs of WMLs instead of grouping newly arising lesions or persistent lesions since these two kinds of lesions contribute to clinical disability and cognitive impairment differently (Masek et al., 2008; Louapre et al., 2017). In our RRMS cohort, newly arising lesions, considered to be more related to the progression in clinical disability and cognitive impairment (Summers et al., 2008; Rovira et al., 2013; Eijlers et al., 2018), may only account for an extremely small proportion of all the inclusive WMLs. The EDSS scores reflect several domains including vision, speech, sensorimotor, and bladder function, lacking specificity, which may cause the poor correlation with the imaging parameters. However, most DKI parameter values in NAWM were related to the cognitive decline, mainly manifested by MMSE and SDMT scores. Previous studies have applied quantitative MRI to detect the injury of NAWM when exploring the cognitive impairment in patients with MS. At the same time, our results are consistent with previous myelin water imaging (MTI) and DTI studies. MTI has proved the efficacy in evaluating the relationship between NAWM myelin heterogeneity and cognitive processing speed performance by calculating the MWF (Abel et al., 2020). The loss of NAWM integrity has demonstrated the correlation with the cognitive impairment in a cohort of pediatric MS patients by measuring the DTI parameters (Bethune et al., 2011). Since NAWM is diffusely abnormal in patients with MS (Elliott et al., 2021) and has a more pronounced correlation with clinical progression (Filippi et al., 2012), DKI could become an effective tool to not only characterize widespread microstructural damage in the NAWM but also reflect the severity of the disease by imaging.

Moreover, among the four DKI-derived parameters, only MK values in T1Ls, pure-T2Ls, and NAWM ($p = 0.011$, $r = 0.371$; $p = 0.006$, $r = 0.400$; $p = 0.003$, $r = 0.427$) were correlated with the SDMT scores. To our knowledge, although de Kouchkovsky et al. (2016) reported that DKI-based white matter tract integrity (WMTI) in NAWM significantly correlated with SDMT scores, and DKI-based axonal water fraction (AWF) in NAWM associated with EDSS scores, while Nygaard et al. (2021) found that the DKI-derived parameters in cortex were associated with walking and cognitive performance, this is the first study to demonstrate that the widespread white matter damage (including WMLs and NAWM) in RRMS patients reflected by MK values is correlated with the cognitive status reflected by SDMT scores. Combined with the good performance of MK values in distinguishing the four tissue types mentioned above, therefore, MK values could be a potential biomarker to evaluate the white matter damage and its correlation with the cognitive impairment.

There are several limitations in our study. First, as previously mentioned, this is a cross-sectional study, and we could not detect the newly arising lesions and calculate the increase of the accumulation of lesions volume longitudinally. Further studies

will be needed to longitudinally compare the newly arising lesion microstructure changes with other white matter tissue types and investigate its relationship with the clinical progression. Second, we must admit the difficulty of obtaining pathological data. Since the pathological correlation was not available for our research group, we aimed to provide insights into clinico-radiological features avoiding pathology to evaluate the disease severity by the imaging parameters and find the potential biomarker of clinically relevant white matter injury. Last, in this work, we only used the DKI sequence to quantitatively evaluate the white matter microstructural damage. Other advanced MRI techniques such as T1 mapping, quantitative susceptibility mapping (QSM), ultra-short echo time (UTE), and MTR will be necessarily selected for further investigation.

CONCLUSION

In conclusion, our findings demonstrated the heterogeneity of white matter microstructure changes, which could be well-distinguished by DKI parameters. The damage in NAWM reflected by DKI parameters correlated to the cognitive impairment, and the MK value could be a potential biomarker to evaluate the white matter damage and its correlation with the cognitive impairment. This imaging-based classification in white matter may help evaluate the disease severity and progression.

DATA AVAILABILITY STATEMENT

The raw data supporting the conclusions of this article will be made available by the authors, without undue reservation.

ETHICS STATEMENT

The studies involving human participants were reviewed and approved by the Institutional Review Board of the First Affiliated Hospital of Chongqing Medical University, Chongqing, China. The patients/participants provided their written informed consent to participate in this study. Written informed consent was obtained from the individual(s) for the publication of any potentially identifiable images or data included in this article.

AUTHOR CONTRIBUTIONS

QZu and XC offered the research idea. QZu prepared the manuscript. XC and QZe offered the data processing support. XC and DL assisted in imaging processing. QZe assisted in completing the statistics and experimental design. QZe, XC, DL, YP, ZY, XW, and YL provided guidance and critical reviews. All authors contributed to the article and approved the submitted version.

FUNDING

This study was supported by the Key Project of Technological Innovation and Application Development of Chongqing Science and Technology Bureau (CSTC2021 jscx-gksb-N0008).

ACKNOWLEDGMENTS

We would like to thank all the subjects who participated in this study.

REFERENCES

Abel, S., Vavasour, I., Lee, L. E., Johnson, P., Ackermans, N., Chan, J., et al. (2020). Myelin damage in normal appearing white matter contributes to impaired cognitive processing speed in multiple sclerosis. *J. Neuroimaging* 30, 205–211. doi: 10.1111/jon.12679

Andersson, J. L., Skare, S., and Ashburner, J. (2003). How to correct susceptibility distortions in spin-echo echo-planar images: application to diffusion tensor imaging. *Neuroimage* 20, 870–888. doi: 10.1016/s1053-8119(03)00336-7

Andersson, J. L. R., Graham, M. S., Drobnjak, I., Zhang, H., Filippini, N., and Bastiani, M. (2017). Towards a comprehensive framework for movement and distortion correction of diffusion MR images: within volume movement. *Neuroimage* 152, 450–466. doi: 10.1016/j.neuroimage.2017.02.085

Ashburner, J., and Friston, K. J. (2000). Voxel-based morphometry–the methods. *Neuroimage* 11(6 Pt 1), 805–821. doi: 10.1006/nimg.2000.0582

Barkhof, F., Calabresi, P. A., Miller, D. H., and Reingold, S. C. (2009). Imaging outcomes for neuroprotection and repair in multiple sclerosis trials. *Nat. Rev. Neurol.* 5, 256–266. doi: 10.1038/nrneurol.2009.41

Bethune, A., Tipu, V., Sled, J. G., Narayanan, S., Arnold, D. L., Mabbott, D., et al. (2011). Diffusion tensor imaging and cognitive speed in children with multiple sclerosis. *J. Neurol. Sci.* 309, 68–74. doi: 10.1016/j.jns.2011.07.019

Coutu, J. P., Chen, J. J., Rosas, H. D., and Salat, D. H. (2014). Non-Gaussian water diffusion in aging white matter. *Neurobiol. Aging.* 35, 1412–1421. doi: 10.1016/j.neurobiolaging.2013.12.001

Dal-Bianco, A., Grabner, G., Kronnerwetter, C., Weber, M., Höftberger, R., Berger, T., et al. (2017). Slow expansion of multiple sclerosis iron rim lesions: pathology and 7 T magnetic resonance imaging. *Acta Neuropathol.* 133, 25–42. doi: 10.1007/s00401-016-1636-z

de Kouchkovsky, I., Fieremans, E., Fleysher, L., Herbert, J., Grossman, R. I., and Inglese, M. (2016). Quantification of normal-appearing white matter tract integrity in multiple sclerosis: a diffusion kurtosis imaging study. *J. Neurol.* 263, 1146–1155. doi: 10.1007/s00415-016-8118-z

Eijlers, A. J. C., van Geest, Q., Dekker, I., Steenwijk, M. D., Meijer, K. A., Hulst, H. E., et al. (2018). Predicting cognitive decline in multiple sclerosis: a 5-year follow-up study. *Brain* 141, 2605–2618. doi: 10.1093/brain/awy202

Elliott, C., Momayyezsiahkal, P., Arnold, D. L., Liu, D., Ke, J., Zhu, L., et al. (2021). Abnormalities in normal-appearing white matter from which multiple sclerosis lesions arise. *Brain Commun.* 3:fcab176. doi: 10.1093/braincomms/fcab176

Evangelou, N., Esiri, M. M., Smith, S., Palace, J., and Matthews, P. M. (2000). Quantitative pathological evidence for axonal loss in normal appearing white matter in multiple sclerosis. *Ann. Neurol.* 47, 391–395.

Faizy, T. D., Thaler, C., Kumar, D., Sedlacik, J., Broocks, G., Grosser, M., et al. (2016). Heterogeneity of multiple sclerosis lesions in multislice

myelin water imaging. *PLoS One.* 11:e0151496. doi: 10.1371/journal.pone.0151496

Falangola, M. F., Guilfoyle, D. N., Tabesh, A., Hui, E. S., Nie, X., Jensen, J. H., et al. (2014). Histological correlation of diffusional kurtosis and white matter modeling metrics in cuprizone-induced corpus callosum demyelination. *NMR Biomed.* 27, 948–957. doi: 10.1002/nbm.3140

Filippi, M., Preziosa, P., and Rocca, M. A. (2018). MRI in multiple sclerosis: what is changing? *Curr. Opin. Neurol.* 31, 386–395.

Filippi, M., Rocca, M. A., Barkhof, F., Brück, W., Chen, J. T., Comi, G., et al. (2012). Association between pathological and MRI findings in multiple sclerosis. *Lancet Neurol.* 11, 349–360. doi: 10.1016/s1474-4422(12)70003-0

Gillen, K. M., Mubarak, M., Nguyen, T. D., and Pitt, D. (2018). Significance and *in vivo* detection of iron-laden microglia in white matter multiple sclerosis lesions. *Front. Immunol.* 9:255. doi: 10.3389/fimmu.2018.00255

Glenn, G. R., Helpern, J. A., Tabesh, A., and Jensen, J. H. (2015). Quantitative assessment of diffusional kurtosis anisotropy. *NMR Biomed.* 28, 448–459. doi: 10.1002/nbm.3271

Grinberg, F., Maximov, I. I., Farrher, E., Neuner, I., Amort, L., Thönneßen, H., et al. (2017). Diffusion kurtosis metrics as biomarkers of microstructural development: a comparative study of a group of children and a group of adults. *Neuroimage* 144, 12–22. doi: 10.1016/j.neuroimage.2016.08.033

Guglielmetti, C., Veraart, J., Roelant, E., Mai, Z., Daans, J., Van Audekerke, J., et al. (2016). Diffusion kurtosis imaging probes cortical alterations and white matter pathology following cuprizone induced demyelination and spontaneous remyelination. *Neuroimage* 125, 363–377. doi: 10.1016/j.neuroimage.2015.10.052

Hui, E. S., Cheung, M. M., Qi, L., and Wu, E. X. (2008). Towards better MR characterization of neural tissues using directional diffusion kurtosis analysis. *Neuroimage* 42, 122–134. doi: 10.1016/j.neuroimage.2008.04.237

Jenkinson, M., Beckmann, C. F., Behrens, T. E., Woolrich, M. W., and Smith, S. M. (2012). FSL *Neuroimage* 62, 782–790. doi: 10.1016/j.neuroimage.2011.09.015

Jensen, J. H., Helpern, J. A., Ramani, A., Lu, H., and Kaczynski, K. (2005). Diffusional kurtosis imaging: the quantification of non-gaussian water diffusion by means of magnetic resonance imaging. *Magn. Reson Med.* 53, 1432–1440. doi: 10.1002/mrm.20508

Karlsen, R. H., Einarsen, C., Moe, H. K., Håberg, A. K., Vik, A., Skandsen, T., et al. (2019). Diffusion kurtosis imaging in mild traumatic brain injury and postconcussional syndrome. *J. Neurosci. Res.* 97, 568–581. doi: 10.1002/jnr.24383

Kellner, E., Dhital, B., Kiselev, V. G., and Reisert, M. (2016). Gibbs-ringing artifact removal based on local subvoxel-shifts. *Magn. Reson Med.* 76, 1574–1581. doi: 10.1002/mrm.26054

Lee, J. J., Chang, W. N., Hsu, J. L., Huang, C. W., Chang, Y. T., Hsu, S. W., et al. (2018). Diffusion kurtosis imaging as a neuroimaging biomarker in patients with carbon monoxide intoxication. *Neurotoxicology.* 68, 38–46. doi: 10.1016/j.neuro.2018.07.001

Leemans, A., and Jones, D. K. (2009). The B-matrix must be rotated when correcting for subject motion in DTI data. *Magn. Reson Med.* 61, 1336–1349. doi: 10.1002/mrm.21890

Li, T., Zhang, Y., Fu, X., Zhang, X., Luo, Y., and Ni, H. (2021). Microstructural white matter alterations in Alzheimer's disease and amnestic mild cognitive impairment and its diagnostic value based on diffusion kurtosis imaging: a tract-based spatial statistics study. *Brain Imaging Behav.* 16, 31–42. doi: 10.1007/s11682-021-00474-z

Lipp, I., Jones, D. K., Bells, S., Sgarlata, E., Foster, C., Stickland, R., et al. (2019). Comparing MRI metrics to quantify white matter microstructural damage in multiple sclerosis. *Hum. Brain Mapp.* 40, 2917–2932. doi: 10.1002/hbm.24568

Louapre, C., Bodini, B., Lubetzki, C., Freeman, L., and Stankoff, B. (2017). Imaging markers of multiple sclerosis prognosis. *Curr. Opin. Neurol.* 30, 231–236. doi: 10.1097/wco.0000000000000456

MacKay, A., Laule, C., Vavasour, I., Bjarnason, T., Kolind, S., and Mädler, B. (2006). Insights into brain microstructure from the T2 distribution. *Magn. Reson Imaging.* 24, 515–525. doi: 10.1016/j.mri.2005.12.037

Margoni, M., Petracca, M., Schiavi, S., Fabian, M., Miller, A., Lublin, F. D., et al. (2019). Axonal water fraction as marker of white matter injury in primary-progressive multiple sclerosis: a longitudinal study. *Eur. J. Neurol.* 26, 1068–1074. doi: 10.1111/ene.13937

Masek, M., Vaneckova, M., Krasensky, J., Danes, J., Havrdova, E., Hrebikova, T., et al. (2008). Secondary-progressive form of multiple sclerosis: MRI changes versus clinical status. *Neuro. Endocrinol. Lett.* 29, 461–466.

Nygaard, M. K. E., Langeskov-Christensen, M., Dalgas, U., and Eskildsen, S. F. (2021). Cortical diffusion kurtosis imaging and thalamic volume are associated with cognitive and walking performance in relapsing-remitting multiple sclerosis. *J. Neurol.* 268, 3861–3870. doi: 10.1007/s00415-021-10543-4

Polman, C. H., Reingold, S. C., Banwell, B., Clanet, M., Cohen, J. A., Filippi, M., et al. (2011). Diagnostic criteria for multiple sclerosis: 2010 revisions to the McDonald criteria. *Ann. Neurol.* 69, 292–302. doi: 10.1002/ana.22366

Reich, D. S., Lucchinetti, C. F., and Calabresi, P. A. (2018). Multiple sclerosis. *N. Engl. J. Med.* 378, 169–180. doi: 10.1056/NEJMra1401483

Rovira, A., Auger, C., and Alonso, J. (2013). Magnetic resonance monitoring of lesion evolution in multiple sclerosis. *Ther. Adv. Neurol. Disord.* 6, 298–310. doi: 10.1177/1756285613484079

Schiavi, S., Petracca, M., Sun, P., Fleysher, L., Cocozza, S., El Mendili, M. M., et al. (2021). Non-invasive quantification of inflammation, axonal and myelin injury in multiple sclerosis. *Brain* 144, 213–223. doi: 10.1093/brain/awaa381

Schmidt, P., Gaser, C., Arsic, M., Buck, D., Förschler, A., Berthele, A., et al. (2012). An automated tool for detection of FLAIR-hyperintense white-matter lesions in multiple sclerosis. *Neuroimage* 59, 3774–3783.

Steven, A. J., Zhuo, J., and Melhem, E. R. (2014). Diffusion kurtosis imaging: an emerging technique for evaluating the microstructural environment of the brain. *AJR Am. J. Roentgenol.* 202, W26–W33. doi: 10.2214/ajr.13.11365

Summers, M., Swanton, J., Fernando, K., Dalton, C., Miller, D. H., Cipolotti, L., et al. (2008). Cognitive impairment in multiple sclerosis can be predicted by imaging early in the disease. *J. Neurol. Neurosurg. Psychiatry.* 79, 955–958.

Tabesh, A., Jensen, J. H., Ardekani, B. A., and Helpern, J. A. (2011). Estimation of tensors and tensor-derived measures in diffusional kurtosis imaging. *Magn. Reson. Med.* 65, 823–836. doi: 10.1002/mrm.22655

Thaler, C., Faizy, T., Sedlacik, J., Holst, B., Stellmann, J. P., Young, K. L., et al. (2015). T1- thresholds in black holes increase clinical-radiological correlation in multiple sclerosis patients. *PLoS One.* 10:e0144693. doi: 10.1371/journal.pone.0144693

Thaler, C., Kyselyova, A. A., Faizy, T. D., Nawka, M. T., Jespersen, S., Hansen, B., et al. (2021). Heterogeneity of multiple sclerosis lesions in fast diffusional kurtosis imaging. *PLoS One.* 16:e0245844. doi: 10.1371/journal.pone.0245844

Thompson, A. J., Banwell, B. L., Barkhof, F., Carroll, W. M., Coetzee, T., Comi, G., et al. (2018). Diagnosis of multiple sclerosis: 2017 revisions of the McDonald criteria. *Lancet Neurol.* 17, 162–173. doi: 10.1016/s1474-4422(17)30470-2

Tournier, J. D., Smith, R., Raffelt, D., Tabbara, R., Dhollander, T., Pietsch, M., et al. (2019). MRtrix3: a fast, flexible and open software framework for medical image processing and visualisation. *Neuroimage.* 202:116137. doi: 10.1016/j.neuroimage.2019.116137

Tuch, D. S., Reese, T. G., Wiegell, M. R., and Wedeen, V. J. (2003). Diffusion MRI of complex neural architecture. *Neuron* 40, 885–895. doi: 10.1016/s0896-6273(03)00758-x

Veraart, J., Novikov, D. S., Christiaens, D., Ades-Aron, B., Sijbers, J., and Fieremans, E. (2016). Denoising of diffusion MRI using random matrix theory. *Neuroimage* 142, 394–406. doi: 10.1016/j.neuroimage.2016.08.016

Wolinsky, J. S., Narayana, P. A., Nelson, F., Datta, S., O'Connor, P., Confavreux, C., et al. (2013). Magnetic resonance imaging outcomes from a phase III trial of teriflunomide. *Mult. Scler.* 19, 1310–1319. doi: 10.1177/1352458513475723

Wu, E. X., and Cheung, M. M. (2010). MR diffusion kurtosis imaging for neural tissue characterization. *NMR Biomed.* 23, 836–848. doi: 10.1002/nbm.1506

Ye, Z., George, A., Wu, A. T., Niu, X., Lin, J., Adusumilli, G., et al. (2020). Deep learning with diffusion basis spectrum imaging for classification of multiple sclerosis lesions. *Ann. Clin. Transl. Neurol.* 7, 695–706. doi: 10.1002/acn3.51037

Yoshida, M., Hori, M., Yokoyama, K., Fukunaga, I., Suzuki, M., Kamagata, K., et al. (2013). Diffusional kurtosis imaging of normal-appearing white matter in multiple sclerosis: preliminary clinical experience. *Jpn J. Radiol.* 31, 50–55. doi: 10.1007/s11604-012-0147-7

Yushkevich, P. A., Piven, J., Hazlett, H. C., Smith, R. G., Ho, S., Gee, J. C., et al. (2006). User-guided 3D active contour segmentation of anatomical structures:

significantly improved efficiency and reliability. *Neuroimage* 31, 1116–1128. doi: 10.1016/j.neuroimage.2006.01.015

Conflict of Interest: The authors declare that the research was conducted in the absence of any commercial or financial relationships that could be construed as a potential conflict of interest.

Publisher's Note: All claims expressed in this article are solely those of the authors and do not necessarily represent those of their affiliated organizations, or those of the publisher, the editors and the reviewers. Any product that may be evaluated in this article, or claim that may be made by its manufacturer, is not guaranteed or endorsed by the publisher.

frontiers in Neuroscience

REVIEW
published: 31 March 2022
doi: 10.3389/fnins.2022.807473

Recent Advances in the Modeling of Alzheimer's Disease

Hiroki Sasaguri[1], Shoko Hashimoto[1], Naoto Watamura[1], Kaori Sato[1,2], Risa Takamura[1,2], Kenichi Nagata[3], Satoshi Tsubuki[1], Toshio Ohshima[2], Atsushi Yoshiki[4], Kenya Sato[1,5], Wakako Kumita[1,5], Erika Sasaki[5,6], Shinobu Kitazume[7], Per Nilsson[8], Bengt Winblad[8], Takashi Saito[9,10], Nobuhisa Iwata[11]* and Takaomi C. Saido[1]**

[1] Laboratory for Proteolytic Neuroscience, RIKEN Center for Brain Science, Wako, Japan, [2] Laboratory for Molecular Brain Science, Department of Life Science and Medical Bioscience, Waseda University, Shinjuku City, Japan, [3] Department of Functional Anatomy and Neuroscience, Nagoya University Graduate School of Medicine, Nagoya, Japan, [4] Experimental Animal Division, RIKEN BioResource Research Center, Tsukuba, Japan, [5] Department of Marmoset Biology and Medicine, Central Institute for Experimental Animals, Kawasaki, Japan, [6] Laboratory for Marmoset Neural Architecture, RIKEN Center for Brain Science, Wako, Japan, [7] Department of Clinical Laboratory Sciences, School of Health Sciences, Fukushima Medical University, Fukushima, Japan, [8] Division of Neurogeriatrics, Department of Neurobiology, Care Sciences and Society, Bioclinicum, Karolinska Institutet, Stockholm, Sweden, [9] Department of Neurocognitive Science, Institute of Brain Science, Nagoya City University Graduate School of Medical Sciences, Nagoya, Japan, [10] Department of Neuroscience and Pathobiology, Research Institute of Environmental Medicine, Nagoya University, Nagoya, Japan, [11] Department of Genome-Based Drug Discovery and Leading Medical Research Core Unit, Graduate School of Biomedical Sciences, Nagasaki University, Nagasaki, Japan

OPEN ACCESS

Edited by:
Brian Hansen,
Aarhus University, Denmark

Reviewed by:
Eugenio Gutiérrez Jiménez,
Aarhus University, Denmark
Yingjun Zhao,
Xiamen University, China

***Correspondence:**
Takashi Saito
saito-t@med.nagoya-cu.ac.jp
Nobuhisa Iwata
iwata-n@nagasaki-u.ac.jp
Takaomi C. Saido
takaomi.saido@riken.jp

Specialty section:
This article was submitted to Neurodegeneration, a section of the journal Frontiers in Neuroscience

Received: 02 November 2021
Accepted: 22 February 2022
Published: 31 March 2022

Citation:
Sasaguri H, Hashimoto S, Watamura N, Sato K, Takamura R, Nagata K, Tsubuki S, Ohshima T, Yoshiki A, Sato K, Kumita W, Sasaki E, Kitazume S, Nilsson P, Winblad B, Saito T, Iwata N and Saido TC (2022) Recent Advances in the Modeling of Alzheimer's Disease. Front. Neurosci. 16:807473. doi: 10.3389/fnins.2022.807473

Since 1995, more than 100 transgenic (Tg) mouse models of Alzheimer's disease (AD) have been generated in which mutant amyloid precursor protein (APP) or APP/presenilin 1 (PS1) cDNA is overexpressed (***1st generation models***). Although many of these models successfully recapitulate major pathological hallmarks of the disease such as amyloid β peptide (Aβ) deposition and neuroinflammation, they have suffered from artificial phenotypes in the form of overproduced or mislocalized APP/PS1 and their functional fragments, as well as calpastatin deficiency-induced early lethality, calpain activation, neuronal cell death without tau pathology, endoplasmic reticulum stresses, and inflammasome involvement. Such artifacts bring two important uncertainties into play, these being (1) why the artifacts arise, and (2) how they affect the interpretation of experimental results. In addition, destruction of endogenous gene loci in some Tg lines by transgenes has been reported. To overcome these concerns, single *App* knock-in mouse models harboring the Swedish and Beyreuther/Iberian mutations with or without the Arctic mutation (App^{NL-G-F} and App^{NL-F} mice) were developed (***2nd generation models***). While these models are interesting given that they exhibit Aβ pathology, neuroinflammation, and cognitive impairment in an age-dependent manner, the model with the Artic mutation, which exhibits an extensive pathology as early as 6 months of age, is not suitable for investigating Aβ metabolism and clearance because the Aβ in this model is resistant to proteolytic degradation and is therefore prone to aggregation. Moreover, it cannot be used for preclinical immunotherapy studies owing to the discrete affinity it shows for anti-Aβ antibodies. The weakness of the latter model (without the Arctic mutation) is that the pathology may require up to 18 months before it becomes sufficiently apparent for experimental investigation.

Nevertheless, this model was successfully applied to modulating Aβ pathology by genome editing, to revealing the differential roles of neprilysin and insulin-degrading enzyme in Aβ metabolism, and to identifying somatostatin receptor subtypes involved in Aβ degradation by neprilysin. In addition to discussing these issues, we also provide here a technical guide for the application of *App* knock-in mice to AD research. Subsequently, a new double knock-in line carrying the App^{NL-F} and $Psen1^{P117L/WT}$ mutations was generated, the pathogenic effect of which was found to be synergistic. A characteristic of this ***3rd generation model*** is that it exhibits more cored plaque pathology and neuroinflammation than the App^{NL-G-F} line, and thus is more suitable for preclinical studies of disease-modifying medications targeting Aβ. Furthermore, a derivative App^{G-F} line devoid of Swedish mutations which can be utilized for preclinical studies of β-secretase modifier(s) was recently created. In addition, we introduce a new model of cerebral amyloid angiopathy that may be useful for analyzing amyloid-related imaging abnormalities that can be caused by anti-Aβ immunotherapy. Use of the *App* knock-in mice also led to identification of the α-endosulfine-K_{ATP} channel pathway as components of the somatostatin-evoked physiological mechanisms that reduce Aβ deposition *via* the activation of neprilysin. Such advances have provided new insights for the prevention and treatment of preclinical AD. Because tau pathology plays an essential role in AD pathogenesis, knock-in mice with human tau wherein the entire murine *Mapt* gene has been humanized were generated. Using these mice, the carboxy-terminal PDZ ligand of neuronal nitric oxide synthase (CAPON) was discovered as a mediator linking tau pathology to neurodegeneration and showed that tau humanization promoted pathological tau propagation. Finally, we describe and discuss the current status of mutant human tau knock-in mice and a non-human primate model of AD that we have successfully created.

Keywords: Alzheimer's disease, amyloid – beta, amyloidosis, tau propagation, somatostatin, mouse model, non-human primate (NHP)

1st, 2nd, AND 3rd GENERATION MOUSE MODELS OF ALZHEIMER'S DISEASE

The deposition of amyloid β peptide (Aβ) in the brain is the major pathological hallmark of Alzheimer's disease (AD), which is considered the most common type of dementia in the world (Karran and De Strooper, 2016; Selkoe and Hardy, 2016). To date, disease-associated mutations in the *presenilin 1* (*PSEN1*) and *presenilin 2* (*PSEN2*) genes number more than 300, while more than 50 mutations have been reported in the *amyloid precursor protein* (*APP*) gene (Alzforum[1]). In response to these findings, many transgenic mouse models overexpressing mutant APP or APP/PSEN1 cDNAs have been developed (**1st generation models**) (Sasaguri et al., 2017), however they often suffer from experimental limitations resulting from the mislocalization of APP (**Figure 1**) and by the overproduction of APP fragments such as the C-terminal fragment of APP generated by β-secretase (CTF-β) and APP intracellular domain (AICD). Neither of these fragments appears to accumulate in AD brains, meaning that artificial endosomal abnormalities (Kwart et al., 2019) and transcriptional malfunctions (Nalivaeva et al., 2014), respectively, may be induced. Other overexpression artifacts include calpain activation (Saito et al., 2016), calpastatin deficiency-induced early lethality (Higuchi et al., 2012), and endoplasmic reticulum stresses (Hashimoto et al., 2018). Furthermore, it was demonstrated that the random insertion of transgene(s) resulted in the destruction of unexpectedly large regions of endogenous gene loci in the host animal (Gamache et al., 2019). We suggest that all transgenic mouse models being used in research in which APP or APP/PSEN1 are overexpressed should undergo whole genome sequencing (WGS) so that destroyed loci that possibly affect their phenotypes can be identified (Sasaguri et al., 2017).

To overcome these drawbacks, single *App* knock-in mice, i.e., $App^{NL-G-F/NLG-F}$ knock-in (App^{NL-G-F}) and $App^{NL-F/NL-F}$ knock-in (App^{NL-F}) lines, were generated that harbor the Swedish (KM670/671NL) (Citron et al., 1992; Mullan et al., 1992) and Beyreuther/Iberian (I716F) (Lichtenthaler et al., 1999) mutations with or without the Arctic (E693G) (Nilsberth et al., 2001) mutation (**2nd generation models**) (**Figure 2**) (Saito et al., 2014; Sasaguri et al., 2017). These mice, which exhibit typical Aβ pathology, neuroinflammation and memory impairment

[1]http://www.alzforum.org

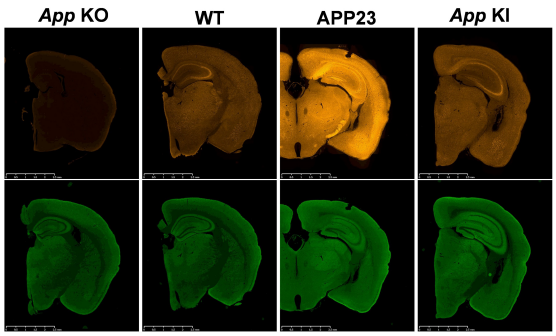

FIGURE 1 | Mislocalization of APP in APP-overexpressing mice. *App* KO mice, WT mice, APP23 (APP-overexpressing mice) and *App* KI mice ($App^{NL-F/NL-F}$) were subjected to immunohistochemistry using antibodies to APP, 22C11 **(upper panels)** and synaptophysin, a synaptic vesicle marker **(lower panels)** as indicated. *App* KO mice were used as negative controls for APP staining. While APP is selectively expressed in the axons of WT and KI mice, APP23 expresses unphysiologically high levels of APP not only in the axons but also in the soma and dendrites. The scale bar indicates 2 mm.

(Saito et al., 2014; Masuda et al., 2016), are being used in more than 500 research laboratories world-wide. At present, the App^{NL-G-F} line is being used more frequently than the App^{NL-F} line given that it develops Aβ pathology approximately three times faster (Saito et al., 2014) and can be used to analyze downstream events such as neuroinflammation (Shirotani et al., 2019; Chen et al., 2020; Sobue et al., 2021), pericyte signaling (Nortley et al., 2019), oxidative stress (Hashimoto et al., 2019; Hongo et al., 2020; Uruno et al., 2020), tau propagation (Saito et al., 2019), and spatial memory impairment (Masuda et al., 2016; Jun et al., 2020; Sutoko et al., 2021; **Table 1**). Human Arctic mutation carriers are indistinguishable from other familial and sporadic AD patients in pathological and neurological terms except for low retention of ^{11}C-labeled Pittsburgh compound B (PiB) in PET study (Basun et al., 2008), indicating that the mutant mice are relevant models for studying AD in general.

In addition to App^{NL-F} and App^{NL-G-F} models, *App* knock-in mice devoid of the Swedish mutations (App^{G-F} mice) have been recently developed, in which the Swedish mutations (NL) were replaced by a wild-type sequence (KM) (**Figure 3** and **Table 2**). The App^{G-F} mice are more suitable for preclinical studies of β-secretase inhibition given that the Swedish mutation affects the reactivity of APP to β-site amyloid precursor protein cleaving enzyme 1 (BACE1) and most AD patients do not carry Swedish mutations (Watamura et al., 2021b).

Despite the advantages mentioned above, the App^{NL-G-F} line is not suitable for investigating the metabolism, clearance or deposition of Aβ because the Arctic mutation present in the middle of the Aβ sequence results in an Aβ that is resistant to proteolytic degradation (Tsubuki et al., 2003) and susceptible to aggregation (Nilsberth et al., 2001). Moreover, this model is not suitable for use in preclinical immunotherapy studies due to its affinity for anti-Aβ antibodies, even in the presence of guanidine hydrochloride (GuHCl) (Saito et al., 2014). The Arctic mutation may also directly or indirectly interfere with interactions between Aβ deposition and the apolipoprotein E genotype (Morishima-Kawashima et al., 2000), although there is no experimental evidence for this. In contrast, the App^{NL-F} line accumulates wild-type human Aβ, but it may take up to 18 months for the pathology to become sufficiently evident for investigational studies to be carried out (Saito et al., 2014), which is too long for researchers to wait in a practical sense. Therefore, a new mouse model that accumulates wild-type human Aβ as quickly as the App^{NL-G-F} model, but did not depend on the presence of the Arctic mutation was desired.

To achieve this, the heterozygous $Psen1^{P117L/WT}$ mutant line ($Psen1^{P117L}$) which, of the several *Psen1* mutants, exhibits the largest increase in $Aβ_{42}/Aβ_{40}$ ratio in the brain (Sasaguri et al., 2018) was utilized. The $Psen1^{P117L}$ line was generated by base editing technology (Komor et al., 2016). The App^{NL-F} mice were crossed with $Psen1^{P117L}$ mice, despite it being unclear whether their pathogenic effects, both of which act on the γ-cleavage of CTF-β, would be additive or not *in vivo* (**Figure 4**). The pathological phenotypes of App^{NL-F} mice were markedly enhanced in a synergistic manner with the $Psen1^{P117L}$ mutation (Sato et al., 2021), with App^{NL-F} X $Psen1^{P117L/WT}$ mice showing a more aggressive cored plaque pathology and neuroinflammation than the App^{NL-G-F} mice (**Figure 5**). These double mutant mice (**3rd generation model**) will likely become highly relevant tools for examining the pathologic mechanisms upstream of Aβ deposition. Moreover, these mice can be highly useful for the preclinical screening of disease-modifying therapy candidates promoting Aβ degradation or disaggregation, without the added concern associated with artificial effects caused by the Arctic mutation. We expect the double homozygous line, App^{NL-F} X $Psen1^{P117L/P117L}$, to exhibit an even more-aggressive pathology. In any case, the App^{NL-F} X $Psen1^{P117L}$ mice are superior to the App^{NL-G-F} mice or the App^{NL-G-I} mice (Xia et al., 2021) for universal and unbiased drug screening particularly because the Aβ-degrading enzyme, neprilysin (NEP: Neutral endopeptidase), has become a therapeutic target. The App^{NL-G-I} mice are similarly designed as the App^{NL-G-F} mice, in which the Beyreuther/Iberian mutation was replaced by the Austrian mutation (Kumar-Singh et al., 2000). The characteristics of the *App* knock-in mouse lines are listed in **Table 3**.

PRECAUTIONS REGARDING THE UTILITY OF *App* KNOCK-IN MICE

There are several precautions to be aware of to make the best use of the *App* knock-in mice.

Nomenclature

A number of the *App* knock-in mouse users use incorrect nomenclature such as APP-NLF, APP^{NLF} and APP^{NL-F} instead of the App^{NL-F} mice, which accords with international rules of standard genomic nomenclature. Genetic names always need to be italicized.

Line-Ups and Biochemical Analyses

Approximately 20 lines of mutant mice, published or unpublished, can currently or in the very near future be

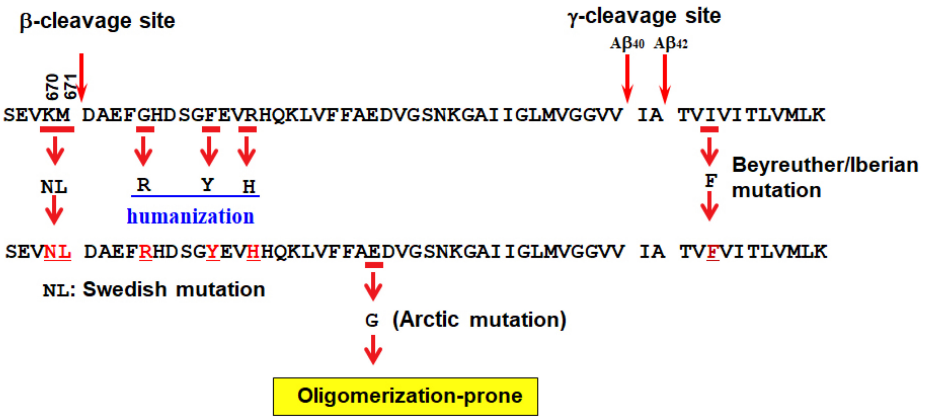

FIGURE 2 | Second generation mouse models of Alzheimer's disease. See text for detailed explanation.

TABLE 1 | Successful application of the 2nd generation mouse models.

(1) Behavioral analysis using IntelliCage (Masuda et al., 2016; Sutoko et al., 2021).
(2) Three-dimensional visualization of amyloid pathology by transparency (Hama et al., 2015; Susaki et al., 2020).
(3) Impairment of gamma oscillations in medial entorhinal cortex (Nakazono et al., 2017).
(4) Additional genetic manipulation of the 2nd generation models through genome editing (Nagata et al., 2018; Watamura et al., 2021b).
(5) Generation of the double knock-in mouse models (Hashimoto et al., 2019; Saito et al., 2019; Sato et al., 2021).
(6) Assessment of vascular dysfunction in the 2nd generation models (Nortley et al., 2019; Tachida et al., 2020).
(7) Assessment of sleep dysfunction in the 2nd generation models (Maezono et al., 2020).
(8) Assessment of place cell dysfunction in the 2nd generation models (Jun et al., 2020; Takamura et al., 2021).
(9) Analyses of various aspects of neuroinflammation (Shirotani et al., 2019; Chiasseu et al., 2020; Salobrar-García et al., 2020; Barrett et al., 2021; Sobue et al., 2021).
(10) Application of spatial transcriptomics (Chen et al., 2020).

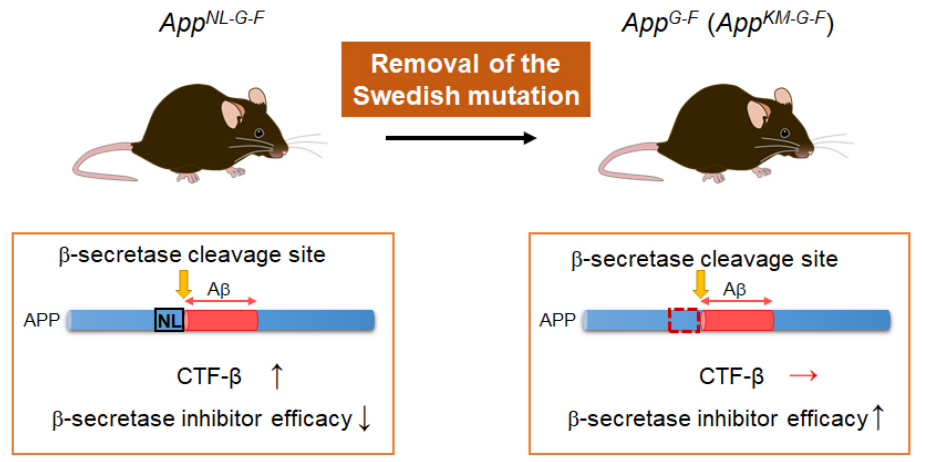

FIGURE 3 | App^{G-F} mice suitable for studies of BACE1 inhibitors. The App^{G-F} line is devoid of the Swedish mutation that influences the β-secretase activity and elevates the quantity of CTFβ. (The App^{G-F} line instead carries a wild-type sequence: KM.) The App^{G-F} model would be appropriate for use in preclinical studies of β-secretase inhibitors without the interference of the Swedish mutation.

provided to academic and not-for-profit researchers for non-commercial research in a timely fashion with minimum restrictions (**Table 2**; Saito et al., 2014; Sasaguri et al., 2018). It is also recommended that scientists use optimized protocols for isolating Aβ from animal brain as previously described (Iwata et al., 2005; **Figure 6**). The method allows the most sensitive quantification of both soluble and insoluble Aβ with the smallest protocol deviations.

TABLE 2 | List of mutant mice that are and will be made available to the research community.

Strains	Gene(s)	Modification Information	Availability*[5]	References*[5]
App^{NL} KI	*App*[*1]	KM670/671NL (Swedish)	RBRC[*6] (RBRC06342)	Saito et al., 2014
App^{NL-F} KI	*App*[*1]	KM670/671NL (Swedish), I716F (Iberian/Beyreuther)	RBRC (RBRC06343)	Saito et al., 2014
App^{NL-G-F} KI	*App*[*1]	KM670/671NL (Swedish), E693G (Arctic), I716F (Iberian/Beyreuther)	RBRC (RBRC06344)	Saito et al., 2014
App^{G-F} KI	*App*[*1]	E693G (Arctic), I716F (Iberian/Beyreuther)	Soon to be available from RBRC	Watamura et al., 2021b
$App^{huA\beta}$ KI	*App*[*1]	No mutation (humanized Aβ sequence)	Soon to be available from RBRC	Watamura et al., 2021b
$Psen1^{P436S}$ KI	*Psen1*[*2]	P436S	Available*[7]	Sasaguri et al., 2018
$Psen1^{P117L/A}$ KI	*Psen1*[*3]	P117L/A	Available*[7]	Sasaguri et al., 2018; Sato et al., 2021
App^{NL-F} KI/ $Psen1^{P117L}$ KI	*App*[*1], *Psen1*[*3]	*App*: KM670/671NL, I716F Psen1: P117L	Soon to be available from RBRC	Sato et al., 2021
MAPT KI	*MAPT*[*4]	Humanization of the *Mapt* gene	RBRC (RBRC09995)	Hashimoto et al., 2019; Saito et al., 2019
App^{NL} KI/*hMAPT* KI	*App*[*1], *MAPT*[*4]	*App*: KM670/671NL *MAPT*: No mutation	RBRC (RBRC10041)	Saito et al., 2019
App^{NL-F} KI/*hMAPT* KI	*App*[*1], *MAPT*[*4]	*App*: KM670/671NL, I716F, *MAPT*: No mutation	RBRC (RBRC10042)	Saito et al., 2019
App^{NL-G-F} KI/*hMAPT* KI	*App*[*1], *MAPT*[*4]	*App*: KM670/671NL E693G, I716F, *MAPT*: No mutation	RBRC (RBRC10043)	Saito et al., 2019
$hMAPT^{P301L}$ KI	*MAPT*[*4]	P301L	Available*[7]	Watamura et al., 2021b
$hMAPT^{P301S}$ KI	*MAPT*[*4]	P301S	Available*[7]	Watamura et al., 2021b
$hMAPT^{P301V}$ KI	*MAPT*[*4]	P301V	Available*[7]	Watamura et al., 2021b
$hMAPT^{Intron10+3G>A}$ KI	*MAPT*[*4]	Intron10 + 3 G > A	Available*[7]	Watamura et al., 2021b
$hMAPT^{P301L;Intron10+3G>A}$ KI	*MAPT*[*4]	P301L; Intron10 + 3 G > A	Available*[7]	Watamura et al., 2021b
$hMAPT^{P301S;Intron10+3G>A}$ KI	*MAPT*[*4]	P301S; Intron10 + 3 G > A	Available*[7]	Watamura et al., 2021b
$hMAPT^{S305N;Intron10+3G>A}$ KI	*MAPT*[*4]	S305N; Intron10 + 3 G > A	Available*[7]	Watamura et al., 2021b

*[1] *Knock-in of APP sequence (from intron 15 to intron 17) including a humanized Aβ region.*
*[2] *The mutation was introduced into the murine Psen1 gene by using Base Editor (BE) or Target-AID.*
*[3] *The mutation was introduced into the murine Psen1 gene by using VQR-BE.*
*[4] *Replaced the entire genomic sequence of the murine Mapt gene (from exon 1 to exon 14) with the human MAPT gene from the ATG codon of exon 1 to the 3′-UTR.*
*[5] *As of September 30, 2021.*
*[6] *RIKEN BioResource Research Center (https://web.brc.riken.jp/en/).*
*[7] *All strains are available through TCS (takaomi.saido@riken.jp).*

Maintaining Mouse Lines on a Clean C57BL6/J Background

In most cases, the knock-in mice are used in a homozygous state to accelerate the generation of pathological and behavioral phenotypes. However, the number of recessive mutations increases over time if the breeding of mice is maintained in this way. It is necessary therefore to back-cross heterozygous mutant mice with the wild-type C57B6/J mice to remove these extraneous mutations, preferentially for 5–10 generations at an interval of 5–10 generations. Those groups dealing with poor reproductive output of mice due to their extremely inbred nature can contact RIKEN BioResource Research Center (email: animal.brc@riken.jp), a national mouse repository of Japan (Mizuno-Iijima et al., 2021), to renew their strains.

Choosing Appropriate Anti-Aβ Antibodies

It was previously indicated that some anti-Aβ antibodies are inappropriate for biochemically and pathologically detecting the Arctic Aβ produced by App^{NL-G-F} mice (Saito et al., 2014; **Figure 7**). Note that the App^{NL-G-F} is the most frequently used model because it recapitulates Aβ pathology and neuroinflammation much faster than other lines. This applies to all other transgenic and knock-in mice that carry intra-Aβ mutations, including the Arctic and Dutch mutations (Van Broeckhoven et al., 1990; Li et al., 2014). In contrast, there is no restriction regarding use of antibodies for the App^{NL-F} X $Psen1^{P117L}$ mice.

Preclinical Nature of Behaviors

In our experience, the most sensitive and reproducible test involves contextual fear conditioning, although its irreversible nature can be problematic. In a more complex sense, the application of a multi-task paradigm such as ***IntelliCage*** (NewBehavior AG, Zurich, Switzerland) would be more informative (Codita et al., 2010; Masuda et al., 2016). We recently showed that the mouse genotypes can be predicted from their behavioral parameters by machine learning (Sutoko et al., 2021). It should be emphasized that the *App* knock-in

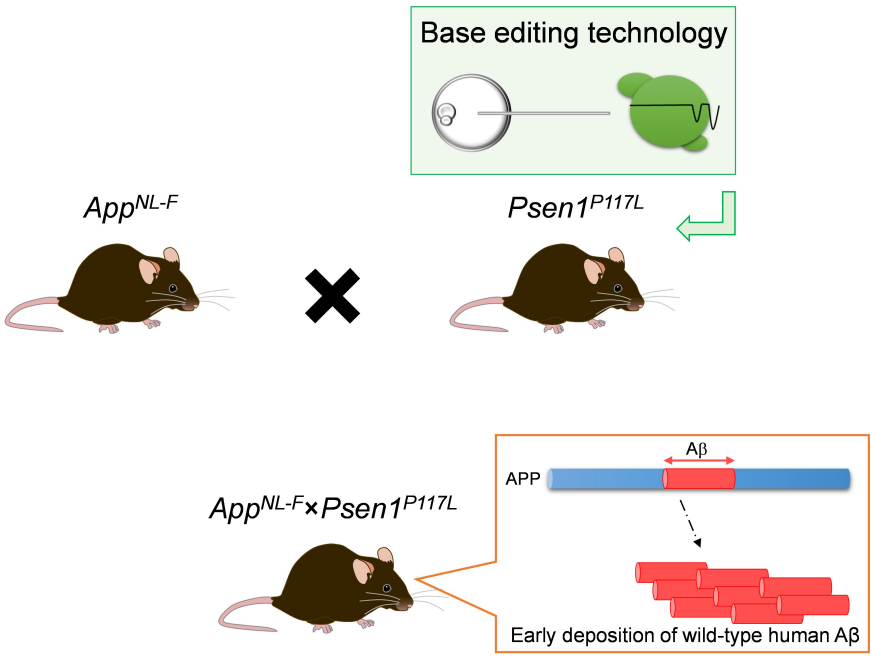

FIGURE 4 | Scheme of App^{NL-F} × $Psen1^{P117L}$ double-mutant mice. For the generation of the double-mutant mice, the App^{NL-F} line was crossbred with the $Psen1^{P117L}$ line whose mutation was introduced in the endogenous *Psen1* gene utilizing base editing technology. The synergistic effects of the pathogenic mutations in the *App* and *Psen1* genes strongly accelerates the deposition of wild-type human Aβ in mouse brains.

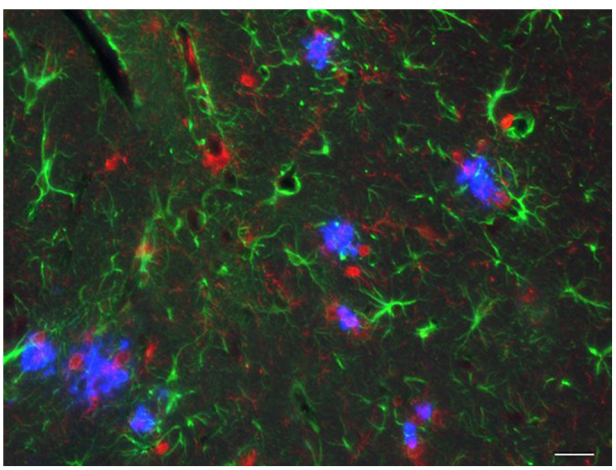

FIGURE 5 | AD pathology in the hippocampus of a 3rd generation model mouse. A 12-month-old App^{NL-F} X $Psen1^{P117L/WT}$ mouse was analyzed by immunohistochemistry. Blue: Aβ plaques; red: microglia; green: astrocytes. The bar indicates 25 μm.

mice are models of preclinical AD because the *App* knock-in mice, like all the APP and APP/PS1 transgenic mice, do not recapitulate tau pathology alone (Sasaguri et al., 2017). Consistently, we observe only mild cognitive decline in these mice. In contrast, the *App* knock-in mice crossbred with mutant *MAPT* knock-in mice exhibited accelerated tau pathology (**Table 2**).

A NEW MODEL OF CEREBRAL AMYLOID ANGIOPATHY

Most AD patients exhibit parenchymal and vascular Aβ deposition in the brains, and both pathologies seem to be driven by impaired Aβ clearance within the interstitial fluid and perivascular drainage pathways (Greenberg et al., 2020). Iliff et al. (2012) injected fluorescent tracers into Tie2-GFP:NG2-DsRed double reporter mice, which express GFP in all cerebral blood vessels and DsRed in perivascular cells, and successfully observed glymphatic pathway; subarachnoid CSF influx into the brain parenchyma and bulk ISF solute clearance from the parenchyma within the perivascular spaces. Importantly, in AD model mice, glymphatic CSF influx is reduced and the clearance of Aβ is severely impaired (Peng et al., 2016). Impaired glymphatic pathway may contribute to the deposition of Aβ in the blood vessels of the brain, cerebral amyloid angiopathy (CAA). Although CAA is profoundly observed in most AD patients (Brenowitz et al., 2015), limited model mice, such as those with Dutch/Iowa mutation, exhibit apparent CAA, thus making it difficult to determine how CAA contributes to the pathogenesis of sporadic AD. Notably, human vascular endothelial cells express significant level of APP770 and human plasma contains ∼100 ng/ml of sAPP770 (Kitazume et al., 2010). Since peripheral blood cells other than platelet do not express APP, and platelets release sAPP770 upon their activation (Miura et al., 2020), it is considered that plasma sAPP770 is mostly derived from endothelial APP770. Because in rodents

TABLE 3 | Characteristics of the *App* knock-in mouse lines.

	Stain	Gene mutations		Genetic background	Aβ plaques (first appearance)	Tangles	Neuronal loss	Cognitive impairment	Strengths	Weaknesses
		App	*Psen1*							
Single *App* knock-in	$App^{huA\beta}$	Humanized Aβ	–	C57BL/6J	–	NR	NR	NR	A control for other models	–
	App^{NL}	Humanized Aβ KM670/671NL	–	C57BL/6J	–	–	–	–	A control for other models	No amyloid pathology No cognitive deficits Increased CTF-β
	App^{NL-F}	Humanized Aβ KM670/671NL I716F	–	C57BL/6J	6 months	–	–	18 months	Deposition of wild type human Aβ	Long time required for amyloid pathology and cognitive deficits Increased CTF-β
	App^{NL-G-F}	Humanized Aβ KM670/671NL E693G I716F	–	C57BL/6J	2 months	–	–	6 months	Early appearance of amyloid pathology	The Arctic mutation inside the Aβ sequence Increased CTF-β
	App^{G-F}	Humanized Aβ E693G I716F	–	C57BL/6J	4 months	NR	NR	NR	Absence of the Swedish mutation No increase of CTF-β	The Arctic mutation inside the Aβ sequence
App and *Psen1* double mutant	App^{NL-F} $Psen1^{P117L}$	Humanized Aβ KM670/671NL I716F	P117L	C57BL/6J	3 months	NR	NR	NR	Early appearance of amyloid pathology Deposition of wild type human Aβ	Mutations in both *App* and *Psen1* genes

The Swedish mutations; KM670/671NL.
The Iberian/Beyreuther mutation; I716F.
The Arctic mutation; E693G.
NR denotes data not reported.

plasma sAPP is a markedly lower (∼100 pg/ml) than that of humans (Kitazume et al., 2012), it's possible that low level of endothelial APP expression in mice could be one of the reasons that *App* knock-in mice exhibit mild CAA pathology. To overcome this, a mouse line that specifically expresses human APP770 in endothelial cells has just been generated (unpublished). In brief, floxed hAPP770NL mice under the CMV early enhancer/chicken β-actin promoter were first generated. These mice were then crossed with Tie2-Cre mice, in which the Tie2 promoter directs the expression of Cre recombinase in the endothelial cells to obtain double transgenic (Tg) mice.

App knock-in mouse models were previously produced by Li et al. (2014) who used multiple pathogenic mutations. These mice carry the Swedish (K670N/M671L), Dutch (E693Q), and London (V717I) mutations with the humanized Aβ sequence. The Dutch mutation results in an intensive CAA pathology in humans, thereby causing brain hemorrhage and early mortality (Levy et al., 1990; Van Broeckhoven et al., 1990). This mutation is therefore not specifically responsible for causing FAD. These mice did not develop prominent Aβ deposits over their lifespan, but when they were crossbred with $Psen1^{M146V}$ knock-in mice, an age-dependent deposition of Aβ was seen in the resultant double knock-in mice. The deposition of Aβ was detected not only in the parenchyma of the cerebral cortex but also in the cerebral vasculature, similar to that seen in CAA in humans. Double knock-in mice that did not have the Dutch mutation exhibited virtually no vascular pathology. In this way, if the authors had used the Beyreuther/Iberian or Austrian mutation instead of the London mutation in the mouse *App* gene then they probably would not have had to introduce the *Psen1* knock-in mice. Knock-in mice harboring the Dutch mutation can still serve as relevant models for CAA; however they may not be appropriate for examining the effect of immunotherapy on CAA because the Dutch mutation is present in the middle of the Aβ sequence.

NEPRILYSIN-SENSITIVE AMYLOIDOGENIC Aβ AS A PROBABLE CAUSE FOR SPORADIC ALZHEIMER'S DISEASE

NEP and insulin-degrading enzyme (IDE) are considered the two major catabolic enzymes that degrade Aβ (Qiu et al., 1998; Iwata et al., 2000, 2001; Farris et al., 2003; Leissring et al., 2003). NEP is capable of degrading both soluble and insoluble Aβ

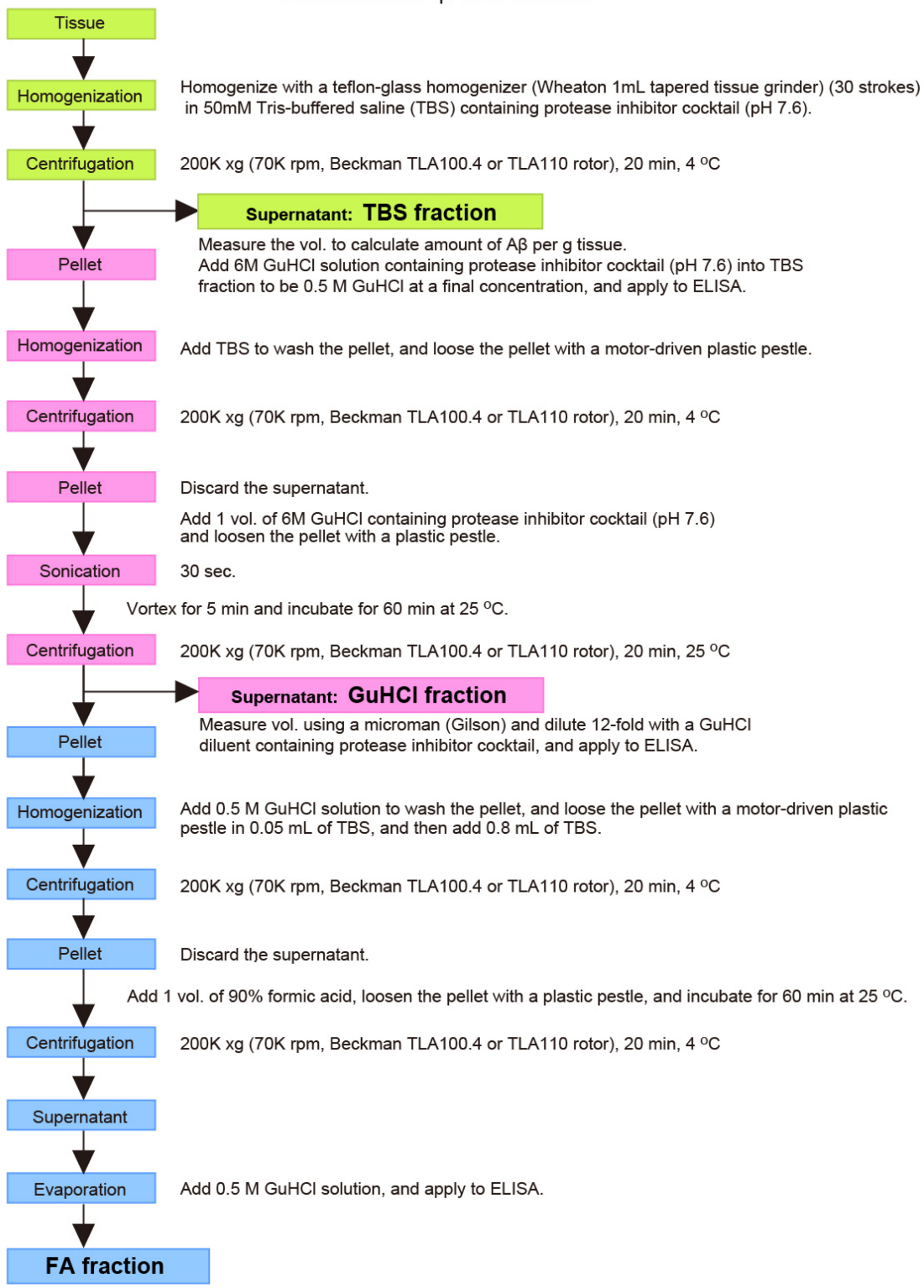

FIGURE 6 | Outlined protocols for extraction and quantification of Aβ from tissues. See text for detailed explanation.

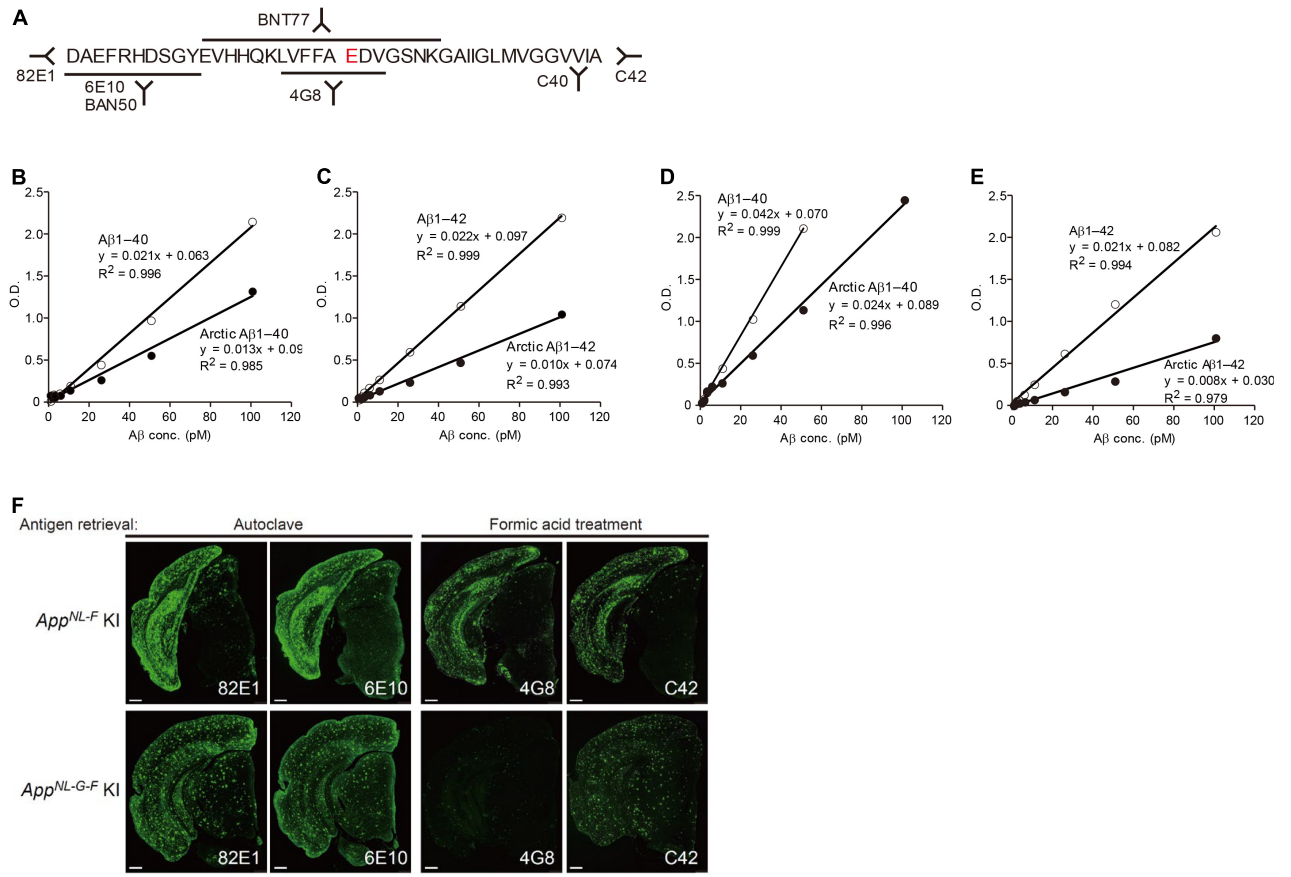

FIGURE 7 | Reactivity of different antibodies to Arctic Aβ in App^{NL-G-F} mice. **(A)** Epitope map of anti-Aβ antibodies. **(B,C)** Quantification of Arctic Aβ species using BNT77 as a capture antibody. BNT77 binds to the mid-portion of Aβ [see epitope map **(A)**]. A sandwich ELISA kit (Wako, Japan) was used to quantify Aβx-40 **(C)** and Aβx-42 **(D)**, respectively. **(D,E)** Quantification of Arctic Aβ species using BAN50 as a capture antibody. BAN50 binds to the N-terminal region of Aβ [see epitope map **(A)**]. A sandwich ELISA kit (Wako, Japan) was used to quantify Aβx-40 **(D)** and Aβx-42 **(E)**, respectively. BNT77 and BAN50 captured Arctic Aβ more weakly than wild-type Aβ. **(F)** Immunohistochemistry using various anti-Aβ antibodies. Brain sections derived from App^{NL-F} mice (24 months old) were immunostained using antibodies with different epitopes after antigen retrieval as indicated (upper panels); those of App^{NL-G-F} mice (9 months old) were similarly immunostained (lower panels). Scale bars represent 500 μm.

(Iwata et al., 2000, 2001; Huang et al., 2006), but it is not clearly shown whether endogenous IDE could degrade insoluble Aβ in the mouse brains (Farris et al., 2003), rather IDE appears to be involved in metabolism of AICD. Unfortunately, their roles in Aβ metabolism *in vivo* have never been compared in an impartial and side-by-side manner. Once double mutants crossbred single *App* knock-in mice with NEP (*Mme*) KO mice and with IDE (*Ide*) KO mice were analyzed in detail for their biochemical properties and Aβ pathology properties, it would be clear their distinct roles in APP metabolism and the AD pathogenesis.

Further to the above, a deficiency of NEP had no significant impact on the levels of various neuropeptides (Sasaguri et al., 2018) as well as enkephalins (Saria et al., 1997) that are well known to be *in vitro* substrates for NEP (Turner et al., 1996, 2000, 2001; Turner and Nalivaeva, 2006) in the cerebral cortex and hippocampal formation of mice, presumably because NEP is mainly expressed in secretory vesicles and on the presynaptic membranes of excitatory neurons (Iwata et al., 2002, 2004, 2013), while most if not all neuropeptides are secreted from inhibitory neurons. This argues against the concern that NEP up-regulation for the treatment of preclinical AD would reduce the levels of these neuropeptides. These findings also indicate that NEP relatively selectively degrades Aβ in the brain. Whereas familial AD (FAD) is unambiguously caused by an increased anabolism of Aβ, and of $Aβ_{42}$ and $Aβ_{43}$ in particular (Selkoe and Hardy, 2016), the anabolism of Aβ appears unaffected prior to its deposition in the brain that subsequently leads to the onset of sporadic AD (SAD). These observations suggest that NEP-sensitive amyloidogenic Aβ likely plays a primary pathogenic role in the etiology of SAD. Our findings are consistent with the aging-dependent decline of NEP expression in the human brain and with recent genome-wide association studies (GWAS) indicating that variants of the gene encoding NEP (*MME*) are associated with the risk of SAD development (Bellenguez et al., 2020). Taken together, our results imply that the aging-associated decrease in NEP expression is a primary cause of SAD and could thus be a target for the treatment of preclinical AD once other factors such as apolipoprotein E genotypes have also been considered.

REGULATION OF Aβ METABOLISM *VIA* SOMATOSTATIN RECEPTOR SUBTYPES THROUGH MODULATION OF NEP ACTIVITY

Since NEP is a major Aβ-degrading enzyme and it is downregulated upon aging, its decreased levels in the brain will most likely lead to increased Aβ levels (Yasojima et al., 2001; Carpentier et al., 2002; Iwata et al., 2002; Maruyama et al., 2005; Hellström-Lindahl et al., 2008). NEP is regulated by the neuropeptide somatostatin (Saito et al., 2005). Somatostatin, which binds to somatostatin receptors, is also decreased upon aging and in AD possibly due to loss of somatostatin-positive interneurons (Davies et al., 1980; Beal et al., 1985; Bergström et al., 1991; Hayashi et al., 1997; van de Nes et al., 2002; Lu et al., 2004; Gahete et al., 2010). Somatostatin, which was first identified to regulate secretion of growth hormone from pituitary, has been traditionally abbreviated as SRIF (somatotropin release-inhibiting factor) (Møller et al., 2003), so we will keep to this nomenclature in this review. SST_1, SST_2, SST_3, SST_4, and SST_5 are used to express somatostatin receptor subtypes 1–5. Interestingly, mutations in SRIF are linked to AD (Vepsäläinen et al., 2007). By using a combination of *in vitro* and *in vivo* approaches to identify the subtype specificity of the five SSTs expressed in the brain and considered to be involved in the regulation of NEP. We would like to emphasize that it is necessary to use a co-culture system of primary neurons from the cortex, hippocampus, and striatum for *in vitro* experiments (Kakiya et al., 2012; Nilsson et al., 2020; Watamura et al., 2021a).

Using a battery of *Sst* double knockout (dKO) mice, we found that NEP is regulated by SST_1 and SST_4 in a redundant manner. Sst_1 and Sst_4 dKO mice exhibit a specific decrease of presynaptic NEP in the Lacunosum molecular layer. Moreover, a genetic deficiency of Sst_1 and Sst_4 in the *App* knock-in mice aggravated the Aβ pathology in the hippocampus. As a first proof of concept towards an Aβ-lowering strategy involving NEP, a treatment with an agonist selective for SST_1 and SST_4 could ameliorates the Aβ pathology and improves cognitive outcomes in the *App* knock-in AD mouse model as schematized in **Figure 8** (Nilsson et al., 2020). These results indicate that a combination of SST_1 and SST_4 homodimers or the SST_1 and SST_4 heterodimer may become a target for pharmaceutical intervention to treat preclinical AD. Of note, the expression of SRIF in human brain declines with aging and in AD (Davies et al., 1980; Lu et al., 2004) and may causally contribute to AD pathogenesis *via* reduction of NEP activity/expression.

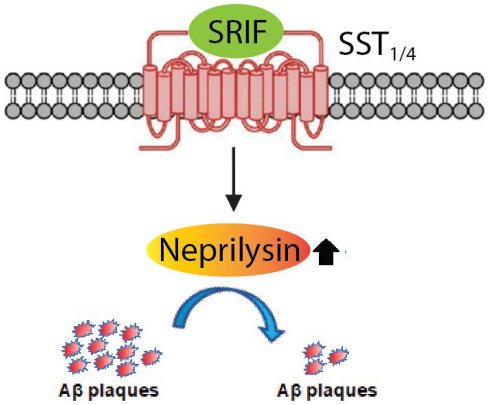

FIGURE 8 | Somatostatin receptor subtypes 1 and 4 ($SST_{1/4}$) regulate the Aβ-degrading enzyme NEP. The neuropeptide somatostatin (SRIF) was identified as a regulator of NEP activity through *in vitro* screening. Subsequent analysis of the effect of genetic deletion of somatostatin receptor (SST) subtypes in mice revealed that SST_1 and SST_4 regulate NEP in a redundant manner. This was further confirmed by concurrently deleting SST_1 and SST_4 in *App* KI mice, which aggravated the Aβ pathology. $SST_{1/4}$ can be either a combination of SST_1 and SST_4 homodimers or an SST_1/SST_4 heterodimer.

SRIF-EVOKED Aβ CATABOLISM IN THE BRAIN: MECHANISTIC INVOLVEMENT OF THE α-ENDOSULFINE-K_{ATP} CHANNEL PATHWAY

Although SRIF is known to regulate Aβ catabolism by enhancing NEP-catalyzed proteolytic degradation, the mechanism by which SRIF actually regulates NEP activity is yet to be fully elucidated. Proteomic analyses enabled α-endosulfine (ENSA), an endogenous ligand of the ATP-sensitive potassium (K_{ATP}) channel, to be identified as a negative regulator of NEP downstream of SRIF signaling (Watamura et al., 2021a). The expression of ENSA is significantly increased in AD mouse models and in patients with AD. In addition, NEP directly contributes to the degradation of ENSA, suggesting a substrate-dependent feedback loop regulating NEP activity.

It was also discovered the specific K_{ATP} channel subtype [sulfonylurea receptor subunit 1 (SUR1) and inwardly rectifying K^+ channel 6.2 (Kir6.2)] that modulates NEP activity, resulting in altered Aβ levels in the brain. Pharmacological intervention targeting this particular K_{ATP} channel by diazoxide attenuated Aβ deposition, with impaired memory function rescued *via* the NEP activation in our AD mouse model. These findings provide a mechanism explaining the molecular link between K_{ATP} channels and NEP activation. They also provide new insights into how ENSA and the K_{ATP} channel could profile as a new therapeutic target for lowering Aβ and thus provide an alternative strategy to prevent AD. **Figure 9** summarizes the NEP activation mechanism that involves SRIF receptor subtypes, ENSA and K_{ATP} channel involvement.

HUMANIZATION OF THE ENTIRE MURINE *Mapt* GENE TO GENERATE *hMAPT* KNOCK-IN MICE

To date, most if not all, mouse models of tauopathy have been unable to recapitulate the tau pathology without overexpressing mutant human tau protein. As a novel *in vivo* platform for studying human tauopathy, human *MAPT* knock-in mice have been developed in which the entire *Mapt* gene including all exons

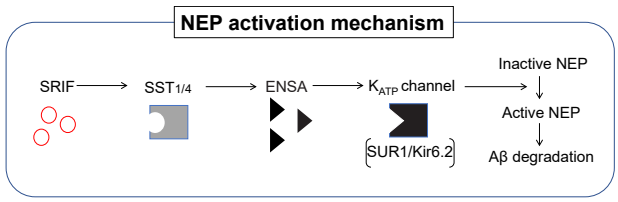

FIGURE 9 | Role of ENSA in the regulation of NEP activity. Schematic illustration of the mechanism describing NEP activity in the brain. ENSA, a downstream protein of SST-$SST_{1/4}$ signaling, plays a role as a ligand of the K_{ATP} channel composed of sulfonylurea receptor subunit 1 (SUR1) and inwardly rectifying K^+ channel 6.2 (Kir6.2), resulting in the activation of NEP. $SST_{1/4}$ can be either a combination of SST_1 and SST_4 homodimers or an SST_1/SST_4 heterodimer.

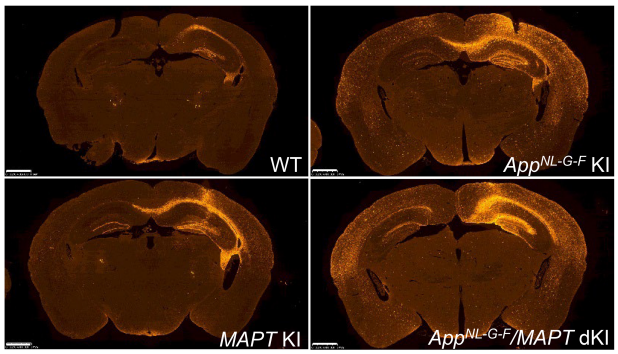

FIGURE 10 | Propagation of AD-tau in mouse brains. Propagation of tau in each mouse line was observed 3 months after AD-tau injection. Brain sections were immunostained with AT8 (red). Humanization of the host animal tau affects the transmission of the pathogenic agents. App^{NL-G-F}/*MAPT* dKI mice exhibited greater pathological propagation than App^{NL-G-F} KI mice.

and introns are humanized (Hashimoto et al., 2019). In each strain, the *MAPT* and *Mapt* genes encoded human and murine tau proteins, respectively. This was done by crossing *MAPT* knock-in mice with single *App* knock-in mice in order to study the role of the Aβ-tau axis in the etiology of AD. The double knock-in mice exhibited a more pronounced tau phosphorylation status than single *MAPT* knock-in mice but lacked evidence of tau pathology and neurodegeneration (in a manner similar to that of single *App* knock-in mice) even after waiting until the mice were 24 months old.

In both the absence and presence of Aβ amyloidosis, the tau humanization has been found to significantly accelerate the propagation of AD brain-derived pathological tau (**Figure 10**; Saito et al., 2019). Tau accumulation was intensified in the latter case and closely associated with dystrophic neurites, consistently showing that Aβ amyloidosis affects tau pathology. These results indicated that pathological human tau interacted better with human tau than with murine tau, and suggest the presence of a species-defined preference between the pathogenic proteins. The *MAPT* knock-in mice also facilitate the investigation of behavioral properties and of human tau characteristics in living animal models. In addition, mutant *MAPT* knock-in mice carrying various pathogenic mutations have been generated (**Table 2**). These mice exhibit aging-dependent tau aggregation and cognitive impairment in a manner accelerated by Aβ pathology and are being provided to the research community upon request.

THE ROLE OF CAPON IN TAU PATHOLOGY-MEDIATED TOXICITY

Pathological tau causes synaptic dysfunction and loss of synapses. One of promising molecules that mediates tau pathology-induced neurotoxicity is *N*-methyl-D-aspartate receptor (NMDAR). For example, tau accumulation disturbs synaptic plasticity through JAK2/STAT1-mediated suppression of NMDAR (Li et al., 2019). Phosphorylation of tau at Tyr18, which is mediated by the tyrosine kinase Fyn, enhances NMDAR-dependent excitotoxicity (Guo et al., 2020). Several reports indicated that glutamate-induced excitotoxicity was prevented by downmodulation of tau (Roberson et al., 2007) (Ittner et al., 2010). We also previously identified a NMDAR-related molecule as a tau binding protein which is involved in tau pathology- induced neurodegeneration.

To elucidate key molecules underlying tau accumulation-induced neurodegeneration, a comprehensive screening of tau-interacting proteins (tau interactome) was constructed. Tau-binding proteins were isolated by immunoprecipitation-LC-MS/MS (IP-MS) using a Flag-tag antibody and wild-type tau Tg (wtau-Tg) mice, which is expressing human tau tagged with a flag epitope (Kimura et al., 2007). Considering that tau is a microtubule-binding protein, we validated the methods used to generate the tau interactome by identifying the tubulin beta-4A chain as one of the tau-binding proteins.

Of the many proteins identified in the tau interactome, we focused on carboxy-terminal PDZ ligand of neuronal nitric oxide synthase (CAPON) (Hashimoto et al., 2019), which is an adaptor protein of neuronal nitric oxide synthase (nNOS). CAPON acts as an enzyme for the production of nitric oxide (NO) and is involved in NMDAR-mediated excitotoxicity (Jaffrey et al., 1998). It is thought to recruit substrates to nNOS and facilitate their NO-mediated modification through protein-protein interactions (Jaffrey et al., 1998). The presence of CAPON polymorphisms associated with schizophrenia and other psychiatric disorders has been reported in several studies (Brzustowicz, 2008; Freudenberg et al., 2015). Moreover, CAPON was shown to positively regulate spine density (Richier et al., 2010) and to regulate neuronal cell death downstream of the NMDAR (Li et al., 2013). These findings suggest that CAPON contributes to neurotransmission and neuronal excitotoxicity. In addition, one report showed that CAPON is upregulated in CA1 pyramidal cells in the AD brain (Hashimoto et al., 2012), implying that CAPON may play an important role in the pathogenesis of AD. The mechanism(s) underlying these effects nevertheless remain(s) unknown.

To further elucidate the effects of CAPON on AD pathology, we introduced CAPON cDNA into the brains of App^{NL-G-F} and App^{NL-G-F} X *MAPT* (hTau) double-KI mice using a

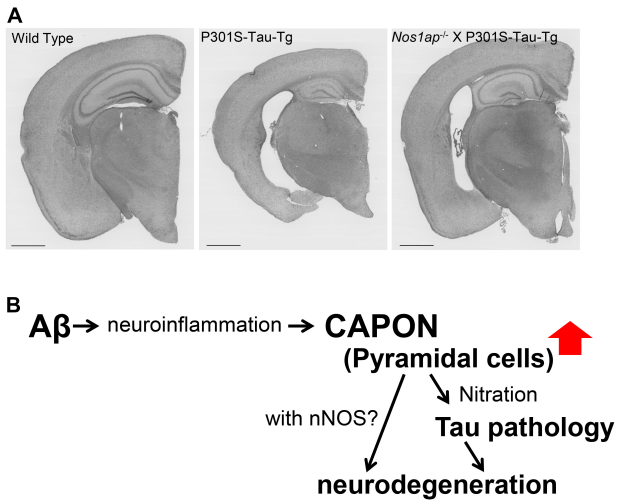

FIGURE 11 | Functions of CAPON in neurodegeneration. **(A)** Brain sections from WT, P301S-Tau-Tg or *nos1ap*-/-/P301S-Tau-Tg mice stained by the conventional method using hematoxylin and eosin (H&E). A CAPON (*Nos1ap*) deficiency restores AD-related pathological phenotypes in P301S-Tau-Tg mice. **(B)** Scheme of CAPON action. Aβ pathology elevates the level and localization of CAPON in hippocampal pyramidal cells. CAPON-induced neuronal cell death is closely associated with the pathological tau protein, although there appears to be a tau-independent mechanism in play as well.

FIGURE 12 | Photograph of common marmosets (*Callithrix jacchus*). The photo shows members of captive common marmoset family. Their small body size, fecundity, and high cognitive functions are a suitable model for neuroscience. The photograph of marmosets was taken by WK at CIEA.

newly developed adeno-associated virus (AAV)-mediated approach. We analyzed the effects of human tau protein as it is known that the hTau-KI mouse expresses an endogenous level of WT human tau. These experiments revealed that CAPON expression facilitates hippocampal atrophy in conjunction with neuronal cell death, and that a deficiency of CAPON in the P301S-Tau-Tg tauopathy mouse model suppressed tau pathology and neurodegeneration (**Figure 11**). From our results, an intervention in the interaction between CAPON-tau or CAPON-nNOS could be a new approach for the treatment of AD.

GENERATION OF NON-HUMAN PRIMATE MODELS OF FAMILIAL ALZHEIMER'S DISEASE

Common marmosets (marmosets, *Callithrix jacchus*) are small non-human primates that belong to the New World Primates (**Figure 12**; Mansfield, 2003). They have been increasingly utilized in neuroscience because of advantages that were observed over other research primates (Okano, 2021; Park and Sasaki, 2021). Marmosets possess physiological functions, brain structures and complex cognitive/social behaviors similar to those of humans; they communicate mainly *via* visual and auditory measures. In association with AD research, the amino acid sequence of Aβ in marmosets is identical to that of humans, with aged wild-type marmosets starting to accumulate Aβ from 7 years of age or even earlier (Geula et al., 2002; Rodriguez-Callejas et al., 2016). In addition, adolescent marmosets exhibit tau hyperphosphorylation, but not neurofibrillary tangle formation, in the brain that increases with aging (Rodriguez-Callejas et al., 2016). Their life spans in captivity are as long as 10–15 years, making them suitable for age-related research (Tardif et al., 2011). Their immune systems and metabolic functions resemble those of humans (t Hart and Massacesi, 2009; Tardif et al., 2011) and thus may affect the pathogenic processes related to AD (Ennerfelt and Lukens, 2020; Kellar and Craft, 2020; Rosario et al., 2020). Because sleep disorder is an early clinical symptom of AD (Pyun et al., 2019), it is noteworthy that marmosets share with humans the sleep phases composed of rapid eye movement (REM) and non-REM cycles (Crofts et al., 2001). Among various non-human primate species, the marmoset seems most applicable to genetic manipulation, i.e., generation of designed mutants, for which their high reproductive efficacy is advantageous (Sasaki et al., 2009; Sato et al., 2016; Park and Sasaki, 2021). Furthermore, fecundity characteristics of marmosets, such as a short period of sexual maturity, multiple births, and short gestation interval, are suitable for producing genetically modified disease models (Tardif et al., 2003).

Majority of FAD-causing mutations reside in the *PSEN1* gene (Scearce-Levie et al., 2020). Typically, deletion mutations in exon 9 (Crook et al., 1998; Prihar et al., 1999; Smith et al., 2001; Dumanchin et al., 2006; Le Guennec et al., 2017) or point mutations at the 3′ splice site (acceptor site) of exon 9 in the *PSEN1* gene cause dominantly inherited FAD. The point mutations instigate exon 9 elimination and S290C modification in the corresponding mRNA at the junction sites of exons 8 and 10 *via* the conversion of alternative splicing (Hutton et al., 1996; Kwok et al., 1997; Steiner et al., 1999; Brooks et al., 2003; Blauwendraat et al., 2016). Thus, generation of a marmoset model of AD is set out in which exon 9 of the *PSEN1* gene product is deleted using gene-editing technologies to produce AD marmoset

models. Since TALEN exhibited high genome-editing efficacy, generates few off-target effects, and produces little mosaicism, the TALEN would be a suitable tool for producing exon 9 deletion in the *PSEN1* gene (Sato et al., 2016; Zhang et al., 2019). Although it is a non-peer review data, the exon 9 deletion in the *PSEN1* gene that is an AD causing mutation has been successfully introduced into non-human primates by TALEN (Sato et al., 2020).

AUTHOR CONTRIBUTIONS

All authors listed have made a substantial, direct, and intellectual contribution to the work, and approved it for publication.

FUNDING

Part of the work described was supported by the following research grants: JSPS KAKENHI Grant Number JP18K07402 (HS); JSPS KAKENHI Grant Numbers JP15K19036 and JP19K16271 and RIKEN Special Postdoctoral Research program (SH); JSPS KAKENHI Grant Number JP21K15378 (NW); AMED Grant Number JP19dm0207065 (ES), AMED Grant Number JP18am0101036 (SK); The Swedish Research Council 2018-02843 (BW); Hållsten Research Foundation (PN); JSPS KAKENHI Grant Number JP20H03564/AMED Grant Numbers JP21gm1210010s0102 and JP21dk0207050h001/JST [Moonshot R&D] Grant Number JPMJMS2024/Grant-in-aid for Research in Nagoya City University Grant Number 2021101/the Hori Sciences and Arts Foundation, and Toyoaki Scholarship Foundation (TS); AMED Grant Numbers JP16dm0107068h, JP17dm0107068h, JP18dm0107068h (NI and TS); AMED Grant Number JP15dm0207001 and RIKEN Aging Project (TCS).

ACKNOWLEDGMENTS

We thank Yukiko Nagai-Watanabe for secretarial assistance.

REFERENCES

Barrett, T., Stangis, K. A., Saito, T., Saido, T., and Park, K. H. J. (2021). Neuronal cell cycle re-entry enhances neuropathological features in AppNLF knock-in mice. *J. Alzheimers Dis.* 82, 1683–1702. doi: 10.3233/jad-210091

Basun, H., Bogdanovic, N., Ingelsson, M., Almkvist, O., Naslund, J., Axelman, K., et al. (2008). Clinical and neuropathological features of the arctic APP gene mutation causing early-onset Alzheimer disease. *Arch. Neurol.* 65, 499–505. doi: 10.1001/archneur.65.4.499

Beal, M. F., Mazurek, M. F., Tran, V. T., Chattha, G., Bird, E. D., and Martin, J. B. (1985). Reduced numbers of somatostatin receptors in the cerebral cortex in Alzheimer's disease. *Science* 229, 289–291. doi: 10.1126/science.2861661

Bellenguez, C., Küçükali, F., Jansen, I., Andrade, V., Moreno-Grau, S., Amin, N., et al. (2020). New insights on the genetic etiology of Alzheimer's and related dementia. *medRxiv [preprint]* doi: 10.1101/2020.10.01.20200659

Bergström, L., Garlind, A., Nilsson, L., Alafuzoff, I., Fowler, C. J., Winblad, B., et al. (1991). Regional distribution of somatostatin receptor binding and modulation of adenylyl cyclase activity in Alzheimer's disease brain. *J. Neurol. Sci.* 105, 225–233. doi: 10.1016/0022-510x(91)90149-2

Blauwendraat, C., Wilke, C., Jansen, I. E., Schulte, C., Simon-Sanchez, J., Metzger, F. G., et al. (2016). Pilot whole-exome sequencing of a German early-onset Alzheimer's disease cohort reveals a substantial frequency of PSEN2 variants. *Neurobiol. Aging* 37, 208.e11–208.e17. doi: 10.1016/j.neurobiolaging.2015.09.016.

Brenowitz, W. D., Nelson, P. T., Besser, L. M., Heller, K. B., and Kukull, W. A. (2015). Cerebral amyloid angiopathy and its co-occurrence with Alzheimer's disease and other cerebrovascular neuropathologic changes. *Neurobiol. Aging* 36, 2702–2708. doi: 10.1016/j.neurobiolaging.2015.06.028

Brooks, W. S., Kwok, J. B., Kril, J. J., Broe, G. A., Blumbergs, P. C., Tannenberg, A. E., et al. (2003). Alzheimer's disease with spastic paraparesis and 'cotton wool' plaques: two pedigrees with PS-1 exon 9 deletions. *Brain* 126, 783–791. doi: 10.1093/brain/awg084

Brzustowicz, L. M. (2008). NOS1AP in schizophrenia. *Curr. Psychiatry Rep.* 10, 158–163.

Carpentier, M., Robitaille, Y., DesGroseillers, L., Boileau, G., and Marcinkiewicz, M. (2002). Declining expression of neprilysin in Alzheimer disease vasculature: possible involvement in cerebral amyloid angiopathy. *J. Neuropathol. Exp. Neurol.* 61, 849–856. doi: 10.1093/jnen/61.10.849

Chen, W. T., Lu, A., Craessaerts, K., Pavie, B., Sala Frigerio, C., Corthout, N., et al. (2020). Spatial transcriptomics and *in situ* sequencing to study alzheimer's disease. *Cell* 182, 976-991.e19. doi: 10.1016/j.cell.2020.06.038.

Chiasseu, M., Fesharaki-Zadeh, A., Saito, T., Saido, T. C., and Strittmatter, S. M. (2020). Gene-environment interaction promotes Alzheimer's risk as revealed by synergy of repeated mild traumatic brain injury and mouse App knock-in. *Neurobiol. Dis.* 145:105059. doi: 10.1016/j.nbd.2020.105059

Citron, M., Oltersdorf, T., Haass, C., McConlogue, L., Hung, A. Y., Seubert, P., et al. (1992). Mutation of the beta-amyloid precursor protein in familial Alzheimer's disease increases beta-protein production. *Nature* 360, 672–674. doi: 10.1038/360672a0

Codita, A., Gumucio, A., Lannfelt, L., Gellerfors, P., Winblad, B., Mohammed, A. H., et al. (2010). Impaired behavior of female tg-ArcSwe APP mice in the IntelliCage: a longitudinal study. *Behav. Brain Res.* 215, 83–94. doi: 10.1016/j.bbr.2010.06.034

Crofts, H. S., Wilson, S., Muggleton, N. G., Nutt, D. J., Scott, E. A., and Pearce, P. C. (2001). Investigation of the sleep electrocorticogram of the common marmoset (*Callithrix jacchus*) using radiotelemetry. *Clin. Neurophysiol.* 112, 2265–2273. doi: 10.1016/s1388-2457(01)00699-x

Crook, R., Verkkoniemi, A., Perez-Tur, J., Mehta, N., Baker, M., Houlden, H., et al. (1998). A variant of Alzheimer's disease with spastic paraparesis and unusual plaques due to deletion of exon 9 of presenilin 1. *Nat. Med.* 4, 452–455. doi: 10.1038/nm0498-452

Davies, P., Katzman, R., and Terry, R. D. (1980). Reduced somatostatin-like immunoreactivity in cerebral cortex from cases of Alzheimer disease and Alzheimer senile dementa. *Nature* 288, 279–280. doi: 10.1038/288279a0

Dumanchin, C., Tournier, I., Martin, C., Didic, M., Belliard, S., Carlander, B., et al. (2006). Biological effects of four PSEN1 gene mutations causing Alzheimer disease with spastic paraparesis and cotton wool plaques. *Hum. Mutat.* 27:1063. doi: 10.1002/humu.9458

Ennerfelt, H. E., and Lukens, J. R. (2020). The role of innate immunity in Alzheimer's disease. *Immunol Rev.* 297, 225–246. doi: 10.1111/imr.12896

Farris, W., Mansourian, S., Chang, Y., Lindsley, L., Eckman, E. A., Frosch, M. P., et al. (2003). Insulin-degrading enzyme regulates the levels of insulin, amyloid beta-protein, and the beta-amyloid precursor protein intracellular domain *in vivo*. *Proc. Natl. Acad. Sci. U S A.* 100, 4162–4167. doi: 10.1073/pnas.0230450100

Freudenberg, F., Alttoa, A., and Reif, A. (2015). Neuronal nitric oxide synthase (NOS1) and its adaptor, NOS1AP, as a genetic risk factors for psychiatric disorders. *Genes Brain Behav.* 14, 46–63. doi: 10.1111/gbb.12193

Gahete, M. D., Rubio, A., Durán-Prado, M., Avila, J., Luque, R. M., and Castaño, J. P. (2010). Expression of Somatostatin, cortistatin, and their receptors, as well as dopamine receptors, but not of neprilysin, are reduced in the temporal lobe of Alzheimer's disease patients. *J. Alzheimers. Dis.* 20, 465–475. doi: 10.3233/jad-2010-1385

Gamache, J., Benzow, K., Forster, C., Kemper, L., Hlynialuk, C., Furrow, E., et al. (2019). Factors other than hTau overexpression that contribute to tauopathy-like phenotype in rTg4510 mice. *Nat. Commun.* 10:2479. doi: 10.1038/s41467-019-10428-1

Geula, C., Nagykery, N., and Wu, C. K. (2002). Amyloid-beta deposits in the cerebral cortex of the aged common marmoset (*Callithrix jacchus*): incidence and chemical composition. *Acta Neuropathol.* 103, 48–58. doi: 10.1007/s004010100429

Greenberg, S. M., Bacskai, B. J., Hernandez-Guillamon, M., Pruzin, J., Sperling, R., and van Veluw, S. J. (2020). Cerebral amyloid angiopathy and Alzheimer disease - one peptide, two pathways. *Nat. Rev. Neurol.* 16, 30–42. doi: 10.1038/s41582-019-0281-2

Guo, T., Zhang, D., Zeng, Y., Huang, T. Y., Xu, H., and Zhao, Y. (2020). Molecular and cellular mechanisms underlying the pathogenesis of Alzheimer's disease. *Mol. Neurodegener.* 15:40. doi: 10.1186/s13024-020-00391-7

Hama, H., Hioki, H., Namiki, K., Hoshida, T., Kurokawa, H., Ishidate, F., et al. (2015). ScaleS: an optical clearing palette for biological imaging. *Nat. Neurosci.* 18, 1518–1529. doi: 10.1038/nn.4107

Hashimoto, M., Bogdanovic, N., Nakagawa, H., Volkmann, I., Aoki, M., Winblad, B., et al. (2012). Analysis of microdissected neurons by 18O mass spectrometry reveals altered protein expression in Alzheimer's disease. *J. Cell Mol. Med.* 16, 1686–1700. doi: 10.1111/j.1582-4934.2011.01441.x

Hashimoto, S., Ishii, A., Kamano, N., Watamura, N., Saito, T., Ohshima, T., et al. (2018). Endoplasmic reticulum stress responses in mouse models of Alzheimer's disease: overexpression paradigm versus knockin paradigm. *J. Biol. Chem.* 293, 3118–3125. doi: 10.1074/jbc.M117.811315

Hashimoto, S., Matsuba, Y., Kamano, N., Mihira, N., Sahara, N., Takano, J., et al. (2019). Tau binding protein CAPON induces tau aggregation and neurodegeneration. *Nat. Commun.* 10:2394. doi: 10.1038/s41467-019-10278-x

Hayashi, M., Yamashita, A., and Shimizu, K. (1997). Somatostatin and brain-derived neurotrophic factor mRNA expression in the primate brain: decreased levels of mRNAs during aging. *Brain Res.* 749, 283–289. doi: 10.1016/s0006-8993(96)01317-0

Hellström-Lindahl, E., Ravid, R., and Nordberg, A. (2008). Age-dependent decline of neprilysin in Alzheimer's disease and normal brain: inverse correlation with a beta levels. *Neurobiol. Aging* 29, 210–221. doi: 10.1016/j.neurobiolaging.2006.10.010

Higuchi, M., Iwata, N., Matsuba, Y., Takano, J., Suemoto, T., Maeda, J., et al. (2012). Mechanistic involvement of the calpain-calpastatin system in Alzheimer neuropathology. *FASEB J.* 26, 1204–1217. doi: 10.1096/fj.11-187740

Hongo, N., Takamura, Y., Nishimaru, H., Matsumoto, J., Tobe, K., Saito, T., et al. (2020). Astaxanthin ameliorated parvalbumin-positive neuron deficits and Alzheimer's disease-related pathological progression in the hippocampus of App(NL-G-F/NL-G-F) Mice. *Front. Pharmacol.* 11:307. doi: 10.3389/fphar.2020.00307

Huang, S. M., Mouri, A., Kokubo, H., Nakajima, R., Suemoto, T., Higuchi, M., et al. (2006). Neprilysin-sensitive synapse-associated amyloid-beta peptide oligomers impair neuronal plasticity and cognitive function. *J. Biol. Chem.* 281, 17941–17951. doi: 10.1074/jbc.M601372200

Hutton, M., Busfield, F., Wragg, M., Crook, R., Perez-Tur, J., Clark, R. F., et al. (1996). Complete analysis of the presenilin 1 gene in early onset Alzheimer's disease. *Neuroreport* 7, 801–805. doi: 10.1097/00001756-199602290-00029

Iliff, J. J., Wang, M., Liao, Y., Plogg, B. A., Peng, W., Gundersen, G. A., et al. (2012). A paravascular pathway facilitates CSF flow through the brain parenchyma and the clearance of interstitial solutes, including amyloid β. *Sci. Transl. Med.* 4:147ra111. doi: 10.1126/scitranslmed.3003748

Ittner, L. M., Ke, Y. D., Delerue, F., Bi, M., Gladbach, A., van Eersel, J., et al. (2010). Dendritic function of tau mediates amyloid-beta toxicity in Alzheimer's disease mouse models. *Cell* 142, 387–397. doi: 10.1016/j.cell.2010.06.036

Iwata, N., Higuchi, M., and Saido, T. C. (2005). Metabolism of amyloid-beta peptide and Alzheimer's disease. *Pharmacol. Ther.* 108, 129–148. doi: 10.1016/j.pharmthera.2005.03.010

Iwata, N., Mizukami, H., Shirotani, K., Takaki, Y., Muramatsu, S., Lu, B., et al. (2004). Presynaptic localization of neprilysin contributes to efficient clearance of amyloid-beta peptide in mouse brain. *J. Neurosci.* 24, 991–998. doi: 10.1523/jneurosci.4792-03.2004

Iwata, N., Sekiguchi, M., Hattori, Y., Takahashi, A., Asai, M., Ji, B., et al. (2013). Global brain delivery of neprilysin gene by intravascular administration of AAV vector in mice. *Sci. Rep.* 3:1472. doi: 10.1038/srep01472

Iwata, N., Takaki, Y., Fukami, S., Tsubuki, S., and Saido, T. C. (2002). Region-specific reduction of a beta-degrading endopeptidase, neprilysin, in mouse hippocampus upon aging. *J. Neurosci. Res.* 70, 493–500. doi: 10.1002/jnr.10390

Iwata, N., Tsubuki, S., Takaki, Y., Shirotani, K., Lu, B., Gerard, N. P., et al. (2001). Metabolic regulation of brain Abeta by neprilysin. *Science* 292, 1550–1552. doi: 10.1126/science.1059946

Iwata, N., Tsubuki, S., Takaki, Y., Watanabe, K., Sekiguchi, M., Hosoki, E., et al. (2000). Identification of the major Abeta1-42-degrading catabolic pathway in brain parenchyma: suppression leads to biochemical and pathological deposition. *Nat. Med.* 6, 143–150. doi: 10.1038/72237

Jaffrey, S. R., Snowman, A. M., Eliasson, M. J., Cohen, N. A., and Snyder, S. H. (1998). CAPON: a protein associated with neuronal nitric oxide synthase that regulates its interactions with PSD95. *Neuron* 20, 115–124. doi: 10.1016/s0896-6273(00)80439-0

Jun, H., Bramian, A., Soma, S., Saito, T., Saido, T. C., and Igarashi, K. M. (2020). Disrupted place cell remapping and impaired grid cells in a knockin model of Alzheimer's disease. *Neuron* 107, 1095-1112.e6. doi: 10.1016/j.neuron.2020.06.023.

Kakiya, N., Saito, T., Nilsson, P., Matsuba, Y., Tsubuki, S., Takei, N., et al. (2012). Cell surface expression of the major amyloid-beta peptide (A beta)-degrading enzyme, neprilysin, depends on phosphorylation by mitogen-activated protein kinase/extracellular signal-regulated kinase kinase (MEK) and dephosphorylation by protein phosphatase 1a. *J. Biol. Chem.* 287, 29362–29372. doi: 10.1074/jbc.M112.340372

Karran, E., and De Strooper, B. (2016). The amyloid cascade hypothesis: are we poised for success or failure? *J. Neurochem.* 139(Suppl. 2), 237–252. doi: 10.1111/jnc.13632

Kellar, D., and Craft, S. (2020). Brain insulin resistance in Alzheimer's disease and related disorders: mechanisms and therapeutic approaches. *Lancet Neurol.* 19, 758–766. doi: 10.1016/s1474-4422(20)30231-3

Kimura, T., Yamashita, S., Fukuda, T., Park, J. M., Murayama, M., Mizoroki, T., et al. (2007). Hyperphosphorylated tau in parahippocampal cortex impairs place learning in aged mice expressing wild-type human tau. *EMBO J.* 26, 5143–5152. doi: 10.1038/sj.emboj.7601917

Kitazume, S., Tachida, Y., Kato, M., Yamaguchi, Y., Honda, T., Hashimoto, Y., et al. (2010). Brain endothelial cells produce amyloid {beta} from amyloid precursor protein 770 and preferentially secrete the O-glycosylated form. *J. Biol. Chem.* 285, 40097–40103. doi: 10.1074/jbc.M110.144626

Kitazume, S., Yoshihisa, A., Yamaki, T., Oikawa, M., Tachida, Y., Ogawa, K., et al. (2012). Soluble amyloid precursor protein 770 is released from inflamed endothelial cells and activated platelets: a novel biomarker for acute coronary syndrome. *J. Biol. Chem.* 287, 40817–40825. doi: 10.1074/jbc.M112.398578

Komor, A. C., Kim, Y. B., Packer, M. S., Zuris, J. A., and Liu, D. R. (2016). Programmable editing of a target base in genomic DNA without double-stranded DNA cleavage. *Nature* 533, 420–424. doi: 10.1038/nature17946

Kumar-Singh, S., De Jonghe, C., Cruts, M., Kleinert, R., Wang, R., Mercken, M., et al. (2000). Nonfibrillar diffuse amyloid deposition due to a gamma(42)-secretase site mutation points to an essential role for N-truncated a beta(42) in Alzheimer's disease. *Hum. Mol. Genet.* 9, 2589–2598. doi: 10.1093/hmg/9.18.2589

Kwart, D., Gregg, A., Scheckel, C., Murphy, E. A., Paquet, D., Duffield, M., et al. (2019). A large panel of isogenic APP and PSEN1 mutant human iPSC neurons reveals shared endosomal abnormalities mediated by APP β-CTFs, Not Aβ. *Neuron* 104, 256–270.e5. doi: 10.1016/j.neuron.2019.07.010.

Kwok, J. B., Taddei, K., Hallupp, M., Fisher, C., Brooks, W. S., Broe, G. A., et al. (1997). Two novel (M233T and R278T) presenilin-1 mutations in early-onset Alzheimer's disease pedigrees and preliminary evidence for association of presenilin-1 mutations with a novel phenotype. *Neuroreport* 8, 1537–1542. doi: 10.1097/00001756-199704140-00043

Le Guennec, K., Veugelen, S., Quenez, O., Szaruga, M., Rousseau, S., Nicolas, G., et al. (2017). Deletion of exons 9 and 10 of the presenilin 1 gene in a patient with early-onset Alzheimer disease generates longer amyloid seeds. *Neurobiol. Dis.* 104, 97–103. doi: 10.1016/j.nbd.2017.04.020

Leissring, M. A., Farris, W., Chang, A. Y., Walsh, D. M., Wu, X., Sun, X., et al. (2003). Enhanced proteolysis of beta-amyloid in APP transgenic mice prevents plaque formation, secondary pathology, and premature death. *Neuron* 40, 1087–1093. doi: 10.1016/s0896-6273(03)00787-6

Levy, E., Carman, M. D., Fernandez-Madrid, I. J., Power, M. D., Lieberburg, I., van Duinen, S. G., et al. (1990). Mutation of the Alzheimer's disease amyloid gene in hereditary cerebral hemorrhage, Dutch type. *Science* 248, 1124–1126. doi: 10.1126/science.2111584

Li, H., Guo, Q., Inoue, T., Polito, V. A., Tabuchi, K., Hammer, R. E., et al. (2014). Vascular and parenchymal amyloid pathology in an Alzheimer disease knock-in mouse model: interplay with cerebral blood flow. *Mol. Neurodegener.* 9:28. doi: 10.1186/1750-1326-9-28

Li, L. L., Ginet, V., Liu, X., Vergun, O., Tuittila, M., Mathieu, M., et al. (2013). The nNOS-p38MAPK pathway is mediated by NOS1AP during neuronal death. *J. Neurosci.* 33, 8185–8201. doi: 10.1523/JNEUROSCI.4578-12.2013

Li, X. G., Hong, X. Y., Wang, Y. L., Zhang, S. J., Zhang, J. F., Li, X. C., et al. (2019). Tau accumulation triggers STAT1-dependent memory deficits by suppressing NMDA receptor expression. *EMBO Rep.* 20:e47202. doi: 10.15252/embr.201847202

Lichtenthaler, S. F., Wang, R., Grimm, H., Uljon, S. N., Masters, C. L., and Beyreuther, K. (1999). Mechanism of the cleavage specificity of Alzheimer's disease gamma-secretase identified by phenylalanine-scanning mutagenesis of the transmembrane domain of the amyloid precursor protein. *Proc. Natl. Acad. Sci. U S A.* 96, 3053–3058. doi: 10.1073/pnas.96.6.3053

Lu, T., Pan, Y., Kao, S. Y., Li, C., Kohane, I., Chan, J., et al. (2004). Gene regulation and DNA damage in the ageing human brain. *Nature* 429, 883–891. doi: 10.1038/nature02661

Maezono, S. E. B., Kanuka, M., Tatsuzawa, C., Morita, M., Kawano, T., Kashiwagi, M., et al. (2020). Progressive changes in sleep and its relations to Amyloid-β distribution and learning in single app knock-in mice. *eNeuro* 7:ENEURO.0093-20.2020. doi: 10.1523/ENEURO.0093-20.2020

Mansfield, K. (2003). Marmoset models commonly used in biomedical research. *Comp. Med.* 53, 383–392.

Maruyama, M., Higuchi, M., Takaki, Y., Matsuba, Y., Tanji, H., Nemoto, M., et al. (2005). Cerebrospinal fluid neprilysin is reduced in prodromal Alzheimer's disease. *Ann. Neurol.* 57, 832–842. doi: 10.1002/ana.20494

Masuda, A., Kobayashi, Y., Kogo, N., Saito, T., Saido, T. C., and Itohara, S. (2016). Cognitive deficits in single app knock-in mouse models. *Neurobiol. Learn. Mem.* 135, 73–82. doi: 10.1016/j.nlm.2016.07.001

Miura, S., Yoshihisa, A., Misaka, T., Yamaki, T., Kojima, T., Toyokawa, M., et al. (2020). Amyloid precursor protein 770 is specifically expressed and released from platelets. *J. Biol. Chem.* 295, 13194–13201. doi: 10.1074/jbc.RA120.012904

Mizuno-Iijima, S., Nakashiba, T., Ayabe, S., Nakata, H., Ike, F., Hiraiwa, N., et al. (2021). Mouse resources at the RIKEN bioresource research center and the national bioresource project core facility in Japan. *Mamm. Genome* Online ahead of print. doi: 10.1007/s00335-021-09916-x

Møller, L. N., Stidsen, C. E., Hartmann, B., and Holst, J. J. (2003). Somatostatin receptors. *Biochim. Biophys. Acta* 1616, 1–84. doi: 10.1016/s0005-2736(03)00235-9

Morishima-Kawashima, M., Oshima, N., Ogata, H., Yamaguchi, H., Yoshimura, M., Sugihara, S., et al. (2000). Effect of apolipoprotein E allele epsilon4 on the initial phase of amyloid beta-protein accumulation in the human brain. *Am. J. Pathol.* 157, 2093–2099. doi: 10.1016/s0002-9440(10)64847-x

Mullan, M., Crawford, F., Axelman, K., Houlden, H., Lilius, L., Winblad, B., et al. (1992). A pathogenic mutation for probable Alzheimer's disease in the APP gene at the N-terminus of beta-amyloid. *Nat. Genet.* 1, 345–347. doi: 10.1038/ng0892-345

Nagata, K., Takahashi, M., Matsuba, Y., Okuyama-Uchimura, F., Sato, K., Hashimoto, S., et al. (2018). Generation of app knock-in mice reveals deletion mutations protective against Alzheimer's disease-like pathology. *Nat. Commun.* 9:1800. doi: 10.1038/s41467-018-04238-0

Nakazono, T., Lam, T. N., Patel, A. Y., Kitazawa, M., Saito, T., Saido, T. C., et al. (2017). Impaired *in vivo* gamma oscillations in the medial entorhinal cortex of knock-in Alzheimer model. *Front. Syst. Neurosci.* 11:48. doi: 10.3389/fnsys.2017.00048

Nalivaeva, N. N., Belyaev, N. D., Kerridge, C., and Turner, A. J. (2014). Amyloid-clearing proteins and their epigenetic regulation as a therapeutic target in Alzheimer's disease. *Front. Aging Neurosci.* 6:235. doi: 10.3389/fnagi.2014.00235

Nilsberth, C., Westlind-Danielsson, A., Eckman, C. B., Condron, M. M., Axelman, K., Forsell, C., et al. (2001). The 'Arctic' APP mutation (E693G) causes Alzheimer's disease by enhanced Abeta protofibril formation. *Nat. Neurosci.* 4, 887–893. doi: 10.1038/nn0901-887

Nilsson, P., Sörgjerd, K., Kakiya, N., Sasaguri, H., Watamura, N., Shimozawa, M., et al. (2020). Somatostatin receptor subtypes 1 and 4 redundantly regulate neprilysin, the major amyloid-beta degrading enzyme in brain. *bioRxiv [preprint]* doi: 10.1101/2020.05.09.085795

Nortley, R., Korte, N., Izquierdo, P., Hirunpattarasilp, C., Mishra, A., Jaunmuktane, Z., et al. (2019). Amyloid β oligomers constrict human capillaries in Alzheimer's disease *via* signaling to pericytes. *Science* 365:eaav9518. doi: 10.1126/science.aav9518

Okano, H. (2021). Current status of and perspectives on the application of marmosets in neurobiology. *Annu. Rev. Neurosci.* 44, 27–48. doi: 10.1146/annurev-neuro-030520-101844

Park, J. E., and Sasaki, E. (2021). Assisted reproductive techniques and genetic manipulation in the common marmoset. *Ilar J.* Online ahead of print. doi: 10.1093/ilar/ilab002

Peng, W., Achariyar, T. M., Li, B., Liao, Y., Mestre, H., Hitomi, E., et al. (2016). Suppression of glymphatic fluid transport in a mouse model of Alzheimer's disease. *Neurobiol. Dis.* 93, 215–225. doi: 10.1016/j.nbd.2016.05.015

Prihar, G., Verkkoniem, A., Perez-Tur, J., Crook, R., Lincoln, S., Houlden, H., et al. (1999). Alzheimer disease PS-1 exon 9 deletion defined. *Nat. Med.* 5:1090. doi: 10.1038/13383

Pyun, J. M., Kang, M. J., Yun, Y., Park, Y. H., and Kim, S. (2019). APOE ε4 and REM sleep behavior disorder as risk factors for sundown syndrome in Alzheimer's disease. *J. Alzheimers. Dis.* 69, 521–528. doi: 10.3233/jad-190032

Qiu, W. Q., Walsh, D. M., Ye, Z., Vekrellis, K., Zhang, J., Podlisny, M. B., et al. (1998). Insulin-degrading enzyme regulates extracellular levels of amyloid beta-protein by degradation. *J. Biol. Chem.* 273, 32730–32738. doi: 10.1074/jbc.273.49.32730

Richier, L., Williton, K., Clattenburg, L., Colwill, K., O'Brien, M., Tsang, C., et al. (2010). NOS1AP associates with scribble and regulates dendritic spine development. *J. Neurosci.* 30, 4796–4805. doi: 10.1523/JNEUROSCI.3726-09.2010

Roberson, E. D., Scearce-Levie, K., Palop, J. J., Yan, F., Cheng, I. H., Wu, T., et al. (2007). Reducing endogenous tau ameliorates amyloid beta-induced deficits in an Alzheimer's disease mouse model. *Science* 316, 750–754. doi: 10.1126/science.1141736

Rodriguez-Callejas, J. D., Fuchs, E., and Perez-Cruz, C. (2016). Evidence of tau hyperphosphorylation and dystrophic microglia in the common marmoset. *Front. Aging Neurosci.* 8:315. doi: 10.3389/fnagi.2016.00315

Rosario, D., Boren, J., Uhlen, M., Proctor, G., Aarsland, D., Mardinoglu, A., et al. (2020). Systems biology approaches to understand the host-microbiome interactions in neurodegenerative diseases. *Front. Neurosci.* 14:716. doi: 10.3389/fnins.2020.00716

Saito, T., Iwata, N., Tsubuki, S., Takaki, Y., Takano, J., Huang, S. M., et al. (2005). Somatostatin regulates brain amyloid beta peptide Abeta42 through modulation of proteolytic degradation. *Nat. Med.* 11, 434–439. doi: 10.1038/nm1206

Saito, T., Matsuba, Y., Mihira, N., Takano, J., Nilsson, P., Itohara, S., et al. (2014). Single App knock-in mouse models of Alzheimer's disease. *Nat. Neurosci.* 17, 661–663. doi: 10.1038/nn.3697

Saito, T., Matsuba, Y., Yamazaki, N., Hashimoto, S., and Saido, T. C. (2016). Calpain activation in Alzheimer's model mice is an artifact of APP and presenilin overexpression. *J. Neurosci.* 36, 9933–9936. doi: 10.1523/jneurosci.1907-16.2016

Saito, T., Mihira, N., Matsuba, Y., Sasaguri, H., Hashimoto, S., Narasimhan, S., et al. (2019). Humanization of the entire murine Mapt gene provides a murine model of pathological human tau propagation. *J. Biol. Chem.* 294, 12754–12765. doi: 10.1074/jbc.RA119.009487

Salobrar-García, E., López-Cuenca, I., Sánchez-Puebla, L., de Hoz, R., Fernández-Albarral, J. A., Ramírez, A. I., et al. (2020). Retinal thickness changes over time in a murine AD model APP (NL-F/NL-F). *Front. Aging Neurosci.* 12:625642. doi: 10.3389/fnagi.2020.625642

Saria, A., Hauser, K. F., Traurig, H. H., Turbek, C. S., Hersh, L., and Gerard, C. (1997). Opioid-related changes in nociceptive threshold and in tissue levels of enkephalins after target disruption of the gene for neutral endopeptidase

(EC 3.4.24.11) in mice. *Neurosci. Lett.* 234, 27–30. doi: 10.1016/s0304-3940(97)00660-5

Sasaguri, H., Nagata, K., Sekiguchi, M., Fujioka, R., Matsuba, Y., Hashimoto, S., et al. (2018). Introduction of pathogenic mutations into the mouse Psen1 gene by base editor and Target-AID. *Nat. Commun.* 9:2892. doi: 10.1038/s41467-018-05262-w

Sasaguri, H., Nilsson, P., Hashimoto, S., Nagata, K., Saito, T., De Strooper, B., et al. (2017). APP mouse models for Alzheimer's disease preclinical studies. *EMBO J.* 36, 2473–2487. doi: 10.15252/embj.201797397

Sasaki, E., Suemizu, H., Shimada, A., Hanazawa, K., Oiwa, R., Kamioka, M., et al. (2009). Generation of transgenic non-human primates with germline transmission. *Nature* 459, 523–527. doi: 10.1038/nature08090

Sato, K., Oiwa, R., Kumita, W., Henry, R., Sakuma, T., Ito, R., et al. (2016). Generation of a nonhuman primate model of severe combined immunodeficiency using highly efficient genome editing. *Cell Stem Cell* 19, 127–138. doi: 10.1016/j.stem.2016.06.003

Sato, K., Sasaguri, H., Kumita, W., Inoue, T., Kurotaki, Y., Nagata, K., et al. (2020). A non-human primate model of familial Alzheimer's disease. *bioRxiv [preprint]* doi: 10.1101/2020.08.24.264259

Sato, K., Watamura, N., Fujioka, R., Mihira, N., Sekiguchi, M., Nagata, K., et al. (2021). A 3(rd) generation mouse model of Alzheimer's disease shows early and increased cored plaque pathology composed of wild-type human amyloid β peptide. *J. Biol. Chem.* 297:101004. doi: 10.1016/j.jbc.2021.101004

Scearce-Levie, K., Sanchez, P. E., and Lewcock, J. W. (2020). Leveraging preclinical models for the development of Alzheimer disease therapeutics. *Nat. Rev. Drug Discov.* 19, 447–462. doi: 10.1038/s41573-020-0065-9

Selkoe, D. J., and Hardy, J. (2016). The amyloid hypothesis of Alzheimer's disease at 25 years. *EMBO Mol. Med.* 8, 595–608. doi: 10.15252/emmm.201606210

Shirotani, K., Hori, Y., Yoshizaki, R., Higuchi, E., Colonna, M., Saito, T., et al. (2019). Aminophospholipids are signal-transducing TREM2 ligands on apoptotic cells. *Sci. Rep.* 9:7508. doi: 10.1038/s41598-019-43535-6

Smith, M. J., Kwok, J. B., McLean, C. A., Kril, J. J., Broe, G. A., Nicholson, G. A., et al. (2001). Variable phenotype of Alzheimer's disease with spastic paraparesis. *Ann. Neurol.* 49, 125–129.

Sobue, A., Komine, O., Hara, Y., Endo, F., Mizoguchi, H., Watanabe, S., et al. (2021). Microglial gene signature reveals loss of homeostatic microglia associated with neurodegeneration of Alzheimer's disease. *Acta Neuropathol. Commun.* 9:1. doi: 10.1186/s40478-020-01099-x

Steiner, H., Romig, H., Grim, M. G., Philipp, U., Pesold, B., Citron, M., et al. (1999). The biological and pathological function of the presenilin-1 Deltaexon 9 mutation is independent of its defect to undergo proteolytic processing. *J. Biol. Chem.* 274, 7615–7618. doi: 10.1074/jbc.274.12.7615

Susaki, E. A., Shimizu, C., Kuno, A., Tainaka, K., Li, X., Nishi, K., et al. (2020). Versatile whole-organ/body staining and imaging based on electrolyte-gel properties of biological tissues. *Nat. Commun.* 11:1982. doi: 10.1038/s41467-020-15906-5

Sutoko, S., Masuda, A., Kandori, A., Sasaguri, H., Saito, T., Saido, T. C., et al. (2021). Early identification of Alzheimer's disease in mouse models: application of deep neural network algorithm to cognitive behavioral parameters. *iScience* 24:102198. doi: 10.1016/j.isci.2021.102198

t Hart, B. A., and Massacesi, L. (2009). Clinical, pathological, and immunologic aspects of the multiple sclerosis model in common marmosets (*Callithrix jacchus*). *J. Neuropathol. Exp. Neurol.* 68, 341–355. doi: 10.1097/NEN.0b013e31819f1d24

Tachida, Y., Miura, S., Imamaki, R., Ogasawara, N., Takuwa, H., Sahara, N., et al. (2020). Endothelial expression of human APP leads to cerebral amyloid angiopathy in mice. *bioRxiv [preprint]* doi: 10.1101/2020.07.22.215418

Takamura, R., Mizuta, K., Sekine, Y., Islam, T., Saito, T., Sato, M., et al. (2021). Modality-Specific impairment of hippocampal CA1 neurons of Alzheimer's disease model mice. *J. Neurosci.* 41, 5315–5329. doi: 10.1523/jneurosci.0208-21.2021

Tardif, S. D., Mansfield, K. G., Ratnam, R., Ross, C. N., and Ziegler, T. E. (2011). The marmoset as a model of aging and age-related diseases. *ILAR J.* 52, 54–65. doi: 10.1093/ilar.52.1.54

Tardif, S. D., Smucny, D. A., Abbott, D. H., Mansfield, K., Schultz-Darken, N., and Yamamoto, M. E. (2003). Reproduction in captive common marmosets (*Callithrix jacchus*). *Comp. Med.* 53, 364–368.

Tsubuki, S., Takaki, Y., and Saido, T. C. (2003). Dutch, Flemish, Italian, and Arctic mutations of APP and resistance of Abeta to physiologically relevant proteolytic degradation. *Lancet* 361, 1957–1958. doi: 10.1016/s0140-6736(03)13555-6

Turner, A. J., and Nalivaeva, N. N. (2006). Proteinase dysbalance in pathology: the neprilysin (NEP) and angiotensin-converting enzyme (ACE) families. *Cell Mol. Biol. (Noisy-le-grand)* 52, 40–48.

Turner, A. J., Brown, C. D., Carson, J. A., and Barnes, K. (2000). The neprilysin family in health and disease. *Adv. Exp. Med. Biol.* 477, 229–240. doi: 10.1007/0-306-46826-3_25

Turner, A. J., Isaac, R. E., and Coates, D. (2001). The neprilysin (NEP) family of zinc metalloendopeptidases: genomics and function. *Bioessays* 23, 261–269. doi: 10.1002/1521-1878(200103)23:3<261::AID-BIES1036>3.0.CO;2-K

Turner, A. J., Murphy, L. J., Medeiros, M. S., and Barnes, K. (1996). Endopeptidase-24.11 (neprilysin) and relatives: twenty years on. *Adv. Exp. Med. Biol.* 389, 141–148. doi: 10.1007/978-1-4613-0335-0_17

Uruno, A., Matsumaru, D., Ryoke, R., Saito, R., Kadoguchi, S., Saigusa, D., et al. (2020). Nrf2 suppresses oxidative stress and inflammation in app knock-in Alzheimer's disease model mice. *Mol. Cell Biol.* 40:e00467-19. doi: 10.1128/mcb.00467-19

Van Broeckhoven, C., Haan, J., Bakker, E., Hardy, J. A., Vanhul, W., Wehnert, A., et al. (1990). Amyloid-Beta protein-precursor gene and hereditary cerebral-hemorrhage with amyloidosis (DUTCH). *Science* 248, 1120–1122. doi: 10.1126/science.1971458

van de Nes, J. A., Sandmann-Keil, D., and Braak, H. (2002). Interstitial cells subjacent to the entorhinal region expressing somatostatin-28 immunoreactivity are susceptible to development of Alzheimer's disease-related cytoskeletal changes. *Acta Neuropathol.* 104, 351–356. doi: 10.1007/s00401-002-0551-7

Vepsäläinen, S., Helisalmi, S., Koivisto, A. M., Tapaninen, T., Hiltunen, M., and Soininen, H. (2007). Somatostatin genetic variants modify the risk for Alzheimer's disease among Finnish patients. *J. Neurol.* 254, 1504–1508. doi: 10.1007/s00415-007-0539-2

Watamura, N., Kakiya, N., Nilsson, P., Tsubuki, S., Kamano, N., Takahashi, M., et al. (2021a). Somatostatin-evoked Aβ catabolism in the brain: mechanistic involvement of α-endosulfine-KATP channel pathway. *Mol. Psychiatry* Online ahead of print. doi: 10.1038/s41380-021-01368-8

Watamura, N., Sato, K., Shiihashi, G., Iwasaki, A., Kamano, N., Takahashi, M., et al. (2021b). An isogenic panel of single app knock-in mouse models of Alzheimer's disease confers differential profiles of β-secretase inhibition and endosomal abnormalities. *bioRxiv [preprint]* doi: 10.1101/2021.08.22.457278

Xia, D., Lianoglou, S., Sandmann, T., Calvert, M., Suh, J. H., Thomsen, E., et al. (2021). Fibrillar Aβ causes profound microglial metabolic perturbations in a novel APP knock-in mouse model. *bioRxiv [preprint]* doi: 10.1101/2021.01.19.426731

Yasojima, K., Akiyama, H., McGeer, E. G., and McGeer, P. L. (2001). Reduced neprilysin in high plaque areas of Alzheimer brain: a possible relationship to deficient degradation of beta-amyloid peptide. *Neurosci. Lett.* 297, 97–100. doi: 10.1016/s0304-3940(00)01675-x

Zhang, H. X., Zhang, Y., and Yin, H. (2019). Genome editing with mRNA encoding ZFN, TALEN, and Cas9. *Mol. Ther.* 27, 735–746.

Conflict of Interest: The authors declare that the research was conducted in the absence of any commercial or financial relationships that could be construed as a potential conflict of interest.

Publisher's Note: All claims expressed in this article are solely those of the authors and do not necessarily represent those of their affiliated organizations, or those of the publisher, the editors and the reviewers. Any product that may be evaluated in this article, or claim that may be made by its manufacturer, is not guaranteed or endorsed by the publisher.

frontiers | Frontiers in Human Neuroscience

SYSTEMATIC REVIEW
published: 18 April 2022
doi: 10.3389/fnhum.2022.838666

Brain Gray Matter Alterations in Hepatic Encephalopathy: A Voxel-Based Meta-Analysis of Whole-Brain Studies

Licheng Zhu[1†], Weihua Zhang[1†], Lei Chen[1†], Yanqiao Ren[1], Yanyan Cao[1], Tao Sun[1], Bo Sun[1], Jia Liu[1,2], Jing Wang[1,2*] and Chuansheng Zheng[1,2*]*

[2] Department of Radiology, Union Hospital, Tongji Medical College, Huazhong University of Science and Technology, Wuhan, China, [2] Hubei Province Key Laboratory of Molecular Imaging, Wuhan, China

Background: Previous studies on voxel-based morphometry (VBM) have found that there were gray matter alterations in patients with hepatic encephalopathy (HE). However, the reported results were inconsistent and lack a quantitative review. Therefore, this study aims for a quantitative meta-analysis of VBM analysis on patients with HE.

Methods: The studies in our meta-analysis were collected from Pubmed, Web of Science, and Embase, which were published from January 1947 to October 2021. The seed-based d mapping (SDM) method was applied to quantitatively estimate the regional gray matter abnormalities in patients with HE. A meta-regression analysis was applied to evaluate the relationship between plasma ammonia and gray matter alteration.

Results: There were nine studies, with sixteen datasets consisting of 333 participants with HE and 429 healthy controls. The pooled and subgroup meta-analyses showed an increase in gray matter volume (GMV) in the bilateral thalamus and the calcarine fissure but a decrease in the GMV in the bilateral insula, the basal ganglia, the anterior cingulate gyrus, and the cerebellum. The meta-regression showed that plasma ammonia was positively associated with the GMV in the left thalamus but was negatively associated with the GMV in the cerebellum and the bilateral striatum.

Conclusion: Gray matter volume in patients with HE largely varied and could be affected by plasma ammonia. The findings of this study could help us to better understand the pathophysiology of cognitive dysfunction in patients with HE.

Keywords: seed-based d mapping, voxel-based morphometry, meta-analysis, hepatic encephalopathy, gray matter, plasma ammonia

OPEN ACCESS

Edited by:
Ahmad Raza Khan, Centre of Bio-Medical Research (CBMR), India

Reviewed by:
Sarael Alcauter, Universidad Nacional Autónoma de México, Mexico
Carlo Augusto Mallio, Campus Bio-Medico University, Italy

***Correspondence:**
Jia Liu
liujia_1990512@foxmail.com
Jing Wang
xhwangjing@hust.edu.cn
Chuansheng Zheng
hqzcsxh@sina.com

† These authors have contributed equally to this work and share first authorship

Specialty section:
This article was submitted to Brain Imaging and Stimulation, a section of the journal Frontiers in Human Neuroscience

Received: *18 December 2021*
Accepted: *28 February 2022*
Published: *18 April 2022*

Citation:
Zhu L, Zhang W, Chen L, Ren Y, Cao Y, Sun T, Sun B, Liu J, Wang J and Zheng C (2022) Brain Gray Matter Alterations in Hepatic Encephalopathy: A Voxel-Based Meta-Analysis of Whole-Brain Studies. Front. Hum. Neurosci. 16:838666. doi: 10.3389/fnhum.2022.838666

INTRODUCTION

Hepatic encephalopathy (HE) is a neuropsychiatric syndrome, which is featured by a range of clinical manifestations, such as psychometric changes, numbness, and coma. Minimal HE (MHE) is a subset of HE in which symptoms are undetectable by routine examination and can only be diagnosed by neuropsychological measurements and neurophysiological tests (Tao et al., 2013). As reported, MHE can reduce the quality of life and the working ability (Bajaj et al., 2009), and MHE is prone to progress to overt HE (OHE) without proper treatment. Patients with cirrhosis with OHE usually develop poor prognosis and a loss of learning ability (Umapathy et al., 2014). Thus, even patients recovering from the disease can still have abnormal neuropsychiatric function and high recurrence rates (Sharma et al., 2010).

The voxel-based morphometry (VBM) method has many advantages over the region of interest (ROI) analysis ability (Pereira et al., 2010), such as automation, assumption-free, operator independence, and whole-brain gray matter abnormalities. With VBM, MRI morphometry studies have focused on structural abnormalities of gray matter and white matter. However, the structures to be evaluated need to be determined in advance, because of the major limitations of ROI-based brain morphological change measurement techniques (Busatto et al., 2008). Because of the different sample sizes of participants and different research methods, the results of these studies were contradicted (Costafreda et al., 2009). In comparison, VBM is a more accurate method than the manual volume approach and can overcome the limitations of the ROI approach. It is important to confirm unanimous results of VBM studies on gray matter volume (GMV) in those with HE based on a meta-analysis (Wang et al., 2015).

At present, several VBM studies of GMV in HE have been published. However, the results are diverse. For instance, one study found that regional gray matter atrophy was mostly confined in bilateral frontal regions, the bilateral temporal pole, and the cerebellum (García-García et al., 2017), while another study suggested that the loss of gray matter was observed in the precuneus, the bilateral insular cortex, and the caudate nucleus (Chen et al., 2012).

Seed-based d mapping (SDM) is a statistical software for meta-analysis, using neuroimaging technology to detect differences in brain activity. The SDM, combining positive and negative differences, has proven to be better than methods such as the activation likelihood estimation and the multilevel kernel density analysis (Radua et al., 2012). In addition, to assess the robustness and heterogeneity of the results, SDM enables several complementary analyses, such as jack-knife and subgroup analysis (Radua et al., 2012). However, SDM has not been applied to a meta-analysis comparing patients with HE with normal controls. In this study, we have used SDM to evaluate the published VBM studies on patients with HE and the control group for identifying consistent regional gray matter abnormalities.

METHODS

Search Strategy

Our study followed the Preferred Reporting Items for Systematic Reviews and Meta-Analyses (PRISMA) guidelines (Liberati et al., 2009). The studies in our meta-analysis were collected from Pubmed, Web of Science, and Embase, which were published from January 1947 to October 2021. The last search was run on October 25, 2021. The keywords we used were "hepatopathy" or "cirrhosis" or "hepatic fibrosis" or "HE" plus "VBM" or "voxel-based morphometry" or "gray matter" or "voxel-wise" or "voxel-based." In addition, we also manually checked the reference lists of the included studies.

At the same time, manual retrieval was performed on the bibliography of the included literature. The inclusion criteria were as follows: (1) the studies that reported a VBM (GM volume) comparison between patients with HE and controls; (2) the results of the stereotactic changes of the whole brain's three-dimensional coordinates (X, Y, and Z) were reported; and (3) the significance threshold was corrected by multiple comparisons based on voxels or the threshold corrected without a spatial range. We found that some studies had many independent patient samples, which were considered separate studies in our meta-analysis. The exclusion criteria are as follows: (1) not enough data could be obtained even if the corresponding author has been asked for more information; (2) there are less than 10 cases in the HE group and the control group; (3) overlapping with data from other publications; (4) uncorrected results and spatial thresholds were not reported; (5) no control group was present; (6) the analysis was limited to a specific ROI; and (7) the coordinates were not in Talairach or the Montreal Neurological Institute (MNI) space.

Data Extraction

Two investigators (LCZ and WHZ) independently examined abstracts from the initial search, and disagreements were discussed with a third author to reach a consensus. Authors were blinded to the articles' authors, their institutions, and the source of funding to minimize potential bias. The full texts of studies thought to fulfill the inclusion criteria were assessed in detail to confirm eligibility. Furthermore, we found that some studies had multiple independent patient samples who were compared with the same healthy control groups, which were considered in this study as separate studies in our meta-analysis. Coordinates were extracted independently by two authors using anisotropic effect size-SDM.

Voxel-Wise Meta-Analysis

We used the SDM to analyze the gray matter difference. First, we had a pooled meta-analysis of these selected studies. Then, we conducted 3 subgroup meta-analyses, namely, non-HE (NHE), MHE, and OHE, which were three different types of HE. The SDM method has been described clearly in other articles (Radua and Mataix-Cols, 2009; Radua et al., 2011, 2012). All the reported peak coordinates were selected.

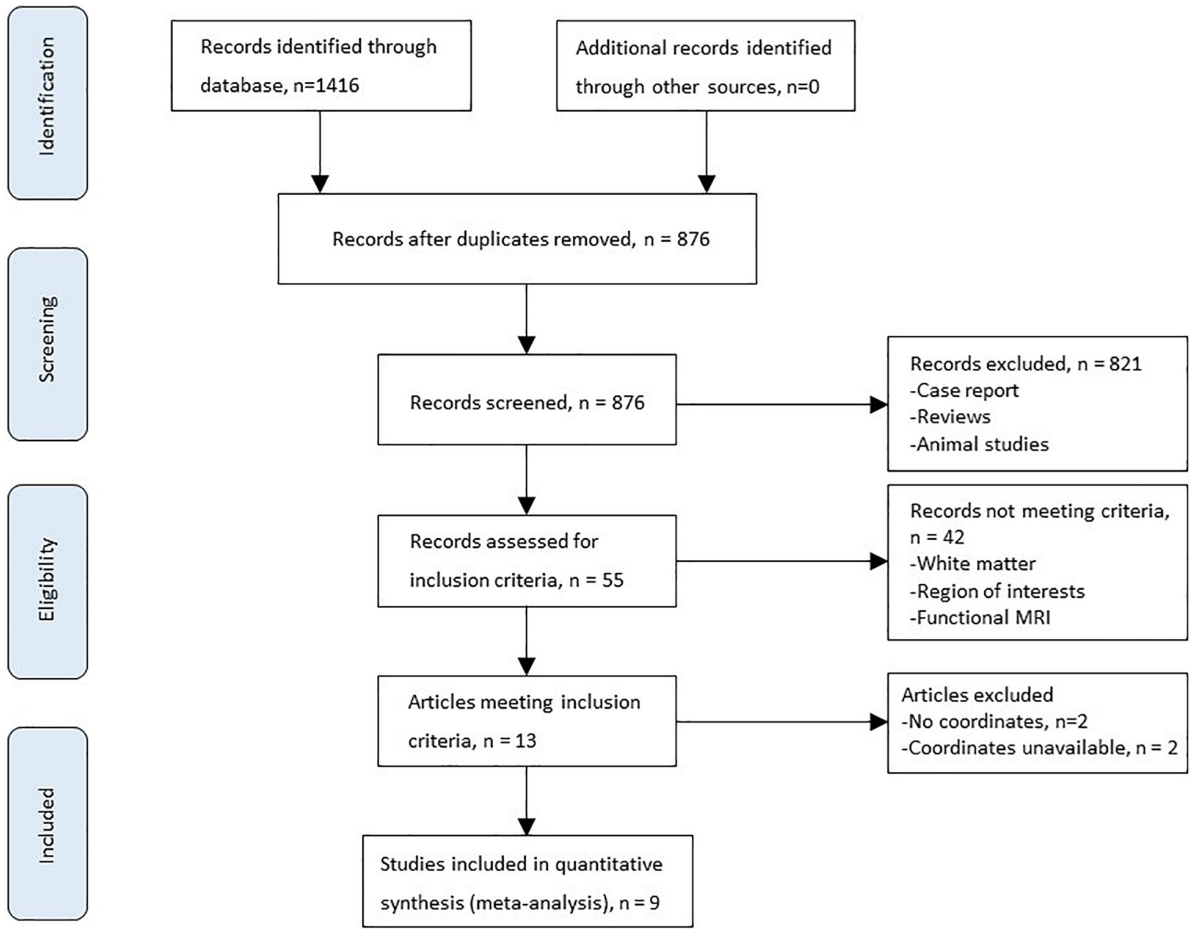

FIGURE 1 | A flowchart of the inclusion and identification in the current meta-analysis.

To avoid potential bias, all studies used the same statistical threshold. Second, the standard MNI plots of gray matter differences for each study were reconstructed. The peak *t*-value of Hedges' effect size was the basis of the peak coordinates' reconstruction. The zero findings in the study were reconstructed with the same effect size, and the only difference was that all the voxels in the effect size graph were estimated to be zero. Third, an analysis was carried out by studying the average value of maps. Thus, a study that had a larger sample size would have a larger contribution. Finally, after determining the statistical significance, a zero distribution was created and the *P*-value was obtained directly. The default SDM kernel sizes and thresholds were used (full width at half-maximum D 20 mm, voxel p D 0.005, peak height Z D 1, and cluster extent D 10 voxels) (Radua et al., 2012). In addition, the robustness of the findings was assessed by using jack-knife sensitivity. For instance, data were repeatedly analyzed fifteen times in polled meta-analyses, and whenever one study was removed, a repeat analysis was performed. If a previously important brain region remained important in most of the study combinations, the finding was supposed to be highly repetitive.

Meta-Regression Analysis

The main output of each variable was a regression slope graph. A simple linear regression can be used to assess the impact of sociodemographic and clinical variables (Radua et al., 2012). According to the previous analyses, the detection of reduced spurious associations, with a probability threshold of 0.00005, required anomalies to be found in the slope and one extreme of explanatory variables, with discarded results found in other areas of the analysis. Finally, we examined the regression graph to exclude fitting driven by too few studies (Radua and Mataix-Cols, 2009).

RESULTS

Included Studies and Sample Characteristics

Figure 1 shows the flowchart of inclusion and identification in this meta-analysis. In total, 1,416 documents were identified by the search strategy, and 9 (Chen et al., 2012; Iwasa et al., 2012; Zhang et al., 2012; Qi et al., 2013c; Tao et al., 2013; García-García et al., 2017; Wang et al., 2017, 2019;

TABLE 1 | Demographic and clinical characteristics of studies included in the current meta-analysis.

	Patient information							Healthy controls		
Study	**Types**	**No**	**Female (%)**	**Mean age (year)**	**Child-Pugh A/B/C**	**Comorbidity**	**Plasma ammonia (μmol/L)**	**No**	**Female (%)**	**Mean age (year)**
Zhang et al. (2012)	NHE	31	26.7	49.7	NA	Negative	58.9	40	35.0	49.8
	MHE	18	26.7	49.7	NA	Negative	58.9	40	35.0	49.8
	OHE	11	26.7	49.7	NA	Negative	58.9	40	35.0	49.8
Iwasa et al. (2012)	NHE	18	72.2	65.7	11/4/3	Negative	65.8	16	56.3	68.7
Tao et al., 2013	NHE	24	33.3	47.7	10/8/6	Negative	48.5	33	33.3	45.2
	MHE	23	26.1	44.7	4/6/13	Negative	56.5	33	33.3	45.2
	OHE	24	29.2	47.1	0/2/22	Negative	75.4	33	33.3	45.2
Wang et al. (2019)	NHE	20	45.0	56.0	4/4/7	Negative	51.6	20	30.0	51.0
Liu et al. (2019)	OHE	23	8.7	45.9	10/10/3	Negative	NA	23	13.0	51.8
	OHE	23	8.7	50.4	4/16/3	HM	NA	23	13.0	51.8
García-García et al. (2017)	NHE	26	23.1	63.0	23/3/0	Negative	NA	24	33.3	61.0
	MHE	13	7.7	64.0	8/5/0	Negative	NA	24	33.3	61.0
Wang et al. (2017)	NHE	17	29.4	53.4	15/1/1	Negative	39.0	17	29.4	54.4
	NHE	17	29.4	54.8	15/1/1	Diabetes	54.5	17	29.4	54.4
Chen et al. (2012)	OHE	20	14.2	51.9	NA	Negative	NA	21	15.0	51.2
Qi et al. (2013c)	MHE	25	28.0	56.2	12/12/1	Negative	70.1	25	28.0	53.7

NHE, non hepatic encephalopathy; MHE, minimal hepatic encephalopathy; OHE, overt hepatic encephalopathy; NA, not available, HM, Hepatic myelopathy.

TABLE 2 | Technique details of VBM studies for GMV on HE in meta-analysis.

Study	**Scanner (T)**	**Software**	**FHWH (mm)**	***P*-value**	**Coordinates**
Zhang et al. (2012)	3	SPM8	8	$P < 0.01$ (FDR correction)	36
Iwasa et al. (2012)	1.5	SPM8	8	$P < 0.001$ (uncorrected)	5
Tao et al. (2013)	3	SPM8	8	$P < 0.05$ (FDR correction)	22
Wang et al. (2019)	3	SPM8	3	$P < 0.0002$ (FWE correction)	7
Liu et al., 2019	3	SPM8	12	$P < 0.05$ (AlphaSim correction)	21
García-García et al. (2017)	3	SPM12	8	$P < 0.001$ (uncorrected)	49
Wang et al. (2017)	3	SPM8	8	$P < 0.05$ (Alphasim correction)	19
Chen et al. (2012)	1.5	SPM5	4	$P < 0.05$ (FDR corrected)	24
Qi et al. (2013c)	3	SPM8	8	$P < 0.05$ (FDR correction)	15

HE, hepatic encephalopathy; FDR, false discovery rate; FEW, family-wise error; FWHM, full width at half-maximum; SPM, Statistical Parametric Mapping; T, Tesla; VBM, voxel-based morphometry; GMV, gray matter volume.

Liu et al., 2019) VBM studies met the inclusion criterion of comparison of GMV alterations. In five studies, the analysis was based on two or three different HE subgroups and was compared with the same healthy control group. As a result, a total of 16 groups of data were included for meta-analysis. **Table 1** shows the clinical and demographical data. **Table 2** shows the technical details of the included studies. All the studies included in the meta-analysis were prospective. There were 333 patients and 429 healthy controls included. No statistical difference was found in age and gender in each study.

Pooled Meta-Analysis of All the Studies

The GMV reduction in patients with HE was mainly found in four clusters (**Table 3** and **Figure 2**). The largest cluster is located in the bilateral insula, which extended into the bilateral basal ganglia. The second largest cluster is located in the left cerebellar hemisphere and the cerebellar vermis. GMV also decreased in the bilateral anterior cingulate gyrus and the right inferior frontal gyrus. Meanwhile, GMV increment was observed in the bilateral thalamus, the lingual gyrus, and the calcarine fissure and its surrounding cortex in patients with HE.

Subgroup Meta-Analysis of Studies Including Patients With Non-hepatic Encephalopathy

A total of seven studies, including patients with NHE, as a subgroup were analyzed, including seven sets of data, 153 patients with NHE, and 167 healthy controls (**Table 1**). Subgroup analysis showed GMV reduced in the cerebellar, the bilateral basal ganglia, and the insula compared with the control group. Furthermore, the volume of gray matter in the bilateral thalamus and the calcarine fissure and its surrounding cortex increased compared with the control group (**Table 4** and **Figure 2**).

TABLE 3 | Altered gray matter volume for pooled meta-analysis of all the included studies.

	Maximum			Cluster		Jackknife sensitivity analysis (combination of studies detecting the differences)
Brain regions	**MNI coordinates, x, y, z**	**SDM value**	***P*-value**	**No. of voxels**	**Breakdown (no. of voxels)**	
HE > control						
R thalamus	6, −20, 12	4.293	<0.001	1062	R thalamus (466) L thalamus (447) R lingual gyrus, BA 27 (40) L hippocampus, BA 27 (33) R hippocampus (11) L lingual gyrus (8)	16 out of 16
R calcarine fissure / surrounding cortex	4, −64, 10	2.186	<0.001	1017	L calcarine fissure / surrounding cortex, BA 17 (211) R lingual gyrus, BA 18 (274) L lingual gyrus, BA 17 (266) R calcarine fissure / surrounding cortex, BA 17 (159) Cerebellum, vermic lobule IV/V (56) R precuneus, BA 30 (25) L precuneus, BA 17 (26)	16 out of 16
HE < control						
L insula, BA 48	−28, 12, 6	−3.764	<0.001	4344	L insula, BA 48 (973) R striatum (574) L striatum (490) R lenticular nucleus, putamen, BA 48 (464) R insula, BA 48 (419) L lenticular nucleus, putamen, BA 48 (269) R caudate nucleus (260) L caudate nucleus (225) R amygdala, BA 34 (194) L amygdala, BA 34 (188) L parahippocampal gyrus, BA 28 (114) R temporal pole, superior temporal gyrus (89) R parahippocampal gyrus, BA 28 (85)	16 out of 16
L cerebellum, hemispheric lobule	−6, −62, −40	−4.121	<0.001	3049	L cerebellum, hemispheric lobule (1853) Cerebellum, vermic lobule (722) R cerebellum, hemispheric lobule (474)	16 out of 16
R anterior cingulate / paracingulate gyri	10, 40, 14	−3.415	<0.001	2211	R anterior cingulate / paracingulate gyri, BA 32 (551) L superior frontal gyrus, medial, BA 32 (501) L anterior cingulate / paracingulate gyri, BA 32 (611) R median cingulate / paracingulate gyri, BA 32 (266) L median cingulate / paracingulate gyri, BA 24 (166) R superior frontal gyrus, medial, BA 9 (116)	16 out of 16
R inferior frontal gyrus	50, 32, −2	−2.244	0.003	59	R inferior frontal gyrus, BA 45 (59)	14 out of 16

MNI, montreal neurological institute; HE, hepatic encephalopathy; R, right; BA, brodmann area; L, left.

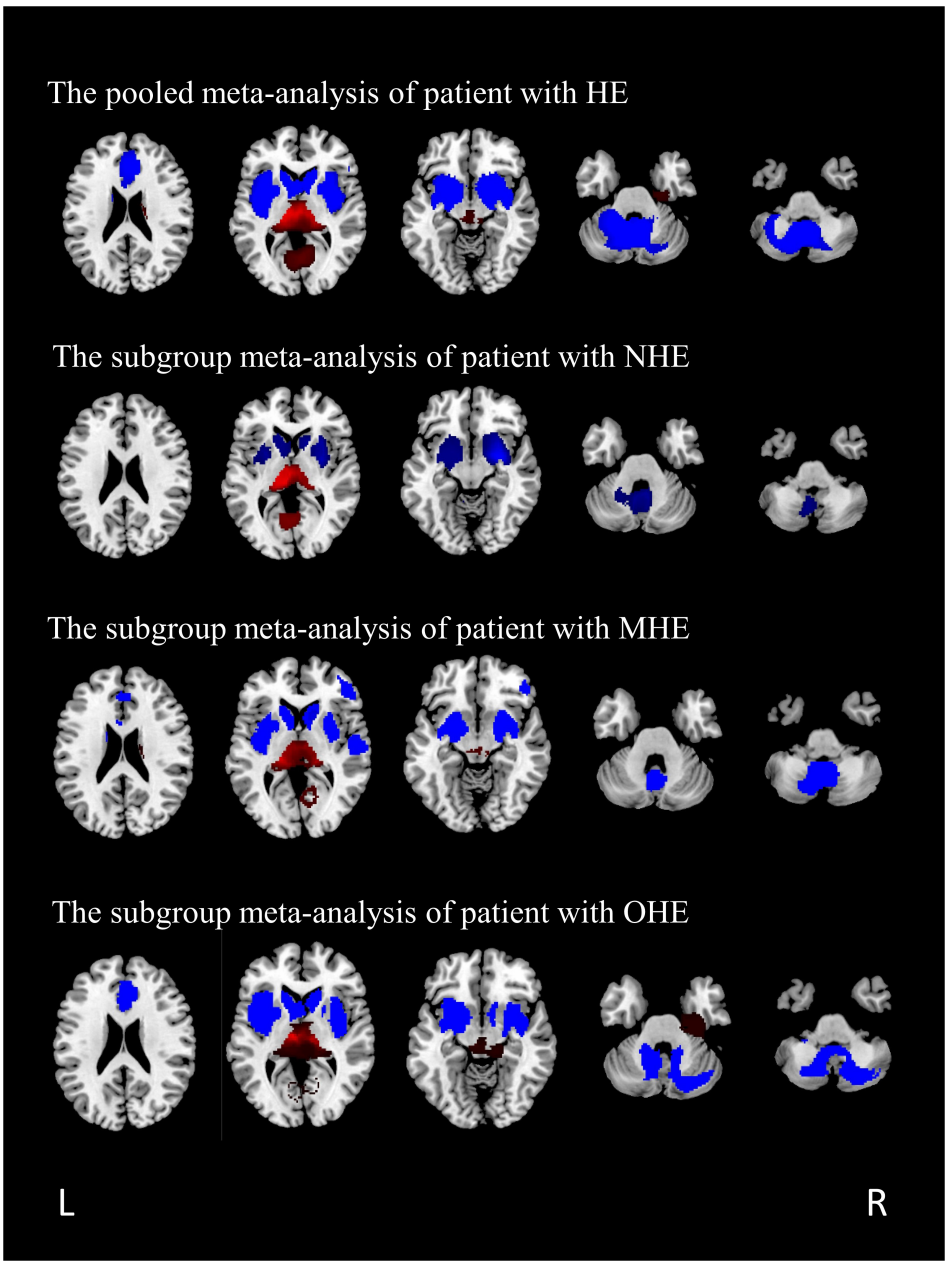

FIGURE 2 | The regions of decreased (blue) and increased (red) gray matter volumes (GMVs) in patients with HE compared with healthy controls in a pooled meta-analysis and three subgroup meta-analyses. The results are displayed on a 2D axial rendered brain. HE, hepatic encephalopathy; NHE, non-hepatic encephalopathy; MHE, minimal hepatic encephalopathy; OHE, overt hepatic encephalopathy; L, left; R, right.

Subgroup Meta-Analysis of Studies Including Patients With Minimal Hepatic Encephalopathy

All the patients with MHE were analyzed, including four sets of data, 79 patients, and 122 healthy controls (**Table 1**). The study showed GMV reduced in five brain regions, namely, the bilateral basal ganglia, the insula, the cerebellar hemisphere and the cerebellar vermis, the bilateral anterior cingulate gyrus extended to the right inferior frontal gyrus, and the superior temporal gyrus. GMV of patients with MHE increased in the bilateral thalamus, the right lingual gyrus, and the right calcarine fissure (**Table 5** and **Figure 2**).

Subgroup Meta-Analysis of Studies Including Patients With Overt Hepatic Encephalopathy

A total of four studies with patients with OHE were analyzed, including five sets of data comparing 101 patients and 140

TABLE 4 | Altered gray matter volume for subgroup meta-analyses between patients with NHE and healthy controls.

	Maximum			Cluster		
Brain regions	**MNI coordinates, x, y, z**	**SDM value**	***P*-value**	**No. of voxels**	**Breakdown (no. of voxels)**	**Jackknife sensitivity analysis (combination of studies detecting the differences)**
NHE > control						
L thalamus	−4, −24, 8	2.920	<0.001	830	L thalamus (431) R thalamus (399)	7 out of 7
L calcarine fissure / surrounding cortex	−4, −64, 8	1.461	<0.001	457	L calcarine fissure / surrounding cortex, BA 17 (176) L lingual gyrus, BA 17 (131) R lingual gyrus, BA 17 (75) L precuneus, BA 23 (48) R calcarine fissure / surrounding cortex, BA 17 (27)	7 out of 7
NHE < control						
R striatum	18, 10, 0	−2.435	0.001	1225	R striatum (498) R lenticular nucleus, putamen (459) R amygdala, BA 34 (158) R insula, BA 48 (49) R caudate nucleus, BA 25 (61)	7 out of 7
L striatum	−26, 6, 2	−2.269	<0.001	998	L striatum (397) L lenticular nucleus, putamen, BA 48 (315) L amygdala, BA 34 (174) L insula, BA 48 (63) L caudate nucleus, BA 25 (49)	7 out of 7
L cerebellum, hemispheric lobule	−8, −62, −38	−2.590	0.001	558	L cerebellum, hemispheric lobule (272) Cerebellum, vermic lobule (266) R cerebellum, hemispheric lobule (20)	7 out of 7

MNI, montreal neurological institute; SDM, seed-based d mapping; NHE, non-hepatic encephalopathy; BA, Brodmann area; R, right; L, left.

healthy controls (**Table 1**). The subgroup analysis identified GMV reduction in the bilateral insula, the bilateral basal ganglia, the bilateral cingulate gyrus, and the cerebellum. GMV increased in the bilateral thalamus, the lingual gyrus, and the calcaneal fissure (**Table 6** and **Figure 2**).

Sensitivity Analysis

According to **Table 3**, the GMV alteration of the right thalamus, the right calcarine fissure and its surrounding cortex, the left insula, the cerebellum, and the right anterior cingulate gyri were highly replicable for the reason that they were kept throughout all of the 16 combinations of studies. The sensitivity analysis showed that theGMV decrease in the right inferior frontal gyrus were also significant in all but two combinations of the datasets.

Whole-brain jack-knife sensitivity analyses of the subgroup meta-analysis of studies involving patients with NHE show that the left thalamus, the left calcarine fissure and its surrounding cortex, the bilateral striatum, and the cerebellum were highly replicable, being preserved through all of the 7 combinations of studies (**Table 4**). In patients with MHE, the altered GMV in the left thalamus, the right lingual gyrus, the cerebellum, the right striatum, the left insula, and the right anterior cingulate were highly replicable, as they were kept throughout all of the 4 combinations of studies (**Table 5**). As for OHE, altered GMV in the left thalamus, left calcareous clef and peripheral cortex, left insula, cerebellum, and right anterior cingulate were highly reproducible because these findings were kept in all the five dataset combinations (**Table 6**).

Meta-Regression

A meta-regression analysis was used to analyze the association between plasma ammonia and GMV alteration in patients with HE. These variables were available for all the 228 participants in the 11 datasets. The plasma ammonia level positively correlated with the GMV in the left thalamic infract and negatively correlated with the GMV in the cerebellum and the bilateral striatum (**Figure 3**).

DISCUSSION

To the best of our knowledge, this is the first study to analyze the changes in brain GMV of patients with HE with SDM software and three subgroup analyses. Both the comprehensive analysis and the subgroup analysis have confirmed that patients with HE had extensive symmetry changes in gray matter. Our research

TABLE 5 | Altered gray matter volume for subgroup meta-analyses between patients with MHE and healthy controls.

	Maximum			Cluster		
Brain regions	**MNI coordinates, x, y, z**	**SDM value**	***P*-value**	**No. of voxels**	**Breakdown (no. of voxels)**	**Jackknife sensitivity analysis (combination of studies detecting the differences)**
MHE > control						
L thalamus	−14, −28, 10	3.521	<0.001	885	L thalamus (406) R thalamus (423) L hippocampus, BA 27 (48) R hippocampus (8)	4 out of 4
R lingual gyrus	8, −62, −2	1.081	<0.001	282	R lingual gyrus, BA 18 (237) R calcarine fissure / surrounding cortex, BA 17 (45)	4 out of 4
MHE < control						
L cerebellum, hemispheric lobule	−10, −60, −22	−2.676	<0.001	1703	L cerebellum, hemispheric lobule (877) Cerebellum, vermic lobule (576) R cerebellum, hemispheric lobule, BA 19 (250)	4 out of 4
R striatum	20, 2, −4	−3.120	<0.001	1494	R lenticular nucleus, putamen, BA 48 (447) R striatum (384) R amygdala, BA 34 (160) R caudate nucleus (192) R parahippocampal gyrus, BA 28 (158) R temporal pole, superior temporal gyrus, BA 38 (109) R insula, BA 48 (44)	4 out of 4
L insula	−30, 10, 10	−2.676	<0.001	1465	L insula, BA 48 (596) L striatum (286) L lenticular nucleus, putamen, BA 48 (334) L amygdala, BA 34 (189) L parahippocampal gyrus, BA 28 (60)	4 out of 4
R anterior cingulate / paracingulate gyri	8, 32, 22	−2.701	<0.001	947	R anterior cingulate / paracingulate gyri, BA 32 (361) L anterior cingulate / paracingulate gyri, BA 24 (398) L superior frontal gyrus, medial, BA 32 (188)	4 out of 4
R inferior frontal gyrus	46, 44, 0	−2.937	0.001	499	R inferior frontal gyrus, BA 45 (499)	3 out of 4
R superior temporal gyrus	52, −16, 4	−2.467	0.001	327	R superior temporal gyrus, BA 48 (247) R heschl gyrus, BA 48 (80)	3 out of 4

MNI, montreal neurological institute; SDM, seed-based d mapping; MHE, minimal hepatic encephalopathy; BA, brodmann area; R, right; L, left.

may help to understand the potential neurodegenerative process of HE. An important finding of subgroup analysis is that, in patients with different degrees of HE, the changing area of brain GMV is similar, and the range of symptoms increases with the aggravation.

The current voxel meta-analysis mainly showed that GMV increased in the bilateral thalamus, the bilateral hippocampus, and the bilateral lingual gyrus extending to the calcarine fissure and the precuneus. In addition, the GMV decreased in the bilateral insula, the basal ganglia, the anterior cingulate gyrus extending to the superior frontal gyrus, and the cerebellum. The results of the sensitivity analysis remained largely unchanged and the results were robust and highly reproducible.

Several neuroimaging findings suggested that changes in the cortico-striato-thalamic pathway could play a crucial role in HE (Qi et al., 2012, 2013b, 2015). As information from the cortex is returned to the thalamus indirectly or directly through the striatum—white matter system, the thalamus may act as a filter for sensory input (Nakajima et al., 2019). The basal ganglia are considered to be playing an important role in the pathophysiology of HE (Qi et al., 2013a). In previous studies, basal ganglia indicated functional disconnection with other brain regions and abnormalities in metabolism (Sharma et al., 2010; Chen et al., 2012), which resulted in the disinhibition of the thalamic activity and inputs more inhibitory information into the cortex, leading to neurocognitive dysfunction (Grillner and Robertson, 2015; He et al., 2020). In addition, manganese is known to deposit within intracranial

TABLE 6 | Altered gray matter volume for subgroup meta-analyses between patients with OHE and healthy controls.

	Maximum			Cluster		
Brain regions	**MNI coordinates, x, y, z**	**SDM value**	***P*-value**	**No. of voxels**	**Breakdown (no. of voxels)**	**Jackknife sensitivity analysis (combination of studies detecting the differences)**
OHE > control						
L thalamus	−8, −24, 4	8.224	<0.001	950	R thalamus (433) L thalamus (424) R lingual gyrus, BA 27 (93)	5 out of 5
L calcarine fissure / surrounding cortex	−14, −74, 0	1.192	0.001	252	L calcarine fissure / surrounding cortex, BA 17 (76) L lingual gyrus, BA 18 (66) R lingual gyrus, BA 18 (60) R calcarine fissure / surrounding cortex, BA 17 (50)	5 out of 5
OHE < control						
L insula, BA 48	−28, 12, 6	−3.764	<0.001	3058	L insula, BA 48 (679) L striatum (490) R striatum (422) R insula, BA 48 (388) L lenticular nucleus, putamen, BA 48 (335) R lenticular nucleus, putamen, BA 48 (309) R amygdala, BA 34 (216) L caudate nucleus (97) R caudate nucleus (66) L amygdala, BA 34 (56)	5 out of 5
L cerebellum, hemispheric lobule	−10, −60, −22	−2.676	<0.001	2008	L cerebellum, hemispheric lobule (967) R cerebellum, hemispheric lobule, BA 19 (787) Cerebellum, vermic lobule (254)	5 out of 5
R anterior cingulate / paracingulate gyri	0, 40, 28	−5.181	0.003	1141	R anterior cingulate / paracingulate gyri, BA 32 (508) L anterior cingulate / paracingulate gyri, BA 24 (398) L superior frontal gyrus, BA 32 (390) R median cingulate / paracingulate gyri, BA 32 (145)	5 out of 5

MNI, montreal neurological institute; SDM, seed-based d mapping; OHE, overt hepatic encephalopathy; BA, brodmann area; R, right; L, left.

structures, mainly the globus pallidus and the pituitary gland (Dietemann et al., 1998; Rovira et al., 2008). Previous studies have shown that manganese deposition is also one of the reasons for the loss of basal ganglia neurons (Kano and Morishima, 2021). Moreover, manganese can colocalize in such intracranial structures with other elements, such as iron or gadolinium. These elements showed cellular toxicity in neurons, which may also be the reason for the reduction of GMV in basal ganglia (Mallio et al., 2020). An increase in thalamic volume may indicate hypertrophy or hyperplasia of neurons or glia. It is speculated that the increase of thalamic volume is a compensatory effect of basal ganglia dysfunction, but the increase of thalamic volume cannot completely improve brain function (He et al., 2020).

The results showed that patients with HE also suffered from obvious increase in some brain regions, namely, the bilateral precuneus, the lingual gyrus, and the calcarine fissure and its surrounding cortex. Notably, these areas were linked to the visual functions (Rao et al., 2007; Rita Machado et al., 2017), which are relative to impaired visual information processing in patients with cirrhosis. The increase in the cortical thickness observed in patients with cirrhosis seems to contradict previous works of research (Montoliu et al., 2012; Wernberg et al., 2019). The reason for such inconsistency remains unclear. However, a previous study's results were similar to ours, which speculated that the increase of cortical thickness was related to mild brain edema in patients with HE (Wu et al., 2015). With the progression of the disease, the scope of the increase in the volume of related brain regions is reduced. We speculated that the progressive atrophy of the cortex caused by dysfunction weakens the increase in the GMV. The related neuropathological mechanism is not clear and is worthy of further study.

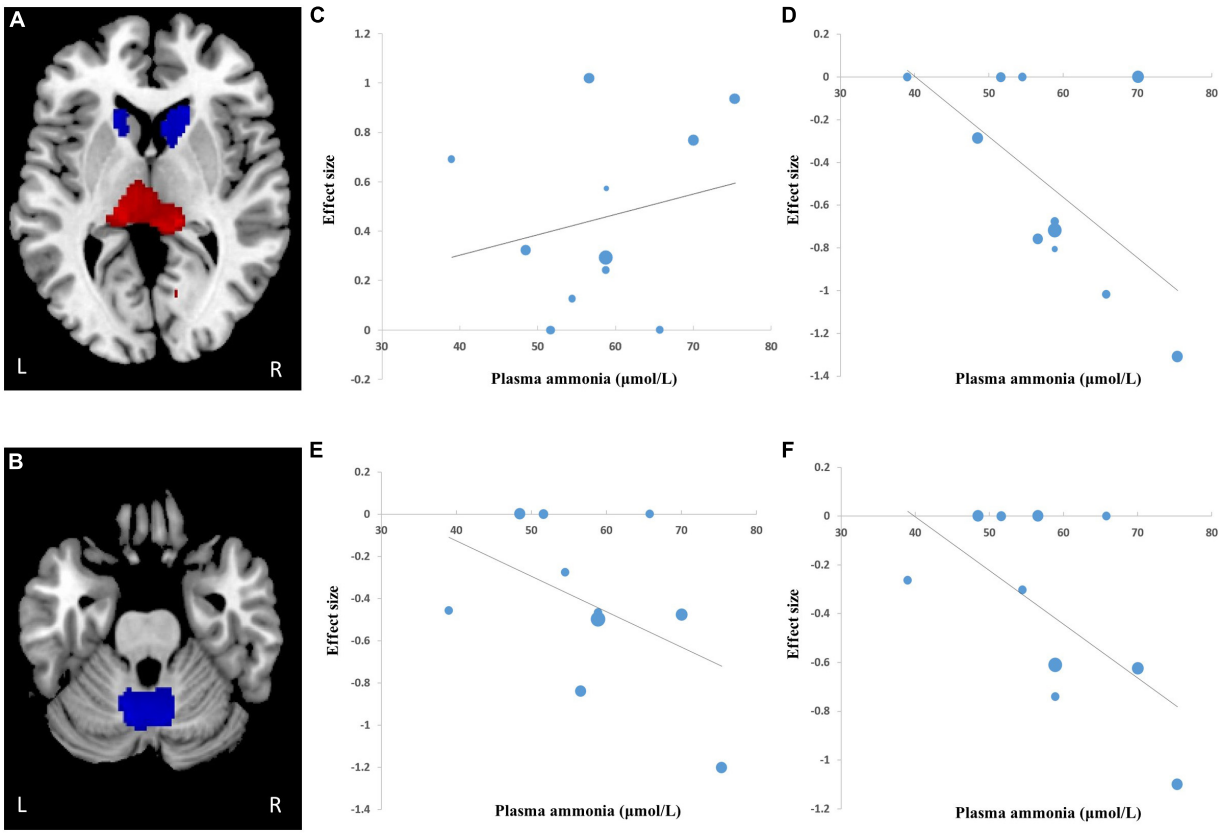

FIGURE 3 | Results of meta-regression analysis of studies of patients with HE compared with healthy controls. **(A,B)** The regions of decreased (blue) and increased (red) gray matter with changes in plasma ammonia concentration. **(C)** The plasma ammonia concentration of patients with HE was positively associated with gray matter volume (GMV) in the left thalamus. The plasma ammonia of patients with HE was negatively associated with GMV in the cerebellum **(D)**, the right striatum **(E),** and the left striatum **(F)**. In the figure, the effect size required to create this plot has been extracted from the peak with the maximum slope significance, and each study is represented by a point whose size reflects the sample size; L, left; R, right.

Our study found that, in comparison with the healthy control group, patients with HE had wider GMV reduction areas with the progress of the disease. These findings have been shown in previous studies (Garcia-Martinez et al., 2011; Lin et al., 2019). The bilateral insula is the most significant area of GMV reduction, the decreased insula volume has been revealed in HE, which correlates with cognitive alterations (Chen et al., 2017; García-García et al., 2017). It is found that the resting-state neuronal activity represents abnormal regional uniformity in the insula of patients with HE (Ni et al., 2012; Chen et al., 2016). The insula integrates internal and external stimuli and plays an important role in episodic memory processing. The anterior cingulate cortex is a significant region for attentional control, response suppression, and error detection (Kerns et al., 2004). The anterior cingulate cortex and the insula participate in the detection and the location of external stimuli and internal events (Flook et al., 2020) and is also a key brain region of the default mode network (DMN; Zhang et al., 2013; Wertz et al., 2020). Studies have shown that DMN has high metabolic activity at rest. Therefore, decreased gray matter voxel of the anterior cingulate cortex may be the neurobiological basis of cognitive impairment. In addition, we also noted that, without HE, the volume of the anterior cingulate cortex region did not change in patients with cirrhosis, which maybe because of the early stage of the disease.

The cerebellum is a regulator of motor function, but a link between cerebellum changes and impaired executive function has been established (Kühn et al., 2012). Our results showed that the area of reduced cerebellar volume increased significantly with the progression of the disease. Studies have shown that the cerebellum was more susceptible to the harmful effects of hyperammonemia than the cerebral cortex (Rodrigo et al., 2010). Our study also found that the volume of the bilateral striatum and the thalamus changed with the increase of plasma ammonia, which could be caused by an increased blood flow of related brain regions in patients with cirrhosis (Felipo et al., 2014). Cerebral blood flow in patients with HE has regionally selective changes, such as decreased blood flow to cortical regions but significantly increased blood flow to the basal ganglia, the cerebellum, and the thalamic structures (Butterworth, 2019). These regions are more susceptible to plasma ammonia. New animal models using ammonia as a precipitation factor also confirmed cerebellar neuron loss (García-Lezana et al., 2017). Gray matter loss reflects ammonia-related neurological changes.

The discovery and measurement of HE are challenging in clinical practice. Nowadays, artificial intelligence and machine learning have been increasingly applied to disease diagnosis, especially medical image recognition (Supekar et al., 2022). We reviewed previous articles and obtained a relatively unified result of GMV change in patients with HE, which provides a basis for delineating ROIs in machine learning. EEG is a common tool for monitoring HE (Amodio and Montagnese, 2015). However, EEG signals may be damaged by background noise, which leads to inconsistent diagnostic accuracy (Mutanen et al., 2018). Machine learning algorithms can analyze records containing a large number of variables and can find complex linear or non-linear relationships between variables (Gazda et al., 2021). Machine learning and deep learning methods have been used to analyze EEG to predict various chronic psychiatric illnesses (Natu et al., 2022; Paul et al., 2022). Using artificial intelligence and machine learning to comprehensively analyze MRI and EEG to diagnose HE more accurately may be the direction of future research.

This study still has some limitations. First, due to the sample size, the power of the results of this study may be limited, which is similar to the early voxel-based meta-analysis. Second, there are still some deviations in the VBM method, especially in areas with large anatomical variation; it may excessively show population differences, which is due to its relative insensitivity to more spatial changes (Bookstein, 2001; Tisserand et al., 2002). Another issue is that the meta-analysis is related to coordinates in published studies, leading to less accurate results (Zhou et al., 2014). Moreover, only 9 studies met the inclusion criteria for the quantitative analysis in our research. A small number of studies would reduce the credibility of the results, especially the subgroup analysis should be interpreted with caution as they were driven by less than 10 studies. In addition, the lack of a protocol with *a priori* methods, the inclusion of English language papers only, the absence of searches for gray literature, and the use of a non-validated quality assessment checklist may have introduced a range of biases.

CONCLUSION

Based on the available imaging works of literature, this meta-analysis revealed widespread and significant changes in GMV in patients with HE. The subgroup analysis suggested that, in patients with different degrees of HE, the changing area of GMV was similar and the range of symptoms increased with aggravation. The change of GMV in patients with HE was significantly related to plasma ammonia.

DATA AVAILABILITY STATEMENT

The raw data supporting the conclusions of this article will be made available by the authors, without undue reservation.

AUTHOR CONTRIBUTIONS

JL, JW, and CZ: conceptualization, methodology, and project administration. LZ, WZ, and LC: investigation. TS and YR: resources and data curation. LZ and YC: writing—original. BS and LC: draft, formal analysis, and visualization. All authors contributed to the article and approved the submitted version.

FUNDING

This study was supported by the National Natural Science Foundation of China (Grant Nos. 81873919 and 82001801).

REFERENCES

Amodio, P., and Montagnese, S. (2015). Clinical neurophysiology of hepatic encephalopathy. *J. Clin. Exp. Hepatol.* 5, S60–S68. doi: 10.1016/j.jceh.2014.06.007

Bajaj, J. S., Saeian, K., Schubert, C. M., Hafeezullah, M., Franco, J., Varma, R. R., et al. (2009). Minimal hepatic encephalopathy is associated with motor vehicle crashes: the reality beyond the driving test. *Hepatology (Baltimore, Md)* 50, 1175–1183. doi: 10.1002/hep.23128

Bookstein, F. L. (2001). "Voxel-based morphometry" should not be used with imperfectly registered images. *NeuroImage* 14, 1454–1462. doi: 10.1006/nimg.2001.0770

Busatto, G. F., Diniz, B. S., and Zanetti, M. V. (2008). Voxel-based morphometry in Alzheimer's disease. *Expert Rev. Neurother.* 8, 1691–1702.

Butterworth, R. F. (2019). Hepatic encephalopathy in cirrhosis: pathology and pathophysiology. *Drugs* 79, 17–21. doi: 10.1007/s40265-018-1017-0

Chen, H. J., Liu, P. F., Chen, Q. F., and Shi, H. B. (2017). Brain microstructural abnormalities in patients with cirrhosis without overt hepatic encephalopathy: a voxel-based diffusion kurtosis imaging study. *AJR Am. J. Roentgenol.* 209, 1128–1135. doi: 10.2214/AJR.17.17827

Chen, H. J., Zhu, X. Q., Shu, H., Yang, M., Zhang, Y., Ding, J., et al. (2012). Structural and functional cerebral impairments in cirrhotic patients with a history of overt hepatic encephalopathy. *Eur. J. Radiol.* 81, 2463–2469. doi: 10.1016/j.ejrad.2011.10.008

Chen, Q. F., Chen, H. J., Liu, J., Sun, T., and Shen, Q. T. (2016). Machine learning classification of cirrhotic patients with and without minimal hepatic encephalopathy based on regional homogeneity of intrinsic brain activity. *PLoS One* 11:e0151263. doi: 10.1371/journal.pone.0151263

Costafreda, S. G., David, A. S., and Brammer, M. J. (2009). A parametric approach to voxel-based meta-analysis. *NeuroImage* 46, 115–122. doi: 10.1016/j.neuroimage.2009.01.031

Dietemann, J. L., Reimund, J. M., Diniz, R. L., Reis, M. Jr., Baumann, R., Neugroschl, C., et al. (1998). High signal in the adenohypophysis on T1-weighted images presumably due to manganese deposits in patients on long-term parenteral nutrition. *Neuroradiology* 40, 793–796. doi: 10.1007/s002340050686

Felipo, V., Urios, A., Giménez-Garzó, C., Cauli, O., Andrés-Costa, M. J., González, O., et al. (2014). Non invasive blood flow measurement in cerebellum detects minimal hepatic encephalopathy earlier than psychometric tests. *World J. Gastroenterol.* 20, 11815–11825. doi: 10.3748/wjg.v20.i33.11815

Flook, E. A., Feola, B., Avery, S. N., Winder, D. G., Woodward, N. D., Heckers, S., et al. (2020). BNST-insula structural connectivity in humans. *NeuroImage* 210:116555. doi: 10.1016/j.neuroimage.2020.116555

García-García, R., Cruz-Gómez, ÁJ., Mangas-Losada, A., Urios, A., Forn, C., Escudero-García, D., et al. (2017). Reduced resting state connectivity and gray matter volume correlate with cognitive impairment in minimal hepatic encephalopathy. *PLoS One* 12:e0186463. doi: 10.1371/journal.pone.0186463

García-Lezana, T., Oria, M., Romero-Giménez, J., Bové, J., Vila, M., Genescà, J., et al. (2017). Cerebellar neurodegeneration in a new rat model of episodic hepatic encephalopathy. *J. Cereb. Blood Flow Metab.* 37, 927–937. doi: 10.1177/0271678X16649196

Garcia-Martinez, R., Rovira, A., Alonso, J., Jacas, C., Simón-Talero, M., Chavarria, L., et al. (2011). Hepatic encephalopathy is associated with posttransplant cognitive function and brain volume. *Liver Transplant.* 17, 38–46. doi: 10.1002/lt.22197

Gazda, J., Drotar, P., Drazilova, S., Gazda, J., Gazda, M., Janicko, M., et al. (2021). Artificial intelligence and its application to minimal hepatic encephalopathy diagnosis. *J. Pers. Med.* 1:1090. doi: 10.3390/jpm11111090

Grillner, S., and Robertson, B. (2015). The basal ganglia downstream control of brainstem motor centres–an evolutionarily conserved strategy. *Curr. Opin. Neurobiol.* 33, 47–52. doi: 10.1016/j.conb.2015.01.019

He, X., Chaitanya, G., Asma, B., Caciagli, L., Bassett, D. S., Tracy, J. I., et al. (2020). Disrupted basal ganglia-thalamocortical loops in focal to bilateral tonic-clonic seizures. *Brain* 143, 175–190. doi: 10.1093/brain/awz361

Iwasa, M., Mifuji-Moroka, R., Kuroda, M., Moroka, H., Fujita, N., Kobayashi, Y., et al. (2012). Regional reduction in gray and white matter volume in brains of cirrhotic patients: voxel-based analysis of MRI. *Metab. Brain Dis.* 27, 551–557. doi: 10.1007/s11011-012-9314-x

Kano, Y., and Morishima, R. (2021). Pallidal manganese concentration in hepatic encephalopathy. *Clin. Gastroenterol. Hepatol.* 19:e114. doi: 10.1016/j.cgh.2020.07.039

Kerns, J. G., Cohen, J. D., MacDonald, A. W. III, Cho, R. Y., Stenger, V. A., and Carter, C. S. (2004). Anterior cingulate conflict monitoring and adjustments in control. *Science (New York, NY).* 303, 1023–1026. doi: 10.1126/science.1089910

Kühn, S., Romanowski, A., Schubert, F., and Gallinat, J. (2012). Reduction of cerebellar grey matter in Crus I and II in schizophrenia. *Brain Struct. Funct.* 217, 523–529. doi: 10.1007/s00429-011-0365-2

Liberati, A., Altman, D. G., Tetzlaff, J., Mulrow, C., Gøtzsche, P. C., Ioannidis, J. P., et al. (2009). The PRISMA statement for reporting systematic reviews and meta-analyses of studies that evaluate health care interventions: explanation and elaboration. *J. Clin. Epidemiol.* 62, e1–e34.

Lin, W., Chen, X., Gao, Y. Q., Yang, Z. T., Yang, W., and Chen, H. J. (2019). Hippocampal atrophy and functional connectivity disruption in cirrhotic patients with minimal hepatic encephalopathy. *Metab. Brain Dis.* 34, 1519–1529. doi: 10.1007/s11011-019-00457-6

Liu, K., Chen, G., Ren, S. Y., Zhu, Y. Q., Yu, T. L., Tian, P., et al. (2019). Regional gray matter abnormality in hepatic myelopathy patients after transjugular intrahepatic portosystemic shunt: a voxel-based morphometry study. *Neural Regen. Res.* 14, 850–857. doi: 10.4103/1673-5374.249233

Mallio, C. A., Lo Vullo, G., Messina, L., Beomonte Zobel, B., Parizel, P. M., and Quattrocchi, C. C. (2020). Increased T1 signal intensity of the anterior pituitary gland on unenhanced magnetic resonance images after chronic exposure to gadodiamide. *Invest. Radiol.* 55, 25–29. doi: 10.1097/RLI.0000000000000604

Montoliu, C., Gonzalez-Escamilla, G., Atienza, M., Urios, A., Gonzalez, O., Wassel, A., et al. (2012). Focal cortical damage parallels cognitive impairment in minimal hepatic encephalopathy. *NeuroImage* 61, 1165–1175. doi: 10.1016/j.neuroimage.2012.03.041

Mutanen, T. P., Metsomaa, J., Liljander, S., and Ilmoniemi, R. J. (2018). Automatic and robust noise suppression in EEG and MEG: the sound algorithm. *NeuroImage* 166, 135–151. doi: 10.1016/j.neuroimage.2017.10.021

Nakajima, M., Schmitt, L. I., and Halassa, M. M. (2019). Prefrontal cortex regulates sensory filtering through a basal ganglia-to-thalamus pathway. *Neuron* 103, 445–458.e410. doi: 10.1016/j.neuron.2019.05.026

Natu, M., Bachute, M., Gite, S., Kotecha, K., and Vidyarthi, A. (2022). Review on epileptic seizure prediction: machine learning and deep learning approaches. *Comput. Math. Methods Med.* 2022:7751263. doi: 10.1155/2022/7751263

Ni, L., Qi, R., Zhang, L. J., Zhong, J., Zheng, G., Zhang, Z., et al. (2012). Altered regional homogeneity in the development of minimal hepatic encephalopathy: a resting-state functional MRI study. *PLoS One* 7:e42016. doi: 10.1371/journal.pone.0042016

Paul, S., Maindarkar, M., Saxena, S., Saba, L., Turk, M., Kalra, M., et al. (2022). Bias investigation in artificial intelligence systems for early detection of parkinson's disease: a narrative review. *Diagnostics (Basel, Switzerland)* 12:166. doi: 10.3390/diagnostics12010166

Pereira, J. M., Xiong, L., Acosta-Cabronero, J., Pengas, G., Williams, G. B., and Nestor, P. J. (2010). Registration accuracy for VBM studies varies according to region and degenerative disease grouping. *NeuroImage* 49, 2205–2215. doi: 10.1016/j.neuroimage.2009.10.068

Qi, R., Zhang, L. J., Chen, H. J., Zhong, J., Luo, S., Ke, J., et al. (2015). Role of local and distant functional connectivity density in the development of minimal hepatic encephalopathy. *Sci. Rep.* 5:13720. doi: 10.1038/srep13720

Qi, R., Zhang, L. J., Xu, Q., Zhong, J., Wu, S., Zhang, Z., et al. (2012). Selective impairments of resting-state networks in minimal hepatic encephalopathy. *PLoS One* 7:e37400. doi: 10.1371/journal.pone.0037400

Qi, R., Zhang, L. J., Zhong, J., Zhang, Z., Ni, L., Jiao, Q., et al. (2013a). Altered effective connectivity network of the basal ganglia in low-grade hepatic encephalopathy: a resting-state fMRI study with Granger causality analysis. *PLoS One* 8:e53677. doi: 10.1371/journal.pone.0053677

Qi, R., Zhang, L. J., Zhong, J., Zhang, Z., Ni, L., Zheng, G., et al. (2013b). Disrupted thalamic resting-state functional connectivity in patients with minimal hepatic encephalopathy. *Eur. J. Radiol.* 82, 850–856. doi: 10.1016/j.ejrad.2012.12.016

Qi, R., Zhang, L. J., Zhong, J., Zhu, T., Zhang, Z., Xu, C., et al. (2013c). Grey and white matter abnormalities in minimal hepatic encephalopathy: a study combining voxel-based morphometry and tract-based spatial statistics. *Eur. Radiol.* 23, 3370–3378. doi: 10.1007/s00330-013-2963-2

Radua, J., and Mataix-Cols, D. (2009). Voxel-wise meta-analysis of grey matter changes in obsessive-compulsive disorder. *Br. J. Psychiatry* 195, 393–402. doi: 10.1192/bjp.bp.108.055046

Radua, J., Mataix-Cols, D., Phillips, M. L., El-Hage, W., Kronhaus, D. M., Cardoner, N., et al. (2012). A new meta-analytic method for neuroimaging studies that combines reported peak coordinates and statistical parametric maps. *Eur. Psychiatry* 27, 605–611. doi: 10.1016/j.eurpsy.2011.04.001

Radua, J., Via, E., Catani, M., and Mataix-Cols, D. (2011). Voxel-based meta-analysis of regional white-matter volume differences in autism spectrum disorder versus healthy controls. *Psychol. Med.* 41, 1539–1550. doi: 10.1017/S0033291710002187

Rao, H., Wang, J., Tang, K., Pan, W., and Detre, J. A. (2007). Imaging brain activity during natural vision using CASL perfusion fMRI. *Hum. Brain Mapping* 28, 593–601. doi: 10.1002/hbm.20288

Rita Machado, A., Carvalho Pereira, A., Ferreira, F., Ferreira, S., Quendera, B., Silva, E., et al. (2017). Structure-function correlations in Retinitis Pigmentosa patients with partially preserved vision: a voxel-based morphometry study. *Sci. Rep.* 7:11411. doi: 10.1038/s41598-017-11317-7

Rodrigo, R., Cauli, O., Gomez-Pinedo, U., Agusti, A., Hernandez-Rabaza, V., Garcia-Verdugo, J. M., et al. (2010). Hyperammonemia induces neuroinflammation that contributes to cognitive impairment in rats with hepatic encephalopathy. *Gastroenterology.* 139, 675–684. doi: 10.1053/j.gastro.2010.03.040

Rovira, A., Alonso, J., and Córdoba, J. (2008). MR imaging findings in hepatic encephalopathy. *AJNR Am. J. Neuroradiol.* 29, 1612–1621. doi: 10.3174/ajnr.a1139

Sharma, P., Sharma, B. C., and Sarin, S. K. (2010). Prevalence of abnormal psychometric tests and critical flicker frequency after clinical recovery of overt hepatic encephalopathy. *Neurol. India* 58, 220–224. doi: 10.4103/0028-3886.63797

Supekar, K., de Los Angeles, C., Ryali, S., Cao, K., Ma, T., and Menon, V. (2022). Deep learning identifies robust gender differences in functional brain organization and their dissociable links to clinical symptoms in autism. *Br. J. Psychiatry* 13, 1–8. doi: 10.1192/bjp.2022.13

Tao, R., Zhang, J., You, Z., Wei, L., Fan, Y., Cui, J., et al. (2013). The thalamus in cirrhotic patients with and without hepatic encephalopathy: a volumetric MRI study. *Eur. J. Radiol.* 82, e715–e720. doi: 10.1016/j.ejrad.2013.07.029

Tisserand, D. J., Pruessner, J. C., Sanz Arigita, E. J., van Boxtel, M. P., Evans, A. C., Jolles, J., et al. (2002). Regional frontal cortical volumes decrease differentially in aging: an MRI study to compare volumetric approaches and voxel-based morphometry. *NeuroImage* 17, 657–669. doi: 10.1006/nimg.2002.1173

Umapathy, S., Dhiman, R. K., Grover, S., Duseja, A., and Chawla, Y. K. (2014). Persistence of cognitive impairment after resolution of overt hepatic encephalopathy. *Am. J. Gastroenterol.* 109, 1011–1019. doi: 10.1038/ajg.2014.107

Wang, M., Cui, J., Liu, Y., Zhou, Y., Wang, H., Wang, Y., et al. (2019). Structural and functional abnormalities of vision-related brain regions in cirrhotic patients: a MRI study. *Neuroradiology* 61, 695–702. doi: 10.1007/s00234-019-02199-9

Wang, W. Y., Yu, J. T., Liu, Y., Yin, R. H., Wang, H. F., Wang, J., et al. (2015). Voxel-based meta-analysis of grey matter changes in Alzheimer's disease. *Transl. Neurodegener.* 4:6. doi: 10.1186/s40035-015-0027-z

Wang, Y. F., Kong, X., Lu, G. M., and Zhang, L. J. (2017). Diabetes mellitus is associated with more severe brain spontaneous activity impairment and gray matter loss in patients with cirrhosis. *Sci. Rep.* 7:7775. doi: 10.1038/s41598-017-08075-x

Wernberg, C. W., Schaffalitzky de Muckadell, O. B., Vilstrup, H., and Lauridsen, M. M. (2019). Prediction of overt hepatic encephalopathy by the continuous reaction time method and the portosystemic encephalopathy syndrome test in clinically mentally unimpaired patients with cirrhosis. *PLoS One* 14:e0226283. doi: 10.1371/journal.pone.0226283

Wertz, C. J., Chohan, M. O., Flores, R. A., and Jung, R. E. (2020). Neuroanatomy of creative achievement. *NeuroImage* 209:116487. doi: 10.1016/j.neuroimage.2019.116487

Wu, X., Lv, X. F., Zhang, Y. L., Wu, H. W., Cai, P. Q., Qiu, Y. W., et al. (2015). Cortical signature of patients with HBV-related cirrhosis without overt hepatic encephalopathy: a morphometric analysis. *Front. Neuroanat.* 9:82. doi: 10.3389/fnana.2015.00082

Zhang, G., Zhang, H., Li, X., Zhao, X., Yao, L., and Long, Z. (2013). Functional alteration of the DMN by learned regulation of the PCC using real-time fMRI. *IEEE Trans. Neural Syst. Rehabil. Eng.* 21, 595–606. doi: 10.1109/TNSRE.2012.2221480

Zhang, L. J., Qi, R., Zhong, J., Xu, Q., Zheng, G., and Lu, G. M. (2012). The effect of hepatic encephalopathy, hepatic failure, and portosystemic shunt on brain volume of cirrhotic patients: a voxel-based morphometry study. *PLoS One* 7:e42824. doi: 10.1371/journal.pone.0042824

Zhou, X., Zhang, J., Chen, Y., Ma, T., Wang, Y., Wang, J., et al. (2014). Aggravated cognitive and brain functional impairment in mild cognitive impairment patients with type 2 diabetes: a resting-state functional MRI study. *J. Alzheimers Dis.* 41, 925–935. doi: 10.3233/JAD-132354

Conflict of Interest: The authors declare that the research was conducted in the absence of any commercial or financial relationships that could be construed as a potential conflict of interest.

Publisher's Note: All claims expressed in this article are solely those of the authors and do not necessarily represent those of their affiliated organizations, or those of the publisher, the editors and the reviewers. Any product that may be evaluated in this article, or claim that may be made by its manufacturer, is not guaranteed or endorsed by the publisher.

frontiers | Frontiers in Human Neuroscience

ORIGINAL RESEARCH
published: 17 May 2022
doi: 10.3389/fnhum.2022.782579

Cerebellar Abnormalities on Proton MR Spectroscopy and Imaging in Patients With Gluten Ataxia: A Pilot Study

*Vishwa Rawat[1], Ritu Tyagi[1], Inder Singh[2], Prasenjit Das[3], Achal Kumar Srivastava[2], Govind K. Makharia[4] and Uma Sharma[1]**

[1] Department of NMR and MRI Facility, All India Institute of Medical Sciences, New Delhi, India, [2] Department of Neurology, All India Institute of Medical Sciences, New Delhi, India, [3] Department of Pathology, All India Institute of Medical Sciences, New Delhi, India, [4] Department of Gastroenterology and Human Nutrition, All India Institute of Medical Sciences, New Delhi, India

OPEN ACCESS

Edited by:
Ahmad Raza Khan,
Centre of Bio-Medical Research (CBMR), India

Reviewed by:
Ines Carrera,
Willows Veterinary Centre, United Kingdom
Dinesh Kumar Deelchand,
University of Minnesota Twin Cities, United States

***Correspondence:**
Uma Sharma
umasharma69@gmail.com

Specialty section:
This article was submitted to Brain Imaging and Stimulation, a section of the journal Frontiers in Human Neuroscience

Received: 28 September 2021
Accepted: 21 March 2022
Published: 17 May 2022

Citation:
Rawat V, Tyagi R, Singh I, Das P, Srivastava AK, Makharia GK and Sharma U (2022) Cerebellar Abnormalities on Proton MR Spectroscopy and Imaging in Patients With Gluten Ataxia: A Pilot Study. Front. Hum. Neurosci. 16:782579. doi: 10.3389/fnhum.2022.782579

Gluten ataxia is a rare immune-mediated neurological disorder caused by the ingestion of gluten. The diagnosis is not straightforward as antibodies are present in only up to 38% of patients, but often at lower titers. The symptoms of ataxia may be mild at the onset but lead to permanent damage if remain untreated. It is characterized by damage to the cerebellum however, the pathophysiology of the disease is not clearly understood. The present study investigated the neurochemical profile of vermis and right cerebellum and structural changes in various brain regions of patients with gluten ataxia ($n = 6$, age range 40–65 years) and compared it with healthy controls ($n = 10$, 40–55 years). Volumetric 3-D T1 and T1-weighted magnetic resonance imaging (MRI) in the three planes (axial, coronal, and sagittal) of the whole brain and single-voxel ^{1}H- magnetic resonance spectroscopy (MRS) of the vermis and right cerebellum were acquired on 3 T human MR scanner. The metabolite concentrations were estimated using LC Model (6.1–4A) while brain volumes were estimated using the online tool volBrain pipeline and CERES and corrected for partial volumes. The levels of neuro-metabolites (N-acetyl aspartate + N-acetyl aspartate glutamate, glycerophosphocholine + phosphocholine, and total creatine) were found to be significantly lower in vermis, while N-acetyl aspartate + N-acetyl aspartate glutamate and glycerophosphocholine + phosphocholine was lower in cerebellum regions in the patients with gluten ataxia compared to healthy controls. A significant reduction in the white matter of (total brain, cerebellum, and cerebrum); reduction in the volumes of cerebellum lobe (X) and thalamus while lateral ventricles were increased in the patients with gluten ataxia compared to healthy controls. The reduced neuronal metabolites along with structural changes in the brain suggested neuronal degeneration in the patients with gluten ataxia. Our preliminary findings may be useful in understanding the gluten-induced cerebral damage and indicated that MRI and MRS may serve as a non-invasive useful tool in the early diagnosis, thereby enabling better management of these patients.

Keywords: gluten ataxia, cerebellar abnormalities, MR spectroscopy, magnetic resonance imaging, celiac disease, cerebellum, cerebrum

INTRODUCTION

Gluten sensitivity-related disorders have many immune-mediated clinical manifestations such as enteropathy, dermatopathology, and neurological abnormalities (Marsh, 1995). Gluten ataxia (GA) is the most typical neurological disorder with serological evidence of gluten sensitivity, i.e., the presence of anti-gliadin antibodies (AGA IgA and AGA IgG) (Hadjivassiliou et al., 2018). It accounts for up to 40% of the cases of idiopathic sporadic ataxia and 20 % of all ataxias, with the prevalence of <0.001 in the Asia-pacific region (Hadjivassiliou et al., 1998; Ashtari et al., 2019). A strict gluten-free diet provides an improvement in the symptoms of GA (Hadjivassiliou et al., 2017). GA is characterized by damage to the cerebellum due to the widespread deposition of transglutaminase antibodies around the brain vessels. The pathophysiology of neurodegeneration in GA is not clearly understood. However, it has been reported that gluten-mediated neurological pathogenesis may occur due to deposition of immune-complex, cross-reaction of antibodies, and direct neurotoxicity, leading to an inflammatory response in the nervous system (Zelnik et al., 2004; Bushara, 2005; Abenavoli, 2010; Parisi et al., 2015). It has been reported that the antibodies generated against gliadin make the gut leaky and also cross-react with Purkinje cells in the cerebellum causing their irreversible depletion (Hadjivassiliou et al., 2016). Lymphocytic infiltration of the dorsal columns and even peripheral nerves has also been documented (Fitzsimmons et al., 2010).

The diagnosis of GA is not straightforward as antibodies are present in only up to 38% of the GA patients. In the rest of the patients, low titers (undetectable levels) make the diagnosis difficult (Benson et al., 2013). Furthermore, it has also been reported that gluten sensitivity can also be manifested without enteropathy (Aziz et al., 2012), rendering the diagnosis of such GA patients difficult. The symptoms of GA include gait ataxia, dysarthria, upper limb/lower limb ataxia, and ocular signs (Hernandez-Castillo et al., 2016). However, the onset of GA is usually not apparent, but it can rapidly progress, mimicking paraneoplastic cerebellar degeneration (Zis and Hadjivassiliou, 2019). Moreover, the symptoms may be mild at the outset, but they may lead to permanent damage if they remain untreated. Hence, there is a need to understand the pathophysiology of GA and identify non-invasive biomarker/s that may provide an early indication of gluten-induced cerebral damage and treatment management.

Magnetic resonance (MR) based techniques like magnetic resonance imaging (MRI) and MR spectroscopy (MRS) are non-invasive. They play an important role in elucidating the pathophysiology of various brain pathologies (Sharma and Jagannathan, 2004; Symms et al., 2004; Oz et al., 2014; Baldarçara et al., 2015). Of these, MRI provides anatomical images in multiple planes enabling tissue characterization and volumetric measurements. Several structural MRI studies have shown the potential for assessing atrophy patterns in different brain regions in hereditary and spinocerebellar ataxia (Vavla et al., 2018; Deelchand et al., 2019; Hernandez-Castillo et al., 2019; Cocozza et al., 2020). It has been suggested that volumetric measurements can evaluate the disease progression better than the clinical scores (Baldarçara et al., 2015; Vavla et al., 2018; Deelchand et al., 2019; Hernandez-Castillo et al., 2019; Cocozza et al., 2020). Hadjivassiliou et al. (2019) have investigated the correlation between antibodies to Transglutaminase 6 (TG6) and neurological deficits in patients with celiac disease using volumetric MRI. They suggested a link between brain atrophy and autoimmunity to TG6 in these patients (Hadjivassiliou et al., 2019). A review of MRI studies of GA patients recently reported that these patients usually have cerebral atrophy with particular involvement of the cerebellar vermis (Currie et al., 2013a,b). However, in addition to the cerebellum, 40% of the patients with GA have sensory (cerebrum) ataxia rather than cerebellar ataxia and showed no cerebellum atrophy on MRI (Bürk et al., 2001).

In-vivo proton magnetic resonance spectroscopy (^{1}H MRS) is a valuable technique for assessing the neurochemical abnormalities associated with cerebral damage. The MRS has been widely used to investigate the pathophysiology of various neurological conditions such as Parkinson's disease, dementia, and ataxia (Hadjivassiliou et al., 1998; Firbank et al., 2002; Graff-Radford et al., 2014; Ashizawa et al., 2018). The potential use of MRS in assessing surveillance of patients with paraneoplastic cerebellar degeneration by measuring temporal changes in the level of N-acetyl aspartate (NAA) was also reported (Hadjivassiliou et al., 2013). However, only a few MRS studies in the literature characterize neurochemical abnormalities in patients with GA by a single research group (Wilkinson et al., 2005; Hadjivassiliou et al., 2017). *In-vivo* MRS study by Wilkinson et al. has reported significant differences in the neurochemical profile of NAA and NAA/choline ratios in the cerebellum of patients with GA compared to healthy controls. The authors have concluded that cerebellar neuronal physiology is altered in GA patients even in the absence of cerebellar structural deficit (Wilkinson et al., 2005). Recently, Hadjivassiliou et al. (2017) evaluated the effect of a gluten-free diet on MRS of the cerebellum in patients with GA and found an increase in NAA/creatine ratio after gluten-free diet compared to baseline. These studies have reported relative ratios of neurochemicals. However, there is a lack of data on the absolute measures of neurochemicals in patients with GA. Though a single research group has reported few brain MRI and MRS studies in the Caucasian population in the literature, there is a lack of such a study understanding the neurochemical changes and volumetric brain changes in the patients with GA in the Indian population.

It has been reported that MRS findings can be dependent on population characteristics, ethnicity or race and can change according to the changing environment and racial characteristics (Isamah et al., 2010; Chee et al., 2011). Furthermore, the difference in brain size has been reported between the Indian and Caucasian populations (Sivaswamy et al., 2019). Therefore, the present study investigated the structural changes in the brain using MRI and absolute concentration of neurochemicals (cerebellum and vermis) in GA patients and healthy controls using *in-vivo* MRS to get an insight into the pathophysiology and to identify the putative non-invasive biomarker/s for early indication of gluten-induced cerebral damage in Indian population.

PATIENTS AND METHODS

Patients

The study was conducted in well established Ataxia Clinic, Department of Neurology in collaboration with Celiac Disease (CeD) Clinic, Department of Gastroenterology, All India Institute of Medical Sciences (AIIMS), New Delhi, India. Ataxia patients (both sporadic and familial) positive for serological assays forms part of this study group. We enrolled six right-handed (five males and one female) patients (mean age 50.16 ± 9.28 years) and age range 40–65 years. They were clinically and genetically diagnosed with cerebellar ataxia (CA). As a part of the routine genetic testing, they were tested using standard laboratories protocols for the ataxia-causing known genes in India—SCA1, SCA2, SCA3, SCA7, and SCA12. Two were found to be genetically positive, 2 had a positive family history of ataxias, one had idiopathic sporadic ataxia and one did not undergo genetic testing. Ten healthy, age and ethnically matched controls were also included in the study (mean age 42.7 ± 9.12 years) and age range 30–55 years. At the time of their recruitment, none of the healthy controls had any neurological and genetic illness, nor they were on any treatment with medications active on the central nervous system. The study was approved by Institute Ethics Committee, AIIMS, New Delhi, and written informed consent was obtained from all patients and controls.

Screening of Patients for Gluten Sensitivity

Four milliliters of blood were drawn from each participant for serological assays. For measuring concentration following commercially available ELISA kits were used: IgA anti tTG ab by QUANTA Lite® h-tTG IgA kits. The AGA IgA and AGA IgG by QUANTA Lite®Gliadin IgA II and QUANTA Lite® Gliadin IgG II kits respectively and TG6 by kits procured from ZEDIRA GmbH, Darmstadt, Germany. The ELISA was done in duplicate in all the sera samples as per the manufacturer's instructions. Positive and negative controls were used. For the study serum titer of >4 U/ml, >20 U/ml, and >41 U/ml were considered positives for IgA anti-TG2 Ab, AGA (IgA and IgG), and anti-TG6 Ab, respectively. Patients were considered gluten sensitive if their serum was found with circulating antibodies.

Magnetic Resonance Imaging

All sixteen subjects included in the study underwent MR Imaging, on a 3T whole-body MR system (Philips, Ingenia) with a 32-channel head coil. Subjects were positioned supine with their heads supported and immobilized within the head coil using foam pads to minimize head movement and gradient noise. After localization, T1_weighted images were obtained in three planes using Magnetization-Prepared Rapid Gradient Echo (MPRAGE) sequence with the following parameters: matrix size = 320 × 318, slice thickness = 0.9 mm, field of view (FOV) = 240 × 240 mm, TR = 10 ms, TE = 4.7 ms, voxel size = 0.75 × 0.75 × 0.75. T2 weighted images were obtained with 30 interleaved 5-mm thick slices without any interslice gap (TE) = 80 ms, TR = 2,676 ms, matrix size = 436 × 357, FOV = 240 × 240 mm, flip angle = 90 degrees, voxel size = 0.55 × 0.65 × 5 mm^3. The T1 weighted images provide a better contrast-to-noise ratio in white matter regions and are used for the segmentation. The T2-weighted images are good for demonstrating pathology, discriminating structural differences in fluid-filled regions, and important for tracking long-term disease progression (Braga et al., 2012). No contrast agent was administered either for T1 or T2 imaging.

Structural MRI Data Processing

3D T1 imaging was done and the digital imaging and communications in medicine (DICOM) images were converted into neuroimaging informatics technology initiative (NIfTI) file format. In all 16 subjects the segmental volumetric calculation of the whole brain and cerebellar structures was performed by uploading the file in NIfTI format to VolBrain and CERES pipeline (Manjón and Coup, 2016). volBrain (http://volbrain.upv.es), and CERES are open-access pipeline, in which pre-processing of the images is based on spatially adaptive non-local means denoising, rough inhomogeneity correction, affine registration to MNI space, fine SPM based inhomogeneity correction and intensity normalization. Here the quality of input images is improved and the images are set into a specific geometry and intensity space. After pre-processing, the images are segmented according to tissues of interest. Segmentation includes non-local intracranial cavity extraction (NICE), tissue classification, non-local hemisphere segmentation (NABS) and non-local subcortical structure segmentation. CERES is mainly used for the segmentation of sub cerebellar structures.

In-vivo MRS

For volume-localized ^{1}H-MR spectroscopy first the scout images, T1 weighted images, and multislice T2-weighted images in the axial, coronal and sagittal planes of the whole brain were acquired using a standard spin-echo pulse sequence. Using the reference MR images, single-voxel proton MR spectra were acquired using the point-resolved spin-echo pulse sequence (PRESS) with the following parameters: TR = 2000 ms; TE = 30 ms; TA = 9 minutes 8 s; the number of averages (NA) = 256. We have used short TE for MRS as it offers a higher signal-to-noise ratio (SNR), improved detection and quantification of molecules with short T2 such as myoinositol (mI), glutamine/glutamate (Glx), due to less relaxation-induced signal loss (Cianfoni et al., 2011). The disadvantage associated with short TE is incorrect baseline determination which may lead to an artifactual elevation in the determination of concentration (Brief et al., 2005). On the contrary, it is easier to correct the baseline in the spectrum acquired with long TE, however, it provides information on a lesser number of metabolites (Brief et al., 2005). Further, Cr has a significantly shorter T2 relaxation time compared to metabolites like NAA and Cho, which leads to incorrect estimation of relative (metabolite/Cr) and absolute metabolite concentrations in a long TE MRS without applying T2 correction (Brief et al., 2005).

In order to optimize the magnetic field both global and voxel shims were carried out. Automated global shimming minimizes the B_0 inhomogeneities while localized voxel shimming further minimizes the B_0 field variations over the voxel of interest. The spectra were acquired from right cerebellum and vermis with voxel size of 15 mm × 15 mm × 15 mm and care was

taken to minimize the inclusion of cerebrospinal fluid within the prescribed spectroscopic volume for methodological consistency. The cerebellar vermis has a serpentine or wormlike shape and it varies slightly according to the individual. The MRS studies reported in the literature on patients with ataxia and GA have used the varied voxel size of vermis in the range of 20 mm × 20 mm × 20 mm (Lirng et al., 2012), 25 mm × 10 mm × 25 mm (Adanyeguh et al., 2015), 20 mm × 10 mm × 20 mm (Currie et al., 2013b), 15 mm × 15 mm × 15 mm (Guerrini et al., 2009). A width of 15 mm of the voxel in vermis may have minor contributions from the surrounding areas of the vermis in our study.

The line-width after voxel shim ranged from 5 to 14 Hz depending on the region studied. Additionally, a spectrum of the same voxel without water suppression was also acquired and the unsuppressed water signal was used as an internal reference to estimate the metabolite concentrations. The absolute concentration of metabolites was determined using an (LC Model) user-independent, frequency domain fitting program, version 6.1-4A, with a basis set of model metabolites. An eddy-current correction was also carried out. The errors in the determined metabolite concentration are expressed in the percent standard deviation (%SD) of the concentration and represent the 95% confidence interval of the estimated concentration. In the present study, we have considered the absolute metabolites values when the Cramer-Rao lower bound or the LC model concentrations were below 20%, indicating that these metabolites could be reliably estimated. The concentration of metabolites was expressed as institutional units related to millimoles per kg (mM/kg).

Segmentation

3D T1-weighted images acquired with magnetization-prepared rapid gradient echo (MPRAGE) sequence were used to carry out segmentation of tissue subtypes in the SVS voxel using the segment-editor module of an open-source neuroimaging package 3D-Slicer (Fedorov et al., 2012). Screenshots of the exact position of the SVS voxel on MR images in all the axial, sagittal, and coronal slices were captured on the MR scanner and were used as voxel prescription images. A mask representing the 3D SVS voxel was then created manually using these screenshots as a reference. The mask was then co-registered to the DICOM image at the exact position as the actual 3D SVS voxel in the voxel prescription images and fractions of white matter (WM), gray matter (GM), and cerebrospinal fluid (CSF) were determined using the segmentation module.

Partial Volume Correction for Metabolite Concentration

The concentration of metabolites was then corrected for the amount of CSF using the following equation given by (Quadrelli et al., 2016).

$$C = C_0\,[1/(1 - V_{CSF})]$$

where,

C = corrected metabolite concentration;

TABLE 1 | Demographic characteristics, clinical manifestations, and serology of patients with Gluten Ataxia.

Demographic characteristics	
Number of patients	$n = 6$
Mean age ± SD; (range)	50.2 ± 9.3; (40–65) years
Age of onset (mean ± SD)	46.2 ± 7.1 years
Gender	Male ($n = 5$), female ($n = 1$)
Clinical manifestations	
Symptoms	Loss of balance, diarrhea, constipation, weakness
Severity of ataxia	Mild ($n = 4$), moderate ($n = 1$), severe ($n = 1$)
Serology	
IgA anti-AGA	Positive ($n = 4$); Negative ($n = 2$)
Mean ± SD	31.76 ± 20.56 ($n = 4$)
Cut off value	>20
Anti-TG 6	Positive ($n = 1$); Negative ($n = 5$)
Concentration	62.1 ($n = 1$)
Cut off value	>41
Anti-tTG	Positive ($n = 1$); Negative ($n = 5$)
Concentration	94.6 ($n = 1$)
Cut off value	>4

IgA, immunoglobulin A; anti-AGA, antibodies to gliadin; anti-tTG, antibodies to tissue transglutaminase 2; anti-TG 6, antibodies to tissue transglutaminase 6.

C_0 = metabolite concentration obtained through LC Model;

V_{CSF} = volume fraction of CSF contained within the SVS voxel;

We have also calculated the weighted measures (Wc) of the concentration of metabolites according to the relative proportion of gray matter (GM) and white matter (WM) following the procedure given in the literature (Mato Abad et al., 2014) for white matter changes in patients with GA and for their better discrimination. The equation used for the determination of Wc is given below (Mato Abad et al., 2014):

$$Wc = LC_c \cdot P(M_c)$$

Where, Wc = Weighted measure; LC_c = Concentration of metabolite from LC Model; P(Mc) = Theoretical distribution of metabolites in a particular voxel according to the relative proportions of GM, WM, and CSF.

P(Mc) was determined as follows:

$$P(Mc) = P(GM)\cdot P(Mc|GM) + P(WM)\cdot P(Mc|WM) + P(CSF)\cdot P(Mc|CSF)$$

Where,

P(GM), P(WM), and P(CSF) are, respectively, the proportion of GM, WM, and CSF inside the voxel.

P(Mc|GM), P(Mc|WM) and P(Mc|CSF) are the probabilities of the metabolite concentration given this volume of GM, WM, and CSF (Mato Abad et al., 2014).

Thus, Wc is a measure of the concentration of metabolite which was corrected for the theoretically expected ratio of metabolite and the atrophy of volume within a voxel

(Mato Abad et al., 2014). The concentrations of metabolites published in the literature (Tal et al., 2012; Bustillo et al., 2017) were used to obtain the contribution of GM and WM to the quantity of metabolites. The contribution of CSF to metabolite concentration was considered negligible (Hetherington et al., 2001).

Statistical Analysis

The percentage of different brain volumes and the concentration of different neurochemicals were calculated for GA patient and HC group and presented as mean ± standard deviation. A student t-test was used to evaluate the difference between patients and controls for ^{1}H MRS and volumetric data using the SPSS 20.0 software (SPSS Inc. Chicago, IL, USA). The level of significance was set at $p < 0.05$. The Pearson correlation was used to calculate the correlation of the concentration neurochemicals and the volumetric changes in the brain of GA patients.

RESULTS

The demographic characteristics of GA patient group are presented in **Table 1**. GA patient group consisted of 6 patients (five men, one woman; aged between 40 and 65 years). Of these, four patients had mild (mobilizing independently or with one walking aid), one patient had moderate (mobilizing with two walking aids) while one had severe (wheelchair dependant) ataxia. Control group consisted of 10 healthy volunteers (5 men, 5 women; age range (30–55 years) with no neurological/psychiatric disease/no medical or family history of ataxia.

Comparison of Whole Brain Volume and Brain Parts Between GA Patients and HCs

Figures 1A,B show the representative volBrain images of brain and sub-parts obtained from a 44 years old male healthy control and a patient with gluten ataxia (male, 55 years old), respectively. **Figures 2A,B** show the representative CERES images showing

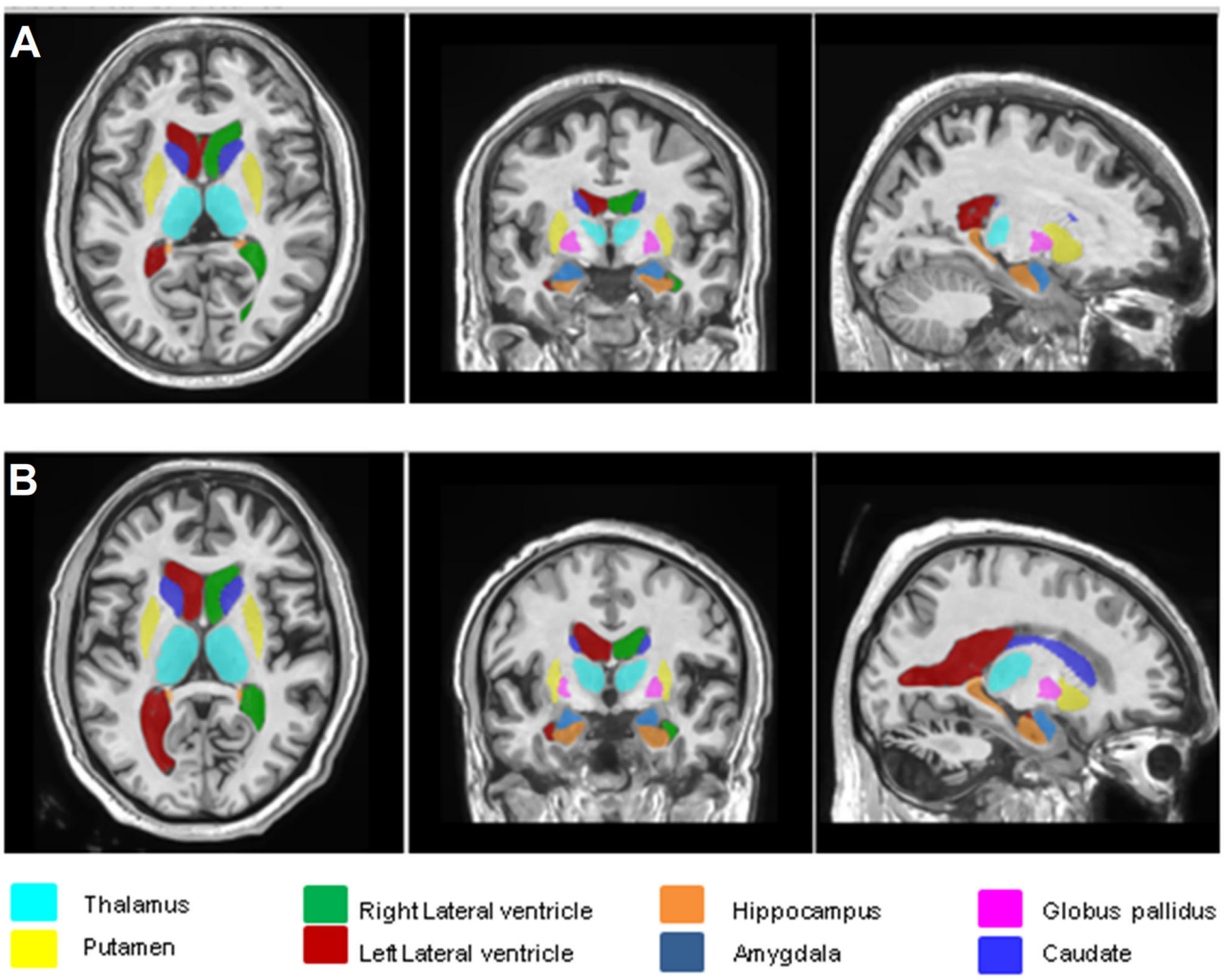

FIGURE 1 | Representative volBrain images of brain and sub-parts obtained from a healthy control (male, 44 years old) **(A)** and a patient with gluten ataxia (male, 55 years old) **(B)**.

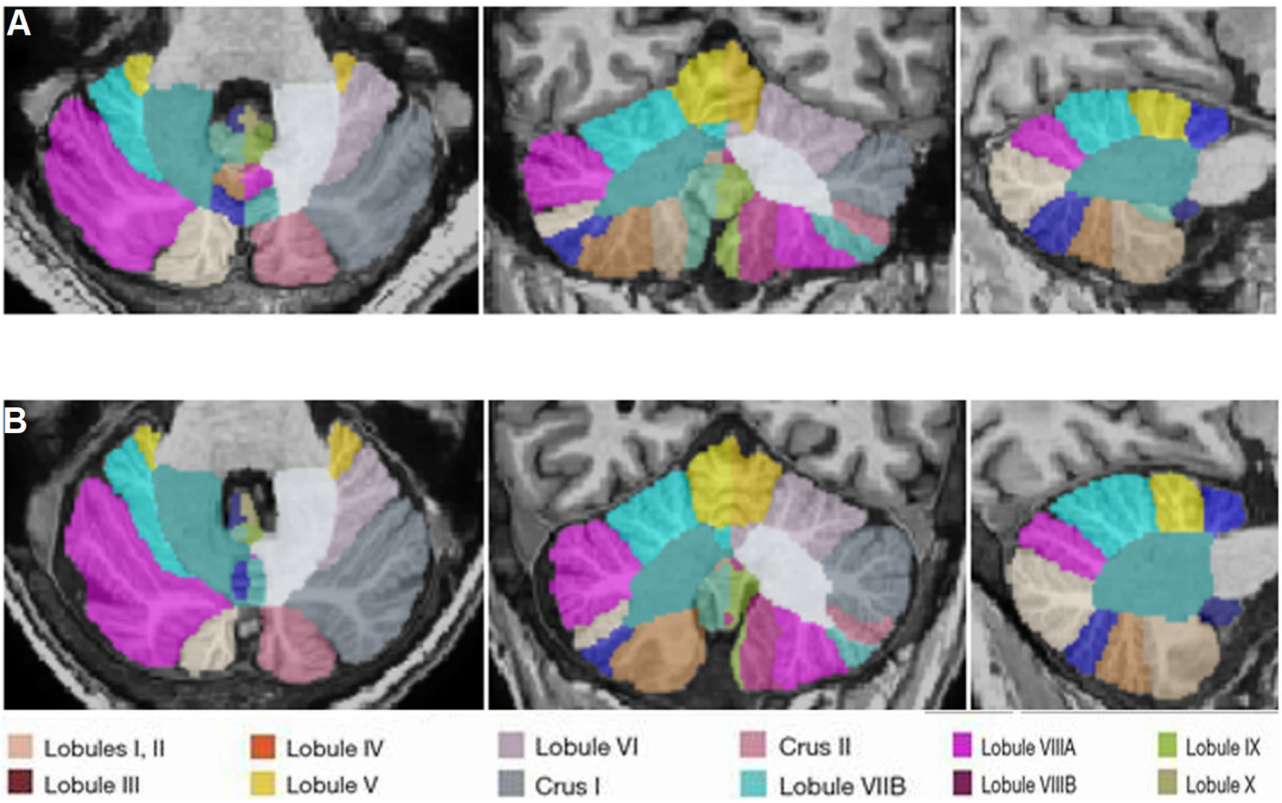

FIGURE 2 | Representative CERES images of cerebellum and lobules taken from a healthy control (male, 44 years old) **(A)** and a patient with gluten ataxia (male, 55 years old) **(B)**.

segmentation of lobules of the cerebellum from a healthy control (male, 44 years old) and a patient with gluten ataxia (male, 55 years old), respectively. The result of the volumetric analysis is reported as % of total intracranial volume (**Tables 2**, **3**). GA patients showed a significant reduction in total brain white matter (WM) ($p < 0.03$), the white matter of the cerebrum ($p < 0.04$), the volume of lateral ventricles ($p < 0.04$) and thalamus ($p < 0.01$) compared to healthy controls (**Table 2**). GA patients also showed significantly reduced total cerebellar WM ($p < 0.02$) significantly affecting the lobule X ($p < 0.03$) (**Table 3**). The volume of caudate, hippocampus, putamen, accumbens, globus pallidus, and amygdala were not significantly different between the two groups (**Table 2**).

Comparison of Neurochemical Profile Between Patients With GA and HCs

Figures 3A–D show the T1-weighted MR images of healthy control (female, 44 years old) and a patient with gluten ataxia (female, 50 years old) in axial, coronal, and sagittal planes and representative LCModel fitted ^{1}H-magnetic resonance spectroscopy spectra for vermis acquired from these subjects. The T1-weighted images of the brain in all the three planes and the representative LCModel fitted ^{1}H-magnetic resonance spectroscopy spectra for the right cerebellum acquired from the same healthy control and the patient with gluten ataxia are shown in **Figures 4A–D**. The concentrations (corrected for CSF) of neurochemicals determined using ^{1}H-MRS are summarized in **Table 4**. The patients with GA had statistically significantly reduced concentration of total N-acetyl aspartate (tNAA: N-acetyl aspartate+ N-acetyl aspartate glutamate) ($p < 0.008$) and total choline (tCho: glycerophosphocholine+phosphocholine) ($p < 0.05$) in the vermis. In the right cerebellum, GA patient group showed a statistically significant reduction in the concentration of tNAA ($p < 0.02$). The proportions of gray matter P(GM), white matter P(WM), and cerebrospinal fluid P(CSF) in the MRS voxel for vermis and right cerebellum of GA patients and HCs were not significantly different (**Table 5**).

We have also calculated the Wc of the concentration of metabolites according to the relative proportion of gray matter (GM) and white matter (WM) following the procedure given in the literature (Mato Abad et al., 2014) and presented in **Table 4**. The Wc of the tNAA, tCho and tCr in vermis, while tNAA and tCho were found to be significantly lower in the patients with GA compared to HC (**Table 4**).

Correlation of the Concentration of the Neurochemicals and Brain Volumetric Changes

A significant correlation ($r = 0.9$, $p = <0.05$) was observed between the concentration of tNAA (both cerebellum and vermis) and tCho (vermis) with lobule X of the cerebellum.

TABLE 2 | Volumetric analysis of individual brain regions of patients with Gluten Ataxia (GA) and Healthy Controls (HC).

Regions of interest	Volume percentage (mean ± SD)		*p* value
	GA ($n = 6$)	HC ($n = 10$)	
Total brain			
WM + GM	78.64 ± 7.68	84.38 ± 5.53	0.12
WM	31.89 ± 6.65	38.97 ± 4.26	**0.03**
GM	46.75 ± 3.73	45.41 ± 8.86	0.74
CSF	21.35 ± 7.68	15.62 ± 5.53	0.12
Cerebrum			
WM + GM	69.57 ± 6.43	73.3 ± 5.21	0.24
GM	40.29 ± 2.45	38.38 ± 8.52	0.60
WM	29.27 ± 5.71	34.92 ± 4.03	**0.04**
Cerebellum			
WM + GM	7.65 ± 2.39	9.33 ± 0.65	0.07
GM	6.04 ± 1.93	6.69 ± 0.70	0.38
WM	1.61 ± 0.89	2.91 ± 0.96	**0.02**
Other regions			
Caudate	0.51 ± 0.07	0.55 ± 0.12	0.58
Hippocampus	0.56 ± 0.04	0.51 ± 0.12	0.40
Amygdala	0.12 ± 0.02	0.10 ± 0.05	0.34
Lateral ventricles	2.01 ± 1.32	0.88 ± 0.52	**0.04**
Putamen	0.55 ± 0.07	0.62 ± 0.06	0.06
Thalamus	0.74 ± 0.08	0.85 ± 0.06	**0.01**
Accumbens	0.04 ± 0.01	0.04 ± 0.01	0.95
Globus pallidus	0.14 ± 0.02	0.15 ± 0.03	0.42

WM, white matter; GM, gray matter; CSF, cerebrospinal fluid. Bold values indicate significant p value.

TABLE 3 | Volumetric analysis of individual cerebellar regions of patients with gluten ataxia (GA, $n = 6$) and healthy controls (HC, $n = 10$).

Region of interest	Volume percentage (mean ± SD)		*p*-value
	GA	HC	
Cerebellum and lobules			
Cerebellum	7.82 ± 1.80	8.66 ± 0.31	0.22
Lobule i-ii	0.004 ± 0.002	0.004 ± 0.002	0.55
Lobule iii	0.07 ± 0.019	0.08 ± 0.02	0.42
Lobule iv	0.26 ± 0.05	0.29 ± 0.03	0.13
Lobule v	0.48 ± 0.11	0.49 ± 0.05	0.96
Lobule vi	1.09 ± 0.29	1.09 ± 0.14	0.99
Lobule crus i	1.69 ± 0.43	1.75 ± 0.22	0.72
Lobule crus ii	1.06 ± 0.23	1.11 ± 0.16	0.59
Lobule vii-b	0.54 ± 0.15	0.62 ± 0.07	0.20
Lobule viii-a	0.69 ± 0.189	0.77 ± 0.09	0.33
Lobule viii-b	0.48 ± 0.15	0.54 ± 0.06	0.36
Lobule ix	0.49 ± 0.13	0.50 ± 0.06	0.88
Lobule x	0.06 ± 0.02	0.09 ± 0.02	**0.03**

Bold values indicate significant p value.

DISCUSSION

In recent years, the developments in neuroimaging techniques such as MRI and MRS have enabled the characterization of the structural and neurochemical changes, elucidating the pathophysiology of various brain diseases (Symms et al., 2004; Oz et al., 2014). Among many types of ataxias, GA is an auto-immune disease caused by the ingestion of gluten in the genetically susceptible individuals (Hadjivassiliou et al., 2014). The non-invasive nature, versatility and possibility of evaluation of multiple parameters in a short time makes the MRI and MRS as an important tool for understanding the disease pathophysiology and identifying disease biomarkers. Additionally, the possibility of repetitive measurements using these techniques can play an important role in the management of diseases like GA that require long term follow-up for assessment of neurological abnormalities. It is critical to understand the pathophysiology of the GA for the early diagnosis and treatment management strategies, however, till date, it was not investigated at many sites using MRI and MRS. To the best of our knowledge there are only two *in-vivo* MRS study and one study using combined MRI and MRS approach in GA patient in Caucasian population by a single research group (Wilkinson et al., 2005; Hadjivassiliou et al., 2019; Zis and Hadjivassiliou, 2019). The present study has evaluated the volumetric and neurochemical changes in the brain in GA patients compared to HCs using MRI and MRS in Indian population. Several interesting observations emerged from our study.

Our results revealed significantly reduced volume of white matter in the total brain, cerebellum and cerebrum of the patients with GA compared to HC. It is known that white matter is an essential component of neural networks and acts as a connecting link between various gray areas in the brain. White matter contains myelin sheathed axons that relay the information between different brain areas. The reduction in the myelin sheathed cells can cause delay both in passing and processing of the information. Delayed or staggered processing of information may result in clumsy and uncontrolled movements which are generally seen in the patients with GA (Vinagre-Aragón et al., 2018). The loss of white matter has been reported in several neurodegenerative diseases. The alterations in the volume of white matter have been found to affect the cognition (Filley and Fields, 2016). Kang et al. (2014) have reported that disruption of white matter integrity was related to the clinical severity of the disease in the patients suffering with SCA3. Correlation of white matter degeneration and severity of ataxia was also found in the patients with SCA type 7 (Kang et al., 2014). In a volumetric MRI study of patients with celiac disease having TG6 autoantibodies, significant atrophy of subcortical brain regions was reported in 40% of the patients. The white matter abnormalities were also reported in these celiac disease patients, which is in agreement with our findings (Hadjivassiliou et al., 2019). Croall et al. (2020) have recently shown white matter damage in patients with

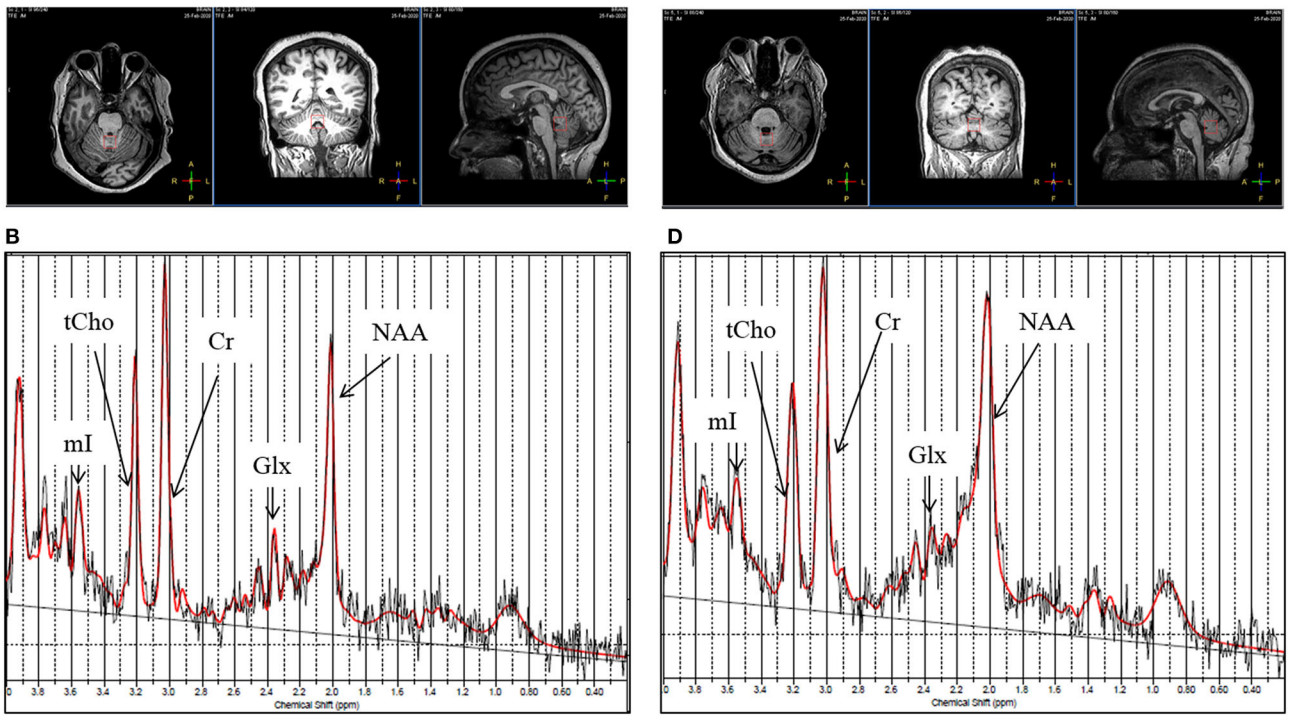

FIGURE 3 | (A) T1-weighted images of a healthy control (female, 44 years old) in axial, coronal, and sagittal plane. **(B)** Representative LC Model fitted ^{1}H-magnetic resonance spectroscopy spectrum obtained from the vermis of the same healthy control from the voxel highlighted in **(A)**. **(C)** T1-weighted image of a patient with gluten ataxia (female, 50 years old) in axial, coronal and sagittal plane. **(D)** Representative LC Model fitted ^{1}H-magnetic resonance spectroscopy spectrum acquired from the vermis of the same patient with gluten ataxia from the voxel highlighted in **(C)**.

celiac disease having indications of worsened mental health and cognitive deficit, compared to the healthy controls.

The significantly reduced volume of white matter in our study might be due to the damage caused by inflammatory response by gluten-sensitive antibodies. It has been reported that the etiology of neurological manifestation of gluten sensitivity has an immunological manifestation (Hernandez-Lahoz et al., 2011). The patients with gluten ataxia have been shown to have positive oligoclonal bands on examination of CSF. Furthermore, the pathological data suggested an inflammatory pathogenesis with evidence of perivascular inflammation with predilection of brainstem, cerebellum and peripheral nerves (Hadjivassiliou and Croall, 2021). Patients with GA have evidence of IgA deposits against tissue transglutaminase on vessels within cerebellum and brainstem. Transglutaminase leads to vascular based inflammation that may results in breakdown of blood brain barrier thus allowing the entry of gluten-sensitive antibodies in brain (Hadjivassiliou et al., 2006), the same antibodies can cross-react with Purkinje cells in the cerebellum causing their irreversible depletion (Hadjivassiliou et al., 2016).

Another interesting observation of our study was significantly reduced volume of lobule X of the cerebellum in the patients with GA compared to HC. The lobule X is also known as flocculonodular lobe and it plays an important role in regulating and orienting the eye movement through vestibulo-ocular reflex (Stoodley and Schmahmann, 2009; Stoodley et al., 2012). It also affects the body equilibrium during stance and gait along with lobule IX (Han et al., 2018). Thus, any change in the volume of lobule X may directly affect movement of eyes which is usually seen in ataxias (nystagmus). This finding is in agreement with the Hadjivassiliou et al. (2019) wherein they have also identified neurological deficit in terms of reduced volume of cerebellum and its IX and X lobes in the patients with celiac disease and positive for TG6 autoantibodies (Hadjivassiliou et al., 2019).

In the present study, we also observed significantly reduced volume of the thalamus in the patients with GA patients compared to healthy controls. The thalamus plays an important role in motor control and acts as a relay center between the cerebellum and the motor cortex (Sommer, 2003). The volume loss in the thalamic subnuclei has also been reported in patients with SCA type 7 (Magon et al., 2020). The patients with CeD with TG6 autoantibodies also showed a reduced volume of the thalamus which is in agreement with our findings. The significant reduction in the volume of the thalamus in GA might be attributed to loss or impairment of TG6+ neurons, potentially affecting GABA-ergic inhibitory pathways, which is supported by brain hyperexcitability reported in the patients with celiac disease (Sarrigiannis et al., 2014).

Our results also showed significantly reduced white matter of cerebrum in the patients with GA in comparison to healthy

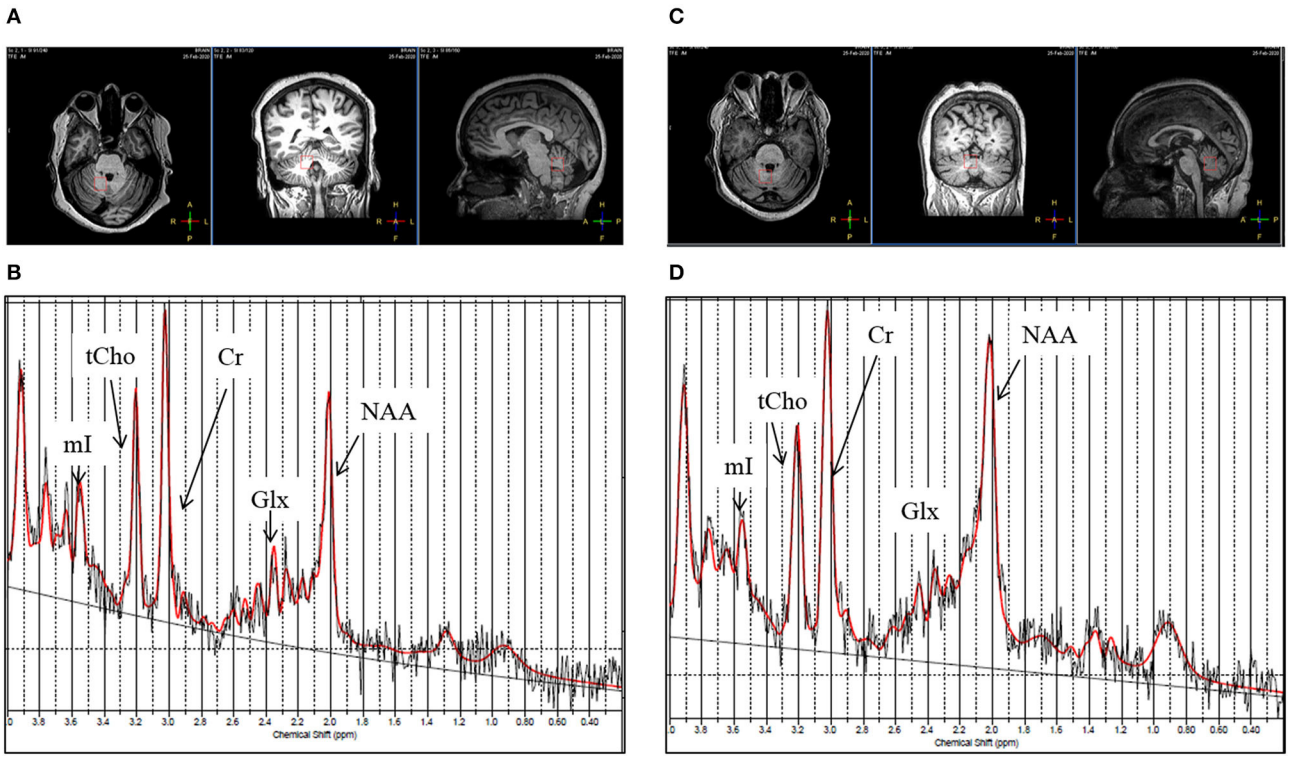

FIGURE 4 | (A) T1-weighted images of a healthy control (female, 44 years old) in axial, coronal and sagittal plane. **(B)** Representative LC Model fitted ^{1}H-magnetic resonance spectroscopy spectrum obtained from the right cerebellum region from the same healthy control from the voxel highlighted in **(A)**. **(C)** T1-weighted image of patient with gluten ataxia (female, 50 years old) in axial, coronal and sagittal plane. **(D)** Representative LC Model fitted ^{1}H-magnetic resonance spectroscopy spectrum acquired from the right cerebellum region of the same patient with gluten ataxia from the voxel highlighted in **(C)**.

TABLE 4 | Comparison of the concentrations of neurochemicals (corrected for CSF) and their weighted measures in the vermis and right cerebellum of patients with Gluten Ataxia (GA) ($n = 6$) and Healthy Controls (HC) ($n = 10$).

Neurochemicals	Vermis		*p*-value	Right Cerebellum		*p*-value
	GA	HC		GA	HC	
Concentrations [mM/Kg, (Mean ± SD)]						
tNAA	5.15 ± 1.25	7.11 ± 0.81	**0.008**	5.75 ± 0.95	7.04 ± 0.67	**0.02**
tCho	1.88 ± 0.46	2.29 ± 0.19	**0.05**	1.97 ± 0.41	1.91 ± 0.13	0.73
tCr	7.53 ± 2.58	8.91 ± 0.95	0.22	7.12 ± 1.86	7.22 ± 1.62	0.91
Glx	11.73 ± 1.37	11.61 ± 2.08	0.91	10.56 ± 2.04	10.58 ± 1.77	0.98
mI	6.97 ± 2.19	6.74 ± 0.91	0.80	6.79 ± 2.59	5.87 ± 0.69	0.38
Weighted measures (Mean ± SD)						
tNAA	2.14 ± 0.91	3.17 ± 0.37	**0.02**	2.50 ± 0.89	3.30 ± 0.33	**0.05**
tCho	0.75 ± 0.24	0.96 ± 0.05	**0.03**	0.83 ± 0.07	0.91 ± 0.05	**0.05**
tCr	2.99 ± 1.18	4.15 ± 0.42	**0.03**	3.02 ± 1.09	3.34 ± 0.53	0.52
Glx	4.72 ± 1.51	5.62 ± 1.04	0.25	3.60 ± 2.49	4.85 ± 0.78	0.23
mI	2.65 ± 0.52	3.03 ± 0.26	0.12	2.74 ± 0.63	2.74 ± 0.27	0.98

tNAA, total NAA (N-acetyl aspartate+ N-acetyl aspartate glutamate); mI, myoinositol; tCho, total choline (glycerophosphocholine+phosphocholine); tCr, total creatine (creatine+phosphocreatine); Glx, glutamate+glutamine. Bold values indicate significant p value.

controls. This is the first report showing the atrophy of the cerebrum in GA patients. It has been reported that 40% of the patients with GA have sensory (cerebrum) ataxia rather than cerebellar ataxia and showed no atrophy of cerebellum on MRI (Bürk et al., 2001). The role of the cerebrum is to initiate and coordinate movement, thus, any change in the volume of the

TABLE 5 | The proportions (mean ± SD) of gray matter P(GM), white matter P(WM), and cerebrospinal fluid in P(CSF) in the voxel placed during MRS in the vermis and right cerebellum of patients with gluten ataxia (GA) and healthy controls (HC).

The proportions of tissue sub-type	Vermis			Right cerebellum		
	GA	HC	*p* value	GA	HC	*p* value
P(GM)	0.42 ± 0.29	0.62 ± 0.09	0.10	0.39 ± 0.27	0.42 ± 0.04	0.76
P(WM)	0.38 ± 0.24	0.26 ± 0.06	0.20	0.46 ± 0.18	0.53 ± 0.06	0.41
P(CSF)	0.20 ± 0.18	0.13 ± 0.06	0.30	0.15 ± 0.13	0.05 ± 0.03	0.10

cerebrum can directly affect the senses and movement. Thus, it remains to be elucidated whether any change in volume of the cerebrum in GA patient is contributing to difficulty in movement. The cerebrum is also thought to regulate the sensory function of the body and is also responsible for memory, speech and emotional response (Abhang et al., 2016). Atrophy in this region may be asymptomatic and could cause memory loss or gait abnormalities (Deutsch and Deangelis, 2014). Thus, the results of the present study depicted significant changes in the volume of the white matter of the cerebrum as well as of the cerebellum in the GA patients. Due to the low sample size in the present study, it further needs to be validated whether GA is pure cerebellar or sensory in nature.

Further, our results showed a significant increase in the volume of lateral ventricles in the patients with GA in comparison to healthy controls. Lateral ventricles are a "C" shaped cavity located one on each side of the cerebral hemisphere. Continuous enlargement in the lateral ventricles has been observed due to cerebral involution through the lifespan (Dima et al., 2021), as the age increases, or due to cell death in the adjacent brain structures (Gupta, 2017). Thus, enlargement of ventricles in the patients with GA in our study might also be indicative of gluten-mediated neurodegeneration.

Further, our MRS data revealed significant neurochemical changes in the patients with GA supporting the neurodegeneration in them compared to healthy controls. Our data showed a significantly lower level of tNAA in the right cerebellum as well as in the vermis of GA patients as compared to HCs. NAA is a neuronal health marker (Wilkinson et al., 2005), which is mainly confined to neuronal cell bodies and axons. NAA has also been implicated to serve as an osmolyte and also acts as a precursor for the synthesis of the myelin sheath of oligodendrocytes by providing acetate (Machová et al., 2009). Thus, a reduced level of tNAA in the cerebellum of GA patients might be attributed to cell dysfunction as well as neuronal loss. These findings are in agreement with an earlier MRS study on GA patients, wherein they reported lower levels of NAA/Cr and NAA/Cho in them in comparison to healthy controls (Wilkinson et al., 2005). It has also been shown that a strict gluten-free diet can lead to improvement in NAA/Cr ratio in patients with GA (Hadjivassiliou et al., 2002).

Our results also indicated a significantly lower concentration of membrane precursors GPC and PC in the vermis of GA patients, which is consistent with another recent study on ataxias of SCA1, 2, and 3 patients (Krahe et al., 2020). Choline readily gets transferred through the blood-brain barrier through three different types of choline transporters (CTLs). Expression of these CTLs was seen to be increased at the time of nerve regeneration suggesting the role of choline and CTLs in proliferation and repair (Che et al., 2002). A decrease in the concentration of these metabolites may be attributed to the decreased membrane synthesis in the cerebellar region or it can be due to the mutations in choline transporters (CTLs) (Che et al., 2002).

We have also determined the weighted measures of the metabolite concentrations for relative proportions of GM and WM in the MRS voxel. The analysis improved the statistical results. Accordingly, the weighted measures of tCr were found to be lower in the vermis of GA patients as compared to HC. Creatine (methyl guanidino-acetic acid) is an amino acid, essential for the energy metabolism of cells and neurons (Adriano et al., 2010). The function of creatine and its phosphorylated form (phosphocreatine) is to move the ATP from the site of synthesis (mitochondrion) to the sites where it is utilized. It provides rapid energy to replenish the depleting energy reserves (Beard and Braissant, 2010). Creatine also has antioxidant properties which are beneficial in degenerative diseases (e. g., ataxia) through protection against energy depletion and oxidant species (Curt et al., 2015). Our results showed that tCr was significantly decreased in the vermis of GA patients which may probably be related to the atrophy and may also indicate that the neurons are susceptible to rapid energy depletion in these patients.

We have also worked out a correlation between neurochemicals in the cerebellum and vermis with the volumetric changes in the brain of GA patients. Interestingly, we found a significant correlation between the concentration of tNAA in both vermis and cerebellum and tCho (vermis) with the volume changes in the lobule X of the cerebellum. Thus, the present study has provided a comprehensive structural characterization of cerebral degeneration in patients with GA, which has been also demonstrated by cerebral neurochemical abnormalities. The lower levels of tNAA have suggested neurodegeneration while lower tCho levels may probably be indicative of the impairment of regeneration and repair activities in the GA patients.

To the best of our knowledge, this is the first MRI and MRS-based study in the same cohort of GA patients in the Indian population. In the present study, both MRI and MRS confirmed the presence of cerebellar as well as cerebrum-related volume loss and significantly altered concentrations of different neurochemicals. The neurochemicals tNAA and tCho may have the potential to serve as early indicators of neuronal damage. Further, our findings suggested that knowledge of voxel composition of GM, WM, and CSF may help in avoiding partial volume variations in MRS, particularly in neurodegenerative diseases (Mato Abad et al., 2014). Our study

has a few limitations. One of the limitations of this study is the low sample size. A similar study with a large number of patients is still warranted that may provide a better insight into the pathophysiology of GA, accurate and early diagnosis and may also help in better clinical management. Further, our study has examined the neurochemical abnormalities in the deep white matter, which may reflect the downstream effects of the cortical abnormalities.

CONCLUSIONS

The present study revealed the neurochemical profile of vermis and right cerebellum and structural changes in various brain regions of patients with GA compared with healthy controls. The concentration of neurometabolites, tNAA, tCho and tCr were significantly lower in vermis and concentration of tCho was significantly reduced in the cerebellum regions in the patients with gluten ataxia compared to healthy controls. The patients with GA also had a significant reduction in the white matter of various brain regions and they also showed a significant reduction in the volume of lateral ventricles and thalamus compared to healthy controls. Thus, the present study has elucidated cerebral degeneration in patients with GA, which has been also demonstrated by cerebral neurochemical abnormalities. The neurochemicals (tNAA, tCho) and structural changes may serve as an indicator of cerebral damage in GA. Though our preliminary study has demonstrated several significant observations related to the pathophysiology of GA in the Indian population, however, study needs to be carried out in a greater number of patients. Further, our study showed that the weighted measures of the metabolite concentrations for relative proportions of GM and WM in the MRS voxel improved the statistical results.

DATA AVAILABILITY STATEMENT

The original contributions presented in the study are included in the article/supplementary material, further inquiries can be directed to the corresponding author/s.

ETHICS STATEMENT

The studies involving human participants were reviewed and approved by Institute Ethics Committee, All India Institute of Medical Sciences, New Delhi. The patients/participants provided their written informed consent to participate in this study.

AUTHOR CONTRIBUTIONS

US: conceptualization, design of the study, final editing of the manuscript, figures, and funding. GM and AS: conceptualization and patient recruitment. VR: data acquisition, analysis, figures, and writing the original draft. IS and RT: editing the draft. PD: pathology. All authors: writing—review and editing. All authors contributed to the article and approved the submitted version.

ACKNOWLEDGMENTS

US would like to thank the All India Institute of Medical Sciences for providing the Funds (A-676). VR would like to thank the Council of Scientific and Industrial Research, India for providing fellowship to carry out research.

REFERENCES

Abenavoli, L. (2010). Nervous system in the gluten syndrome: a close relationship. *Med. Hypotheses*. 74, 204–205. doi: 10.1016/j.mehy.2009.08.012

Abhang, P. A., Gawali, B. W., and Mehrotra, S. C. (2016). "Introduction to emotion, electroencephalography, and speech processing," in *Introduction to EEG- and Speech-Based Emotion Recognition,* ed P. A. Abhang (New York, NY: Academic Press), 1-17. doi: 10.1016/B978-0-12-804490-2.00001-4

Adanyeguh, I. M., Henry, P. G., Nguyen, T. M., Rinaldi, D., Jauffret, C., Valabregue, R., et al. (2015). In vivo neurometabolic profiling in patients with spinocerebellar ataxia types 1, 2, 3, and 7. *Mov Disord*. 30, 662–670. doi: 10.1002/mds.26181

Adriano, E., Garbati, P., Salis, A., Damonte, G., Millo, E., and Balestrino, M. (2010). Creatine salts provide neuroprotection even after partial impairment of the creatine transporter (2010). *Neuroscience*. 115, 297–313. doi: 10.1016/j.neuroscience.2016.02.038

Ashizawa, T., and Öz, G., Paulson, H. L. (2018). Spinocerebellar ataxias: prospects and challenges for therapy development. *Nat. Rev. Neurol*. 14, 590–605. doi: 10.1038/s41582-018-0051-6

Ashtari, S., Pourhoseingholi, M. A., Rostami, K., Aghdaei, H. A., Rostami-Nejad, M., Busani, L., et al. (2019). Prevalence of gluten-related disorders in Asia-Pacific region: a systematic review. *J. Gastrointestin. Liver. Dis*. 28, 95–105. doi: 10.15403/jgld.2014.1121.281

Aziz, I., Hadjivassiliou, M., and Sanders, D. S. (2012). Does gluten sensitivity in the absence of coeliac disease exist? *Br. Med. J*. 345, e7907. doi: 10.1136/bmj.e7907

Baldarçara, L., Currie, S., Hadjivassiliou, M., Hoggard, N., Jack, A., and Jackowski, A. P. (2015). Consensus paper: radiological biomarkers of cerebellar diseases. *Cerebellum*. 14, 175–196. doi: 10.1007/s12311-014-0610-3

Beard, E., and Braissant, O. (2010). Synthesis and transport of creatine in the CNS: importance for cerebral functions. *J. Neurochem*. 115, 297–313. doi: 10.1111/j.1471-4159.2010.06935.x

Benson, B. C., Mulder, C. J., and Laczek, J. T. (2013). Anti-gliadin antibodies identify celiac patients overlooked by tissue transglutaminase antibodies, Hawaii. *J. Med. Public Health*. 72, 14–17.

Braga, B., Yasuda, C. L., and Cendes, F. (2012). White matter atrophy in patients with mesial temporal lobe epilepsy: voxel-based morphometry analysis of T1- and T2-weighted MR images. *Radiol. Res. Pract*. 2012, 481378. doi: 10.1155/2012/481378

Brief, E. E., Whittall, K. P., Li, D. K., and MacKay, A. L. (2005). Proton T2 relaxation of cerebral metabolites of normal human brain over large TE range. *NMR Biomed*. 18, 14–18. doi: 10.1002/nbm.916

Bürk, K., Bösch, S., Müller, C. A., Melms, A., Zühlke, C., Stern, M., et al. (2001). Sporadic cerebellar ataxia associated with gluten sensitivity. *Brain*. 124, 1013–1019. doi: 10.1093/brain/124.5.1013

Bushara, K. O. (2005). Neurologic presentation of celiac disease. *Gastroenterology*. 128, S92–S97. doi: 10.1053/j.gastro.2005.02.018

Bustillo, J. R., Jones, T., Chen, H., Lemke, N., Abbott, C., Qualls, C., et al. (2017). Glutamatergic and neuronal dysfunction in gray and white matter: a spectroscopic imaging study in a large schizophrenia sample. *Schizoph. Bull*. 43, 611–619. doi: 10.1093/schbul/sbw122

Che, Y. H., Yamashita, T., Higuchi, H., and Tohyama, M. (2002). Changes in mRNA for choline transporter-like protein following facial nerve transection.

Brain Res. Mol. Brain Res. 101, 122–125. doi: 10.1016/s0169-328x(02)00182-1

Chee, M. W., Zheng, H., Goh, J. O., Park, D., and Sutton, B. P. (2011). Brain structure in young and old East Asians and Westerners: comparisons of structural volume and cortical thickness. *J. Cogn Neurosci.* 23, 1065–1079. doi: 10.1162/jocn.2010.21513

Cianfoni, A., Law, M., Re, T. J., Dubowitz, D. J., Rumboldt, Z., and Imbesi, S. G. (2011). Clinical pitfalls related to short and long echo times in cerebral MR spectroscopy. *J Neuroradiol.* 38, 69–75. doi: 10.1016/j.neurad.2010.10.001

Cocozza, S., Costabile, T., Pontillo, G., Lieto, M., Russo, C., and Radice, L. (2020). Cerebellum and cognition in Friedreich ataxia: a voxel-based morphometry and volumetric MRI study. *J. Neurol.* 267, 350–358. doi: 10.1007/s00415-019-09582-9

Croall, I. D., Sanders, D. S., Hadjivassiliou, M., and Hoggard, N. (2020). Cognitive deficit and white matter changes in persons with celiac disease: a population-based study. *Gastroenterology.* 158, 2112–2122. doi: 10.1053/j.gastro.2020.02.028

Currie, S., Hadjivassiliou, M., Craven, I. J., Wilkinson, I. D., Griffiths, P. D., and Hoggard, N. (2013a). Magnetic resonance imaging biomarkers in patients with progressive ataxia: current status and future direction. *Cerebellum.* 12, 245–266. doi: 10.1007/s12311-012-0405-3

Currie, S., Hoggard, N., Clark, M. J., Sanders, D. S., Wilkinson, I. D., Griffiths, P. D., et al. (2013b). Alcohol induces sensitization to gluten in genetically susceptible individuals: a case control study. *PloS ONE.* 8, e77638. doi: 10.1371/journal.pone.0077638

Curt, M. J. C., Voicu, P. M., Fontaine, M., Dessein, A. F., Porchet, N., Mulliez, K. M., et al. (2015). Creatine biosynthesis and transport in health and disease. *Biochimie.* 119, 146–165. doi: 10.1016/j.biochi.2015.10.022

Deelchand, D. K., Joers, J. M., Ravishankar, A., Lyu, T., Emir, U. E., Hutter, D., et al. (2019). Sensitivity of volumetric magnetic resonance imaging and magnetic resonance spectroscopy to progression of spinocerebellar ataxia type 1. *Mov. Disord. Clin. Pract.* 6, 549–558. doi: 10.1002/mdc3.12804

Deutsch, M. B., and Deangelis, L. M. (2014). "Neurologic complications of chemotherapy and radiation therapy," in *Aminoff's Neurology and General Medicine (Fifth Edition)*, ed. M. J. Aminoff and S. A. Josephson (New York, NY: Academic Press), 591–609

Dima, D., Modabbernia, A., Papachristou, E., Doucet, G. E., Agartz, I., Aghajani, M., et al. (2021). Subcortical volumes across the lifespan: data from 18,605 healthy individuals aged 3-90 years. *Human Brain Mapping.* 43, 452–469. doi: 10.1002/hbm.25320

Fedorov, A., Beichel, R., Kalpathy-Cramer, J., Finet, J., Fillion-Robin, J. C., Pujol, S., et al. (2012). 3D Slicer as an image computing platform for the Quantitative Imaging Network. *Magn. Reson. Imag.* 30, 1323–1341. doi: 10.1016/j.mri.2012.05.001

Filley, C. M., and Fields, R. D. (2016). White matter and cognition: making the connection. *J. Neurophysiol.* 116, 2093–2104. doi: 10.1152/jn.00221.2016

Firbank, M. J., Harrison, R. M., and O'Brien, J. T. (2002). A comprehensive review of proton magnetic resonance spectroscopy studies in dementia and Parkinson's disease. *Dement. Geriatr. Cogn. Disord.* 14, 64–76. doi: 10.1159/000064927

Fitzsimmons, P. R., Hulley, J. L., and Loharuka, S. (2010). Gluten ataxia and celiac disease-associated cerebellar degeneration in a septuagenarian. *Consultant.* 18.

Graff-Radford, J., Boeve, B. F., Murray, M. E., Ferman, T. J., Tosakulwong, N., and Lesnick, T. G. (2014). Regional proton magnetic resonance spectroscopy patterns in dementia with Lewy bodies. *Neurobiol. Aging.* 35, 1483–1490. doi: 10.1016/j.neurobiolaging.2014.01.001

Guerrini, L., Belli, G., Mazzoni, L., Foresti, S., Ginestroni, A., Della Nave, R., et al. (2009). Impact of cerebrospinal fluid contamination on brain metabolites evaluation with 1H-MR spectroscopy: a single voxel study of the cerebellar vermis in patients with degenerative ataxias. *J. Magn. Reson. Imaging.* 30, 11–17. doi: 10.1002/jmri.21804

Gupta, D. (2017). "Neuroanatomy," in *Essentials of Neuroanesthesia*, ed. H. Prabhakar (New York, NY: Academic Press), 3–40.

Hadjivassiliou, M., and Croall, I. (2021). "Neurological manifestations of gluten sensitivity," in *Biotechnological Strategies for the Treatment of Gluten Intolerance*. Amsterdam: Elseiver.

Hadjivassiliou, M., Croall, I. D., Zis, P., Sarrigiannis, P. G., Sanders, D. S., Aeschlimann, P., et al. (2019). Neurologic deficits in patients with newly diagnosed celiac disease are frequent and linked with autoimmunity to transglutaminase 6. *Clin. Gastroenterol. Hepatol.* 17, 2678-2686.e2. doi: 10.1016/j.cgh.2019.03.014

Hadjivassiliou, M., Currie, S., and Hoggard, N. (2013). MR spectroscopy in paraneoplastic cerebellar degeneration. *J Neuroradiol.* 40, 310–312. doi: 10.1016/j.neurad.2012.08.003

Hadjivassiliou, M., Duker, A. P., and Sanders, D. S. (2014). "Gluten-related neurologic dysfunction," in *Handbook of Clinical Neurology,* ed. J. Biller and J. M. Ferro (Amsterdam: Elseiver), 607–619.

Hadjivassiliou, M., Grünewald, R. A., Chattopadhyay, A. K., Davies-Jones, G. A., Gibson, A., Jarratt, J. A., et al. (1998). Clinical, radiological, neurophysiological, and neuropathological characteristics of gluten ataxia. *Lancet.* 352, 1582–1585. doi: 10.1016/s0140-6736(98)05342-2

Hadjivassiliou, M., Grunewald, R. A., and Davies-Jones, G. A. B. (2002). Gluten ataxia: the effect of gluten free diet. *Ann. Neurol.* 52, S63.

Hadjivassiliou, M., Grünewald, R. A., Sanders, D. S., Shanmugarajah, P., and Hoggard, N. (2017). Effect of gluten-free diet on cerebellar MR spectroscopy in gluten ataxia. *Neurology.* 89, 705–709. doi: 10.1212/WNL.0000000000004237

Hadjivassiliou, M., Grünewald, R. A., Sanders, D. S., Zis, P., Croal, I., Shanmugarajah, P. D., et al. (2018). The significance of low titre antigliadin antibodies in the diagnosis of gluten ataxia. *Nutrients.* 10, 1444. doi: 10.3390/nu10101444

Hadjivassiliou, M., Mäki, M., Sanders, D. S., Williamson, C. A., Grünewald, R. A., Woodroofe, N. M., et al. (2006). Autoantibody targeting of brain and intestinal transglutaminase in gluten ataxia. *Neurology.* 66, 373–377. doi: 10.1212/01.wnl.0000196480.55601.3a

Hadjivassiliou, M., Sanders, D. S., and Aeschlimann, D. (2016). "The neuroimmunology of gluten intolerance," *in The Neuro-Immuno-Gastroenterology* (Cham: Springer).

Han, Q., Yang, J., Xiong, H., and Shang, H. (2018). Voxel-based meta-analysis of gray and white matter volume abnormalities in spinocerebellar ataxia type 2. *Brain Behav.* 8, e01099. doi: 10.1002/brb3.1099

Hernandez-Castillo, C. R., Diaz, R., Vaca-Palomares, I., Torres, D. L., Chirino, A., Campos-Romo, A., et al. (2019). Extensive cerebellar and thalamic degeneration in spinocerebellar ataxia type 10. *Parkinsonism Relat. Disord.* 66, 182–188. doi: 10.1016/j.parkreldis.2019.08.011

Hernandez-Castillo, C. R., Vaca-Palomares, I., Barrios, F., Martinez, L., Boll, M. C., and Fernandez-Ruiz, J. (2016). Ataxia severity correlates with white matter degeneration in spinocerebellar ataxia type 7. *Am. J. Neuroradiol.* 37, 2050–2054. doi: 10.3174/ajnr.A4903

Hernandez-Lahoz, C., Mauri-Capdevila, G., Vega-Villar, J., and Rodrigo, L. (2011). Neurological disorders associated with gluten sensitivity. *Rev. Neurol.* 53, 287–300.

Hetherington, H. P., Spencer, D. D., Vaughan, J. T., and Pan, J. W. (2001). Quantitative (31)P spectroscopic imaging of human brain at 4 Tesla: assessment of gray and white matter differences of phosphocreatine and ATP. *Magn. Reson. Med.* 45, 46–52. doi: 10.1002/1522-2594(200101)45:1 < 46::aid-mrm1008 > 3.0.co;2-*n*

Isamah, N., Faison, W., Payne, M. E., MacFall, J., Steffens, D. C., and Beyer, J. L., et al (2010). Variability in frontotemporal brain structure: the importance of recruitment of African Americans in neuroscience research. *PLoS ONE.* 5, e13642. doi: 10.1371/journal.pone.0013642

Kang, J. S., Klein, J. C., Baudrexel, S., Deichmann, R., Nolte, D., and Hilker, R. (2014). White matter damage is related to ataxia severity in SCA3. *J. Neurol.* 261, 291–299. doi: 10.1007/s00415-013-7186-6

Krahe, J., Binkofski, F., Schulz, J. B., Reetz, K., and Romanzetti, S. (2020). Neurochemical profiles in hereditary ataxias: a meta-analysis of magnetic resonance spectroscopy studies. *Neurosci. Biobehav. Rev.* 108, 854–865. doi: 10.1016/j.neubiorev.2019.12.019

Lirng, J. F., Wang, P. S., Chen, H. C., Soong, B. W., Guo, W. Y., Wu, H. M., et al. (2012). Differences between spinocerebellar ataxias and multiple system atrophy-cerebellar type on proton magnetic resonance spectroscopy. *PloS ONE.* 7, e47925. doi: 10.1371/journal.pone.0047925

Machová, E., O'Regan, S., Newcombe, J., Meunier, F. M., Prentice, J., Dove, R., et al. (2009). Detection of choline transporter-like 1 protein CTL1 in neuroblastoma × glioma cells and in the CNS, and its role in choline uptake. *J. Neurochem.* 110, 1297–1309. doi: 10.1111/j.1471-4159.2009.06218.x

Magon, S., Tsagkas, C., Gaetano, L., Patel, R., Naegelin, Y., Amann, M., et al. (2020). Volume loss in the deep gray matter and thalamic subnuclei: a longitudinal study on disability progression in multiple sclerosis. *J. Neurol.* 267, 1536–1546. doi: 10.1007/s00415-020-09740-4

Manjón, J. V., and Coup,é, P. (2016). volBrain: an online MRI brain volumetry system. *Front. Neuroinform.* 10, 30. doi: 10.3389/fninf.2016.00030

Marsh, M. N. (1995). The natural history of gluten sensitivity: defining, refining and re-defining. *QJM*. 88, 9–13.

Mato Abad, V., Quirós, A., García-Álvarez, R., Loureiro, J. P., Alvarez-Linera, J., Frank, A., et al. (2014). The partial volume effect in the quantification of 1H magnetic resonance spectroscopy in Alzheimer's disease and aging. *JAD* 42, 801–811. doi: 10.3233/JAD-140582

Oz, G., Alger, J. R., Barker, P. B., Bartha, R., Bizzi, A., Boesch, C., et al. (2014). MRS Consensus Group. Clinical proton MR spectroscopy in central nervous system disorders. *Radiology*. 270, 658–679. doi: 10.1148/radiol.13130531

Parisi, P., Pietropaoli, N., Ferretti, A., Nenna, R., Mastrogiorgio, G., Del Pozzo, M., et al. (2015). Role of the gluten-free diet on neurological-EEG findings and sleep disordered breathing in children with celiac disease. *Seizure*. 25, 181–183. doi: 10.1016/j.seizure.2014.09.016

Quadrelli, S., Mountford, C., and Ramadan, S. (2016). Hitchhiker's guide to voxel segmentation for partial volume correction of in vivo magnetic resonance spectroscopy. *Magn. Reson. Insights*. 9, 1–8. doi: 10.4137/MRI.S32903

Sarrigiannis, P. G., Hoggard, N., Aeschlimann, D., Sanders, D. S., Grünewald, R. A., Unwin, Z. C., et al. (2014). Myoclonus ataxia and refractory coeliac disease. *Cereb. Ataxias*. 1, 11. doi: 10.1186/2053-8871-1-11

Sharma, U., and Jagannathan, N. R. (2004). Potential of in vivo magnetic resonance spectroscopy (MRS) in medicine. *Proc. Indian Natl. Sci. Acad*. 70, 555–577.

Sivaswamy, J., Thottupattu, A. J., Mehta, R., Sheelakumari, R., and Kesavadas, C. (2019). Construction of Indian human brain atlas. *Neurol. India*. 67, 229–234. doi: 10.4103/0028-3886.253639

Sommer, M. A. (2003). The role of the thalamus in motor control. *Curr. Opin. Neurobiol*. 13, 663–670. doi: 10.1016/j.conb.2003.10.014

Stoodley, C. J., and Schmahmann, J. D. (2009). Functional topography in the human cerebellum: a meta-analysis of neuroimaging studies. *Neuroimage*. 44, 489–501. doi: 10.1016/j.neuroimage.2008.08.039

Stoodley, C. J., Valera, E. M., and Schmahmann, J. D. (2012). Functional topography of the cerebellum for motor and cognitive tasks: an fMRI study. *Neuroimage*. 59, 1560–1570. doi: 10.1016/j.neuroimage.2011.08.065

Symms, M., Jäger, H. R., Schmierer, K., and Yousry, T. A. (2004). A review of structural magnetic resonance neuroimaging. *J. Neurol. Neurosurg. Psychiatry*. 75, 1235–1244. doi: 10.1136/jnnp.2003.032714

Tal, A., Kirov, I. I., Grossman, R. I., and Gonen, O. (2012). The role of gray and white matter segmentation in quantitative proton MR spectroscopic imaging. *NMR Biomed*. 25, 1392–1400. doi: 10.1002/nbm.2812

Vavla, M., Arrigoni, F., Nordio, A., De Luca, A., Pizzighello, S., Petacchi, E., et al. (2018). Functional and structural brain damage in friedreich's ataxia. *Front Neurol*. 6, 747. doi: 10.3389/fneur.2018.00747

Vinagre-Aragón, A., Zis, P., Grunewald, R. A., and Hadjivassiliou, M. (2018). Movement disorders related to gluten sensitivity: a systematic review. *Nutrients*. 10, 1034. doi: 10.3390/nu10081034

Wilkinson, I. D., Hadjivassiliou, M., Dickson, J. M., Wallis, L., Grünewald, R. A., Coley, S. C., et al. (2005). Cerebellar abnormalities on proton MR spectroscopy in gluten ataxia. *J. Neurol. Neurosurg. Psychiatry*. 76, 1011–1013. doi: 10.1136/jnnp.2004.049809

Zelnik, N., Pacht,. A., Obeid, R., and Lerner, A. (2004). Range of neurologic disorders in patients with celiac disease. *Pediatrics*. 113, 1672–1676. doi: 10.1542/peds.113.6.1672

Zis, P., and Hadjivassiliou, M. (2019). Treatment of neurological manifestations of gluten sensitivity and coeliac disease. *Curr. Treat Options Neurol*. 21, 10. doi: 10.1007/s11940-019-0552-7

Conflict of Interest: The authors declare that the research was conducted in the absence of any commercial or financial relationships that could be construed as a potential conflict of interest.

Publisher's Note: All claims expressed in this article are solely those of the authors and do not necessarily represent those of their affiliated organizations, or those of the publisher, the editors and the reviewers. Any product that may be evaluated in this article, or claim that may be made by its manufacturer, is not guaranteed or endorsed by the publisher.

Advantages of publishing in Frontiers

OPEN ACCESS
Articles are free to read for greatest visibility and readership

FAST PUBLICATION
Around 90 days from submission to decision

HIGH QUALITY PEER-REVIEW
Rigorous, collaborative, and constructive peer-review

TRANSPARENT PEER-REVIEW
Editors and reviewers acknowledged by name on published articles

Frontiers
Avenue du Tribunal-Fédéral 34
1005 Lausanne | Switzerland

Visit us: www.frontiersin.org
Contact us: frontiersin.org/about/contact

REPRODUCIBILITY OF RESEARCH
Support open data and methods to enhance research reproducibility

DIGITAL PUBLISHING
Articles designed for optimal readership across devices

FOLLOW US
@frontiersin

IMPACT METRICS
Advanced article metrics track visibility across digital media

EXTENSIVE PROMOTION
Marketing and promotion of impactful research

LOOP RESEARCH NETWORK
Our network increases your article's readership